Proceedings of The Tenth Asian Congress of Fluid Mechanics
17–21 May 2004, Peradeniya, Sri Lanka

ARE WE CLOSE TO RESOLVING QUESTIONS ON HEAT TRANSPORT SCALING IN TURBULENT CONVECTION?

K. R. Sreenivasan
International Centre for Theoretical Physics, Trieste, Italy

Despite much recent work on turbulent convection, detailed questions on how heat transport scales on the Rayleigh number of the flow, the Prandtl number of the fluid, the aspect ratio of the apparatus, and so forth, have remained partially unanswered. The lecture intends to summarize aspects that have slowed progress, and to share the latest attempts made to resolve them.

Since this lecture honours the memory of Professor Satish Dhawan, a giant figure that he was, a brief summary of his contributions to fluid dynamics will be attempted.

Editor's Note: Full paper not received in time for publication.

Proceedings of the Tenth Asian Congress of Fluid Mechanics
17-21 May 2004, Peradeniya, Sri Lanka

ELEMENTARY VORTEX: ITS DYNAMICAL ROLES IN TURBULENCE

S. Kida
(Department of Mechanical Engineering, Kyoto University, Kyoto, 606-8501, Japan)

ABSTRACT: The elementary vortex is the smallest vortical structure commonly observed in various kinds of turbulence. It plays important roles in turbulence dynamics, such as mixing and vortex generation. A series of studies on the elementary vortex is reviewed, including an eduction method of the vortex by the low-pressure criterion and enhancement of stretching of fluid lines.

1. INTRODUCTION

Turbulence is composed of many vortical motions of different sizes and shapes. The knowledge of the physical characteristics of individual vortices is helpful for understanding of turbulence dynamics. It is generally recognized that tubular swirling regions of high vorticity exist in various kinds of turbulence. They are nicknamed worms in isotropic turbulence, streamwise vortices in wall turbulence, rolls and ribs in free-shared turbulence, and so on. Although the shape of the cross-section and the length of such tubular vortices vary from turbulence to turbulence, the size of the cross-section and the swirl velocity obey, in average, the Kolmogorov scaling law. They are regarded as the smallest vortical structure in turbulence, so that they are called the elementary vortex. The elementary vortex plays significant roles in turbulence dynamics, such as generation and sustenance of turbulence, diffusion and mixing, etc. Here, we review a series of studies on the elementary vortex performed these years by our research group.[1−5]

An eduction method of the elementary vortex from a turbulent field is introduced in §2. A vortex is identified as a low-pressure region and the physical characteristics are discussed. The dynamical roles of the elementary vortex in deformation and stretching of fluid lines are examined in §3. Finally, a future direction in the study of the elementary vortex is viewed in §4.

2. LOW-PRESSURE CRITERION

Among a variety of vortices we focus here the tubular vortices. The pressure is lowered at the central axes of tubular vortices to counter-balance the centrifugal force caused by the swirling motion around the vortices. This fact motivates us to identify and extract the tubular vortices as the low-pressure regions, which are found numerically by searching lines of local minimum (in a plane perpendicular to the line) of pressure. First, we define a plane, at any point $\boldsymbol{x}$ in a flow, that is perpendicular to the eigen-vector of the pressure hessian having the smallest eigen-value. Then, we check whether the pressure on this plane takes a minimum at $\boldsymbol{x}$ or not. The axis of a vortex is constructed by connecting properly the minimum-pressure points thus obtained. The pressure on the plane is concave in the vicinity of $\boldsymbol{x}$. Generally, there is an inflection closed line surrounding $\boldsymbol{x}$ on this plane, across which the concavity of the pressure changes the sign. In the three-dimensional space it gives an inflection surface which defines the core boundary of the elementary vortex (Fig. 1). See references [1,2] for the numerical algorithm.

This low-pressure criterion is applied to an isotropic turbulence, and the axes of elementary vortices are depicted in Fig. 2. Spirals attached to some of the axes are the streamlines which are viewed in frames moving with velocity of the nearest part of the axes. Note that the spiralling streamlines are generally not observed in a fixed frame.

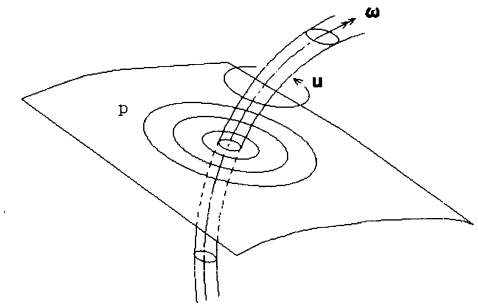

Fig. 1: An elementary vortex. The axis and the core boundary are defined by a line of local minimum of pressure and a surrounding inflection surface.

Visualization of the elementary vortex by the low-pressure criterion reveals some new interesting features of structure and dynamics of vortices.

First, every vortex accompanies the double vortex layers wrapping it. In Fig. 3 we show the vorticity magnitude in a cross-section of a vortex located at the center. High-vorticity is observed not only in the central circular region but also in two surrounding round layers. The vorticity in the central region is parallel to the vortex axis, whereas that in the layers has large angles with the axis. These layers play important roles in enhancement of mixing and of energy dissipation.

Secondly, the physical characteristics of the elementary vortex are evaluated quantitatively. Their diameter in cross-section is about ten times the Kolmogorov length η, and the swirl velocity is about three times the Kolmogorov velocity.

Thirdly, two vortices often approach each other in an anti-parallel manner, i.e. their vorticities are opposite. Therefore, they tend to be broken down due to cross diffusion of vorticity. Anti-parallel pairs of vortices advect quite rapidly in a turbulent flow with mutually induced velocity, which play significant roles in stretching of fluid lines (see §3).

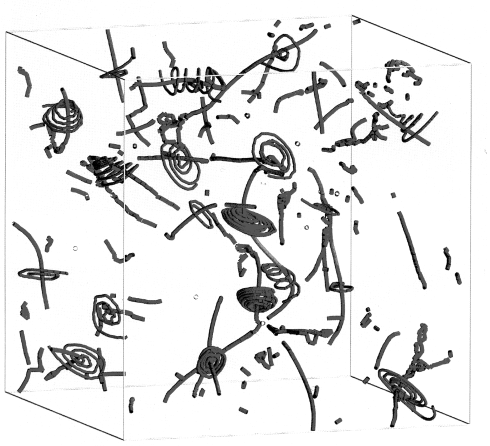

Fig. 2: Axes of elementary vortices and streamlines relative to the axes in a freely decaying turbulence.[1]

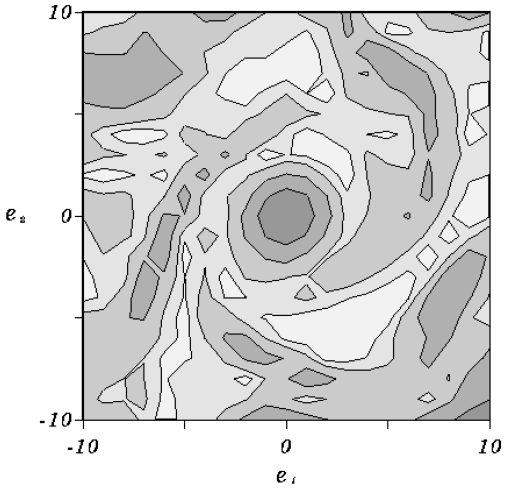

Fig. 3: Double spiral structure. Contours of vorticity magnitude on a cross-section of an elementary vortex which is located at the center. Darker shade implies larger values. The coordinate of the cross-section is measured in the unit of the grid width Δx taken in the numerical simulation. The Kolmogorov length is $2\Delta x$.

3. STRETCHING OF FLUID LINES

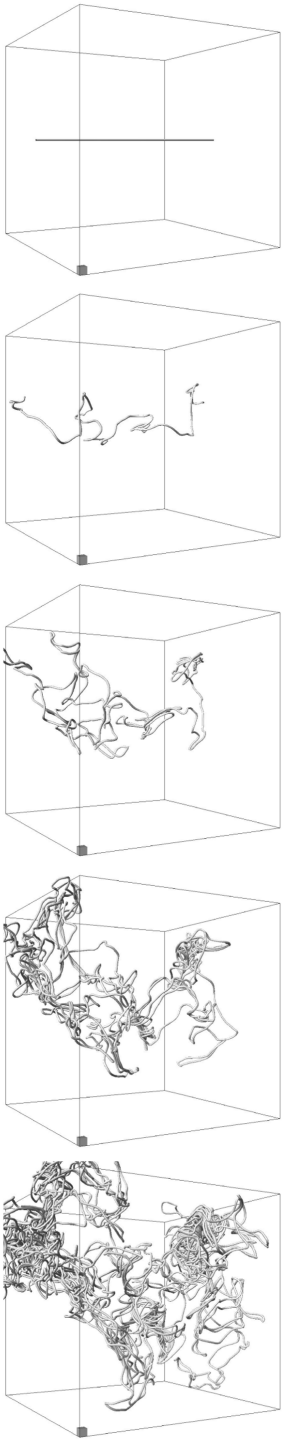

The transport, such as mixing and diffusion, of material objects is one of the most important dynamical properties of fluid flows. The reliable prediction and efficient control of transport coefficients are desirable in various industrial processes as well as in conservation of environment. The efficiency of transport varies depending on the state of fluid motions. It is much enhanced in turbulent states in comparison with laminar states. The complexity of fluid motions, especially, of turbulence, however, makes it very difficult to reveal the mechanism of mixing though some statistically averaged properties have been established. Here, we investigate the deformation of a fluid line, as a fundamental material object, in turbulence with special attention to the dynamical role of the elementary vortex.[6–8]

A fluid line in a statistically stationary turbulence, initially straight, is traced numerically. A temporal evolution of the fluid line is drawn in Fig. 4. Time elapses from top to bottom. Large cubes represent the whole computational domain, the side length of which is about $2\mathcal{L}$, where $\mathcal{L}$ is a length which characterizes energy-containing-scale motions. The side length of small cube is 10η which is comparable with the mean diameter of the elementary vortex. As time progresses, the line gets more and more convoluted. The total length increases, in average, exponentially in time as $L(t) \propto \exp[\gamma t/\tau_\eta]$, where $\gamma = 0.17$ and τ_η is the Kolmogorov time. The radius of curvature is comparable with the mean diameter of the elementary vortex, suggesting that the elementary vortex is involved in deformation of fluid lines.

Anti-parallel pairs of elementary vortices may give a significant contribution to the stretching. In Figs. 5 we show two different views of three nearly-aligned vortices and deformed fluid lines around them.[8] In the top view (Fig. 5(a)) observed are the characteristics of stretching on cross-sections of the vortex cluster, where the central vortex induces a clockwise swirling flow, and the other two vortices do anti-clockwise ones. Two clusters, i.e. a left vertical and the central horizontal white lines, of strongly stretched parts of a fluid line form a T-shape. In a side view (Fig. 5(b)) almost all the strongly stretched parts of the fluid line are parallel to each other and perpendicular to the vortices. In other words, the strong stretching can be regarded as a two-dimensional phenomenon.

Fig. 4. Temporal evolution of a fluid line. Time elapses from top to bottom by $0.2\mathcal{T}$, where $\mathcal{T}$ is an energy-containing-scale time. $R_\lambda = 83$.

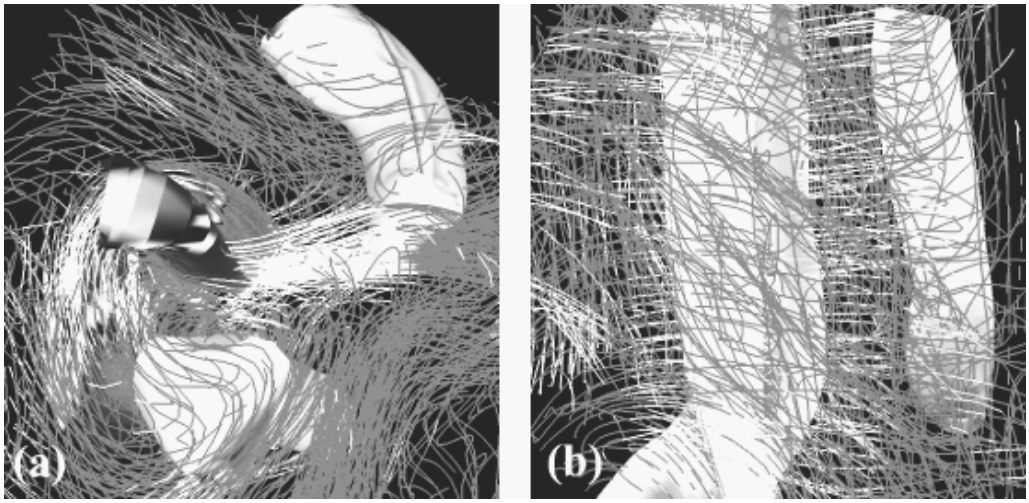

Fig. 5: Stretching enhancement by a vortex cluster. Three thick tubes represent the elementary vortices identified by the low-pressure criterion. Many lines represent a single fluid line with white for strongly stretched parts. Three vortices nearly aligned are seen from two different angles. (a) Top view. The central vortex rotate clockwise and the other two counter-clockwise. (b) Side view. Vorticity of the central vortex points downward and the other two upward.

4. PROSPECTIVE

The elementary vortex educed by the low-pressure criterion is identified individually. Any physical structure can be analyzed by use of various visualization techniques. We have developed an algorithm to trace the temporal evolution of each vortex.[4] A numerical simulation/visualization analysis using the elementary vortex is expected to be useful for understanding of the mechanism of generation, development and decay of vortical structures in turbulence.

REFERENCES

[1] Miura H and Kida S: Identification of tubular vortices in turbulence. *J. Phys. Soc. Jpn.* 1997, **66**, 1331-1334.

[2] Kida S and Miura H: Swirl condition in low-pressure vortices. *J. Phys. Soc. Jpn.* 1998, **67**, 2166-2169.

[3] Kida S and Miura H: Double spirals around a tubular vortex in turbulence. *J. Phys. Soc. Jpn.* 2000, **69**, 3466-3467.

[4] Kida S, Miura H and Adachi T: Flow structure visualization by low-pressure vortex. In Vassilicos JC ed. *Intermittency in Turbulent Flows*, Vol. 69. Cambridge University Press, Cambridge, 2001, 262-276.

[5] Makihara H, Kida S and Miura H: Automatic tracking of low-pressure vortex. *J. Phys. Soc. Jpn.* 2002, **71**, 1622-1625.

[6] Batchelor GK: The effect of homogeneous turbulence on material lines and surfaces. *Proc. R. Soc. Lond. A* 1952, **213**, 349–366.

[7] Kida S and Goto S: Line statistics: Stretching rate of passive lines in turbulence. *Phys. Fluids*, 2002, **14**, 352–361.

[8] Goto S and Kida S. Enhanced Stretching of Material Lines by Antiparallel Vortex Pairs in Turbulence. *Fluid Dyn. Res.* 2002, **33**, 403-431.

Proceedings of The Tenth Asian Congress of Fluid Mechanics
17–21 May 2004, Peradeniya, Sri Lanka

CRITICAL PROCESSES IN GEOPHYSICAL FLOWS WITH STRATIFICATION AND TURBULENCE

Julian Hunt
Department of Space & Climate Physics, University College London, United Kingdom

Editor's Note: Paper not received in time for publication.

Proceedings of the Tenth Asian Congress of Fluid Mechanics
17-21 May 2004, Peradeniya, Sri Lanka

ON THE CONTACT ANGLE IN UNSTEADY FLOWS

P.N.Shankar and R. Kidambi
Computational & Theoretical Fluid Dynamics Division,
National Aerospace Laboratories, Bangalore 560 017, India.

ABSTRACT: We show that in general, the specification of a contact angle condition at the contact line in inviscid fluid motions is incompatible with the classical field equations and boundary conditions generally applicable to them. The limited conditions under which such a specification is permissible are derived; however, these include cases where the static meniscus is not flat. In view of this situation, the status of the many 'solutions' in the literature which prescribe a contact angle in potential flows comes into question. When the fluid is viscous, it is shown that if the contact line is pinned the contact angle has to remain constant. Some implications of this result are discussed.

1. INTRODUCTION

Consider a liquid, under a passive, inert gas, partially filling a smooth walled container. A gravitational field acts on the liquid. The liquid gas interface is subject to surface tension. The interface meets the walls of the container at a line called the contact line. At any point on the contact line, the angle between the normal to the gas-liquid interface and the normal to the solid wall is called the contact angle, α. In the quiescent state, for many pure materials and smooth solid surfaces, the contact angle for many gas/liquid/solid systems is a function of the materials alone. Here, we will assume this to be true and call this contact angle, the static contact angle α_s.

The surface tension at the gas-liquid interface, from now on called the interface, requires that there be a jump in the normal stress across it if it is not flat. In the inviscid case the jump is in the pressure and for a static interface the liquid pressure is just the hydrostatic pressure. Thus the shape of the static interface depends on a Bond number Bo, the ratio of a measure of the gravitational force to a measure of the force due to surface tension. But this shape also depends on the static contact angle α_s, which provides a boundary condition for the differential equation that determines the static interface shape. The static contact angle is therefore a parameter that influences the static meniscus shape and needs to be prescribed in order to calculate the meniscus shape.

When the interface is in motion, the surface tension again requires that a pressure jump, proportional to the interface curvature and to the coefficient of surface tension, exist across it. While the pressure in the liquid will now be determined by the unsteady Bernoulli equation in the inviscid case, in the viscous case the normal stress will be determined from the Navier-Stokes equations. The situation as regards the contact angle, however, is more complicated and confused. If one examines the dynamical equations for the interface it is not at all obvious that one needs to prescribe a condition on the contact angle. Moreover, as is well known, for the case of linearized disturbances between plane, vertical walls where the initial interface is plane, the classical inviscid solution can be obtained without any specification of the contact angle, which turns out to be constant and equal to $\pi/2$ throughout the motion. On the other hand, there are many examples in the literature where analyses and calculations have been made of unsteady potential motions where a condition on the contact angle has been prescribed as a boundary condition at the contact

line. Just a short list of these could include Billingham[3], Miles[7] and Shankar[10]. It appears that the motivation to prescribe the contact angle comes from the apparent behaviour of real, viscous interfaces and the need to tailor inviscid models so that they lead to realistic results for real interfaces. The question that we raise here is: are we really free to prescribe the contact angle in inviscid potential flows?

When the liquid is viscous, the situation is made more complicated by the uncertainties associated with a moving contact line, continually made of new material particles. We will restrict ourselves here, in the viscous case, to motions in which it is fixed. Also, since we do not want to deal with situations where the static meniscus itself is not unique, we will through out assume that there is no contact angle hysteresis. The method we use is very similar to the one used by Benjamin & Ursell[2] ; however we will not restrict ourselves to the linearized case or to one where the mean interface is flat and there will be no restriction on the shape of the container. We will in fact show that the contact angle is actually constant for this class of viscous motions.

Some implications of these results will be discussed.

2. ANALYSIS OF INVISCID FLOWS

We consider the inviscid motion of a liquid in an arbitrary, three-dimensional smooth walled container. The motion is generated by the translational motion of the container. The restriction to translational motions is essential to ensure potential flow in the moving frame, a necessary condition for some of the results that will be derived. The fluid is initially in static equilibrium with the gas above it which is at uniform pressure.[1] The motion is assumed to start and continue with a uniform pressure over the interface; we will assume the gas to be passive, i.e. it only exerts a constant pressure on the liquid interface. In §2.1, we write down the equations governing the motion. In §2.2, we consider planar motions and in §2.3 we summarise the main results.

2.1 Governing equations

We write the equations in a reference frame attached to the container. The container wall is given by $f(x, y, z) = 0$. Rectangular cartesian coordinates are employed with gravity generally in the negative z-direction. Our analysis is restricted to the case when the interface is representable by a single valued smooth function, e.g. by $z = \zeta(x, y, t)$. The interface motion can be of finite amplitude however. The equations governing the liquid motion are the continuity and Euler equations -

$$\nabla \cdot \mathbf{u} = 0, \tag{1}$$

$$\mathbf{u}_t + (\mathbf{u} \cdot \nabla)\mathbf{u} = -\nabla p + \mathbf{F} \tag{2}$$

where $\mathbf{u}$ is the liquid velocity, p is the pressure and $\mathbf{F}$ is the net body force, both real and fictitious. $\mathbf{F}$ can be an arbitrary function of time. These have to be solved subject to the boundary conditions on (a) the container wall and (b) the interface. The condition on the wall is the no-penetration condition $\mathbf{u} \cdot \nabla \mathbf{f} = 0$. The conditions on the interface $z = \zeta(x, y, t)$ are

$$\zeta_t + u\zeta_x + v\zeta_y = w, \tag{3a}$$

$$p - p_a = -\frac{1}{Bo}\kappa \tag{3b}$$

[1]The condition of static equilibrium can be relaxed and, in fact, has to be in the case of time periodic wave motions.

which respectively are the kinematic condition on the interface and the normal stress condition on it. Bo is a suitably defined Bond number, p_a is the constant ambient pressure over the interface and κ is the local interface curvature. The interface $z = \zeta(x, y, t)$ is assumed to intersect the container wall $f(x, y, z) = 0$ in a smooth curve called the contact line. It is further assumed that ζ is analytic in all variables. The possibly time dependent angle α made by the contact line with the wall is given by

$$\frac{f_z - f_x\zeta_x - f_y\zeta_y}{|\nabla f|[1 + \zeta_x^2 + \zeta_y^2]^{\frac{1}{2}}} = \cos\alpha(t) \tag{4}$$

where (4) is to be evaluated at any point $(x_c(t), y_c(t), \zeta(x_c(t), y_c(t), t))$ on the contact line. We will show that no *a priori* prescription of $\alpha(t)$ is possible though in a few cases, it turns out to be a constant equal to its initial value α_s.

2.2 Planar inviscid motions with flat side walls

The container is straight walled, but not necessarily rectangular, and the motion is 2-D in the $x - z$ plane. The contact line in this case consists of just two points (A and B, say). The x and z axes are chosen such that, locally, the body surface is a line of constant x, say $x = 0$. There will be an x component of gravity in this case; the gravity direction has no bearing on the analysis however. The no-penetration condition implies $u(0, z, t) = 0$ from which it follows that $u_{z^{(n)}}(0, z, t) = 0$ where $u_{z^{(n)}}$ is the n^{th} derivative of u with respect to z.

Now, differentiate (3a) with respect to x to obtain an equation valid on the interface and hence on the contact line -

$$\begin{aligned}\zeta_{xt}(x,t) + u(x,\zeta(x,t),t)\zeta_{xx}(x,t) + [u_z(x,\zeta(x,t),t)\zeta_x(x,t)\\ +u_x(x,\zeta(x,t),t)]\zeta_x(x,t) = w_x(x,\zeta(x,t),t) + w_z(x,\zeta(x,t),t)\zeta_x(x,t).\end{aligned} \tag{5a}$$

Using the fact that an inviscid flow starting from rest has to be irrotational both in an inertial frame and a frame translating with respect to the inertial, we get $u_z - w_x = 0$, which with the continuity equation $u_x + w_z = 0$ allows (5a) to be written in the form

$$\zeta_{xt} = u_z - (2u_x + \zeta_x u_z)\zeta_x - u\zeta_{xx}. \tag{5b}$$

where the arguments in (5a) have been dropped to reduce the clutter. When (5b) is applied at the contact line we obtain

$$\zeta_{xt}(0,t) = -2u_x(0,\zeta(0,t),t)\zeta_x(0,t). \tag{6}$$

Note that, if the container were to be rotating as well, $u_z - w_x \neq 0$ and the above analysis would not apply. (6) shows that ζ_{xt} at the contact line cannot be specified arbitrarily; it certainly is not zero in general. This means that the contact angle changes with time in a manner that cannot be prescribed beforehand. However, for $\alpha = \pi/2$, not only is $\zeta_{xt}(0,0) = 0$ but also $\zeta_{xt^{(k)}}(0,0) = 0$ for all $k = 2, 3, \cdots$. We will show this by mathematical induction. Let the induction proposition be

$$P(k) : \zeta_{xt^{(m)}}(0,0) = 0 \ \forall\, m = 0, ..., k.$$

$P(0)$ is true because $\alpha_s = \pi/2$. Assume $P(k)$ is true; we will show that $P(k+1)$ is true. Rewriting (5b) as $\zeta_{xt} = u_z - a(u,\zeta)\zeta_x - u\zeta_{xx}$, the k^{th} time derivative of this equation can be written

$$\zeta_{xt^{(k+1)}} = u_{zt^{(k)}} - [a\zeta_x]_{t^{(k)}} - (u\zeta_{xx})_{t^{(k)}}.$$

With respect to the above equation, we observe the following -

1. $\partial\{u_z\}/\partial t^k = 0$ at x = 0 $\forall$ k = $0, 1, 2, \cdots$
2. $\partial\{a\zeta_x\}/\partial t^k = \sum_{m=0}^{k} b_m a_{t^{(k-m)}} \zeta_{xt^{(m)}}$ where b_m is the binomial coefficient $C(k, m)$. By the truth of $P(k)$, this sum is zero at $x = 0$.
3. $\partial\{u\zeta_{xx}\}/\partial t^k = \sum_{m=0}^{k} C(k, m) u_{t^{(k-m)}} \zeta_{xxt^{(m)}}$. This sum is zero $\forall\, k = 0, 1, \cdots$ as u and all its time derivatives vanish on the contact line.

Thus we have $\zeta_{xt^{(k+1)}}(0, 0) = 0$ which means $P(k + 1)$ is true. Thus, by mathematical induction, $P(n)$ is true $\forall n = 0, 1, \cdots$ and so $\zeta_{xt}(0, t) = 0$. This in turn implies that $\zeta_x(0, t) = 0$ for all time and the contact angle remains at $\pi/2$ for all time. Some observations are noteworthy -

1. Irrotationality of the motion is necessary but not sufficient.
2. This is a nonlinear result i.e. it holds irrespective of the perturbation amplitude and the shape of the static meniscus as long as the initial contact angle α_s is $\pi/2$. In particular, the static meniscus need not be flat.
3. The result holds as long as the region of the body surface over which the contact line moves is flat. The shape of the body elsewhere is immaterial.

2.3 A summary of the results in the inviscid case

A similar analysis can be carried out for 2-D inviscid flows where the side walls are curved; it is found that the contact angle is not preserved even for linearized motions with $\alpha_s = \pi/2$. In 3-D it is found that apart from small disturbances to a flat interface ($\alpha_s = \pi/2$) in a right cylinder of arbitrary cross section, the contact angle is not preserved. Thus the important point is that in inviscid fluid motions starting from rest in a container, the contact angle cannot be prescribed in advance and neither is there need for such a prescription. However, if one insists on prescribing the contact angle, this would necessarily result in a 'weak-type' solution - one that is in violation of the actual behaviour of the contact angle. However, in the special case of $\alpha_s = \pi/2$, there exist situations where the contact angle remains constant throughout the motion. These situations include cases of curved static menisci.

3. ANALYSIS OF VISCOUS FLOWS

We write the equations in a reference frame attached to the moving container. The container wall is given by $f(x, y, z) = 0$. Rectangular cartesian coordinates are employed with gravity in the negative z-direction. Our analysis is restricted to the case when the interface is representable by a single valued smooth function i.e. by $z = \eta(x, y, t)$. The interface motion can be of finite amplitude however. The equations governing the liquid motion are the continuity and the Navier-Stokes equations -

$$\nabla \cdot \mathbf{u} = 0, \tag{7a}$$

$$\mathbf{u}_t + (\mathbf{u} \cdot \nabla)\mathbf{u} = -\nabla p + \mathbf{F} + \frac{1}{Re}\nabla^2 \mathbf{u} \tag{7b}$$

where $\mathbf{u}$ is the liquid velocity, $\mathbf{F}$ is the net body force, both real and fictitious and Re a suitably defined Reynolds number. $\mathbf{F}$ can be an arbitrary function of time. These have to be solved subject

to the boundary conditions on (a) the container wall and (b) the interface. The condition on the wall is the no-slip condition $u = v = w = 0$ where u, v and w are the x, y and z components of velocity. The conditions on the interface $z = \eta(x, y, t)$ are[6]

$$\eta_t + u\eta_x + v\eta_y = w, \tag{8a}$$

$$\eta_x(v_z + w_y) - \eta_y(u_z + w_x) + 2\eta_x\eta_y(u_x - v_y) - (\eta_x^2 - \eta_y^2)(u_y + v_x) = 0, \tag{8b}$$

$$2\eta_x^2(u_x - w_z) + 2\eta_y^2(v_y - w_z) + 2\eta_x\eta_y(u_y + v_x) + (\eta_x^2 + \eta_y^2 - 1)\{\eta_x(u_z + w_x) + \eta_y(v_z + w_y)\} = 0, \tag{8c}$$

$$p - \frac{2}{Re}\frac{\eta_x^2 u_x + \eta_y^2 v_y - \eta_x(u_z + w_x) - \eta_y(v_z + w_y) + \eta_x\eta_y(u_y + v_x) + w_z}{1 + \eta_x^2 + \eta_y^2} = p_a - \frac{1}{Bo}\kappa \tag{8d}$$

which respectively are the interface integrity, the two tangential stress and the normal stress conditions on the interface.

Analysis similar to that in §2 shows that if the contact line is pinned the contact angle α is constant and remains at its initial value α_s.

4. DISCUSSION

Recall that in the classical works the question of the contact angle never arose because confined flows with boundaries and capillarity were not normally studied. Early studies on the latter were confined to linearized, two-dimensional flows between vertical walls; here the classical, exact solutions correspond to a contact angle of $\pi/2$, which is maintained throughout the motion. In the 1960s the space programmes required solutions to more general problems involving curved static interfaces and static contact angles other than $\pi/2$. The difficulty posed by these problems forced approaches that were either semi-analytical or numerical and some like Moore & Perko[8] did not attempt to impose a dynamical contact angle condition; α_s affected the initial conditions alone through the static meniscus. The imperative to impose a contact angle condition at the contact line, not permitted in general by the classical inviscid formulation, appears to have come from experimental observations of real, viscous contact lines. It is well known[4] that real, dynamic viscous contact lines display complex behaviour and are not at all well understood with many parameters playing a role. It is in attempting to model this complicated behaviour in an inviscid frame work that the need for contact angle conditions began to be felt and then applied. The earlier models of a constant contact angle and the one used by Reynolds and Satterlee[9] (essentially to model contact angle hysteresis) are in a sense non-dynamic. Hocking's[5] model is a dynamic one, attempting in an inviscid framework to account for contact line hysteresis or viscous wetting effects at the contact line. In any case, the purpose is to account for viscous and other real effects in a inviscid, potential model of the flow.

Thus the need to more realistically model the dynamic contact line appears to require the freedom to *impose* a condition at the inviscid contact line. But as was shown in §2 the classical field equations and boundary conditions do not in general provide this freedom. Then the natural question is, what is the status of the very large and important body of work in which a contact angle condition is imposed, in violation of the classical formulation? Let us call solutions which are obtained without such a condition 'classical'. Then this body of work referred to does not deal with classical solutions. This means that these 'solutions' will be found to violate at least

some of the boundary conditions at the contact line. The best of these will exactly satisfy the field equations and boundary conditions everywhere else. For want of a better terminology, we will call these solutions 'weak-type solutions', well aware of how imprecise this is.[2] . Even if the 'solutions' found in the literature were exact it is unlikely that they would all fall into the same class of 'weak-type solutions' because the formulations are so different. To make matters worse all the 'solutions' in the literature are approximate; there are no exact solutions even for the simplest of problems. However, the situation is not as bad as it appears. Checks are made between different approaches and with experimental results for the same problem; when there is reasonable agreement between these, which can be improved with further work, one can have some confidence that, at least from a phenomenological point of view if not a mathematical one, the 'solutions' are satisfactory.

On the other hand when the fluid is viscous, we have shown that if the contact line is pinned the contact angle has to remain constant. There are a number of important implications of this result. For example, if a viscous liquid is slowly draining from a container, the contact angle has to remain constant in the draining film at the wall, at least as long as the continuum model holds. Similarly if a plate is withdrawn from a viscous liquid the contact angle has to remain constant. Other interesting consequences will be considered in the talk.

5. CONCLUSION

We have shown that the classical field equations governing the motion of a confined inviscid liquid under a passive gas do not, in general, permit the independent specification of a contact angle condition at the contact line. In fact the only cases where such a condition may be permissible are when the static contact angle is $\pi/2$, the container is straight walled and (i) the motion is two-dimensional or (ii) the motion is a small three-dimensional disturbance from a flat initial interface. The restrictions are indeed surprising as is the difference between two- and three-dimensional motions.

These results have a somewhat serious bearing on the vast literature that exists in which 'solutions' have been found to inviscid motions in which various contact angle conditions have been imposed. It is our contention that these cannot be classical solutions to the classical field equations since classical solutions do not permit the imposition of a contact angle condition. It is suggested that these 'solutions' belong to an improperly defined class of 'weak-type solutions', in the sense that they attempt to solve the field equations in an approximate sense, with some of the equations being solved exactly. The need for such 'solutions' is driven by the compulsion to try to model in an inviscid frame work, the complicated behaviour of moving viscous contact lines.

For a viscous liquid, the contact angle has to remain constant if the contact line is pinned. This result has a number of important consequences, for example in liquid draining and in the drag out problem.

REFERENCES

[1] Benjamin TB and Scott JC. Gravity-capillary waves with edge constraints. *J. Fluid Mech.* 1979, **92**, 241-267.

[2] On the other hand, note the trouble that was taken by Benjamin & Scott[1] to make precise in what sense their solution was a weak solution

[2] Benjamin TB and Ursell F. The stability of the plane free surface of a liquid in vertical periodic motion. *Proc. R. Soc. Lond.* 1954, **A225**, 505-515.

[3] Billingham J. Nonlinear sloshing in zero gravity. *J. Fluid Mech.* 2002, **464**, 365-391.

[4] Dussan V EB. On the spreading of liquids on solid surfaces : static and dynamic contact lines. *Annu. Rev. Fluid Mech.* 1979, **11**, 371-400.

[5] Hocking LM The damping of capillary-gravity waves at a rigid boundary. *J. Fluid Mech.* 1987, **179**, 253-266.

[6] Johnson RS. *A modern introduction to the mathematical theory of water waves.* Cambridge: Cambridge University Press, 1997.

[7] Miles J. The capillary boundary layer for standing waves. *J. Fluid Mech.* 1991, **222**, 197-205.

[8] Moore RE and Perko LM. Inviscid fluid flow in an accelerating container. *J. Fluid Mech.* 1965, **22**, 305-320.

[9] Reynolds WC and Satterlee HM. 1966 "Liquid propellant behaviour at low and zero g", Chapter 11 in Abramson, H.N. *The Dynamic Behaviour of Liquids in Moving Containers*, NASA publication SP-106. 1966, 387-439.

[10] Shankar PN. A simple method for studying low-gravity sloshing frequencies. *Proc. R. Soc.* 2003, A **459**, 3109-3130.

Proceedings of the Tenth Asian Congress of Fluid Mechanics
17-21 May 2004, Peradeniya, Sri Lanka

THE THREE VORTEX PROBLEM AND ITS RAMIFICATIONS

H. Aref
Department of Engineering Science and Mechanics, Virginia Polytechnic Institute and State University

ABSTRACT: A survey of work on the problem of three interacting point vortices, spanning some 125 years, starting with the 1877 thesis of Gröbli, is reviewed. The pivotal role of three-vortex dynamics in several contexts is highlighted.

1. GENERAL OVERVIEW OF THE LECTURE

One may well question the rationale behind giving a lecture at a state-of-the-art meeting on fluid mechanics in 2004 on such an apparently narrow and classical subject as the motion of three interacting point vortices. The reasons for doing so are set out here.

First, in order to discuss this problem it is necessary to bring together aspects of vortex dynamics and the theory of dynamical systems, and to develop the point vortex equations. This in itself provides a sweep through some not inconsequential fluid mechanics.

Second, the problem of three interacting point vortices is quite rich, a lot richer, for example, than its two-body Kepler problem "counterpart" in the mechanics of gravitating mass points. The mathematical exploration of the three-vortex problem brings out a large number of interesting ideas and constructs, many of which go well beyond the confines of the problem itself: canonical transformations, trilinear coordinates [1, 23], projective geometry [4], and elliptic functions [22] are just some of the mathematical tools that one has the opportunity to see "in action" while solving the three-vortex problem in its various settings.

Third, much of the research literature on few-vortex problems is not well known. Even among those familiar with the point vortex equations – and most fluid mechanicians are – the classic work by Gröbli in the late 19th century on the reduction of the three-vortex problem to quadratures is not widely appreciated. And among those who at a formal level understand that the three-vortex problem must be integrable, the details of this problem, i.e., an understanding of the different types of motion that arise as the vortex strengths are varied, is usually lacking. The answer to the question: "What happens in the three-vortex problem?" is long and relatively complex.

The dynamical system defined by three point vortices is integrable on the unbounded plane and in a periodic parallelogram (where periodicity guarantees that the circulations of the three vortices sum to zero). It is not integrable, in general, if the vortices are enclosed in a circular domain, although the two-vortex problem is. For general domains only the one-vortex problem is integrable. Physical many-body systems for which the three-body problem is integrable (without the N-body problem for all larger N being integrable) are rare, so the three-vortex problem is intrinsically interesting for this reason alone. In the two-vortex problem on the unbounded plane the distance between the two vortices is a constant of the motion. One has to go to three vortices in order to achieve relative motion of the vortices and thus temporal changes in the "scales of motion" defined by the inter-vortex distances. This identifies three-vortex motion as the simplest "generator" of the kind of configurations observed in two-dimensional turbulence, a model problem of considerable importance to our understanding of atmospheric and oceanographic flows. For all these reasons some time spent studying the three-vortex problem is not without its rewards.

Fourth, as my understanding of this problem has progressed, it has become increasingly clear that a substantial number of flow phenomena can be explained, or at least partially understood, by appealing to 2D few-vortex motions. There has been a feedback loop at work here, of course: Some experiments have been done precisely because point vortex results suggested that interesting behavior would arise. On the

other hand, as we learn more about what few-vortex systems can do, various experimental results will yield to interpretation in these terms.

The history of few-vortex dynamics in general, and the three-vortex problem in particular, displays an intriguing pattern of discovery and re-discovery. Key results were obtained and then forgotten only to be re-obtained decades later. The interested researcher must, therefore, piece together an account from papers in diverse journals in several languages written over more than a century. The cast of contributors includes several of the great fluid mechanicians and applied mathematicians whose work can be found with relative ease in any modern scientific library: Helmholtz [14, 24], Kirchhoff, Kelvin, Poincaré [19] and Zhukovskii. Two key contributions, however, are the thesis by an almost entirely forgotten Swiss mathematician, W. Gröbli [12], who flourished briefly in research during the period 1875-1880, and a paper by the distinguished applied mathematician J. L. Synge [23], published in the first volume of *Canadian Journal of Mathematics.* Both works have remained unappreciated and largely forgotten until recently.

In this context it is interesting to look up various well known texts to see what the casual reader might derive is known about the N-vortex problem for $N \geq 3$. Among the books that treat point vortex dynamics (and not all do) essentially all give the solution of the two-vortex problem. Many do not even mention the three-vortex problem, presumably on the assumption that it is as complicated as the (generally nonintegrable) three-body problem of celestial mechanics. The singularly influential text by Batchelor [9] contains the following: "When $N = 3$, the details of the motion are not evident, but the ... invariants [of the problem] suggest that all three vortices remain within a distance ... [set by the initial conditions] from the centre of vorticity (except in a case in which the sum of two of [the circulations] is close to zero) and that the distance between any two vortices can never be much less than the smallest distance between any pair of vortices initially." (This turns out to be false in the particular case of what is known as "vortex collapse" [1, 17].) In the classic text by Lamb [16] one finds a footnote reference to the work of Gröbli, with the understated comment that the paper "contain[s] other interesting examples of rectilinear vortex-systems."

Modern interest in the three-vortex problem owes much to a 1975 paper by E. A. Novikov [18]. In essence, Novikov independently re-discovered the solution for the motion of three identical vortices that Gröbli had found a century before. In 1979 while generalizing Novikov's results, and being also unaware of Gröbli's and Synge's 1949 work, I rediscovered much of what they had done [1]. The reason both Novikov's work and my generalization were published in reputable journals was, of course, that the earlier contributions had been entirely forgotten by the fluid mechanics community, including by the referees of our papers. None of the experts in vortex dynamics knew that the problem had already been solved. Hence, both as a scientific problem and as a curious chapter in the history of fluid mechanics the three-vortex problem has held a particular fascination.

Sometime in the Fall of 1985 I received a telephone call from Nicholas Rott, a distinguished Swiss aerodynamicist retired from the Eidgenössische Technishe Hochschule (ETH) in Zürich working at Stanford University. Rott had read my review article [2] in which there is a brief mention of the history of the three-vortex problem and references to the works by Gröbli and Synge. He called to tell me that when he was a student at the ETH, his professor Jakob Ackeret, one of the "grand old men" of aerodynamics, had regularly included in his lectures a description of the three-vortex problem and had shown illustrations from the work by Gröbli. This contact and mutual interest led to discussions on how one might make Gröbli's work more accessible and rescue it from obscurity. A number of obvious issues were considered: Would it be appropriate to publish a full translation of Gröbli's thesis? What had subsequently happened to Gröbli whose dissertation work had clearly been so very well received? Had he done other work in fluid mechanics or mathematics? And so on.

It was ultimately agreed that publication of a translation of a century old dissertation was probably not of sufficient interest to modern day readers – some indication of more recent developments would be required. A detailed historical study was probably not appropriate either, nor were we the right individuals to undertake it. In the end, with the help of some successful detective work by Prof. Hans Thomann, Rott's successor at the ETH, a historical appreciation of Gröbli's work was prepared [7].

Rott went on to do an intriguing analysis of the case of three vortices with zero net circulation [3, 20], which was later generalized substantially to the case of three vortices in a domain with periodic boundary conditions [8, 22].

The lecture attempts, on one hand, to give Gröbli's contribution the recognition and accessibility it deserves and, on the other, to provide the necessary up-to-date account of what has happened since, allowing the modern reader to see the three-vortex problem, and some aspects of what we know about the N-vortex problem for $N \geq 4$ [6, 10, 11, 21], in a richer, more complete context. We encounter quite a spectrum of phenomena, including stationary patterns of vortices in superfluids and electron plasmas [5], chaotic motions of a few vortices, aspects of the dynamics of wakes [15], the famous "vortex tripole" [13], and the ubiquitous problem of two-dimensional turbulence.

ACKNOWLEDGMENTS

My understanding of the three-vortex problem and its role has evolved over the years through collaborations with (in alphabetical order) Phil Boyland, Morten Brøns, Bruno Eckhardt, Yoshi Kimura, Slava Meleshko, Paul Newton, Neil Pomphrey, Nicholas Rott, Mark Stremler, Dmitri Vainchtein and Irek Zawadzki. To all of them I extend my thanks.

REFERENCES

[1] Aref, H.: Motion of three vortices. *Physics of Fluids* 1979, **22**, 393-400.

[2] Aref, H.: Integrable, chaotic, and turbulent vortex motion in two-dimensional flows. *Annual Review of Fluid Mechanics* 1983, **15**, 345-389.

[3] Aref, H.: Three-vortex motion with zero total circulation: Addendum. *Journal of Applied Mathematics and Physics (ZAMP)*. 1989, **40**, 495-500. [Addendum to the paper by N. Rott (1989)]

[4] Aref, H. and Brøns, M.: On stagnation points and streamline topology in vortex flows. *Journal of Fluid Mechanics*, 1998 **370**, 1-27.

[5] Aref, H., Newton, P. K., Stremler, M. A., Tokieda, T. and Vainchtein, D. L.: 2002 Vortex crystals. *Advances in Applied Mechanics*, 2002, **39**, 1-79.

[6] Aref, H. and Pomphrey, N.: Integrable and chaotic motions of four vortices. I. The case of identical vortices. *Proceedings of the Royal Society (London) A*, 1982, **380**, 359-387.

[7] Aref, H., Rott, N. and Thomann, H.: Gröbli's solution of the three-vortex problem. *Annual Review of Fluid Mechanics*, 1992, **24**, 1-20.

[8] Aref, H. and Stremler, M. A.: On the motion of three point vortices in a periodic strip. *Journal of Fluid Mechanics*. 1996, **314**, 1-25.

[9] Batchelor, G. K.: *An Introduction to Fluid Dynamics*, Cambridge University Press, 1967.

[10] Eckhardt, B.: Integrable four vortex motion. *Physics of Fluids*, 1988, **31**, 2796-2801.

[11] Eckhardt, B. and Aref, H.: Integrable and chaotic motions of four vortices II: Collision dynamics of vortex pairs. *Philosophical Transactions of the Royal Society (London) A*, 1988, **326**, 655-696.

[12] Gröbli, W: *Specielle Probleme über die Bewegung geradliniger paralleler Wirbelfäden.* Zürcher und Furrer, Zürich. Republished in *Vierteljahrschrift der naturforschenden Gesellschaft* in Zürich, 1877, **22**, 37-81, 129-167.

[13] van Heijst, G. J. F. and Kloosterziel, R, C.: Tripolar vortices in a rotating fluid. *Nature*, 1989, **338**, 569-571.

[14] Helmholtz H von: Über Integrale der hydro-dynamischen Gleichungen, welche den Wirbelbewegungen entsprechen. *Journal für reine und angewandte Mathematik*, 1858, **55**, 25-55.

[15] Kármán, T von and Rubach, H. L.: Über den Mechanismus des Flüssigkeits- und Luftwiderstandes. *Physikalische Zeitschrift*, 1913, **12**, 49-59.

[16] Lamb, H.: *Hydrodynamics*. Sixth edition. Cambridge University Press, 1932.

[17] Newton, P. K.: The N-Vortex Problem – Analytical Techniques. *Applied Mathematical Sciences*, vol. **145**. Springer-Verlag, 2001.

[18] Novikov, E. A.: Dynamics and statistics of a system of vortices. *Soviet Physics JETP*, 1975, **41**, 937-943.

[19] Poincaré, H.: *Théorie des Tourbillons.* Cours de la Faculté des Sciences de Paris, Georges Carré ed., Paris. (Lectures presented during the second semester, 1891-92), 1893, pp. 211.

[20] Rott, N.: Three-vortex motion with zero total circulation. *Journal of Applied Mathematics and Physics (ZAMP)*, 1989, **40**, 473-494. [With an Addendum by H. Aref (1989)]

[21] Rott, N.: Constrained three- and four-vortex problems. *Physics of Fluids A* 1990, **2**, 1477-1480.

[22] Stremler MA and Aref H: Motion of three vortices in a periodic parallelogram. *Journal of Fluid Mechanics*, 1999, **392**, 101-128.
[23] Synge JL: On the motion of three vortices. *Canadian Journal of Mathematics*, 1949, **1**, 257-270.
[24] Tait PG:On integrals of the hydrodynamical equations, which express vortex-motion. *Philosophical Magazine*, 1867, (4) 33, 485-512.

Proceedings of the Tenth Asian Congress of Fluid Mechanics
17-21 May 2004, Peradeniya, Sri Lanka

FLUID MECHANICS OF URBAN ENVIRONMENTS

H.J.S. Fernando
Department of Mechanical & Aerospace Engineering, Environmental Fluid Dynamics Program
Arizona State University

ABSTRACT: By 2005, the majority of the world's population is expected to be in the urban areas, creating intense demands for basic necessities akin to quality of life. In order to meet these needs without degrading available resources, it is necessary to develop tools and techniques for the optimal management of resources, a key element of which is the use of models that consider numerous inputs and outputs as well as dynamics of urban systems and guide how best a particular course of action ought to be realized. Urban systems are complex, and no models exist that can handle all key elements of urban systems. Currently, such analyses are conducted by sectorial models that take into account one or two major elements of the system. Information from different models is then piecemeal together to guide the development of public policy on urban development. Arizona State University (ASU) is in the process of developing a multi-scale modeling system to deal with flows from synoptic to personal scales. Associated with this project is the development of necessary scientific tools and knowledgebase. A brief overview of this activity and some pertinent key issues are described in this communication.

1. INTRODUCTION

The world is in the middle of a surge of urbanization, with some twenty megacities having arrived by the end of twentieth century. The population influx into cities has necessitated providing clean air and water, food, housing, healthcare and infrastructure for communication, governance, transportation and security. Of these, the quality of air is a factor of paramount importance, given that it is the medium of living and constituents of air are intimately related to human health. Burgeoning population in cities have led to deterioration of air quality, which can be ameliorated only by careful planning and implementation of sound policy. Sound planning strategies not only mitigates deleterious anthropogenic influence on the environment, but also leads to optimal use of resources, especially within the framework of urban sustainability.

The Environmental Fluid Dynamics group at Arizona State University has been involved in research related to the studies of urban airsheds, from the standpoint of a multi-scale analysis from regional to personal scales, cascading down through urban, neighborhood, building-cluster and city canyon scales. In modeling, community modeling systems (MM5 and Models-3/CMAQ) have been used in nested mode for regional to urban scales and a 3-D CFD code was developed for street canyon and personal scales. The observational test beds have been Phoenix, El Paso and Salt Lake City airsheds, where large scale filed observational campaigns have been conducted. Simple analytical models were developed and tested using fluid modeling experiments to identify and parameterize processes occurring in sub-grid scales.

2. MODELING PHILOSOPHY

The modeling system at ASU employs the multi-scale philosophy, in that the outputs of models dealing with larger scales are fed into those of smaller scales. The principle of this methodology is illustrated in Figure 1, wherein ideally the models of climate can be linked to the personal scale models. One would like these models to be interacting with each other feeding information both up and down the scales, but given the complexity of the modeling system and limitations of supercomputer resources only one way coupling (larger scales feeding information into smaller scales) is being used. At ASU, the current emphasis is the coupling of the National Weather Service *eta* model with the computational fluid dynamics model developed in house through intermediate step of MM5 meso-scale meteorological model. Of course, each of these models has their inherent problems, from specifying boundary conditions

to the inaccuracies of sub-grid scale parameterizations of the models. These details can be addressed through fundamental research, especially via improving our basic understanding of processes and their mathematical descriptions. During model execution and in comparisons with observations, critical problems associated with the models can be identified and address them through fundamental research and implements any improvements back into the modeling systems. Needless to say that traditional approach of laboratory, high-resolution numerical and theoretical work can play important roles in these developments. Field work helps validate the models and delineates important processes to be included in the models. The ASU group also works with a number of agencies in applying the model and experimental results for regulatory work.

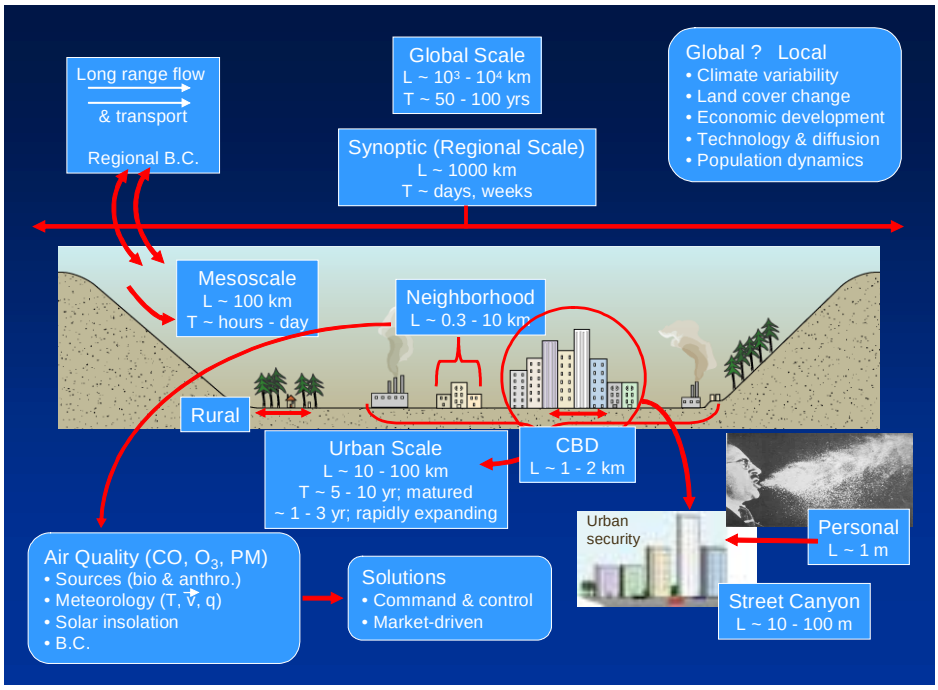

Figure 1: Different scales involved in a multi-scale urban modeling system. The goal is to predict small-scale motions (e.g. urban street canyon scales or the personal scales), starting with regional (synoptic scale) flows. Synoptic scale flow provides boundary conditions for the meso-scale flow models. Mesoscale flow is modified by large urban features to produce urban scale flow, which is again perturbed by the land use inhomogeneities to produce neighborhood scale flow patterns; it is in this scale that typical meteorological and air quality predictions are made and mitigation strategies are negotiated. Mesoscale models can be used down to the higher end of the neighborhood scales, below which the utility of mesoscale models is questionable. Computational fluid dynamics models can be nested with mesoscale models to predict the smaller central business district (CBD) scale and personal scale flows.

3. SOME ISSUES IN URBAN MODELING

Many factors contribute to the uncertainties of forecasts, for example, errors of initial and boundary conditions, inaccuracies of specifying governing parameters (e.g., land use), limitations of governing equations and the inadequacies of the sub-grid parameterizations used in the model. Below an example is presented on how the subgrid scale parameterizations have caused delayed transition from down-slope flows at night to up-slope flows in the morning, which has seriously affected the predictions of air quality.

Recently, meteorological and air quality simulations were performed by the ASU group for Arizona Department of Environmental Quality in support of determining the boundaries of the areas where the new 8-hour ozone air quality standards promulgated by the USEPA are not met. MM5 mesoscale model was used for air flow calculations and the USEPA's latest Models-3/CMAQ air quality modeling and assessment system was used for ozone calculations. The model domain encompassed the entire Phoenix area. Figure 2 shows the maximum 8-hour ozone for a design day, indicating the formation of an ozone blob in the northwestern part of the domain. These elevated levels are absent in the measurements, however, and scrutiny of MM5 and Models-3 simulations clearly indicated that the delayed transition in the flow simulation has caused this anomaly. The ozone formed within the urban core is supposed to be advected to the east by the up-slope flow that initiates following morning transition, but the delayed transition has caused the ozone movement to be biased toward northwest. Currently the morning and evening transition in urban areas with complex topographies are poorly handled in mesoscale models, and sound physics and dynamics based parameterizations that represent transition periods should be a priority in future model refinements.

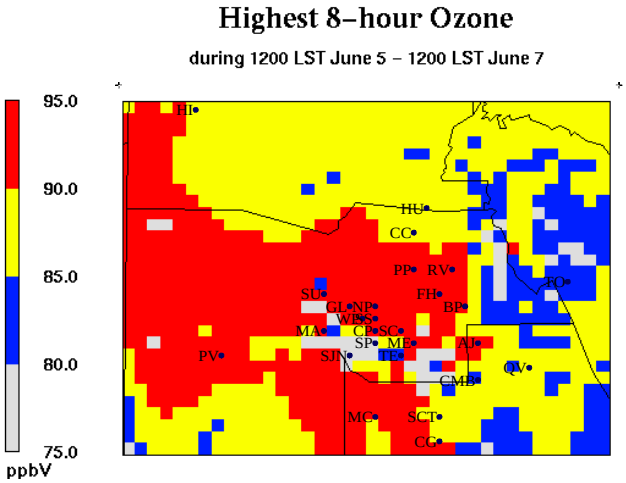

Figure 2: 8-Hour ozone concentrations for Phoenix metropolitan area calculated using MM5 meteorological model, Models-3/CMAQ and an emission inventory for the area The concentration is in parts per billion by volume and the gray scale is used to depict the concentrations.

Another well-recognized problem is the nocturnal period, where subgrid parameterizations used to represent stably stratified periods are known to perform unsatisfactorily. An example is shown in Figure 3, where MM5 predictions for the Salt Lake City air basins for the period of the Vertical Transport and Mixing Experiments conducted by the Department of Energy are compared with the model results; some deficiencies with regard to nocturnal (and transition) periods are well evident. New sub-grid parameterizations were attempted in our work, with encouraging success. For example, the MM5 simulated wind fields with one of the default scheme (MRF) and three modifications based on the diffusivity parameterizations proposed by the ASU group are shown in Figure 3. The new parameterization is based on the measurements taken in Salt Lake City during the Vertical Transport and Mixing Experiment[1]. Note that, with the exception of the third day (8th October, 2000), the new scheme gives better temperature predictions. The disparity observed for all three model predictions on the 8th could be attributed to the low level synoptic influence that was not seeped into the model for several hours.

A CFD model that can be nested with a meso-scale model was developed to predict the building canyon flows in CBDs[2]. This model is based on primitive equations with k-ε closure, and its output is being tested using several building configurations: Mock Urban Test (MUST) and the Joint-Urban (JU-

2003) experiment in the Oklahoma City. The MUST experimental configuration consisted of a uniform array (12 x 10) of large shipping containers (dimensions 12.2 x 2.42 x 2.54m) arranged on a rectangular test grid in the Utah desert to represent a uniform neighborhood of buildings. The dimension of the array was 180 x 176m, with a Plan Index Area of 0.12; therefore, the flow regime therein was near the boundary between isolated roughness and wake interference regimes. Various participants instrumented the site with a host of instruments, such as sonic anemometers, meteorological balloons, thermistors and photo ionization detectors. The focus of ASU group was the first urban canyon of MUST array (the area between the first and second row of containers). Figure 4 shows a comparison of MUST data with those of the CFD model; a good agreement is evident, except that the turbulent kinetic energy was overpredicted by the model (Figure 3). Modifications to the turbulence model are underway to address this discrepancy. The scalar dispersion module of this CFD system can predict the dispersion of released material in an urban area, but the model validation with regard to scalar dispersion await the completion of the processing of JU-2003 data.

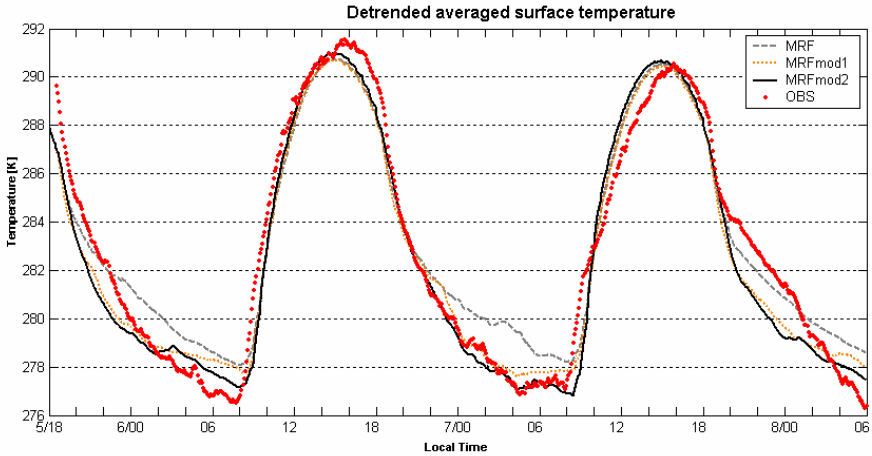

Figure 3: A comparison of the Salt Lake basin-averaged temperature simulated by MM5 with observations. The dots are observations and the default scheme (MRF) and two subgrid modifications based on Monti et al (2002) scheme are shown.

4. SUMMARY

The rapid population growth in urban areas has necessitated novel and improved management and prediction methodologies for urban airsheds. Airflow in urban areas is complicated by the presence of complex topography and built-in elements that create a myriad of motion scales, and with current computational resources these motions can only be tracked through multi-scale analyses modeling. The development of such a multi-scale modeling system is afoot [3], encompassing both community modeling systems and in-house developments. This system is being tested and upgraded to include the state of the science. Such a modeling system can be an extremely useful tool for managing urban airsheds and in assessing the efficacy of various urban growth scenarios.

ACKNOWLEDGMENTS

Urban Fluid Mechanics research at Arizona State University is funded by the Department of Energy, the National Science Foundation and the Department of Army. I wish to thank the ASU group participated in the studies described here, in particular, Drs. Sang-Mi Lee and Susanne Grossman-Clarke (modeling), Dr. Marko Princevac (field studies, VTMX), Mr. Dragan Zajic (CFD computations and MUST experiments) and Professor J.C.R. Hunt (theory).

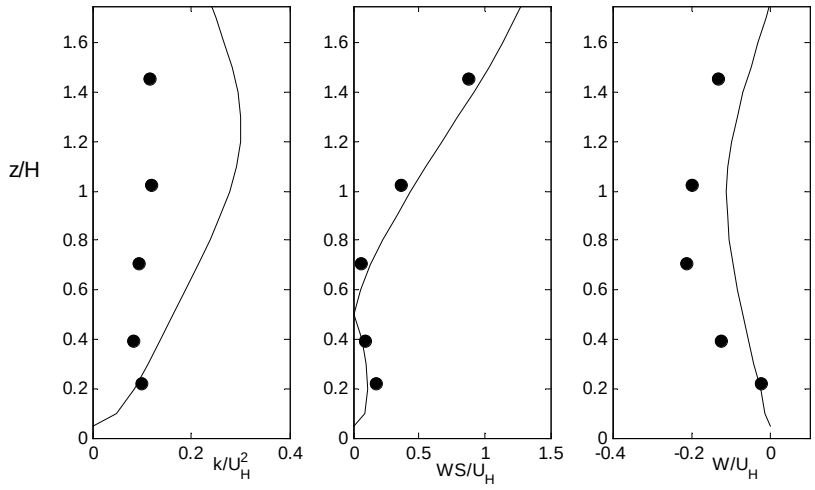

Figure 4. Comparison of normalized model and experimental results for the must experiment carried out on 09/24/2001 at 23:15. (a) turbulent kinetic energy k, (b) horizontal wind speed $WS = \sqrt{U^2 + V^2}$ *(c) vertical velocity W. The inclination of winds to the long axis of the cylinder is* $\alpha = 0^o$*; z is in vertical measured from the ground and H is the cylinder height.*

REFERENCES

[1] Monti, P., Fernando, H.J.S., Chan, W.C., Princevac, M., Kowalewski, T.A. and Pardyjak, E., "Observations of Flow and Turbulence in the Nocturnal Boundary Layer Over a Slope," *Journal of the Atmospheric Sciences*, **59 (17),** 2513-2534, 2002.

[2] Baik, J.J., Kim, J.J. and Fernando, H.J.S. "A CFD Model for Simulating Urban Flow and Dispersion," *Journal of Applied Meteorology* (Accepted for Publication).

[3] Fernando, H.J.S., Lee, S.M., Anderson, J., Princevac, M., Pardyjak, E. and Grossman-Clarke, S., "Urban Fluid Mechanics: Air Circulation and Contaminant Dispersion in Cities," *Journal of Environmental Fluid Mechanics*, **1(1),** 107-164, 2001.

Proceedings of the Tenth Asian Congress of Fluid Mechanics
17-21 May 2004, Peradeniya, Sri Lanka

FLUID MECHANICS, RED TIDES, AND MARICULTURE MANAGEMENT

Joseph H.W. Lee, Ken T.M. Wong and K.W. Choi
(Department of Civil Engineering, The University of Hong Kong, Hong Kong, China)

ABSTRACT: In sub-tropical coastal waters around Hong Kong and South China, algal blooms and red tides (due to the rapid growth of microscopic phytoplankton) are often observed. Under the right environmental conditions these blooms can occur and subside over rather short time scales - in the order of days to a few weeks. Algal blooms can lead to discoloration of the marine water, which may lead to beach closures, severe dissolved oxygen depletion, fish kills, and shellfish poisoning. Hydrographic factors can play an important role in algal bloom and dissolved oxygen dynamics. The integration of physical and biological processes is needed for an understanding of these complex ecological problems, and hydro-ecological modelling provides a scientific basis for mariculture management. We give herein an overview of two recent works related to the observation and modelling of algal blooms. A new method to systematically determine the flushing time of stratified tidal inlets using 3D hydrodynamic modelling is proposed. The method can be coupled with a water quality model to determine the carrying capacity of a fish farm, and has been successfully applied to six fish culture zones in Hong Kong. We present also a novel deterministic Lagrangian NEighbourhood Separation Technique (NEST) for modelling advection-diffusion problems associated with the vertical migration of swimming algal species (dinoflagellates). The particle method is based on relative diffusion concepts and requires far less particles than traditional random walk methods.

1. INTRODUCTION

Hong Kong is situated at the mouth of the Pearl River Estuary. In sub-tropical coastal waters around South China, algal blooms and red tides (due to the rapid growth of microscopic phytoplankton) are often observed. Under the right environmental conditions (favourable temperature, solar radiation, nutrient concentration, predation pressure, wind speed, and tidal flushing) these blooms can occur and subside over rather short time scales - in the order of days to a few weeks. Algal blooms can lead to discoloration of the marine water, which may lead to beach closures, severe dissolved oxygen depletion, fish kills, and shellfish poisoning. The high incidence of red tides and harmful algal blooms (HAB) is believed to be related to the eutrophication caused by excessive and concentrated organic discharges. Hydrographic factors also play an important role, as most of the red tides occur in weakly-flushed, semi-enclosed tidal inlets.

Figure 1 shows the reported number of red tides in the past two decades; a significant portion of them occurred in Tolo Harbour, a land-locked waterbody with relatively long residence times in the eastern waters of Hong Kong (Fig.2). Over the past two decades, massive fish kills due to oxygen depletion have been observed in some of the marine fish culture zones in Hong Kong (Lee *et al*. 1991[1]); a few toxic algal blooms have also been reported. In particular, in April 1998, a devastating red tide (due to the dinoflagellate *Karenia digitatum*) resulted in the worst fish kill in Hong Kong's history - it destroyed over 80 percent (3400 tonnes) of cultured fish stock, with estimated loss of more than HK$312 million (Dickman 1998[2]). 3D hydrodynamic modelling and numerical drogue tracking (Fig.2) have shown that this massive red tide probably originated in the northeastern waters of Hong Kong, and transported into the southern coastal waters due to a change of wind direction under diurnal tide conditions (Lee and Qu 2004[3]).

There is a need to model algal bloom dynamics to provide a scientific basis for mariculture management. In this paper, we present a summary of two recent works on hydro-ecological modelling. The work has been motivated by a practical need to understand the causes of episodic algal bloom events,

and to develop a quantitative methodology for mariculture management. In particular, we discuss recent findings on: (i) computation of flushing time using 3D hydrodynamic modelling and its use in the determination of carrying capacity of fish farms; and (ii) Lagrangian modelling of vertical migration of dinoflagellates using a NEighbourhood Separation Technique (NEST).

2. ENVIRONMENTAL MANAGEMENT OF MARINE FISH CULTURE

2.1 Numerical Determination of Flushing Time for Stratified Waters

It is often advantageous to model a semi-enclosed estuarine or coastal embayment (e.g. fish farms or tidal inlets, or typhoon shelters) as a separate system within a larger water body connected to the outer sea. The water quality of the system depends crucially on its flushing time (or its inverse, flushing rate), which is a lumped measure of the effectiveness of tidal flushing in removing any "pollutant" from the water body. For example, the occurrence of a harmful algal bloom or "red tide" in an inlet depends on the flushing rate relative to the net growth rate of an invading algal species transported into the area (Garcon *et al.* 1986[4]). The local impact of specific pollution generated from fish farming activities (e.g. unconsumed fish feed, pathogenic bacteria, diseases) also depends on the flushing rate in the vicinity of the fish farm. For environmental management purposes, since many water quality processes occur at time scales much larger than that of tidal variation, hydrodynamic and water quality models can be effectively coupled by lumping all the tidal exchanges for a given system into a flushing rate. The main attractiveness of such a simplified approach is the immediate practical value of linking pollution input and ecosystem response in a tractable manner (e.g. Lee and Wong 1997[5]).

In general, the flushing time of a given system depends on the tidal exchanges between the system and the outer sea – which is a complicated function of the freshwater runoff, tidal range, topography and bathymetry, density stratification, and wind. Tidal flushing is a commonly used term; the use of the flushing time concept for a water body can be traced back to the early fifties. It is also known as residence time, turnover time or detention time, but there is no unique agreed definition or method of determination. Traditionally, flushing times are estimated using tidal prism or salt balance concepts (e.g. Dyer 1973[6]). Tidal prism methods tacitly assume complete mixing within the defined segments, and hence tend to produce overly optimistic flushing rates. Salt balance methods rely on long term salinity measurements, and is not applicable in many situations. Flushing times have been determined by numerical models (e.g. Prandle 1984[7]; Signell and Butman 1992[8]), but these are mainly limited to the use of 2D models and the computed results often differ from those estimated by traditional bulk methods. In addition, the numerical determination of flushing times in stratified water bodies has not been studied.

The sustainable management of mariculture requires proper siting of the fish farms and stocking density control. Both of these are related to the carrying capacity of the water body concerned, which is mainly governed by its flushing characteristics. A method to determine the carrying capacity of a fish farm has been developed by using 3D hydrodynamic modelling to compute the flushing rate and linking it to a simple water quality model (Lee *et al.* 2003[9]). A systematic methodology via the use of numerical tracer experiments has been developed to determine the flushing rate of a marine fish culture zone located in semi-enclosed shallow embayments (Fig.3).

First, the 3D tidal circulation in the bay including the fish farm is computed for an assumed tidal condition and vertical salinity distribution at the open boundary; the dynamic steady state can be obtained from a fully 3D calculation. The 3D flow model solves the shallow water equations (hydrostatic pressure approximation) with simple mixing length turbulence closure to describe the reduction of mixing due to vertical density stratification. The continuity and momentum equations are solved using a semi-implicit modal splitting technique, while the 3D solute transport equations are solved by a fractional step method (Choi 2002[10]). Given the tidal velocity field, the flushing rate can be determined by performing a numerical tracer experiment. A mass of hypothetical conservative tracer is instantaneously introduced into a region of interest, such as the fish farm or an entire bay. It is assumed that a unit tracer concentration is initially found inside that region and zero concentration elsewhere. The subsequent change in tracer concentration distribution as a result of barotropic and baroclinic exchanges is computed

by solving the 3D advective diffusion; e.g. Fig.4a) shows the tracer concentration distribution computed by a Lagrangian forward tracking and random walk method after 12 hours. Due to tidal exchange with the 'clean' water outside of the region, the tracer mass within the region of concern decreases with time; Fig.4b) shows the change in tracer mass M(t) with the flood and ebb of tides under stratified flow conditions. It is found that in tidal inlets, the decrease in tracer mass follows a double-exponential decay curve (Choi and Lee 2004[11]); the flushing time, defined as "the average lifetime of a particle in the given volume of water body", can be analytically determined from a best fit of the M(t) curve. In this method, the surrounding water in the vicinity of the fish farm is assumed to be "clean". Essentially, this "local" flushing time is useful for estimating the local impact of any foreign substance or short-term effluent discharge from the fish farm. However, for some water quality parameters such as nutrient concentration, the outer bay has a non-zero concentration due to the return of pollutants with the flood and ebb of tides. For estimating long-term average water quality, the "system-wide" flushing rate is determined by looking at mass removal from a much larger water body that is connected to an adjoining 'clean' ocean. This definition takes into account the interactions between different parts of the water body that are not assumed to be 'clean' and represents the long-term flushing efficiency of the region of interest. In the tracer experiment, mass is released from everywhere inside the water system of interest (e.g. the entire bay containing the tidal inlet in which the fish farm is located). This approach is similar to determining the flushing rate using salinity (or freshwater concentration) as the tracer concentration, but it is applicable even for the cases of weak or negligible longitudinal salinity gradients (e.g. when freshwater runoff is all routed to reservoirs for water supply).

Fig.4b) shows that the system-wide flushing time is much larger than the local flushing time (slower decrease of M(t)), and that the flushing rate is significantly greater in the presence of density stratification in the wet season. Extensive computations and comparison with field data have indicated this "system-wide" flushing rate should be used for determining the water quality and hence the carrying capacity of the fish culture zone. Figure 5 shows an instantaneous tracer concentration distribution in Tolo Harbour computed using a 3D finite difference mass transport model and the tracer mass removal for the Yim Tin Tsai (YTT) fish culture zone for a system-wide dosage. The residence time of the fishfarm – i.e. the time taken to travel from the fish farm to the ocean boundary of the semi-enclosed bay is also determined by a particle tracking method. A number of particles representing a uniform concentration in the fishfarm are released and the particle trajectory is computed by forward tracking (for advection) and random walk (for diffusion) method. The residence time is then computed as the mass weighted average of the time taken by individual particles to leave the system through the open boundary. Numerical experiments confirm that the directly computed residence time is the same as the system-wide flushing time determined from the numerical tracer experiment (Table 1). The flushing times determined by the present model also differ negligibly from those computed using Delft3D, a 3D hydrodynamic model with two-equation turbulence closure.

2.2 Determination of Carrying Capacity

Second, the computed flushing rate is used in a quasi-steady water quality model that includes both the eutrophication kinetics in the water column and the sediment-water interactions (Lee and Wong 1997[5]). The computed flushing time for the dry/wet season is coupled with a quasi-steady diagenetic water quality model that includes the algal growth and nutrient kinetics in the water and the sediment-water-pollutant interactions. The carrying capacity of the fish farm can be determined by reference to key water quality indices: chlorophyll-*a*, dissolved oxygen, organic nitrogen, and potential lowest dissolved oxygen level on a day of negligible photosynthetic production. The predicted average water quality is well-supported by field observations. The carrying capacity of the fish culture zone can be determined in terms of a Potential Lowest Dissolved Oxygen (PLDO) level. The method has been successfully applied to six representative fish culture zones (FCZ) in Hong Kong (Fig.6) with different hydrographic and pollution loading characteristics (Choi 2002[10]). Fig.6 shows the organic loading and computed flushing rate and key water quality variables at the six FCZs for the summer and winter season. Based on the

model, for a specified temperature and flushing rate, the maximum allowable fish stocking density can be obtained by prescribing a target level of dissolved oxygen or algal biomass.

3. LAGRANGIAN MODELLING OF VERTICAL MIGRATION OF DINOFLAGELLATES

3.1 Field Observations

Since 2000 continuous field measurements of algal dynamics have been made at two sites in Hong Kong (Lee *et al.* 2000[12]; Wong and Lee 2003[13]). Fig.7 shows the changes in the algal biomass (chlorophyll fluorescence) and dissolved oxygen (DO) recorded at three depths during a dinoflagellate (*Gonyaulax Polygramma*) bloom. It is seen the diurnal DO fluctuations mirror the algal biomass; vertical DO differentials are also significant during the bloom period but relatively small on days without algal growth. This suggests the possibility of using DO data (for which accurate and cost-effective measurements can be made) to gain insights into the HAB dynamics.

3.2 Governing Equations For Vertical Structure of Water Quality

A hydro-ecological model has been developed to describe the vertical structure of algal dynamics. The water quality is described by an advective-diffusion equation of the form:

$$\frac{\partial c}{\partial t} = \frac{\partial}{\partial z}\left(E\frac{\partial c}{\partial z}\right) - \frac{\partial wc}{\partial z} + \text{rate kinetics} \qquad (1)$$

where $c(z, t)$ = concentration of algae and related water quality variables. E = vertical turbulent diffusivity, and w = vertical velocity. The vertical diffusivity is calculated from the tidal current and wind speed (Bowie *et al.* 1985[14]), while the advective velocity w is the sinking velocity (for diatoms) or the migratory speed (for dinoflagellates). The system of governing equations is solved using a finite volume method, while the mass transport is computed using a newly developed NEighbour Separation Technique (NEST, Wong *et al.* 2004[15]).

The rate kinetics represents the water quality modelling as illustrated in Figure 8; other coupled model state variables include dissolved oxygen, nutrient (nitrogen), sediment nutrient, and sediment carbon. Phytoplankton growth and the associated nutrient and dissolved oxygen (DO) dynamics are governed by a number of interacting physical, biological, and chemical processes. The phytoplankton dynamics and nutrient kinetics are based on a generally accepted framework (Bowie 1985[14]; Thomann and Mueller 1987[16]; Lee *et al.* 1991[1]). The modelling of the vertical structure of algae and dissolved oxygen presents challenges that cannot be resolved by traditional modelling approaches. Dinoflagellates can swim; they have been observed to migrate at night to the bottom where nutrients are more plentiful and migrate upwards to the surface during the day to get sunlight for growth (Cullen and MacIntyre 1998[17]). It is desirable to model the uptake of nutrient and algal growth in terms of an "internal nutrient pool" (Droop 1983[18]) rather than the external nutrient concentration in the water. This however necessitates the use of a Lagrangian method to follow an assemblage of phytoplankton species and track its growth and nutrient uptake in response to environmental conditions. The issue cannot be addressed by mixed Eulerian-Lagrangian methods devised mainly to overcome numerical diffusion problems associated with the advection (e.g. Cheng *et al.* 1984[19]). On the other hand, simulating the diffusion process using the random walk method requires a large number of particles (typically tens or hundreds of thousands) for realistic simulations. Not only is this computationally demanding, the result generated from random walk varies from run to run, and extensive numerical testing is often necessary to assure stability of the result. We present herein a new particle method to solve the advective-diffusion problem. Unlike the mixed Eulerian-Lagrangian approaches, the method treats both the advection and diffusion in a Lagrangian framework. Unlike the random walk method, the diffusion is simulated deterministically by modelling the particle-separation via relative diffusion concepts.

3.3 A Deterministic Lagrangian Particle Method for Advection Diffusion Problems

Richardson (1926)[20] was probably the first to see the possibility of predicting a concentration distribution using particle separation. In his classic paper, he discussed the difficulty of describing turbulent diffusion in an Eulerian framework, and the advantage of viewing diffusion in terms of particle separation. Through the use of a distance-neighbour relationship, Richardson showed that the change in mean square separation of particles can be related to the diffusivity coefficient. Batchelor (1952)[21] also concluded that dispersion of a patch is better described by the relative motion of separating particles instead of the wandering of an individual particle. Although the significance of relative diffusion has been known for a long time (e.g. Csanady 1973[22]), the idea of depicting a diffusion process through the way particles separate had never been incorporated into numerical models.

3.3.1 Particle Separation Rule

In the particle method, the mass of a dispersing substance is represented by a cloud of particles, each particle being equivalent to a proportion of the material. The advection of the particle can be tracked given the flow field. With time, the particles become separated further and further through the process of diffusion. Given the spreading characteristics of a diffusing patch, a general relationship for the way particles separate can be obtained. For simplicity, we consider first only one-dimensional diffusion.

Consider the simplest case of an instantaneous point source of total mass M at the origin ($x=0$) at time $t=0$. The diffusion problem is described by $\frac{\partial c}{\partial t} = E\frac{\partial^2 c}{\partial x^2}$, where $c(x,t)$ = mass concentration, and E=diffusivity. For this case, the analytical solution is well known, $c = \frac{M}{2\sqrt{\pi Et}} exp[- x^2/(4Et)]$. The variance of the concentration distribution of the patch at time t after release is given by:

$$\sigma^2 = 2Et \tag{2}$$

where the variance $\sigma^2 = \int_{-\infty}^{\infty} x^2 c(x,t)dx/M$. Richardson (1926)[18] showed that the mean square separation of a pair of particles, $\overline{S^2}$, is equal to twice the concentration variance of a patch. Therefore, we have:

$$\overline{S^2} = 2\sigma^2 = 4Et \tag{3}$$

If we depict the diffusion process in terms of changes in the separation distance between two neighbouring particles, the simplest way is to set the particle separation s as:

$$s=\sqrt{\overline{S^2}}=2\sqrt{Et} \tag{4}$$

By differentiating s with respect to t, we obtain a "separation speed" for each of the particles:

$$u_s = \frac{1}{2}\frac{ds}{dt} = \frac{E}{s} \tag{5}$$

The departing particle pair is a basic building block of our deterministic particle separation method. To go one step further, we now depict the diffusion process by three neighbouring particles located at $x_i(t)$ with velocity $u_i(t)$ (Figure 9). The separation distance between adjacent particle pairs are $s_i = x_{i+1} - x_i$. Let's assume the outer particles are too far away to be influenced by each other. Therefore, their "separation velocity" will still be given by equation (4), resulting in $u_1 = E/s_1$, $u_3 = E/s_2$. The middle particle is however affected by two neighbouring particles, and its velocity can be obtained by

$$\overline{S^2} = \frac{s_1^2+s_2^2+(s_1+s_2)^2}{3} = 4Et$$

$$\frac{d\overline{S^2}}{dt} = \frac{2}{3}\left(s_1\frac{ds_1}{dt}+s_2\frac{ds_2}{dt}+(s_1+s_2)\left(\frac{ds_1}{dt}+\frac{ds_2}{dt}\right)\right) = 4E$$

substituting $\frac{ds_1}{dt} = u_2 - u_1 = u_2 + \frac{E}{s_1}$, $\frac{ds_2}{dt} = u_3 - u_2 = \frac{E}{s_2} - u_2$, we have

$$s_1(u_2+\frac{E}{s_1}) + s_2(\frac{E}{s_2} - u_2) + (s_1+s_2)(\frac{E}{s_2} + \frac{E}{s_1}) = 6E$$

$$u_2 = E(\frac{1}{s_1} - \frac{1}{s_2}) \tag{6}$$

This is equivalent to combining two pairs of particles with the middle particle overlapping (Fig. 9). In fact $u_i = E(\frac{1}{s_{i-1}} - \frac{1}{s_i})$ can be shown to be the general solution for n particles, with s_0 and s_n taken to be ∞.

3.3.2 Lagrangian Equivalence to Fick's Law

The above separation rule can be interpreted as a Lagrangian equivalent of Fick's Law of diffusion. Consider the 3 particles as shown in Fig.10a. The concentrations in the left and right cells neighboring the middle particle may be viewed as M/s_1 and M/s_2 respectively. Applying Fick's Law,

$$q = uc = E\frac{M/s_1 - M/s_2}{d}$$

Similarly, the concentration at the central node may be viewed as M/d, and the same equation governing particle separation in a diffusion process is recovered.

$$u = E(\frac{1}{s_1} - \frac{1}{s_2}) \tag{7}$$

In most water quality or ecological models, due to the reaction processes, the diffusing substance is not conservative - i.e. mass of particle (particle size) is not constant. The general equation governing particle separation can be expediently obtained using the above Lagrangian equivalence. By replacing the concentration terms with $(M_1+M_2)/2s_1$, $(M_2+M_3)/2s_2$, M_2/d accordingly, we have

$$u = E\left(\frac{(M_1+M_2)}{2M_2s_1} - \frac{(M_2+M_3)}{2M_2s_2}\right) \tag{8}$$

Putting into numerical form, we have:

$$\Delta x = E\Delta t\frac{(M_1+M_2)s_2 - (M_2+M_3)s_1}{2M_2s_1s_2} \tag{9}$$

The above equation gives essentially a general "Fickian-diffusion equivalent" local interaction rule that assumes the movement of a particle is only affected by its immediate neighbours. Given the concentration distribution at time t, $c(x,t)$ (i.e. M_i, x_i or s_i), local diffusivity E_i, the particle positions (and hence the concentration distribution) at the next time level can be obtained explicitly from equation (9). In an Eulerian scheme, the concentration is represented on the grid points. In a particle method, the number of particles (or the total mass of particles) in a given volume, i.e. the particle separation, is a measure of the concentration. For uniformly distributed particles the stability criteria can be shown to be (Fig.10b)

$$\frac{E\Delta t}{s^2} \le \frac{1}{2} \tag{10}$$

Similarly, it can be shown that the stability criterion for the case of variable particle size is:

$$\frac{E\Delta t}{2M_i}\left(\frac{M_{i-1} + M_i}{s_{i-1}^2} + \frac{M_i + M_{i+1}}{s_i^2}\right) \le 1 \tag{11}$$

In initializing a concentration distribution using this particle approach, two conditions must be satisfied: a) The total mass must be conserved, and b) the root mean square displacement of the particles must be the same as the standard deviation of the concentration distribution. Details of the treatment of other initial and boundary conditions can be found in Wong *et al.* (2004)[15].

3.4 Numerical Results

The method has been applied to a number of demanding 1D and 2D advection-dominated problems. The scheme is asked to advect a Gaussian concentration distribution at a constant velocity of u = 0.5 m/s in a uniform flow and with E = 2 m^2/s. The sharp initial Gaussian distribution, $c(x,0) = 1.0 \exp(-$

x^2/σ^2), σ = 264 m, is described by 200 equal mass particles with the same standard deviation. Figure 11 shows the computed concentration distribution at t = 4800s and 9600s along with the exact solution. Figure 12 shows the simulation of 2D diffusion in a plane shear flow, with isotropic diffusivity E =2 m^2/s and the velocity field, $u(x,y) = u_o + \lambda y$, where u_o = 0.1 m/s and $\lambda = 5 \times 10^{-4}$ s^{-1}. The computed skewed concentration contour at two time instants are shown in Fig.12a. Figure 12b) shows representative transects of the numerical solution in the along flow (x-) direction (y = -600, 0, 600 m); the transects in cross flow (y-) direction (x =-1000, 0, 1000 m) are shown in figure 12c. In the example, only 2000 particles have been used. It can be seen that the particle separation method gives very good results (rms error in concentration = 0.002). For the random walk method, the rms error with 2800 particles and 100,000 particles are 0.0074 and 0.0021 respectively. The number of particles that need to be used is much smaller than the number of particles required for a random walk model with similar accuracy.

The scheme has also given good results for the non-Fickian advective diffusion of a 2D continuous source of finite width, as well as continuous source in unsteady flow and actual field application of the 2D tidal flushing of a fish culture zone (Wong *et al*. 2004[15]).

The main advantage of the present method lies in the ability to model particle attributes with a small number of Lagrangian particles. The scheme is applied to simulate the algal dynamics using Eq. (1). In the model, the time dependent vertical distribution of algae at the field station is predicted using the cell quota growth formulation (Droop 1983[18]) in which growth rate depends on the internal nutrient reserve of phytoplankton (the cell attribute) - i.e. the Lagrangian particle model solves the nutrient reserve as a particle attribute. In addition, phytoplantkon undergoes a diel vertical migration (Cullen and MacIntyre 1998[17]) of 20 m/day to uptake nutrient at the sea bottom during night time and utilise solar radiation at the surface during day time.

The algal growth dynamics is simulated using the particle separation scheme with 60 particles. Figure 13 shows the simulated time variation of algal biomass (chlorophyll-*a*) and dissolved oxygen at three depths during a dinoflagellate bloom in May 2000. Compared to the field observations, it can be seen that both model and observations reveal the diel vertical migration of dinoflagellates: i.e. high surface algal concentration during the day, and high algal concentration towards the bottom during the night. The general trend of algal biomass variation is reasonably well-predicted. More interestingly, the relatively higher DO concentration in the surface layer during the day time, and the much stronger drop in DO during the night in the middle and bottom layers is also simulated. Model predictions of DO at mid-depth are however generally higher than observed. This represents the first attempt of simulating cell quota nutrient uptake using a Lagrangian particle method.

4 CONCLUDING REMARKS

We have presented a number of examples to illustrate how hydrodynamic and water quality modeling can be useful in the study of dissolved oxygen and algal dynamics, and in fisheries management. A new systematic procedure of determining flushing time for stratified waters is presented and its application in mariculture management discussed. In response to the need to model the vertical migration of swimming algal species, a new deterministic Lagrangian particle separation method to study advective-diffusion has been presented. These relatively simple models have yielded important insights in the study of coastal water quality. For a variety of reasons, there is a need to integrate the deterministic models with field data to develop a tractable model to track the changes in the complex coastal marine ecosystem. Research into data-driven methods and data-assimilation methods are currently in progress.

ACKNOWLEDGMENTS

The work reported herein was supported by a Hong Kong Research Grants Council group research project (RGC/CA/HKU 2/98 and 1/02C) and in part by the Areas of Excellence Scheme established under the University Grants Committee of the Hong Kong Special Administrative Region, China (Project No. AoE/P-04/2004).

REFERENCES

[1] Lee JHW, Wu RSS and Cheung YK. Forecasting of dissolved oxygen in marine fish culture zone, *Journal of Environmental Engineering, ASCE*, 1991, **117**(6), 816-833.

[2] Dickman M.D. Hong Kong's worst red tide, *Proc. Int. Symp. Env. Hydraulics*, (Ed. Lee J.H.W. *et al.*), Balkema, 1998, 641-645.

[3] Lee JHW and Qu B. Hydrodynamic tracking of the massive spring 1998 red tide in Hong Kong, *J. Environmental Engineering*, ASCE, 2004 (in press).

[4] Garcon VC, Stolzenbach KD and Anderson DM. Tidal flushing of an estuarine embayment subject to recurrent dinoflaggelate blooms", *Estuaries*, 1986. .**9**(3), 179-187.

[5] Lee JHW and Wong PPS. A water quality model for mariculture management, *J. Env. Engr., ASCE*, 1997, **123**(11), 1136-1141.

[6] Dyer KR. ***Estuaries – a physical introduction***, John Wiley & Sons, New York, 1973, 140 pp.

[7] Prandle D. A modelling study of the mixing of ^{137}Cs in the seas of the European continental shelf *Phil. Trans. R. Soc. Lond. A*, 1984, **310**, 407-436.

[8] Signell RP and Butman B. Modelling tidal exchange and dispersion in Boston Harbour, *Journal of Geophysical Research - Oceans*, 1992, **97**(C10), 15591-15606.

[9] Lee JHW, Choi KW and Arega F. Environmental management of marine fish culture in Hong Kong, *Marine Pollution Bulletin*, 2003, **47**(1-6), 202-210.

[10] Choi KW Environmental management of mariculture in Hong Kong. Ph.D. thesis, The University of Hong Kong, 2002

[11] Choi KW and Lee JHW. Numerical determination of flushing time for stratified water bodies, *Journal of Marine Systems*, 2004 (in press).

[12] Lee JHW, Wong KTM, Huang Y and Jayawardena AW. A real time early warning and and modelling system for red tides in Hong Kong' *Proc. 8th International Symposium on Stochastic Hydraulics* (eds. Wang, Z.Y. and Hu, S.X.), July 25-28, 2000, Beijing (invited lecture), Balkema, .659-669.

[13] Wong KTM and Lee JHW. A novel Lagrangian particle method for advective diffusion transport problems, *Proc. 16th ASCE Engineering Mechanics Conference*, July 16-18, 2003, University of Washington, Seattle (CDROM).

[14] Bowie GL *.et al*. Rates, Constants and Kinetics Formulations in Surface Water Quality Modeling, EPA/600/3-85/040, USEPA, Athens, Georgia, 1985.

[15] Wong KTM, Lee JHW and Choi KW. A deterministic Lagrangian particle separation-based method for advective diffusion problems, 2004 (submitted for publication).

[16] Thomann RV and Mueller JA. Principles of surface water quality modeling and control, Harper and Row, New York, 1987.

[17] Cullen JJ and MacIntyre JG. Behaviour, Physiology and the Niche of Depth-Regulating, In *Physiological Ecology of Harmful Algal Blooms*, (Anderson~DM, Cembella~AD, Hallegraeff~GM (eds)), Berlin : Springer, 1998, 559-579.

[18] Droop MR. 25 years of algal growth kinetics, *Botanica Marina*, 1983, **24**, 99-112.

[19] Cheng RT, Casulli V and Milford SN. Eulerian-Lagrangian solution of the convection-dispersion equation in natural coordinates, *Water Resour. Res.*, 1984, **20**(7), 944-952.

[20] Richardson LF. Atmospheric diffusion shown on a Distance-Neighbour Graph, *Proc. Roy. Soc. London A*, 1926, **110**, 709-737.

[21] Batchelor GK. Diffusion in a field of homogeneous turbulence II The relative motion of particles. *Proc. Cambridge Philosophical Society*, 1952, **48**, 345-362.

[22] Csanady GT. ***Turbulent diffusion in the environment***, Reidel, 1973.

Table 1 Computed system-wide flushing time and residence time at selected locations

	Dry season		Wet season	
	System-wide flushing time (days)	Residence time (days)	System-wide flushing time (days)	Residence time (days)
Three Fathoms Cove, Tolo Harbour	23.6	24.3	14.2	13.9
Yim Tin Tsai East, Tolo Harbour	27.2	27.5	14.8	14.7
Yim Tin Tsai, Tolo Harbour	38.0	38.8	14.4	15.8
Sok Kwu Wan, Lamma Island	25.8	24.2	3.5	3.2

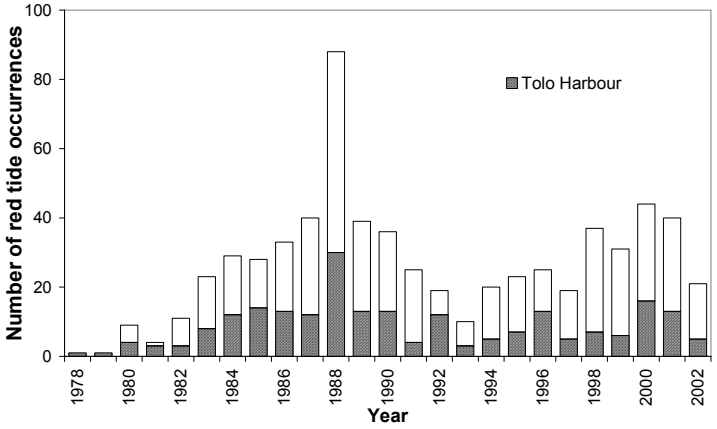

Fig. 1: Red tide occurrences in Hong Kong

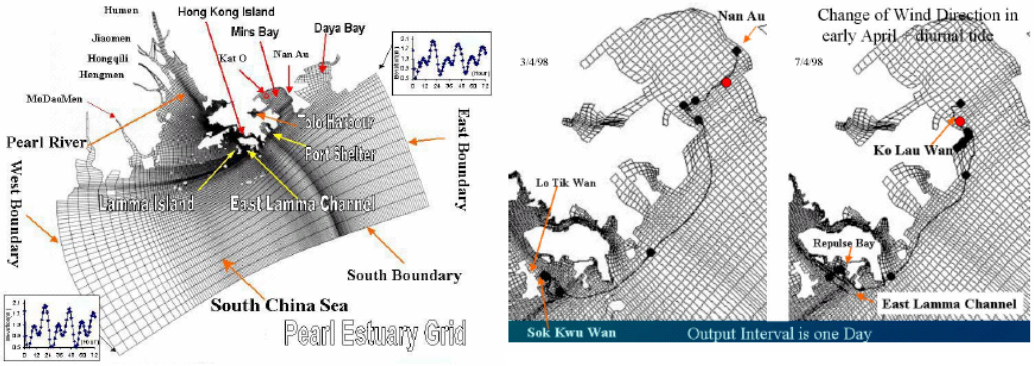

Fig. 2: Pearl River Estuary model for algal bloom tracking and surface drogue tracking for a release in different parts of Mirs Bay during March-April 1998 (output interval=1 day)

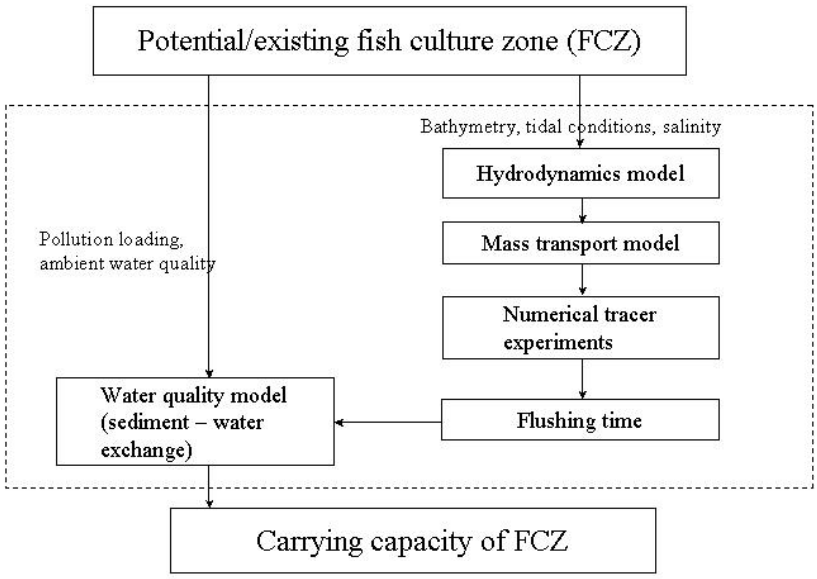

Fig. 3: Framework for modelling of carrying capacity

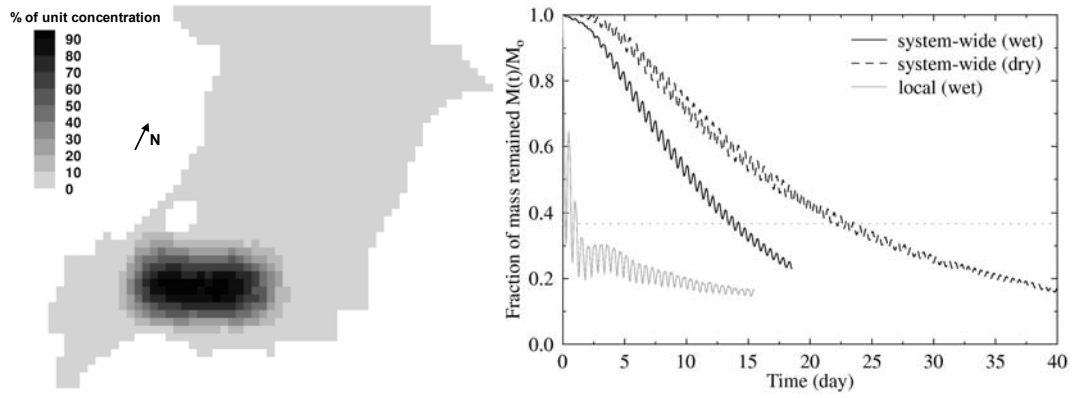

(a) (b)

Fig. 4: a) Computed tracer concentration distribution 12 hours after release of tracer mass in Yung Shue Au fish culture zone, Three Fathoms Cove, Hong Kong; b) tracer mass variation with time for system-wide flushing and "local" flushing, for dry and wet season.

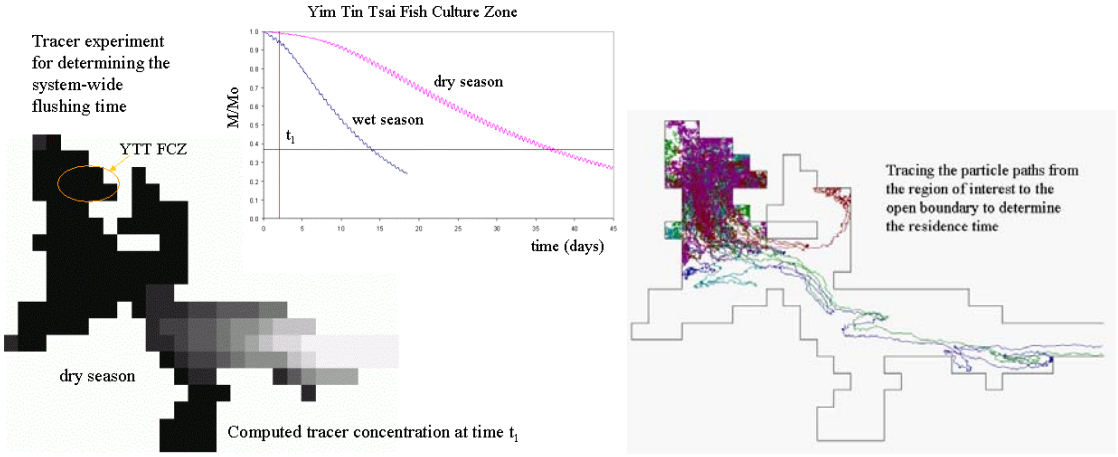

Fig. 5: Computed system-wide flushing time and residence time by numerical tracer experiments

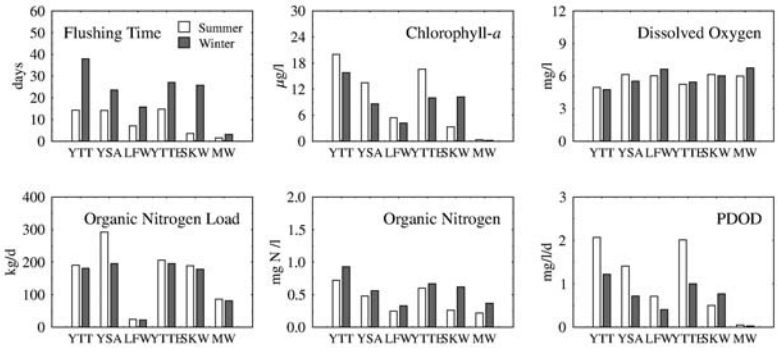

Fig. 6: Organic loads, flushing times and key water quality indicators at six fish culture zones;

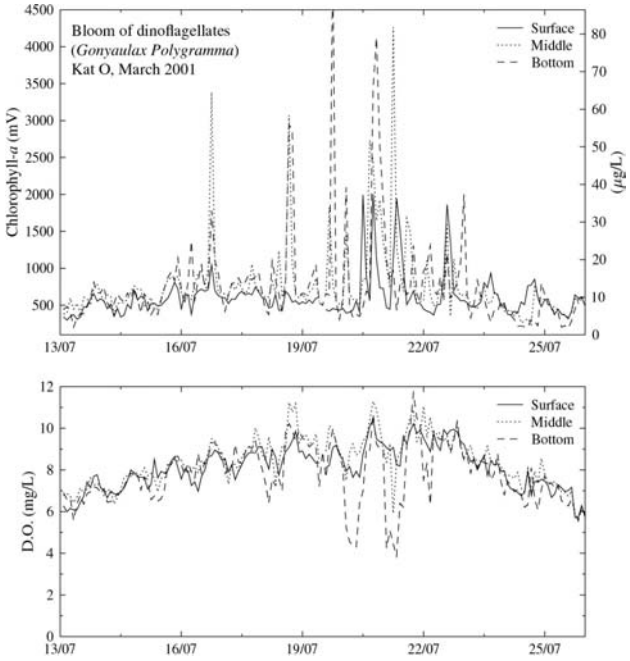

Fig. 7: Observed changes in chlorophyll and dissolved oxygen during a dinoflagellate bloom at Kat O, Hong Kong

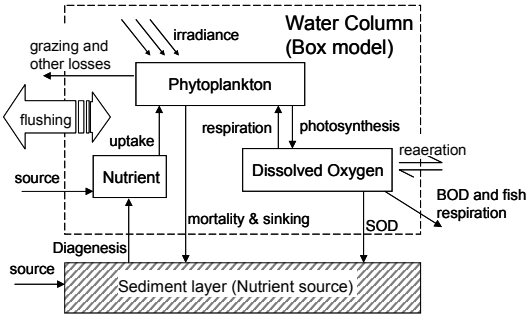

Fig.8: Schematic of water quality model for dissolved oxygen and algal dynamics

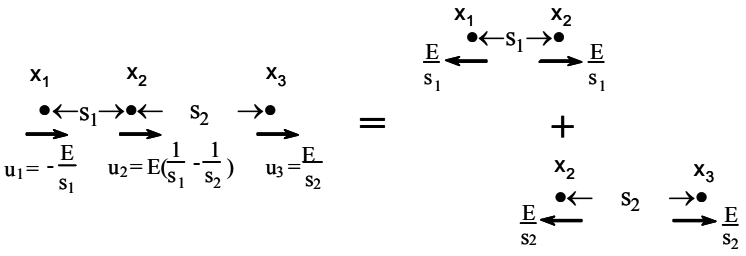

Fig. 9: Lagrangian particle method: separation rule for “a patch of 3 particles”

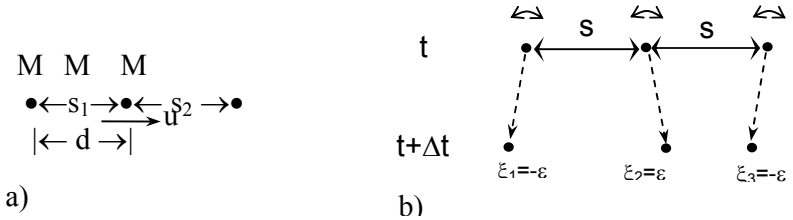

Fig. 10: a) Lagrangian equivalence to Fick's Law; b) stability criterion for neighbourhood separation technique

Error!

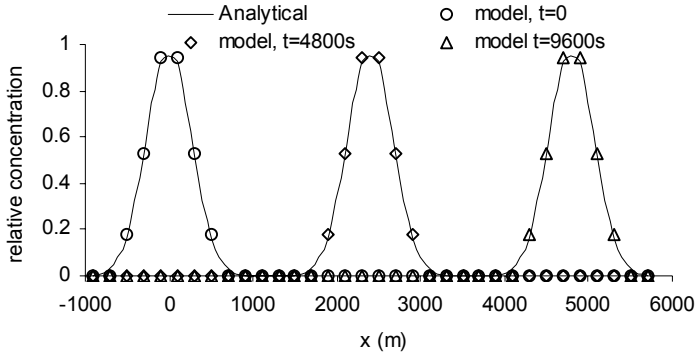

Fig. 11: Simulation of advective diffusion using NEST

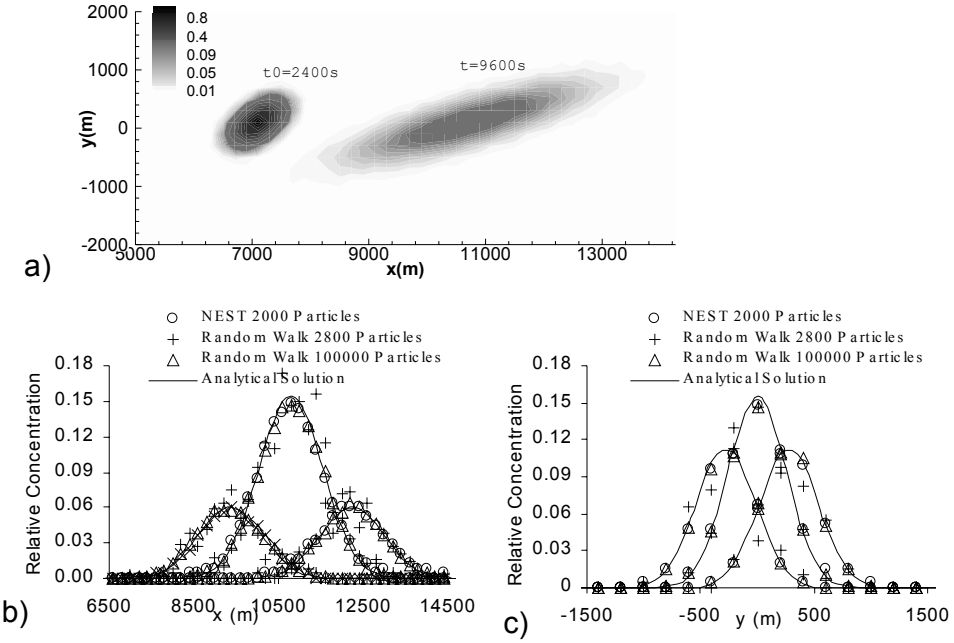

Fig. 12: Numerical simulation of 2D shear diffusion ($u = 0.5m/s$, $E = 2m^2/s$, $\lambda = 0.0005$) a) concentration contours; b,c) concentration along and across flow at $t=9600s$

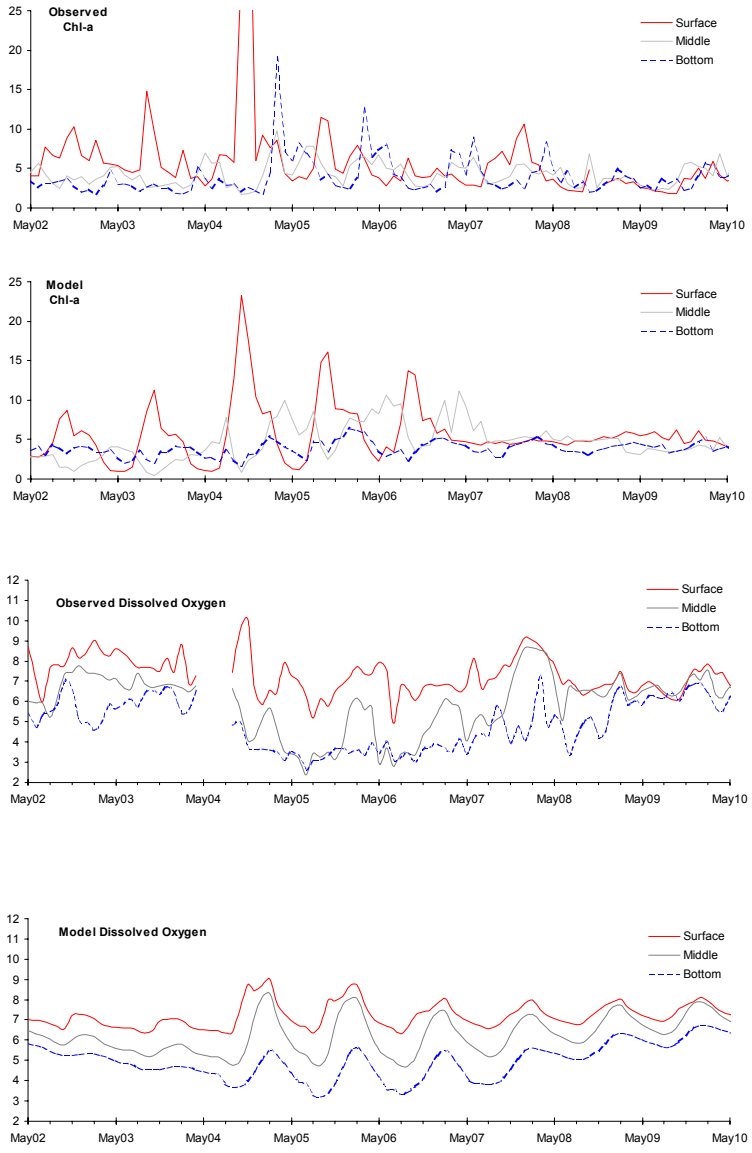

Fig. 13: Observed and simulated changes in chlorophyll and dissolved oxygen concentration during a dinoflagellate bloom at Kat O, Hong Kong, May 2000

Proceeding of the Tenth Asian Congress of Fluid Mechanics
17-21 May 2004, Peradeniya, Sri Lanka

ULTRASONIC DOPPLER METHOD FOR FLOW MEASUREMENT

Yasushi Takeda
Div. Mechanical Science, Graduate School of Engineering, Hokkaido University, Kita-13, Nishi-8, Kita-ku, Sapporo, Japan

ABSTRACT: Ultrasonic Doppler method has been developed to be applied for fluid mechanics and fluid engineering. It uses a pulsed ultrasonic echography together with a detection of instantaneous Doppler shift of the echo. The method can obtain an instantaneous velocity distribution of a velocity component on a line of the ultrasonic beam. This generates a spatio-temporal data of the velocity field. The data was analyzed by orthogonal decomposition techniques and excitation of different modes was obtained to investigate a flow transition in a rotating Couette system. This method is also a powerful tool to measure a velocity distribution in opaque fluids such as liquid metals. Mercury flow was fully investigated. Thanks to an efficient line measurement, flow mapping is also practicable and applied to normal liquids flow as well as mercury flow.

1. INTRODUCTION

During the last two decades, Laser technology for flow measurement has changed the methodology in Experimental Fluid Dynamics and Mechanics. Starting of LDA brought us into a quantitative world of experimental results of high spatial and temporal resolution. It was, however, a point-wise measurement, while the recent development of PIV has stepped up our measurements to two or three-dimensional space.

In parallel to such development of optical methods, ultrasound has been used for quite a long time for flow measurement[1]. Its usage however was limited to medical applications such as cardiovascular flow measurement, or flow metering applications.

Ultrasonic Doppler Method (UDM) for obtaining instantaneous velocity distribution was originally developed in the field of medical engineering, but its application was very limited in the field. Almost twenty years ago, this method was first applied to a general fluid mechanical study[2] and showed to be a power tool for experimental fluid mechanics. Since then, the UDM has been used in quite a diversity of flow configurations, by which this method and the methodology associated with it has been established[3] .

After describing various features of this method, some examples of physics made and engineering applications are presented, followed by the future of this method.

1.1 Working Principle

The method is described in great detail in earlier papers[4] and a device has been marketed[5]. The principle is to use an echography of ultrasound (Fig.1). The ultrasonic pulse is emitted from a transducer and reflected by particles suspended in fluids and received with the same transducer. For deriving instantaneous velocity profile, position information is given by a time lapse between pulse emission and reception of the echo. The velocity information can be obtained from an instantaneous frequency of the echo at each time instant.

By analyzing the echo signal such that instantaneous frequencies at various instant after the emission are computed, the instantaneous velocity profile can be obtained. For the most of the system constructed so far, velocity values at 128 positions with separation of equal distance are obtained with a time resolution of around 132 ms. The measuring volume of each data points has a disc shape of radius 2 mm and thickness 3/4 mm.

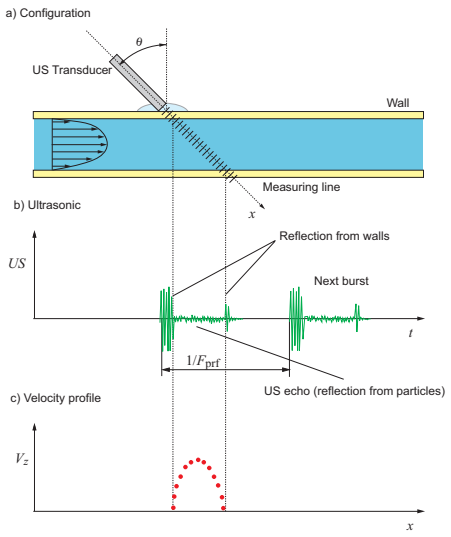

Fig. 1: Illustration of the principle of UDM

The device can be designed for required flow configurations and fields, and those numbers given here are typical for laboratory experiments. Beam characteristics are also strongly dependent on the basic frequency of ultrasound and the dimension of a transducer to be used.

1.2 Characteristics of the Method

The UDM enables us to obtain a spatial distribution of one velocity component to the beam direction as a function of time. An echographic relation determines the maximum attainable length of distribution;

$$P_{\max} = c/2f_{\mathrm{prf}}$$

When one measures large distances, the time until echo returns to the transducer becomes longer and the pulse repetition frequency has to be set lower. The maximum measurable velocity is determined from the Nyquist theorem

$$V_{\max} = cf_{\max}/4f_0$$

From the above two equations, the composite measurement limitation by this method is given as

$$V_{\max}P_{\max} < c/8f_0$$

The spatial resolution depends largely on the pulse characteristics of the ultrasound and not on the parameters of the electronics. The spatial resolution in the axial direction of the beam is determined by the pulse length. Usually, the ultrasonic pulse takes exactly four or more cycles of the basic frequency. A lower basic frequency results in a larger spatial resolution. The lateral resolution is mainly determined by the beam diameter. It should be noted here that a beam divergence is not negligibly small, which depends on the basic frequency of the ultrasound and the size of the transducer.

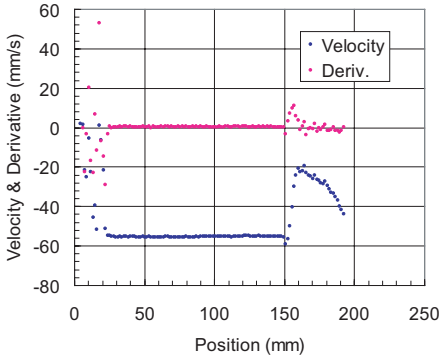

Fig. 2: Time averaged velocity profile of rigid body motion of fluid in a rotating cylinder

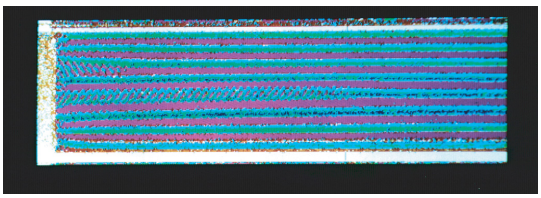

Fig. 3: Color density plot of a Taylor Couette Flow after a sudden start. Coordinate is time and abscissa is position

As this method uses frequency information only of the ultrasound, it is seldom that any other frequency change other than the Doppler shift is induced into the echo signal as noise. As long as the frequency characteristic of the electronics is kept precise, the measurement accuracy can be considered to be very high. Typically the UDM measurement displays a fluctuating velocity For instance, when measuring a laminar flow in a circular pipe, one often observes that the instantaneous velocity profile does not show a parabolic distribution. This is mainly because some kind of oscillation remains in the test apparatus and the flow is not completely stationary with respect to the time resolution of the measuring system. When one takes the average of the velocity profiles over some time period, one can obtain the expected parabolic distribution.

1.3 Methodological Advantages in EFD

Comparing with conventional measurement techniques, this method has the following advantages:
(1) It obtains spatio-temporal information about the flow field.
(2) It can be applied to opaque liquids.
(3) Its line measurement techniques makes flow mapping very practical.

The first character appears to be the final goal of developing measurement techniques in fluid dynamics; to obtain a solution of the Navier-Stokes equation. Although the UDM generates data in one spatial dimension, it enables us for the first time to analyze the flow field using spatio-temporal orthogonal decomposition. The second feature is obviously a great improvement in using opaque liquids such as liquid metals or food materials. This may influence on the engineering studies, especially of rheological flow. The last is important not only in engineering fields but also for validation of computer codes. It is naturally required to validate the code by comparing the obtained velocity fields.

2. FLOW FIELD MEASUREMENTS AND ANALYSIS

As described above, flow field measurement by UDM opens up a new way of analyzing dynamics and structure of the flow. Detail of the analysis is given in references[6], and here only briefly presented. Examples used here are for the rotating Couette flow (TCF) configuration. Detail of the apparatus, experiment and physics discussed are given elsewhere[7].

2.1 1C1D+Time

UDM obtains the field data in the form of spatio-temporal dimension and usually displayed in color density plot as Fig.3. The velocity component obtained is a projection of the true velocity vector on the measurement line ($V_z(z)$ for the present example), but as it is instantaneous for all the data points, it has a spatio-temporal nature in itself. As shown in this example, this nature is clearly depicted and this kind of representation helps greatly to catch the flow nature instinctively. Especially, flow instability reveals as the change of spatial structure of the flow fields at the initial stage, and thereafter spatio-temporal structure changes. In this sense, UDM data is advantageous even though it is 1C1D in spatial coordinate.

2.2 Power and Energy Spectrum and Orthogonal Decomposition

It is an obvious approach to compute a power spectrum by taking Fourier transform on time. This generates space-dependent power spectra, whereby spatial dependence of any distinctive temporal modes can be investigated.

More important of this method is a capability of obtaining Energy Spectral Density directly by taking Fourier transform of the data in space. By point-wise measurements, it was impractical to collect a large data set to obtain such quantity, so that it was usual to convert the power spectrum to energy spectrum adopting the Taylor's frozen hypothesis. It was the first time to have obtained

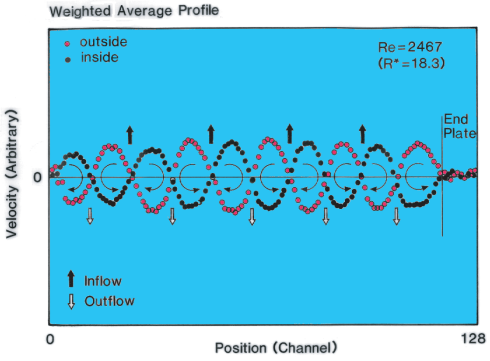

Fig. 4: Time averaged velocity distributions of TVF ($V_z(z)$)

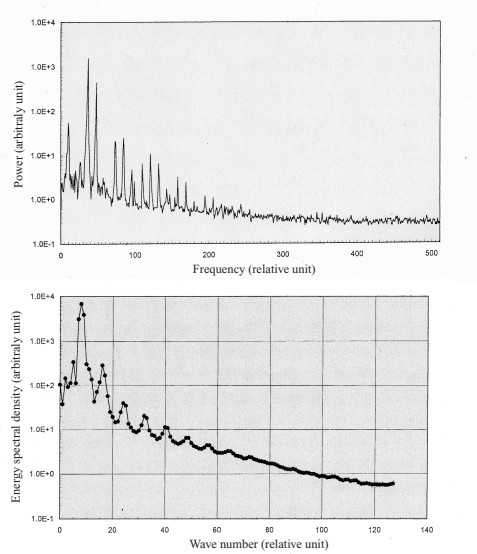

Fig. 5: Space averaged power spectrum (above) and time averaged energy spectral density (bottom)

the energy spectral density as a function of wave number (spatial) without using the Taylor's hypothesis. Further important is that the energy spectral density so obtained is time-dependent.

A spatio-temporal nature of the data obtained by this method is fully used when the data set is analyzed by any kind of orthogonal decomposition techniques. Two-dimensional Fourier analysis (2D-FFT) and Proper Orthogonal Decomposition[7] (POD) are typical in the flow analysis.

We applied this technique to the spatio-temporal data set obtained for Taylor Couette flow. It could extract spatial and spatio-temporal structures such as TVF and WVF[8].

3. ENGINEERING APPLICATIONS

In parallel to physics studies as presented above, various engineering applications have been made. They all are practices of any one of the advantages of this method given in 1.3 A brief description is given here, and detail will be found in the earlier publications.

3.1 2C2D - Flow Mapping

The UDM is a line measurement, which enables us to obtain velocity distribution quite efficiently. Two dimensional velocity mapping is what is required in most of engineering projects and it is efficiently performed by UDM to measure a vector flow field. Furthermore, we believe that a validation of any computer codes should be made on the basis of velocity distribution and it is now possible since UDM obtains experimentally a solution of NS equation. We investigated behaviors of mercury flow in a configuration of the liquid metal target for the neutron source at PSI.

A fairly large number of one-dimensional velocity distributions for different orientations of measurement lines were used. Two velocity components are obtained at the crossing point of two measurement lines, from which flow vector can be computed. The measurement lines are arranged such that many crossing points for a combination of all measurement lines would cover as large area as required and that those points might be distributed uniformly. The number of such crossing points is proportional to N^2, a square of the number of measurement lines, while it is N for the point measurement. From our practical experiences, a typical vector plotting of the velocity field consists of 500 to 1000, even more, data points. Figs.6 and 7 show these examples.

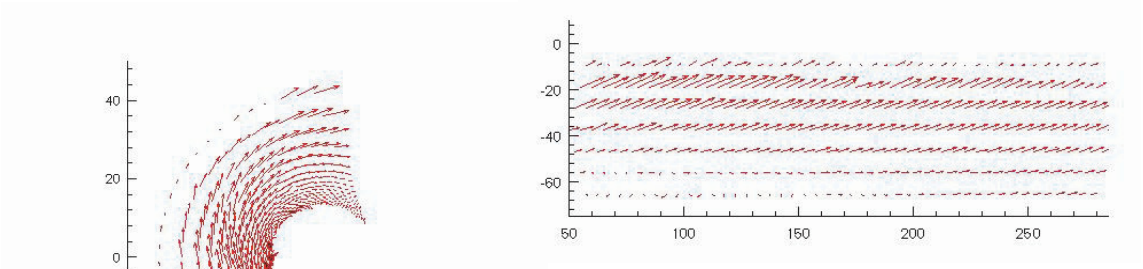

Fig. 6: Measured vector flow map

Fig. 7: Measured vector flow map

3.2 Opaque Fluids

Many fluids are opaque in engineering configurations. Liquid metal is typical as well as food materials, chemical and pharmaceutical materials. Some of them are rheological and difficult in knowing their flow fields by simple model liquids. UDM is a very powerful technique to obtain flow fields in such configurations, and probably the only method available at present. Figs.8, 9 are examples of these measurements.

3.3 Flow Metering

An important application of this method in engineering fields is an adaptation of this method to a novel flow metering system. In principle, flow rate is accurately computed once the velocity distribution in a flowing conduit is obtained, as in no conventional method of flow metering. In this context, the present application is theoretically very correct and is expected to have a much higher accuracy than other methods.

A novel flow metering system has been developed for a pipe flow. A velocity distribution on a radius or a diameter is obtained using a single transducer and an instantaneous flow rate is computed. A transient flow rate was compared with the electromagnetic flow meter and the orifice flow meter, showing a high potential of this system.

The accuracy evaluation of the system was made using two national standard; NIST, Gaithersburg, USA and NMIJ, Tsukuba, Japan. In both cases, the measured values were compared with

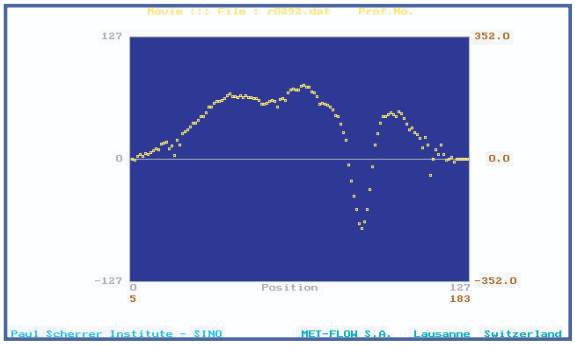

Fig. 8: 14 Example of an instantaneous velocity profile of mercury flow

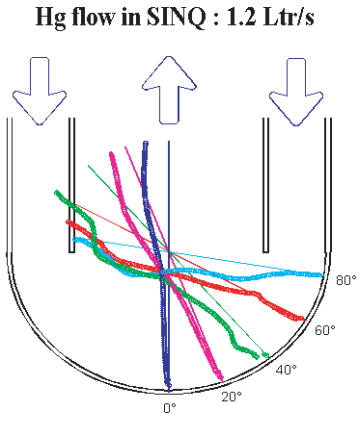

Fig. 9: 1D velocity distributions at various locations of mercury flow

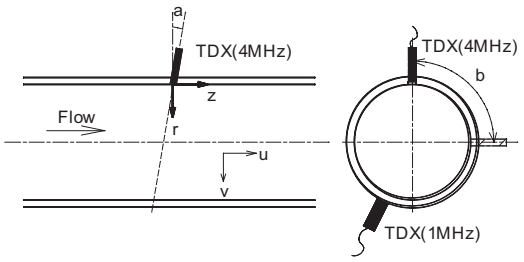

Fig. 10: Arrangement of a novel flow meter

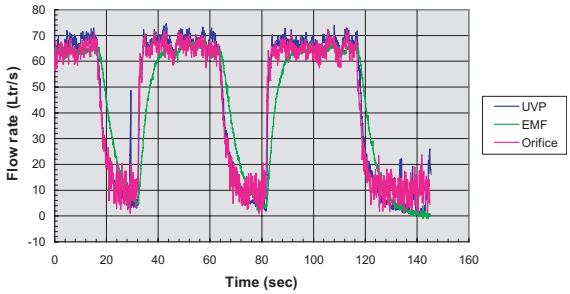

Fig. 11: Transient flow rate in comparison with EMF (green) and OFM (red)

their weighing tank measurements and it was found the difference of the present system from those of weighing measurements ranges from 0.1% to 0.5% depending on the Reynolds number, which confirmed the precision of this flow metering system. This difference is only roughly 1/10 compared to the conventional flow meters, especially ultrasonic flow meter. This breakthrough was only possible by measurement of instantaneous velocity distribution.

4. FUTURE

The Ultrasonic Doppler Method for flow measurement has been developed and established in the filed of fluid mechanics and fluid engineering. It is highly expected that more applications of this method for a wide range of flow configurations in the engineering problems will be made.

As a research tool, further development is under progress. A new algorithm of signal processing and the system is being investigated for a faster sampling time. In the present system, the fastest sampling time is roughly 10msec, which can resolve the temporal structure only up to 100Hz and it is insufficient for a turbulence study. Effort is being made to overcome this problem.

A flow field, especially environment and turbulent flow, is three-dimensional and a vector measurement is indispensable. With the present system, it is still impractical to obtain 3C3D information of the flow. It is expected that a new system be developed for vector measurement.

REFERENCES

[1] Atkinson, P., and Woodcock, J.P., Doppler Ultrasound and Its Use in Clinical Measurement, Academic, New York 1982.

[2] Takeda, Y. 1985 Velocity profile measurement by ultrasound Doppler shift method, Fluid Control and Measurement, Ed. by M.Harada, pp851, Pergaman, Tokyo.

[3] International Symposium on Ultrasonic Doppler method in Fluid Mechanics and Fluid Engineering, 9-11 Sept. 96, PSI, Switzerland.

[4] Y. Takeda, Development of ultrasound velocity profile monitor, Nuclear Engineering & Design, 126 (1990) 277 Y.Takeda, Instantaneous velocity profile measurement by ultrasonice Doppler method, JSME International Journal, Fluids and Thermal Engineering, Vol.38, No.1, (1995) p8 - 16, Takeda,Y., "Velocity profile measurement by ultrasound", p.148, in "New methods for thermofluid flow measurement", Ed. M.Maeda & T.Kamimoto, Yokendo, 1998 (in Japanese).

[5] Met-Flow S.A., visit www.met-flow.ch.

[6] Y.Takeda, W.E.Fischer and J.Sakakibara, Decomposition of the modulated waves in a rotating Couette system, Science, Vol.263, 28.Jan. (1994) p502.

[7] P. Holmes, J.L.Lumley & G.Berkooz, "Turbulence, Coherent Structures, Dynamical Systems and Symmetry", Cambridge University Press, 1996.

[8] Y.Takeda, Quasi-periodic state and transition to turbulence in a rotating Couette system, 389, 81-99, J. Fluid Mech.

Proceedings of the Tenth Asian Congress of Fluid Mechanics
17-21 May 2004, Peradeniya, Sri Lanka

NUMERICAL SOLUTIONS TO SOME PROBLEMS IN FLUID MECHANICS AND HYDRAULICS

P. Wang, M. Yan, P. Echeverria and R. Kahawita

(Department of Civil, Geological and Mining Engineering Ecole Polytechnique de Montréal
Montréal, Québec, Canada, H3C 3A7)

ABSTRACT: This paper presents an overview of numerically obtaining solutions to problems in fluid mechanics and hydraulics using various numerical methods. The majority of this work is devoted to the cubic spline integration technique since many of the examples in computational fluid dynamics presented here were realized with this scheme.

The first part consists of a brief historical review. The second section is devoted to a review of the basic cubic spline relations and a discussion on the discretization accuracy. This is followed by an expose of the numerical algorithms used to compute solutions to second order partial differential equations. Both implicit and explicit formulations together with an examination of their linear stability is presented.

Examples of applications chosen from such diverse fields as the Navier-Stokes Equations, natural convection heat transfer under steady and unsteady flow conditions, density inversion problems, Marangoni convection, oscillatory flow behind bluff bodies and hydrodynamics of rivers and estuaries have been presented. Finally, a numerical model for the computation of dambreak flows in rivers with or without erodible beds that uses a shock-capturing algorithm (not based on splines) will be presented together with some examples of its application.

1 INTRODUCTION

The cubic spline technique constitutes a relatively new subject in the field of numerical methods. The mathematical research and applications of this method to the solution of partial differential equations appears to have been developed during the last three decades or so. However, it is only comparatively recently that the computational methodology has been formally systematized, simplified and formulated. Experience indicates that the spline approximation is very easy to use and may achieve an accuracy comparable to that of corresponding high order finite-difference methods while using fewer grid points, resulting in a significant reduction in computer core memory requirements. Consequently, with the rapid development in hardware performance, many problems involving heat transfer and fluid flow may now be solved on a personal computer.

A further important computational advantage is that boundary conditions containing derivatives may be easily incorporated into the solution procedure since values of first or second derivatives may be evaluated directly (that is, treated as the dependant variable) while preserving the same degree of accuracy.

The historical development of the method is characterized by its applications in solving ordinary and partial differential equations. The main contributions were made by Rubin et al.[1-3]. They systematically studied the cubic spline collocation procedure for the numerical solution of a partial differential equation (PDE), discussed the truncation errors of the procedure and its stability and presented a general formulation resulting in a 3x3 matrix system for treating partial differential equations. Their technique involved an implicit procedure.

Based on Rubin et al.'s work, the present authors developed a procedure to transform the 3x3 matrices into a scalar tridiagonal system [13,14]. The advantage of this formulation is that solutions may be obtained exclusively in terms of the function values themselves, their first derivatives or their second derivatives. Furthermore, a tridiagonal matrix has to be evaluated instead of general 3x3 matrices. According to the particular requirements of the problem and its imposed boundary conditions, any one of the three forms of equations may be chosen for the solution procedure. The implementation of three typical boundary condition types into the solution procedure has been discussed in detail by Wang [6]. Subsequently, a spline explicit method that introduces a weighting parameter into the coefficient of the second derivative term was studied [6-8]. Successful applications of these various formulations in the field of fluid mechanics, hydraulics and themodynamics are reported in [9-12].

Wang [13-14] proposed a Spline Method of Fractional Steps (SMFS). This technique is used to generate an algorithm resulting in a tridiagonal system containing either function values or first derivatives at the grid points. The essential feature of this method is that at each computational step, the problem is treated in a uni-dimensional implicit fashion so that only one (tridiagonal) matrix system need be evaluated. This technique together with the previously developed solution technique simplifies writing the code and significantly reduces CPU time. More recently, Echeverria [29] has introduced an improvement in the technique by using splines under tension for applications in fluvial hydraulics where irregular geometries are the norm.

2 BASIC CUBIC SPLINE RELATIONS

Let x_i be the coordinate of the node points on the interval [a,b]:

$$a = x_0 < x_1 < \ldots < x_{n+1} = b$$

$$h_i = x_i - x_{i-1} > 0$$

The function $u(x)$ is defined on $[a,b]$, at the node points x_i by:

$$u(x_i) = u_i$$

Let:

$$S_p(u,x) = S_p(x)$$

denote the cubic spline function, which is continuous together with its first and second derivatives on $[a,b]$ and satisfies

$$S_p(x_i) = u_i$$

Then, in general:

$$S_p''(x) = M_{i-1}\left(\frac{x_i - x}{h_i}\right) + M_i\left(\frac{x - x_{i-1}}{h_i}\right) \tag{2.1}$$

where : $M_i = S_P''(x_i)$

Integrating twice results in the interpolation formula on (x_i, x_{i-1}):

$$S_p''(x) = M_{i-1}\frac{(x_i - x)^3}{6h_i} + M_i\frac{(x - x_{i-1})^3}{6h_i} + \left(u_{i-1} - \frac{m_{i-1}h_i^2}{6}\right)\frac{x_i - x}{h_i} \tag{2.2}$$

$$+\left(u_i - \frac{m_i h_i^2}{6}\right)\frac{x - x_{i-1}}{h_i}$$

where the integration constants have been evaluated by the requirement of continuity of the function and its first derivative values at the node points.

The main cubic spline relationships are (with $m_i = S_p'(x_i)$):

$$\frac{h_i}{6}M_{i-1} + \frac{h_i + h_{i+1}}{3}M_i + \frac{h_{i+1}}{6}M_{i+1} = \frac{(u_{i+1} - u_i)}{h_{i+1}} - \frac{(u_i - u_{i-1})}{h_i} \tag{2.3}$$

$$\frac{1}{h_i}m_{i-1} + 2\left(\frac{1}{h_i} + \frac{1}{h_{i+1}}\right)m_i + \frac{1}{h_{i+1}}m_{i+1} = \frac{3(u_{i+1} - u_i)}{h_{i+1}^2} - \frac{3(u_i - u_{i-1})}{h_i^2} \tag{2.4}$$

$$m_{i+1} - m_i = \frac{h_{i+1}}{2}(M_i + M_{i+1}) \tag{2.5}$$

$$m_i = \frac{h_i}{3}M_i + \frac{h_i}{6}M_{i-1} + \frac{(u_i - u_{i-1})}{h_i} \tag{2.6}$$

or

$$m_i = -\frac{h_{i+1}}{3} M_i - \frac{h_{i+1}}{6} M_{i+1} + \frac{(u_{i+1} - u_i)}{h_{i+1}} \tag{2.7}$$

$$M_i = \frac{2m_{i-1}}{h_i} + \frac{4m_i}{h_i} - \frac{6(u_i - u_{i-1})}{h_i^2} \tag{2.8}$$

or

$$M_i = \frac{2m_{i+1}}{h_{i+1}} + \frac{4m_i}{h_{i+1}} - \frac{6(u_{i+1} - u_i)}{h_{i+1}^2} \tag{2.9}$$

Accuracy of Discretizations

Discretization errors may be estimated by using the above basic spline relations. From Eq.(2.4), the following results are obtained [1,4]:

$$m_i = (u_x)_i - \frac{h_{i+1}h_i(h_{i+1} - h_i)}{72}(u_{xxxx})_i - \frac{h_{i+1}h_i(h_{i+1}^2 - h_{i+1}h_i + h_i^2)}{180}(u_{xxxxx})_i + O(h_i^5, h_{i+1}^5) \tag{2.10}$$

For a uniform mesh, $h_{i+1} = h_i = h$ and fourth order accuracy, i.e.

$$m_i = (u_x)_i - \frac{h^4}{180}(u_{xxxxx})_i + O(h^6)$$

is obtained.

The accuracy of the second derivative is:

$$M_i = (u_{xx})_i - \frac{h_{i+1}^3 + h_i^3}{12(h_{i+1} + h_i)}(u_{xxxx})_i - \frac{(h_{i+1} - h_i)(6h_{i+1}^2 - 5h_{i+1}h_i + 6h_i^2)}{180}(u_{xxxxx})_i + \tag{2.11}$$

$$+ O(h_i^4, h_{i+1}^4)$$

It is readily seen that the second derivative is approximated to second order independent of the type of mesh spacing employed. However, for uniform grid spacing the accuracy of the second derivative may be improved by combination of Eq.(2.11) with the standard three-point finite-difference approximation to obtain fourth order accuracy [2]:

$$\frac{1}{2}\left(M_i + \frac{u_{i+1} - 2u_i + u_{i-1}}{h^2}\right) = (u_{xx})_i + O(h^4) \tag{2.12}$$

3 SOLUTION OF PARTIAL DIFFERENTIAL EQUATIONS}

In general, a second order one-dimensional partial differential equation may be written:

$$u_t = f(u, u_x, u_{xx}) \tag{3.1}$$

An approximate solution for u_i may be constructed by considering the solution of:

$$(u_t)_i = f(u_i, m_i, M_i) \tag{3.2}$$

where m_i and M_i represents the spline approximated values of $\partial u/\partial x$ and $\partial^2 u/\partial x^2$ at the grid points i, and the time derivative is discretized in the usual finite difference fashion:

$$\frac{u_i^{n+1} - u_i^n}{\Delta t} = (1-\theta) f^n + \theta f^{n+1} \tag{3.3}$$

For $\theta = 0$, an explicit scheme is obtained $\theta = 1$ results in a fully implicit scheme while $\theta = 0.5$ is

the mixed scheme of Crank and Nicholson.

Implicit Schemes

Eq.(3.3) may be written in a more general form [4]:

$$u_i^{n+1} = F_i + R_i m_i^{n+1} + Q_i M_i^{n+1} \quad (i = 0, M) \tag{3.4}$$

where F_i, R_i and Q_i are known from the previous time step.

Eq.(3.4) has been transformed into a single tridiagonal system [4] containing the function values only:

$$A_i u_{i-1}^{n+1} + B_i u_i^{n+1} + C_i u_{i+1}^{n+1} = D_i \quad (i = 1, M-1) \tag{3.5}$$

or another single tridiagonal system for the first derivatives:

$$a_i m_{i-1}^{n+1} + b_i m_i^{n+1} + c_i m_{i+1}^{n+1} = d_i \quad (i = 1, M-1) \tag{3.6}$$

Here A_i, B_i and C_i or a_i, b_i and c_i depend on $F_i, R_i, Q_i, \Delta t$ and h_i only. More detailed expressions may also be found in the appendix of [5,22]. For two-dimensional problems, Rubin and Graves [1] proposed a Spline Alternating Direction Implicit (SADI) procedure analogous to the well known ADI algorithm:

Step I

$$u_{i,j}^{n+1/2} = u_{i,j}^n + \frac{\Delta t}{2} f\left(u_{i,j}^{n+1/2}, m_{i,j}^{n+1/2}, M_{i,j}^{n+1/2}, l_{i,j}^n, L_{i,j}^n\right) \tag{3.7}$$

Step II

$$u_{i,j}^{n+1} = u_{i,j}^{n+1/2} + \frac{\Delta t}{2} f\left(u_{i,j}^{n+1}, m_{i,j}^{n+1/2}, M_{i,j}^{n+1/2}, l_{i,j}^{n+1}, L_{i,j}^{n+1}\right) \tag{3.8}$$

As indicated previously, the Spline Method of Fractional Steps (SMFS) [13,14] is quite easy to use, because only a single tridiagonal matrix system needs to be evaluated in each coordinate direction. For example:

Step I (in direction x)

$$u_{i,j}^{n+1*} = u_{i,j}^n + \Delta t f\left(u_{i,j}^{n+1*}, m_{i,j}^{n+1*}, M_{i,j}^{n+1*}\right) \tag{3.9}$$

Step II (in direction y)

$$u_{i,j}^{n+1} = u_{i,j}^{n+1*} + \Delta t f\left(u_{i,j}^{n+1}, l_{i,j}^{n+1}, L_{i,j}^{n+1}\right) \tag{3.10}$$

The treatment of boundary conditions corresponding to the tridiagonal system Eq.(3.5) or Eq.(3.6) has been studied in detail by Wang [6]

For the stability analysis, the one-dimensional linear form of Burger's equation has been studied as the model equation.

$$u_t + \bar{u} u_x = \nu u_{xx}$$

When $\theta > 0.5$ unconditional stability is obtained [1,4].

In fluvial hydraulics, complex geometries are very frequently involved. This may result in difficulties with evaluating the derivatives required in the partial differential equations. Echeverria [29] has recently initiated the use of splines under tension to surmount this difficulty. The method is based on the work of Pruess [34] who after revision of several interpolating formulae developed a cubic spline with variable tension factors.

As an example, the expression containing the second derivatives is:

$$M_{i-1}h_i\frac{3p(p-1)^2-1}{6p^2}-M_i\left[h_i\frac{3p^3-6p^2+3p(p-1)^2-1}{6p^2}-h_{i+1}\frac{-3p^3+6p^2-3p(p-1)^2+1}{6p^2}\right]-$$
$$-M_{i+1}h_{i+1}\frac{3p(p-1)^2-1}{6p^2}=\frac{y_{i+1}-y_i}{h_{i+1}}-\frac{y_i-y_{i-1}}{h_i} \quad (3.11)$$

Where M is the second derivative, p is the tension factor and the remaining variables have already been defined.

Work is currently in progress on the automatic selection of the optimum tension factor based on a methodology proposed by Renka [35].

4 EXAMPLES OF APPLICATIONS

Computations in such diverse fields as ablation problems [10], fusion welding problems [11], Navier-Stokes Equations [14], natural convection heat transfer in steady and unsteady flow [13,15,16], density inversion problems[17], Marangoni convection [18-20], oscillatory flow behind bluff bodies [21], hydrodynamics of estuaries [9,22] and overland flow [28] have indicated that the spline method is quite versatile, of high accuracy as well as being computationally efficient. Some results from our own computations are presented below. (Due to space limitations, the reader is directed to the corresponding reference for further details).

4.1 Transient Laminar Natural Convection From Horizontal Cylinders

For this example, the non-dimensional governing equations (using cylindrical coordinates) in stream function and vorticity form together with the Boussinesq approximation for the body forces are employed:

The discretization of the governing equations using the fractional step technique as well as the development of the relevant boundary conditions have been discussed in some detail by Wang et al.[15].The fractional step cubic spline technique allows the boundary conditions to be easily treated because in the computational procedure, first and second derivatives of the dependant variables may be used as the "operational variable", thus allowing higher order boundary conditions to be directly incorporated into the numerical procedure. The use of a non-uniform mesh, depending on the characteristics of the particular problem, has evident advantages such as the reduction in storage requirements and machine time.

Unsteady laminar natural convection flow under diverse surface boundary conditions has been studied by Wang et al.[16]. The development of the plume region as well as the surface heat transfer and local flowfield were evaluated. At small times, the numerical solutions approach the boundary layer results and are in good agreement with the results from a scale analysis. A more detailed study of the development of the plume region, using computed particle trajectories is reported in the same reference. Qualitative comparisons between the numerical results and the flow visualisation experiments of Genceli [23], as shown in figure 1, are quite good.

The interesting behavior of the laminar natural convection about a horizontal cylinder maintained at 0^oC in a water ambient close to the point of maximum density has been reported by the authors in [17]. Complete numerical solutions covering both the transient as well as steady state are presented. Principal results indicate that the proximity of the ambient temperature to the point of maximum density plays an important role in the type of convection pattern. Some steady-state flow patterns obtained for different ambient temperatures are reproduced in figure 2. When the ambient temperature is within $4.7^oC<T_{amb}<8^oC$, a ``dual flow" appears around the cylinder with both upward and downward flow occurring in proximity to the cylinder in two distinct recirculating zones, generally separated by the 4^oC isotherm when $T_{amb}<5.7^oC$. The dual flow behavior is significantly modified as the ambient temperature is altered, disappearing when the ambient temperature is above 8^oC, or below 4.7^oC. Furthermore, when the ambient temperature is within about $4.8^oC<T_{amb}<5.5^oC$, a well defined steady state is never attained. Within this same range, solutions with an initially quasi-periodic behaviour which persist for a long time have been observed. Multiple solutions were noted when the above range of ambient temperatures was approached from either side as shown in figure 3.

4.2 Marangoni convection in two superposed immiscible liquid layers

Thermocapillary convection in superposed immiscible liquid layers has many applications in natural and industrial processes. Some industrial processes that involve thermocapillary forces are surface melting and alloying techniques using high power lasers, processing of ceramics and semiconductors that frequently involve a molten and a gaseous phase. One important application that has been commercially introduced is the elimination of evaporation of volatile components and a reduction in thermal convection of a liquid melt by encapsulation with a protective molten material. The buoyancy-thermocapillary convection in two superposed immiscible liquid layers in a finite cavity with side heating has been studied with different boundary conditions. The convection flow induced by a combination of density differences in a gravitational field and by surface tension gradients, is governed by the continuity equation, the two-dimensional Navier-Stokes equation and the energy equation for both fluids (i = 1 or 2).

The computational results for the problem with a free surface agree qualitatively with analytical predictions when the latter are within their range of validity [18]. For a pure Marangoni convection, typical computed streamlines and isotherms with different cells for various values of Ma^* and Ma_1, the purpose of which was to illustrate the influence of these parameters on the flow field are reprinted in Figures 4(a-d). The numerically calculated maximum and minimum stream function values $\psi_{\max}$ and $\psi_{\min}$ are also indicated on each graph for reference.

Ma^* is a new parameter introduced by Wang et al.[18]. $Ma^* = Ma_1 - 0.5\bar{\alpha}\bar{\mu}Ma_2$, where Ma_1 is the interface Marangoni number and Ma_2 is the Marangoni number for the upper layer $\bar{\alpha} = \alpha_2/\alpha_1$ and $\bar{\mu} = \mu_2/\mu_1$ with α_i = thermal diffusivity and μ_i = dynamic viscosity. This parameter uniquely characterizes the velocity and temperature distributions in the lower layer. In particular, as shown in Figure 4d, a value of $Ma^* = 0$ will result in suppression of convective activity in the lower layer under microgravity conditions, which can have useful applications to crystal growth techniques that employ molten encapsulants.

The appearance of oscillatory behaviour in thermocapillary convection with buoyancy forces has been reported by Wang & Kahawita [20] for superposed immiscible liquid layers with a free surface, in which the lower layer consists of a low Prandtl-number fluid. In that investigation, attention was focused on flow instabilities of an oscillatory nature which appear to be induced by the buoyancy forces. An attempt to understand the origin of these instabilities and indications on how to reduce or even avoid them was made.

Figure 5a presents the time-variation of the maximum stream function in both layers for $Ra_1 = 600$, $Ma_1 = Ma_2 = 0$, $Q_\alpha = 0.01$, $Q_\mu = 0.01$, $Pr_1 = 0.015$, $Pr_2 = 1$ and B = 4 in a rectangular cavity with differentially heated end walls ($T_C = -B/2$ and $T_h = B/2$). The nonlinear character of the oscillation is clear.

Figure 5b provides the time variation of the total mean Nusselt number $\overline{Nu}$ at the two endwalls and at the midplane respectively. It may be noted that the variation of $\overline{Nu}$ is stronger near the cold wall than at the midplane, while near the hot wall this variation is comparatively weak.

Figure 6 illustrates the variation of the isotherms and streamlines in the lower layer at six instants (the small circles shown in figure 5a) over a period of oscillation. It is not surprising that the variation of the flow patterns in the lower layer are similar to those obtained in a single fluid layer by Ben Hadid and Roux [24]. This is a particular case where the buoyancy force and the viscous force in the upper layer are very small compared with the lower one. In other words, the influence of the upper layer on the lower one through the interface is very weak so that oscillations in the lower layer are unavoidable.

4.3 Wake flow behind trapezoidal bluff bodies

The wake flow behind an obstacle has been extensively investigated numerically and experimentally, most classical work having focused on circular cylinders. For industrial flowmeters that exploit the relation between the shedding frequency and the flowrate or velocity, a trapezoidal shape is found to be more desirable, since a well-defined vortex emission due to clean separation at its sharp edges is

assured. Two-dimensional numerical simulations of the Bénard-von Kármán hydrodynamic instability behind trapezoidal bluff bodies were realized and the results compared with experiments conducted in a water tunnel [21,25,26].

The time dependent nonlinear coupled partial differential equations were solved by considering a 121×91 grid. In order to accurately describe gradients that are expected to be steep in the boundary layer regions, a non-uniform grid in both the x and y directions was used. It is useful to indicate however that the spline discretized form is directly applicable to a non-uniform mesh in an x-y coordinate system, thus obviating the need for a computational coordinate transformation as is usually required with finite difference schemes. An illustrative mesh is shown in Figure 7. Numerical results comfirm the experimentally observed behavior reported by Goujon-Durand et al.[26], i.e. the maximum amplitude of the velocity component oscillating with the fundamental frequency follows well the scaling law $A_{\max} \sim (\mathrm{Re} - \mathrm{Re}_c)^{0.5}$ and the position $X_{\max} \sim (\mathrm{Re} - \mathrm{Re}_c)^{-0.5}$.

An instantaneous streakline view for Re = 46 is shown in figure 8. Here, the bluff body of trapezoidal section is characterized by its larger base width d, the smaller base having a width of 0.5d with height also being 0.5d. Two orientations of the body, the first having the smaller base perpendicular to the incident flow (case A) and the second with the larger base perpendicular to the flow (case B) were performed. The broken line in figure 8 corresponds to the envelope of transverse (y) values for which the amplitude along the flow direction is a maximum. It is noteworthy that this picture is very similar to the laser induced fluorescent view of vortex emission, obtained by Goujon-Durand et al.[26] in the laboratory. The envelopes of the global modes corresponding to various Reynolds numbers are shown in figure 9. By renormalizing A and X respectively with $A_{\max}$ and $X_{\max}$, the points of $A/A_{\max}$ versus $X/X_{\max}$ for different Reynold numbers (from Re = 42 to 62) collapse into a single universal curve. This confirms that the properties of the global modes are universal and independent of the form of the trapezoidal body.

4.4 Hydraulic Applications

Density Induced Circulation in a Stratified Estuary

In engineering and environmental impact studies of estuaries, it is of paramount importance to be able to accurately predict the hydraulic and dispersive behaviour under the combined influence of natural and artificially imposed constraints. One of the current areas of interest arising from these investigations is the study of the density induced circulation or "DIC" which has a major influence on the salt balance and the dilution of thermal or pollutant discharges. This is of particular importance for evaluating the potential impact on the environment due to very large scale hydro-electric power developments, especially in rivers with strongly stratified estuaries, since relatively small changes in the freshwater inflows can result in significant changes in the ecosystem. The hydrodynamic and salinity dispersion fields are complex, however engineers are turning increasingly towards numerical simulation models as predictive tools.

The governing equations developed for a two-dimensional laterally averaged (X-Z) stratified estuary were solved using cubic spline integration. The model was used [5,22,27] to predict the velocity and salinity distribution in two stratified estuaries in northern Quebec, namely La Grande Riviere de la Baleine (Great Whale River) and La Petite Riviere de la Baleine (Little Whale River) in the James Bay region of Northern Quebec. Both estuaries are fairly strongly stratified and are earmarked for development as part of the James Bay Project. Figure (10) indicates the velocities and isohaline contours obtained for the Little Whale River. Comparison with the field data is satisfactory.

Overland Flow with Pollutant Transport

Overland flow is caused by rainfall when the infiltration capacity of the soil is exceeded. The free surface flow is generally governed by the well known St. Venant Shallow Water Wave Equations. In this project, the initial dissolution of a surface applied solid pollutant and subsequent washoff by the overland flow was simulated. The effects of infiltration and pollutant adsorption were accounted for in semi-empirical terms.

The two dimensional unsteady Shallow Water Wave Equations together with the transport (advective-diffusive) equation in two dimensions were solved using the spline integration technique.

Source terms accounting for adsorption, incident rainfall, infiltration and dissolution of the surface applied pollutant were incorporated into the formulation. In order to evaluate the dissolution rate, the analogy between turbulent mass and momentum transfer was exploited. Some selected results are presented in figures (11) and (12). Figure 11 traces the migration of maximum concentration with time for the case when application of the pollutant is localized at a single spot. It may be noted that the pollutant is depleted as it is transported downstream due to diffusive effects as well as removal by soil infiltration. Figure 12 describes the temporal evolution of the pollutant on the X-Y plane. The plane is assumed to be tilted along its diagonal, which simulates arbitrary inclinations along hillside slopes. The results are physically realistic and behave qualitatively in the expected manner.

The model has also been validated by comparison with laboratory measurements. For detailed results as well as a comprehensive presentation of the mathematical and numerical formulation, the reader is referred to the work of Yan [28]. The quality of the results obtained indicate that the numerical model may be used as a reliable tool for predicting pollutant transport in overland flow. Further refinement of the physical formulation and of the numerical technique would result in even greater model flexibility.

For fluvial hydraulic applications, an extension of the technique using splines under tension to treat the two-dimensional shallow water wave equations has been recently developed by Echeverria [29]. The optimum value for the tension factor is computed automatically thus eliminating laborious trial and error numerical experimentation. The method is currently being tested in a general riverine system.

5 OTHER SCHEMES: SURGE WAVE PROPAGATION ON RIVERS WITH ERODIBLE BEDS

The computation of flood wave propagation following a dambreak on erodible bed rivers is now drawing increasing interest in the hydraulics community since many river beds are unable to resist the extreme erosive forces that appear during the passage of the primary surge wave. This can result in the transport of large quantities of solid material (including debris) that has the potential of causing significantly more damage than clear water alone. Another characteristic of certain rivers is that some reaches may contain steep slopes where control sections with critical flow form, thereby modifying the propagation characteristics of the flood wave. The development of suitably robust numerical algorithms for the computation of the hydraulics and material transport has been initiated at the Ecole Polytechnique de Montreal in collaboration with Hydro-Quebec. This effort forms part of a program to model flood propagation in rivers with steep slopes as well as breach formation in dikes due to overtopping. An essential requirement of such algorithms is that they be suitably robust, with the capacity to treat high Froude number flows as well as possess good shock capturing abilities since frequently there will be reaches, even under base flow conditions, where the flow is supercritical (rapids) followed by a hydraulic jump. In this section, the numerical algorithm used followed by validation on a classical dambreak problem where the analytical result is available will be presented. Finally, some results obtained for the simulation of a dambreak episode on a river with an erodible bed will be presented.

The St. Venant equations for unsteady free surface flow in one dimension describe the conservation of mass and momentum:

$$\frac{\partial \varsigma}{\partial t} + \frac{1}{b}\frac{\partial Q}{\partial x} = 0 \tag{5.1}$$

$$\frac{\partial Q}{\partial t} + \frac{\partial}{\partial x}\left(\frac{Q^2}{A}\right) + gA\frac{\partial \varsigma}{\partial x} + gAS_f = 0 \tag{5.2}$$

Note that they are presented here in non-conservation form. Here Q is discharge, ς is water surface elevation above datum, A is cross-sectional area, b is lateral width, x is the streamwise coordinate and t is time. S_f is the friction slope generally evaluated using the Manning Formula.

The sediment continuity equation in one dimension is:

$$\frac{\partial z_b}{\partial t} + \frac{\partial s_b}{\partial x} = 0 \tag{5.3}$$

Where s_b is sediment transport rate per unit width and z_b is bed elevation. Equations (5.1) to (5.3) define the physics of the problem. In addition, a sediment transport relation to evaluate s_b is required.

Discretization of the equations is inspired by the work of Stelling et al.[30] . The numerical algorithm is based on a staggered grid stencil. Depths and water surface elevations are defined at 'i' the center of a cell. Velocities are defined at the boundaries i+1/2 and i-1/2 of the cell. The model uses a positive depth scheme for the discretisation of the continuity equation so that dry bed conditions may be treated. The discretisation of the sediment continuity equation (5.3) follows along similar lines. The sediment transport formula used in the computation is a slightly modified version of the expression developed by Smart[31]. Initial and boundary conditions must be specified in order to obtain a unique solution. For the test cases, the initial and boundary conditions are well defined. For practical computations in rivers, initial conditions would be the base "steady-state" flow imposed upstream and a known water surface elevation downstream. The upstream flood hydrograph is then imposed with a specified downstream surface elevation. At each time step, the hydraulic variables are calculated followed by application of the sediment transport equation which then modifies the bed elevation. The boundary conditions for the sediment transport equation could be zero or some known sediment inflow at the upstream reach. The model was validated against well-known analytical solutions, with results which were virtually indistinguishable. Figures (13) and (14) present the results of a dam-break computation on a river. An upstream hydrograph consistent with a dam failure is specified, while downstream, a constant water surface elevation is imposed. Figure (13) illustrates the hydrograph imposed upstream together with two computed hydrographs (at kilometers 49.8 and 111.8) downstream. Each hydrograph is composed of a "principal" computed on the basis of a non-erodible (fixed) bed, and its "companion" computed assuming a mobile bed. An examination of figure(13) reveals interestingly enough that the peak discharge is actually increased on an erodible bed. Figure (14) illustrates the temporal evolution of the bed during the dam-break episode. At the upstream end, extremely large amounts of material are eroded during about the first three hours. Most of this material is deposited downstream while the bed appears to reach equilibrium elevation at about 48 hours that corresponds to the tail end of the hydrograph. Figure (15) presents the envelope of maximum water surface elevations likely to be encountered during the flooding assuming a non-erodible bed. Integration of the hydrographs at different sections of the river indicate that mass is conserved to better than 2%.

6 SOME DIRECTIONS FOR FURTHER DEVELOPMENT AND CONCLUDING REMARKS

One possibility being examined seriously by the authors is the study of 3-D flows which is far from trivial, even for a simple geometry such as a cavity, independent of whether analytical, computational, or experimental techniques are used. As mentioned by Shankar et al. [32], computationally the difficulties are compounded by the order-of-magnitude increase in the number of grid points required for a given spatial resolution, by the increase in the number of variables and the complexity of the equations to be solved.

The spline method may be a good choice to mitigate (at least partially!) some of these difficulties. As indicated earlier, it is of high accuracy, boundary conditions containing derivatives may be easily incorporated into the solution procedure as well as being computationally efficient. Furthermore, the possibility of using a non-uniform mesh has evident advantages such as reduction in storage requirements and machine time.

The development of the artificial compressibility method proposed by Chorin [33], adapted to the spline technique, permits discretization of the governing equations with primitive variables. Numerical tests in 2 and 3-D have been performed for the driven flow and for the natural convection flow in a rectangular cavity. Numerical results are very encouraging and will be reported shortly.

ACKNOWLEDGEMENTS:

This work was supported by the Natural Sciences and Engineering Research Council of Canada under Grant Number RGPIN 8846. We are especially grateful to the Dam Safety Group of Hydro-Quebec who also provided considerable financial support, encouragement and data for the hydraulic computations.

REFERENCES

1. Rubin,S.G. and Graves,R.A., 1975 *Viscous Flow Solutions with a Cubic Spline Approximation* , Computers and Fluids , 3, 1.

2. Rubin,S.G. and Khosla,P.K., 1976 *Higher Order Numerical Solutions using Cubic Splines* , AIAA Journal , 14, 851.

3. Rubin,S.G. and Khosla,P.K., 1977 *Polynomial Interpolation Methods for Viscous Flow Calculations*, J. Comput. Phys. , 24, 217.

4. Wang,P. and Kahawita,R., 1983 *Numerical Integration of Partial Differential Equations using Cubic Splines* , Int. J. Computer Math., 13, 271.

5. Wang,P. and Kahawita,R., 1983 *A Two-Dimensional Numerical Model of Estuarine Circulation using Cubic Splines*, Can. J. Civil Eng. , 10, 116.

6. Wang,P., *1983 Numerical solution of second order partial differential equations using cubic spline approximation*, Ecole Polytechnique de Montreal Report , Montreal, Canada.

7. Wang,P. and Kahawita,R., 1984 *The Numerical Solution of Burgers Equation using Splines*, Acta Aerodynamica Sinica , 2(2), 11.

8. Wang,P., 1985 *Spline-Lax-Wendroff Scheme and Spline-Leap-Frog Scheme , Acta Aerodynamica Sinica*, 3(3), 90.

9. Wang,P. and Kahawita,R., *1983 Cubic Spline Techniques in Numerical Models of Estuarine Circulation*, Acta Aerodynamica Sinica , 1(3), 17.

10. Lin,S., Wang,P. and Kahawita,R., 1984 *Cubic Spline Numerical Solution of an Ablation Problem with Convective Backface Cooling*, AIAA Journal , 22, 1176.

11. Wang,P., Lin,S. and Kahawita,R., 1985 *The Cubic Spline Integration Technique for Solving Fusion Welding Problems*, Journal of Heat Transfer , 107, 485.

12. Wang,P. and Kahawita,R., 1987 *The Numerical Solution of the Unsteady Natural Convection Flow in a Square Cavity at High Rayleigh Number using SADI Method*, Applied Mathematics and Mechanics, 8(3), 219.

13. Wang,P., 1987 *Spline Method of Fractional Steps in Numerical Model of Unsteady Natural Convection Flow at High Rayleigh Number*, Numer. Heat Transfer, 11, 95.

14. Wang,P., 1987 *The Method of Fractional Steps for Solving Navier-Stokes Equations using Parametric Splines*, Acta Aerodynamica Sinica, 5(3), 218.

15. Wang,P., Kahawita,R. and Nguyen,T.H., 1990 *Numerical Computation of the Natural Convection Flow about a Horizontal Cylinder using Splines*, Numer. Heat Transfer, Part A, 17, 191.

16. Wang,P., Kahawita,R. and Nguyen,D.L., 1991 *Transient Laminar Natural Convection from Horizontal Cylinder*, Int. J. Heat and Mass Transfer, 34, 1429.

17. Wang,P., Kahawita,R. and Nguyen,D.L., 1992 *Transient Natural Convection with Density Inversion from a Horizontal Cylinder*, Physics of Fluids A, 4(1), 71.

18. Wang,P., Kahawita,R. and Nguyen,D.L., 1994 *Numerical Simulation of Buoyancy-Marangoni Convection in two Superposed Immiscible liquid layers with a free surface*, Int. J. Heat and Mass Transfer, 37, 1111.

19. Wang,P. and Kahawita,R., 1996 *Transient Buoyancy-Thermocapillary Convection in two Superposed Immiscible liquid layers*, Numer. Heat Transfer, Part A, 30, 477.

20. Wang,P. and Kahawita,R., 1998 *Oscillatory Behaviour in Buoyant Thermocapillary Convection of Fluid Layers with a Free Surface,* Int. J. Heat and Mass Transfer, 41, 399.

21. Kahawita,R. and Wang,P., 1998 *Numerical Simulation of Wake Flow behind Trapezoidal Bluff Bodies* , Proc. of the Sixth Conference of the CFD Society of Canada , Quebec,June.

22. Wang,P. and Kahawita,R., 1990 *Hydrodynamic Modelling of Estuarine Circulation using Spline Method of Fractional Steps*, International Journal of Sediment Research, 5(1),67.

23. Genceli,O.F. 1980 *The Onset of Manifest Convection from Suddenly Heated Horizontal Cylinders , Warme-und Stoffubertragung* 13, 163.

24. Ben Hadid,H. and Roux,B., 1992 *Buoyancy- and thermocapillary- driven flows in differentially heated cavities for low-Prandtl-number fluids*, J. Fluid Mechanics , 235, 1.

25. Kahawita,R. and Wang,P., *2002 Numerical Simulation of the Wake Flow Behind Trapezoidal Bluff Bodies, Computers and Fluids*, 31, pp 99-112.

26. Goujon-Durand,S., Renffer,K. and Wesfreid,J.E., 1994 *Downstream evolution of the*

Bénard-von Kármán instability Physical Review E , 50, 308.

27. Wang,P., Kahawita,R. and Briand,M.H., 1993 *Validation of X-Z Cubic Spline Based Numerical Model for Estuarine Circulation* , Proc. of the First Conference of the CFD Society of Canada , June 14-15, Montreal.

28. Yan,M.,*1999 Pollutant transport in overland flow with dissolution, infiltration and adsorption effects*, Ph.D Thesis, Ecole Polytechnique de Montreal, Montreal Quebec, Canada.

29. Echeverria, Patricia, 2004 *Solving the Shallow Water Wave Equations using Splines under Tension*, Ph.D Thesis, (in progress) Ecole Polytechnique de Montreal, Montreal Quebec, Canada.

30. Stelling,G.S.,Kernkamp,H.W.J & Laguzzi,M.M., 1998 *Delft Flooding System: A powerful tool for inundation assessment based upon a positive flow simulation* , Proceedings of the Third International Conference on Hydroinformatics , Babovich & Larsen, Copenhagen, Denmark.

31. Smart,G.M., 1984 *Sediment Transport in Steep Channels , Journal of Hydraulic Engineering*, ASCE, 110, 267-276.

32. Shanker,P.N. and Deshpande,M.D., 2000 *Fluid Mechanics in the driven cavity, Annual Review of Fluid Mechanics* , p.93.

33. Chorin,A.J., 1967 *A Numerical method for solving incompressible viscous flow problems*, J. Comput. Phys. , 2, 12.

34. Pruess, S, 1979 *Alternatives to the Exponential Spline in Tension , Mathematics of Computing* , Vol.33, No.148 p. 1273-1281.

35. Renka, R, 1987 *Interpolatory Tension Splines with Automatic Selection of Tension Factors* , SIAM J. Sci. Stat. Comput. Vol 18, pp393-415

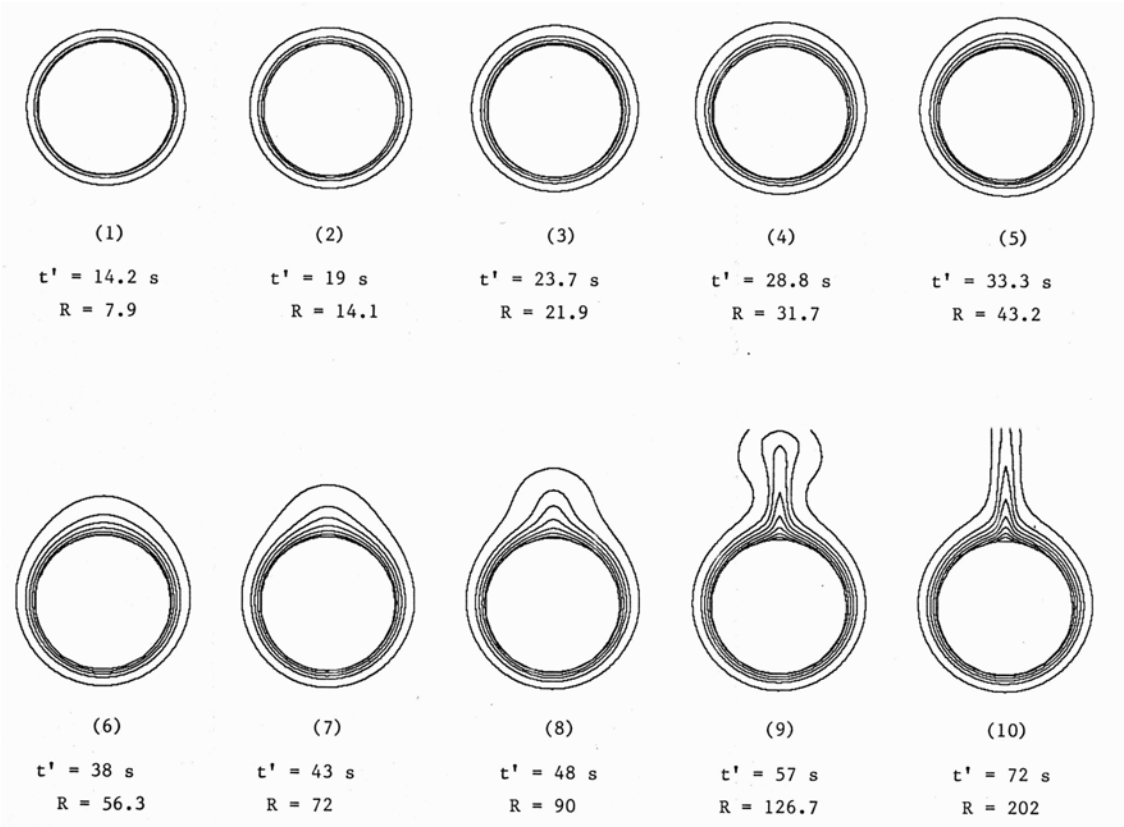

Figure 1a Simulated Transient Isotherms

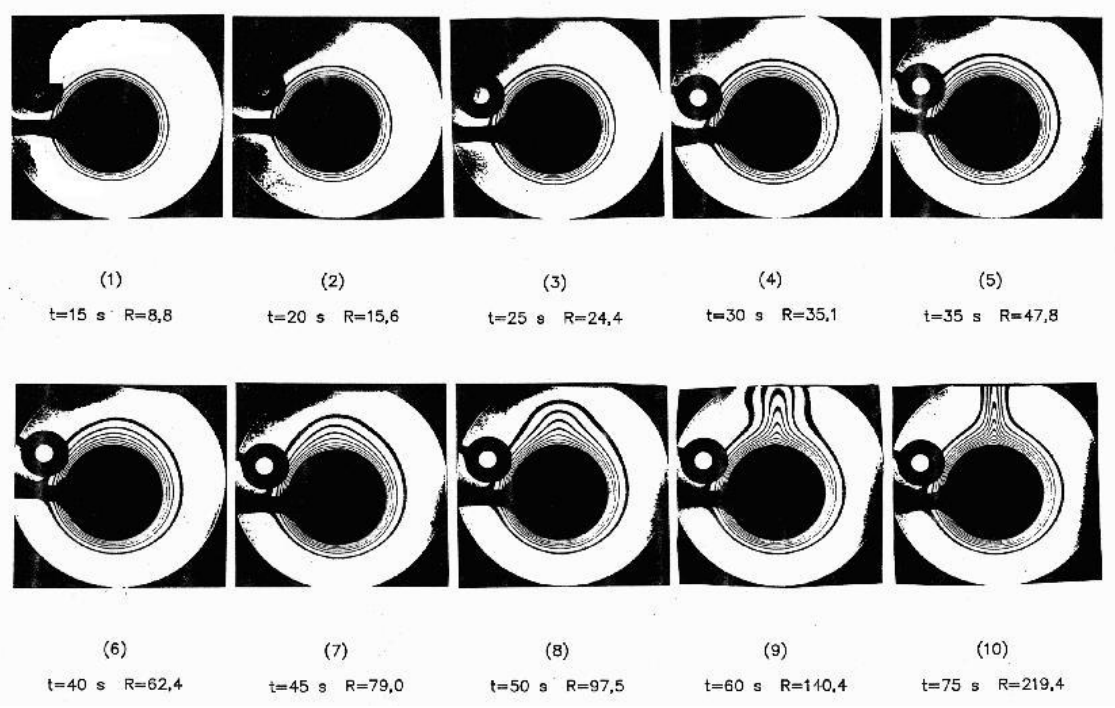

Figure 1b Experimental Visualisation

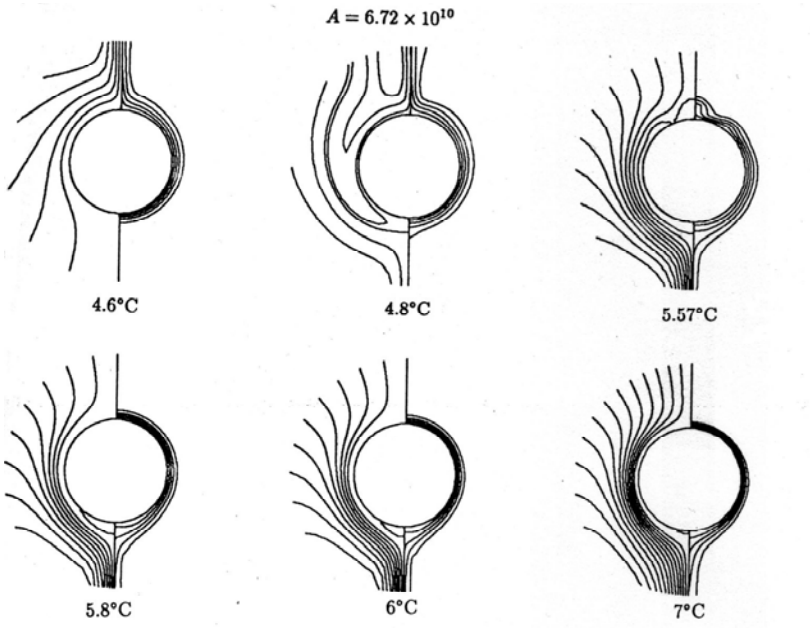

Figure 2 Steady State Isotherms (right) and Streamlines (left) for different T_{amb}

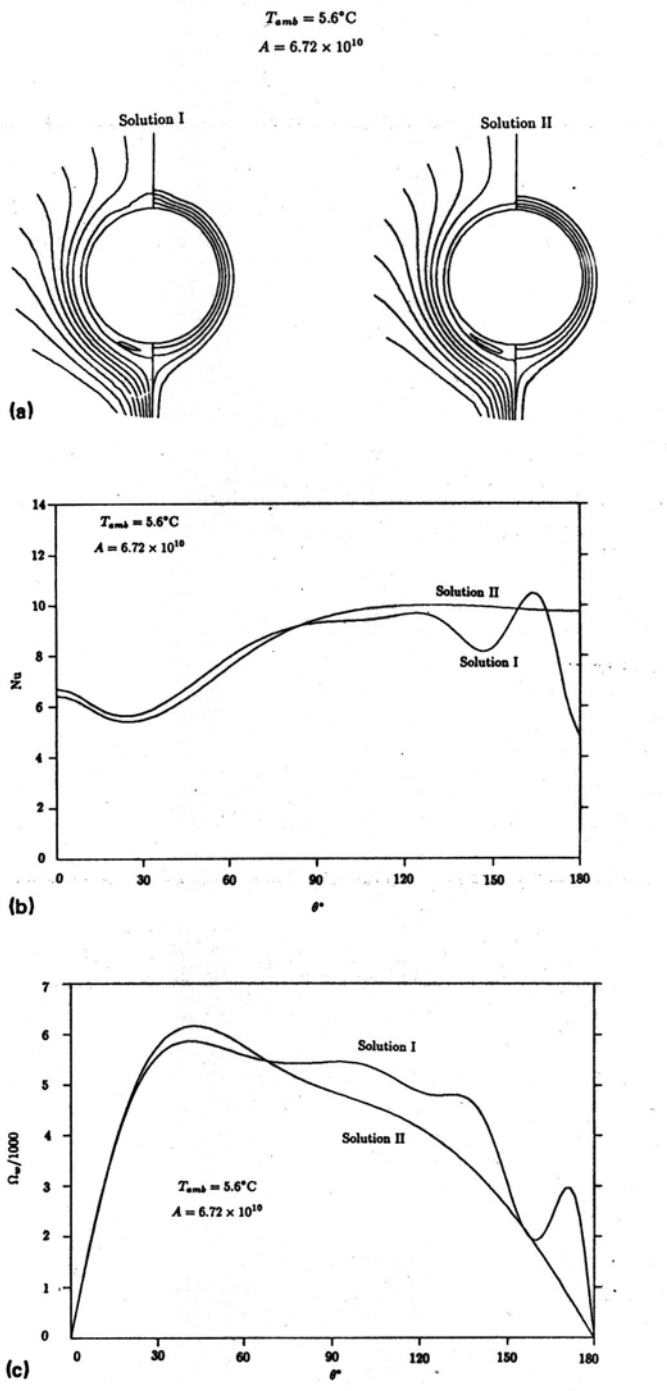

FIG. 3 Two different solutions for $\mathrm{Pr} = 11.6$ and $A = 6.72 \times 10^{10}$ at $T_{\mathrm{amb}} = 5.6\,^{\circ}\mathrm{C}$: (a) Steady-state isotherms and streamlines ($\Delta\Psi = 15$ and $\Delta T = 0.2$); (b) steady-state distribution of local Nusselt numbers; (c) steady-state surface vorticity distribution.

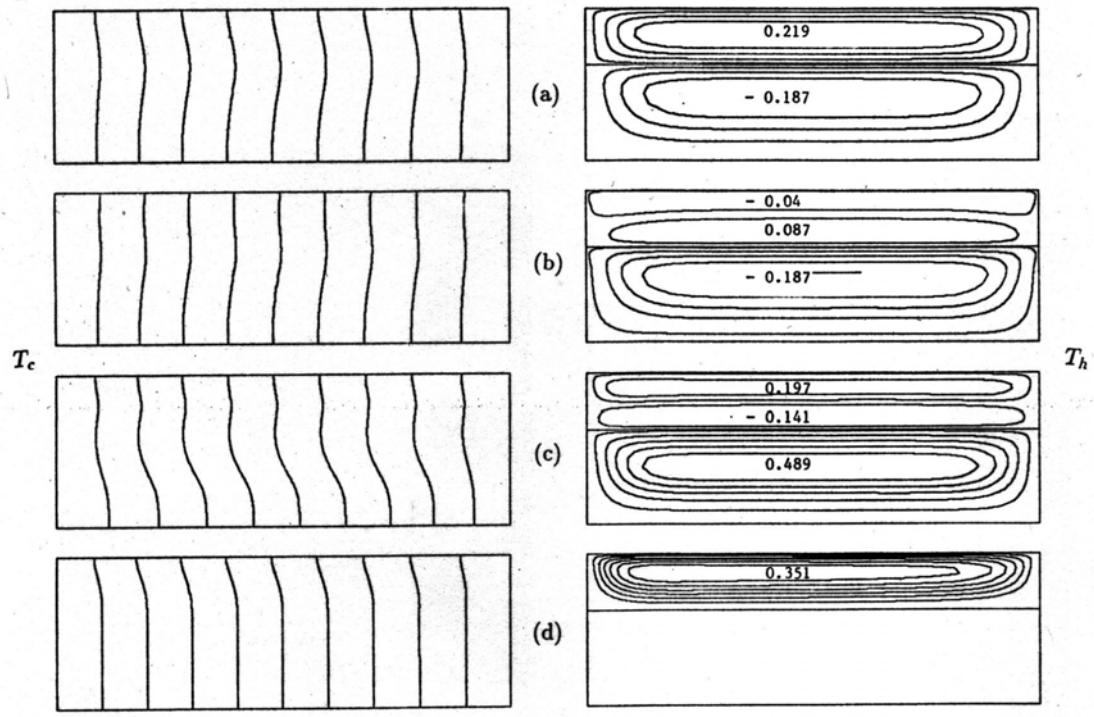

FIG. 4. Typical computed streamlines and isotherms with different cells for $\bar{\alpha} = \bar{k} = 1$, $\bar{\mu} = 1.2$ and $\bar{\eta} = 0.6$. (a) $Ma^* = -100$, $Ma_2 = 50$, (b) $Ma^* = -100$, $Ma_2 = -70$; (c) $Ma^* = 200$, $Ma_2 = 200$; (d) $Ma^* = 0$, $Ma_2 = 200$.

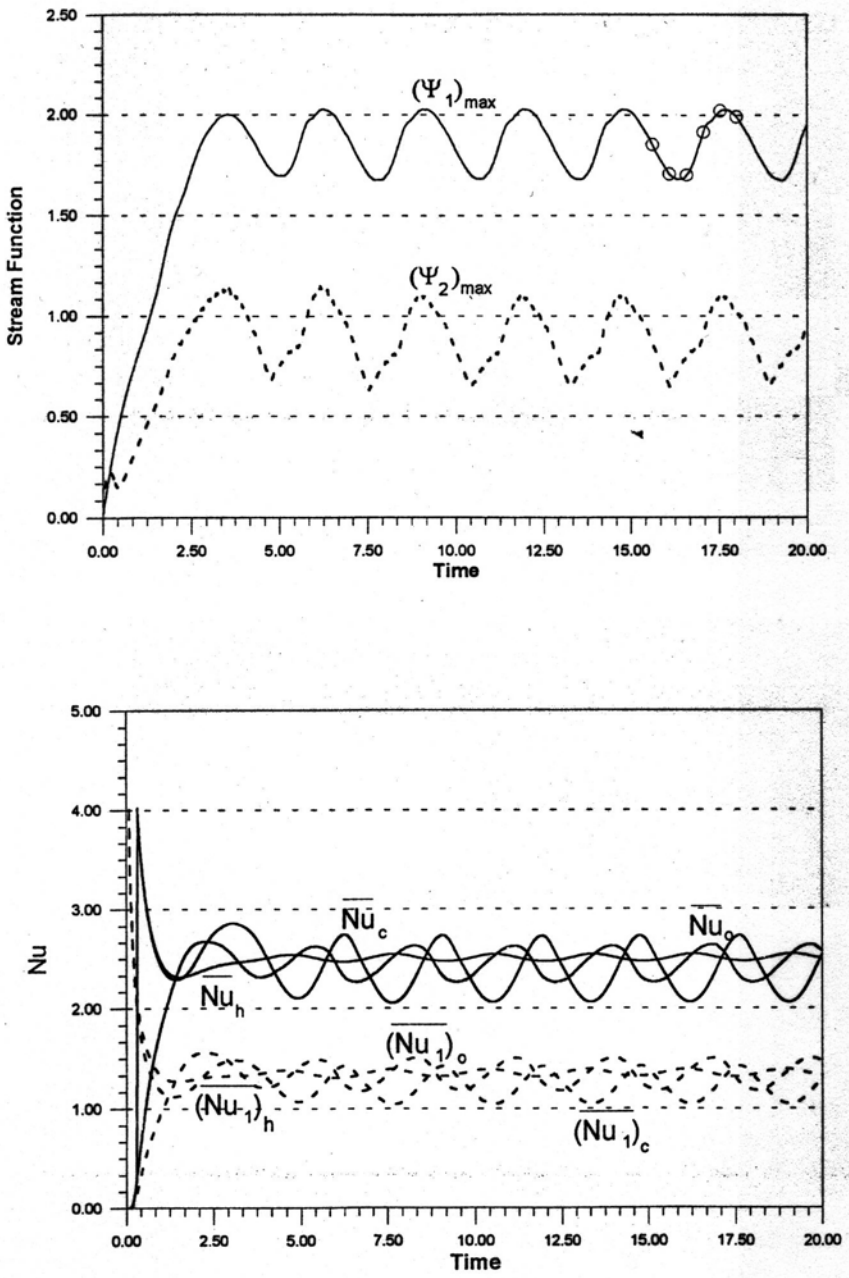

Fig. 5. $Ra_1 = 600$, $Q_\alpha = 0.015$, $Q_\mu = 0.1$, $Pr_1 = 0.015$, $Pr_2 = 1$, $\bar{\alpha} = 1$ and $B = 4$: (a) time variation of the maximum stream function; (b) time variation of Nusselt numbers at the two endwalls (Nu_h and Nu_c) and at the midplane (Nu_0) for two layers.

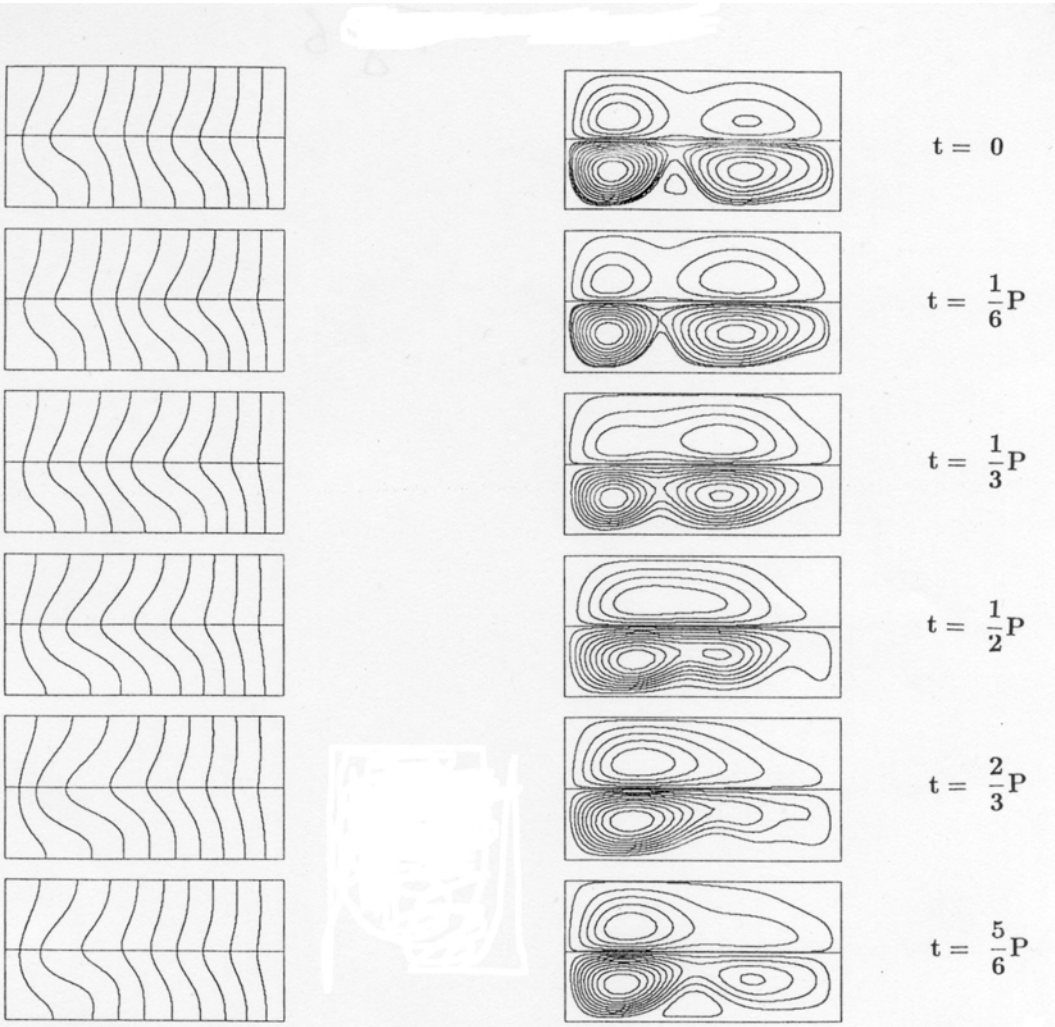

Fig. 6 Time variation of the isotherms and streamlines at six instants over a period of oscillation

Proceedings of the Tenth Asian Congress of Fluid Mechanics
17-21 May 2004, Peradeniya, Sri Lanka

SOME FEATURES OF FLUID FLOW IN A RAPIDLY-ROTATING CONTAINER

Jun Sang Park
Department of Mechanical Engineering, Halla University, Wonju 220-712, Korea

Jae Min Hyun
Department of Mechanical Engineering, KAIST, Taejon 305-702, Korea

Abstract: A theoretical analysis is made of the steady-state flow of a compressible fluid in a rapidly-rotating infinitely-long circular pipe. Flow is induced from the basic state of rigid-body isothermal rotation by imposing a small azimuthally-varying thermal forcing at the pipe wall. The system Ekman number is very small. Solutions are secured for both the axisymmetric and non-axisymmetric cases. It is shown that the axisymmetric solution is obtained from the azimuthally-averaged boundary condition at the wall. The non-axisymmetric solution is based on the azimuthally-fluctuating part of the boundary condition.

1. INTRODUCTION

This paper is concerned with an analytical description of steady flow of a viscous, thermally-conducting compressible gas which is contained in a rapidly-rotating infinitely-long cylindrical pipe. The problem is characterized by the smallness of the Ekman number E of the system, $E \ll 1$. In the basic state, the pipe rotates steadily about the longitudinal central axis at constant rotation rate Ω, and the pipe and gas are in thermal equilibrium at constant temperature T^*_{00}. Here, the rotation rate is sufficiently high so that the compressibility effect, as represented by finite values of the Mach number M of the fluid system, is significant. Also, the effective acceleration in the radial direction overwhelms the conventional earth's gravitational acceleration. Under these circumstances, the gas in the pipe is in rigid-body rotation, and the density increases exponentially in the radially-outward direction [e.g., Sakurai & Matsuda (1974), Nakayama & Usui (1974), Bark & Bark (1976)]. Flow is generated out of this basic-state of rigid-body rotation when a small temperature perturbation is imposed to the pipe wall. The practical relevance of this problem configuration is apparent in the design and operation of high-performance gas centrifuges [e.g., Sakurai & Matsuda (1974)].

The findings of the present treatise are summarized for the case of a compressible fluid. Even when the external thermal forcing at the wall is non-axisymmetric, the fluid in the interior region maintains axisymmetric temperature distributions in the parametric range of $\sigma(\gamma-1)\,M^2 \gg O(E^{1/3})$. However, when $\sigma(\gamma-1)\,M^2 \lesssim O(E^{1/3})$, no z-independent solution can be obtained, and a fully z-dependent three dimensional flow results. In the case of $\sigma(\gamma-1)\,M^2 \gg O(E^{1/3})$, the interior fluid, by way of thermal diffusion process, approaches

rigid-body rotation with its temperature equalized to the average temperature at the wall. On the other hand, the non-axisymmetric component of the thermal forcing at the wall induces a closed circulation in the $E^{1/3}$-thermal layer near the wall. During this process, heat is generated (removed) by compression (or expansion) work which is caused by radial flows. It is ascertained that the impact of non-axisymmetric thermal loading at the wall is absorbed within this boundary layer, and the temperature in the interior is substantially axisymmetric.

2. MATHEMATICAL FORMULATION

The basic state density field is $\rho_{(0)}(r) \equiv \exp\left[-\gamma \frac{M^2}{2}(r^2-1)\right]$. (1)

The linearized governing Navier-Stokes equations, expressed in the cylindrical frame rotating at Ω^*, can be written in nondimensional form as [e.g., Sakurai & Matsuda, 1976; Bark et. al. ; Park & Hyun, 2001]:

$$\frac{1}{r}\frac{\partial}{\partial r}(r\rho_{(0)}u) + \frac{1}{r}\frac{\partial}{\partial \theta}(\rho_{(0)}v) = 0, \tag{2}$$

$$-2\rho_{(0)}v - \gamma M^2 r\rho = -\frac{\partial p}{\partial r} + E\left[\left(\nabla^2 - \frac{1}{r^2}\right)u + \left(\frac{1}{3}+\beta\right)\frac{\partial}{\partial r}(\nabla\cdot\vec{u}) - \frac{2}{r^2}\frac{\partial v}{\partial \theta}\right], \tag{3}$$

$$2\rho_{(0)}u + \frac{1}{r}\frac{\partial p}{\partial \theta} = E\left[\left(\nabla^2 - \frac{1}{r^2}\right)v + \frac{1}{3r}\frac{\partial}{\partial \theta}\nabla\cdot\vec{u} + \frac{2}{r^2}\frac{\partial u}{\partial \theta}\right], \tag{4}$$

$$-\frac{\sigma(\gamma-1)}{\gamma} r\rho_{(0)}u = E\nabla^2 T, \tag{5}$$

$$p = \rho + \rho_{(0)}T. \tag{6}$$

It is convenient to deploy ^ to represent the azimuthal-averaged value of a dependent variable, i.e., $\hat{\phi} = \frac{1}{2\pi}\int_{-\pi}^{\pi}\phi(r,\theta,t)d\theta$.

Furthermore, ~ denotes the departure of ϕ from $\hat{\phi}$, $\tilde{\phi} = \phi(r,\theta,t) - \hat{\phi}$.

The above notations ^ and ~ indicate respectively the axisymmetric and non-axisymmetric components of the variables.

It follows that the arbitrarily-given thermal forcing at the wall can be decomposed into the axisymmetric and non-axisymmetric parts :

$$f(\theta)[\equiv T(r=1,\theta,t)] = \hat{f} + \sum_n \tilde{f}_n e^{in\theta},$$

where the index n refers to the n-th complex Fourier coefficient

$$\tilde{f}_n = \frac{1}{2\pi}\int_{-\pi}^{\pi} f(\theta)\, e^{-in\theta} d\theta .$$

The associated boundary conditions are expressed as :

(for the axisymmetric part)

$$\hat{u}(r, t=0) = \hat{v}(r, t=0) = \hat{T}(r, t=0) = 0 \quad , \tag{7a}$$

and $\hat{u}(r=1, t) = 0$, $\hat{v}(r=1, t) = 0$, $\hat{T}(r=1, t) = \hat{f}$, (7b)

(for the non-axisymmetric part)

$$\tilde{u}(r,\theta,t=0) = \tilde{v}(r,\theta,t=0) = \tilde{T}(r,\theta,t=0) = 0, \tag{7c}$$

and $\tilde{u}(r=1,\theta,t)=0, \quad \tilde{v}(r=1,\theta,t)=0, \quad \tilde{T}(r=1\theta,t) = \sum_n \tilde{f}_n e^{in\theta}$. (7d)

3. ANALYSIS

3.1 Axisymmetric part

The velocity and temperature fields in the steady state, subject to an axisymmetric thermal forcing, i.e., $T_w = \hat{f}$, are now delineated [see Eq.(7a)]. The subscript w denotes the pipe wall at $r = 1.0$. . By imploying the averaging process to the continuity equation (2), the axisymmetric radial velocity is

$$\hat{u}_s(r) = 0. \tag{8}$$

Substituting Eq.(8) into azimuthally-averaged equations of Eqs.(4) & (5) yields

$$\hat{v}_s(r) = 0, \qquad \hat{T}_s(r) = \hat{f}. \tag{9) \& (10}$$

In the above, subscript s refers to the steady state. Obviously, the above results indicate that the steady-state flow is in isothermal rigid-body rotation.

The associated density and pressure fields can be found by undergoing algebraic manipulations. From Eq.(6), one has

$$\hat{p}_s(r) = \hat{\rho}_s(r) + \rho_{(0)}(r)\hat{f} \quad . \tag{11}$$

Bringing Eq.(11) into the axisymmetric part of Eq.(3) produces

$$-\frac{d\hat{\rho}_s}{dr} - \gamma M^2 r \hat{\rho}_s = -\hat{f}\frac{d\rho_{(0)}}{dr} \quad . \tag{12}$$

The solution to Eq.(12) is found to be

$$\hat{\rho}_s(r) = \left(C_1 - \frac{\hat{f}}{2}\gamma M^2 r^2 \right) \rho_{(0)}(r) \quad . \tag{13}$$

The integration constant C_1 is determined by using the global mass continuity, i.e., $\int_0^1 \hat{\rho}_s \cdot 2\pi r dr = 0$:

$$C_1 = \frac{\hat{f}}{2}\left(\frac{\gamma M^2}{1 - e^{-\gamma M^2/2}} - 2 \right).$$

The pressure $\hat{p}_s$ is obtained from Eq.(11) :

$$\hat{p}_s(r) = \frac{\hat{f}}{2}\gamma M^2 \left(\frac{1}{1 - e^{-\gamma M^2/2}} - r^2 \right) \rho_{(0)}(r). \tag{16}$$

The results are shown in Fig.1.

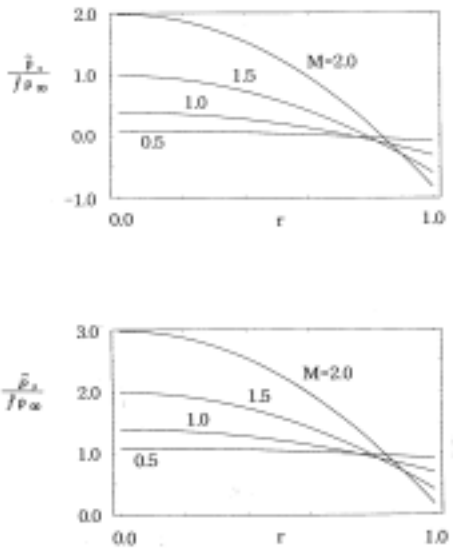

Fig.1 Axisymmetric fields of density [top frame] and pressure [bottom frame].

3.2 Non-axisymmetric part

For $E \ll 1$, to secure a meaningful asymptotic solution, the flow variables are expanded as $\tilde{\Phi} = \sum_{n=0}^{\infty} E^{n/m} \tilde{\Phi}_n(\zeta, \theta)$, in which $\zeta = (1 - r)/E^{1/m}$ and $\tilde{\Phi}$ denotes $\tilde{u}, \tilde{v}, \tilde{\rho}, \tilde{p}$ or $\tilde{T}$. Upon substituting the above expansions into the non-axisymmetric parts of governing equations (2)-(6), one can find a choice of $m = 3$ and $\tilde{u}_0 = \tilde{p}_0 = 0$. Therefore, the problem has a proper expansion parameter of $E^{1/3}$, and the associated boundary layer coordinate is $\zeta = (1 - r)/E^{1/3}$. The leading-order dependent variables are scaled as

$\tilde{u}_s \sim O(E^{1/3})$, $\tilde{v}_s \sim O(1)$, $\tilde{T}_s \sim O(1)$, $\tilde{p}_s \sim O(E^{1/3})$.

In the above, tilde refers to a non-axisymmetric component and subscript s the steady solution. The above scalings are similar to the $E^{1/3}$-Stewartson layer [Bark & Bark (1976)] and to $E^{1/3}$-thermal layer [Matsuda & Nakagawa (1983); Wood & Babarsky(1992)].

The leading-order governing equations for $\tilde{T}_s$ and $\tilde{v}_s$ are

$$\gamma M^2 \frac{\partial \tilde{T}_s}{\partial \theta} = -\frac{\partial^3 \tilde{v}_s}{\partial \zeta^3}, \tag{17a}$$

$$-\frac{\sigma(\gamma-1)}{\gamma} \frac{\partial \tilde{v}_s}{\partial \theta} = -\frac{\partial^3 \tilde{T}_s}{\partial \zeta^3}. \tag{17b}$$

By eliminating $\tilde{v}$ from Eqns.(17a) and (17b), the equation for temperature is obtained :

$$-\frac{\partial^6 \tilde{T}_s}{\partial \zeta^6} + \sigma(\gamma-1) M^2 \frac{\partial^2 \tilde{T}_s}{\partial \theta^2} = 0. \tag{18}$$

The appropriate boundary conditions for Eq.(18) are :

at $\zeta = 0$,
$$\tilde{T}_s = \sum_n \tilde{f}_n e^{in\theta}, \tag{19a}$$
$$\frac{\partial^2 \tilde{T}_s}{\partial \zeta^2} = 0, \quad \frac{\partial^3 \tilde{T}_s}{\partial \zeta^3} = 0, \tag{19b) \& (19c}$$

and, as $\zeta \to \infty$, all the variables tend to zero. Eq.(19a) expresses the imposed thermal loading at the wall, and Eq.(19b) states the non-permeable condition at the wall, i.e., $\tilde{u}_s = 0$ leads to $\partial^2 \tilde{T}_s / \partial \zeta^2 = 0$, and Eq.(19c) states the no-slip condition at the wall , i.e., $\tilde{v}_s = 0$ leads to $\partial^3 \tilde{T}_s / \partial \zeta^3 = 0$.

In a manner similar to Sakurai and Matsuda (1974), the function $\tilde{T}$ is expanded as

$$\tilde{T}_s(\zeta, \theta) = \sum_n T_n(\zeta) e^{in\theta}. \tag{20}$$

By substituting Eq.(20) into Eq.(18), the solution $T_n(\zeta)$, subject to eqs.(19a)-(19c), is acquired :

$$T_n(\zeta) = -\frac{\tilde{f}_n}{2}\left[e^{-\gamma_n \zeta} + e^{-\frac{1}{2}\gamma_n \zeta} \frac{2}{\sqrt{3}} \cos\left(\frac{\sqrt{3}}{2} \gamma_n \zeta - \frac{\pi}{6}\right)\right], \tag{21}$$

in which $\gamma_n = \left(\sigma(\gamma-1) M^2 n^2\right)^{1/6}$.

The radial and azimuthal velocities are given :

$$\tilde{u}_s(\zeta, \theta) = -\frac{\gamma}{\sigma(\gamma-1)} \sum_n U_n(\zeta) e^{in\theta}, \quad \tilde{v}_s(\zeta, \theta) = -\frac{\gamma}{\sigma(\gamma-1)} \sum_n V_n(\zeta) e^{i(n\theta - \pi/2)}, \tag{22)\&(23}$$

in which

$$U_n(\zeta) = -\frac{\tilde{f}_n}{2} \gamma_n^2 \left[e^{-\gamma_n \zeta} + \frac{2}{\sqrt{3}} e^{-\gamma_n \zeta/2} \sin\left(\frac{\sqrt{3}}{2} \gamma_n \zeta - \frac{\pi}{3}\right)\right],$$

$$V_n(\zeta) = -\frac{\tilde{f}_n}{2n} \gamma_n^3 \left[e^{-\gamma_n \zeta} + \frac{2}{\sqrt{3}} e^{-\gamma_n \zeta/2} \sin\left(\frac{\sqrt{3}}{2} \gamma_n \zeta - \frac{2\pi}{3}\right)\right].$$

The primary role of the thermal layer is to adjust the interior flow smoothly to the conditions imposed at the wall. It is, therefore, sufficient to carry out only the leading-order

analysis at this stage.

The above theoretical developments offer succint physical interpretations. As shown in Eq.(18), when $\sigma(\gamma-1)\ M^2 \gg O(E^{1/3})$, the effect of non-axisymmetric thermal forcing at the wall is absorbed in the thermal layer of thickness $O(E^{1/3})$ adjacent to the wall. Inside the thermal layer, the fluid near the wall where the thermal forcing is positive, i.e., in the azimuthal wall sector under heating, undergoes thermal expansion. This causes radially-inward flows [see eq.(22)]. In contrast, in the azimuthal wall sector under cooling, the fluid undergoes thermal compression, which generates radially-outward flows. In response to wall, i.e., when the azimuthal wall sectors under heating and cooling exist, the resulting radially-inward and neighboring radially-outward flows induce azimuthal flows the non-axisymmetric thermal condition at the along the wall within this $O(E^{1/3})$-layer [see eqs.(22) & (23)]. This is clear from the consideration of the continuity equation. [see Fig.2]

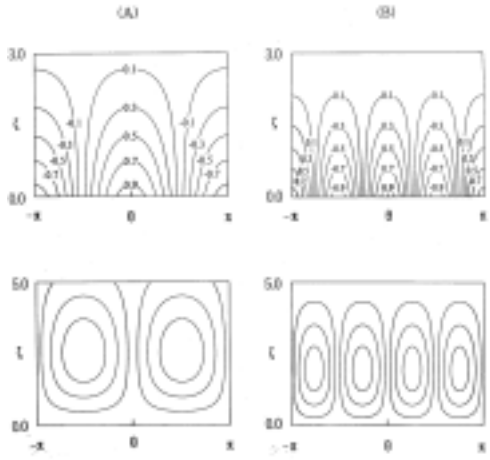

Fig.2 Plots of harmonic components for non-axisymmetric temperature fields (top and stream function (bottom frame). (A), n=1; (B), n=2. $M=1.0,\quad \gamma=1.4$ and $\sigma=0.7.\quad \triangle\Psi=0.3.$

The overall picture inside this thermal layer is that, in the immediate vicinity of the wall, azimuthal flows are generated from a cool to a hot wall sector; in the far region away from the wall, azimuthal flows are in the opposite direction. These internal flows inside the layer create a closed circulation. In this process, the fluid experiences diffusive heating (cooling) from the hot (cold) sector of the wall. Simultaneously, the radially-inward frame) (outward)-moving fluid at hot (cold) sector is cooled (heated) by way of work done by the basic pressure variation, i.e., $-\frac{\sigma(\gamma-1)}{\gamma}\ \tilde{u}_z<0$ ($-\frac{\sigma(\gamma-1)}{\gamma}\ \tilde{u}_z>0$), which is easily confirmed from the energy equation (5). This aspect is absent in the case of an incompressible fluid. For an incompressible fluid, the temperature field is governed by the simplistic diffusion equation. Therefore, a temperature disturbance at the wall is not confined to within the $O(E^{1/3})$ boundary layer; the entire flow domain is directly influenced by the thermal boundary condition at the wall. This qualitative difference between compressible and incompressible flows was emphasized earlier by Matsuda et al. (1976).

In the present discussion for a rapidly-rotating compressible fluid, under $\sigma(\gamma-1)\ M^2 \gg O(E^{1/3})$, the essential dynamical element is the generation of radial motions of $O(E^{1/3})$ due to the imposition of non-axisymmetric thermal forcing at the wall [Remember that $\tilde{u}_z \sim O(E^{1/3})$]. The radially-inward (outward) motion causes volume expansion (compression) of the fluid element owing to the basic-state background pressure distribution, which results in cooling (heating) of the fluid. It is noted that the direct conductive heating (cooling) from the hot (cold) sector of the wall is offset by the cooling (heating) due to the afore-said radial

motions. Consequently, it is possible that the effect of non-axisymmetric thermal forcing at the wall is restricted to within the $E^{1/3}$-thermal layer, rather than propagating to the entire flow domain approaching $r \to 0$.

4. CONCLUSIONS

The axisymmetric part of the thermal forcing at the wall gives rise to the interior temperature, which is equalized to the average value, $\hat{T}_a$, of the temperature distribution at the wall. The attendant flow in the interior is in rigid-body rotation, rotating together with the pipe. In comparison with the original basic-state, the density increases (decreases) in the interior region surrounding the axis for $\hat{T}_a > 0$ ($\hat{T}_a < 0$). Near the wall, density decreases (increases) for $\hat{T}_a > 0$ ($\hat{T}_a < 0$). The pressure increases (decreases) in the entire domain for $\hat{T}_a > 0$ ($\hat{T}_a < 0$).

Due to a z-independent non-axisymmetric thermal forcing at the wall, in the parameter range $\sigma(\gamma-1)\, M^2 \lesssim O(E^{1/3})$, it is not possible to have a z-independent two-dimensional flow on the (r, θ) plane.

In the parameter range $\sigma(\gamma-1)\, M^2 \gg O(E^{1/3})$, forcing at the wall is absorbed in the $E^{1/3}$ -thermal layer close to the wall. In the $E^{1/3}$-layer, regions of non-equal temperatures, deviating from the average value $\hat{T}_a$, are formed due to thermal diffusion from the wall. The accompanying azimuthally-varying density field gives rise to a closed circulation, which is in accord with thermal geostrophic wind relation.

ACKNOWLEDGEMENTS

This work was supported in part by the NRL Project [2-578], South Korea.

REFERENCES

[1] Sakurai T and Matsuda T: Gasdynamics of a centrifugal machine. *J. Fluid Mech.* 1974, **62**, 727-736.

[2] Nakayama W and Usui S: Flow in rotating cylinder of a compressible fluid. *J. Nuclr. Sci. & Tech.* 1974, **11**, 242-262.

[3] Bark FH and Bark TH: On vertical boundary layers in a rapidly rotating gas. *J. Fluid Mech.* 1976, **78**, 815-825.

[4] Park JS and Hyun JM: Transient response of a compressible fluid in a rapidly-rotating circular pipe. *J. Fluid Mech.* 2001, **427**, 275-297.

[5] Matsuda T and Nakagawa K: A new type of boundary layer in a rapidly rotating gas. *J. Fluid Mech.* 1983, **126**, 431-442.

[6] Wood HG and Barbarsky R: Analysis of a rapidly rotating gas in a pie-shaped cylinder. *J. Fluid Mech.*, 1992, **239**, 249-271.

[7] Matsuda T, Hashimoto K and Takeda H: Thermally driven flow in a gas centrifuge with an insulated side wall. *J. Fluid Mech.*1976, **73**, 389-399.

Proceedings of the Tenth Asian Congress of Fluid Mechanics
17-21 May 2004, Peradeniya, Sri Lanka

MEASURING AIR-SEA ENERGY AND MOMENTUM FLUXES OVER THE INDIAN OCEAN

G. S. Bhat and J. V. S. Raju
Centre for Atmospheric and Oceanic Sciences, Indian Institute of Science, Bangalore 560 012, India

ABSTRACT: The measurement/determination of air-sea interface fluxes of momentum, heat and water vapour is important in many climate related studies. However, these measurements were missing over the Indian Ocean till recently. In the present study an experimental arrangement used for measuring fluxes over the Indian Ocean is described. It is shown that there is broad agreement between the latent heat fluxes calculated from three different approaches. However, there are significant individual differences and these differences are considerably reduced when certain conditions on the relative wind direction with respect to the ship axis are imposed. This suggests that the flow distortion caused by the ship structure is nonnegligible for some orientations of ship. It is also shown that the present experimental arrangement enables accurate computation of mean as well as gradients of horizontal velocity, temperature and water vapour concentration at the measurement height. This information can be used for obtaining an independent estimation of fluxes.

1. INTRODUCTION

Water and its transformations play a major role in the transport of energy from the tropics to the polar region and largely responsible for driving the wind systems in the tropics, including the monsoon circulation and devastating cyclones. Atmosphere receives water in the form of vapour from the underlying surface, a large fraction of which is ocean covered. Therefore, accurate measurement /determination of the fluxes of heat, water and momentum at the air-sea interface becomes important and is required in several applications ranging from short term weather predictions (e.g., evolution of a cyclone, maximum ocean wave height) to long term climate change issues. For example, a systematic error of just 10 Wm^{-2} in the net heat flux (comprises of heat, latent heat and radiative fluxes) between ocean and atmosphere leads to over/under estimation of the temperature of the upper layer of the ocean by about 2^oC over a period of one year. Though seems small, this error is not acceptable owing to the fact that the ocean and the atmosphere together constitute a highly nonlinear system and even a 1 ^oC extra warming of the ocean implies drastic changes in atmospheric response. For example, over the Indian Ocean, rain bearing clouds do not form if the **s**ea **s**urface **t**emperature (*SST*) is below 28 ^oC [1], whereas, at a SST of 29 ^oC the frequency of occurrence of these clouds is near its peak[2].

Air-sea flux measurement is not new and several field experiments aimed at this purpose have been carried out during the past 5 decades, and significant improvements have been made in instrumentation and measurement techniques during this period. While 10 Wm^{-2} accuracy in the net heat flux seems inadequate for climate prediction purposes, even with the most sophisticated instruments, this accuracy has not been achieved in the field so far. There are several reasons for this. To appreciate this, we need to examine the components of the net heat flux (Q) at the air-sea interface given by (heat into the ocean is taken as positive)

$$Q = NRF\text{-}SHF\text{-}LHF \tag{1}$$

where *NRF* is the net radiative heat flux (can be measured directly). Heat flux [called sensible heat flux (*SHF*) in meteorology], latent heat flux (*LHF*) and the shear stress (t) are estimated using the following relations.

$$SHF = \rho C_p \overline{q'w'} = -\rho C_p q_* u_* = \rho C_p C_h U_a (T_s - T_a) \tag{2}$$

$$LHF = \rho L \overline{q'w'} = -\rho C_p q_* u_* = \rho L C_q U_a (q_s - q_a) \tag{3}$$

$$t = \rho \overline{u'w'} = \rho u_*^2 = \rho C_d U_a^2 . \tag{4}$$

In the above equations, u is horizontal wind speed, q is potential temperature, q is water vapour concentration, C_p is specific heat of air at constant pressure, L is latent heat, T is temperature, U is the mean wind speed. Prime and the subscript * respectively denote the fluctuating part and scale of respective variables. C_h, C_q and C_d are (empirically determined) bulk transfer coefficients; flux estimated using the equations involving these coefficients is called the bulk flux. Subscripts a and s refer to properties at a standard height (normally 10 m) and at the surface respectively. Computation of the fluxes using the equations after the first equality sign in equations (2)-(4) (which actually define these fluxes and are used for fixing C_h, C_q and C_d), requires velocity, temperature and humidity data at high sampling rates (better than 5 Hz). Turbulent and highly transient nature of the wind makes it impossible to carry out controlled experiments in the atmosphere and at times defining a proper mean itself is not possible. Marine atmosphere is highly corrosive and sensitive laboratory sensors either fail or their performance deteriorate rapidly when continuously exposed. Open oceans are very deep (typically 2-4 km) requiring measurements to be made from moving platforms. The velocities are to be corrected for platform motion (not a serious issue now) but the flow distortion caused by the platform still remains a problem. *LHF* dominates the energy flux from the ocean to the atmosphere and *SHF* is typically less than 10% of *LHF*. There is no instrument capable of directly measuring the *LHF* at present and is computed from velocity and humidity measurements. Accurate measurement of humidity under all weather conditions is not possible. Therefore, determination/ measurement of air-sea fluxes to few Wm^{-2} accuracy is a technological challenge and is among the frontier areas of research in meteorology and oceanography today.

Earlier observational studies were carried out mainly over the Atlantic and Pacific Oceans and the Indian Ocean remained unexplored till recently. The first such attempt over the Indian Ocean using the state of the art instruments was made over the Bay of Bengal during the Bay of Bengal Monsoon Experiment (BOBMEX) in 1998-99[3]. The present work is based on the measurements made from the Indian research ship *ORV Sagra Kanya* during BOBMEX and during the Arabian Sea Monsoon Experiment (ARMEX) carried out during 2002-2003 over the Arabian Sea. The experiments covered pre-monsoon, monsoon and post-monsoon periods. The material is arranged as follows. In section 2, experimental arrangement is briefly described followed by representative results in section 3 and conclusions in section 4.

2. EXPERIMENTAL SET UP

The experiments were carried on board the Indian research ship ORV Sagar Kanya. The details pertaining to the selection of sensors, mounting and data archival procedure can be found in Bhat and Ameenulla[4]. Short and long wave radiative fluxes were directly measured using respective radiometers. Wind velocity was measured by a sonic anemometer which also measured air temperature. Water vapour concentration was measured by an infrared hygrometer (IR-hygrometer). Velocity measured by the sonic anemometer includes a component due to ship motion. Orientation of the sonic anemometer changes with time due to pitching and rolling motions of the ship. A 3-component accelerometer was mounted on the body of the sonic anemometer with axes parallel to velocity components and a 2-component tilt sensor measured the ship pitching and rolling accelerations and angles. The sampling rate was 10 Hz. In the immediate vicinity of the ship, the velocity field is modified by the ship structure. To minimize the ship influence, the instruments were mounted on a 7-meter long boom at the bow of the ship (Fig. 1).

3. RESULTS AND DISCUSSION

The boom with the flux sensors mounted on it was deployed at time series observation stations which were 150-700 km from the coast. Ship slowly drifted during these measurements. Ship navigation data (speed, heading and course) at one minute interval is used for removing the contribution from the mean motion of the ship. Using the tilt meter data, velocity is resolved along three orthogonal components, namely, parallel to ship axis (u), normal to ship axis (v) and along the vertical (w) at each

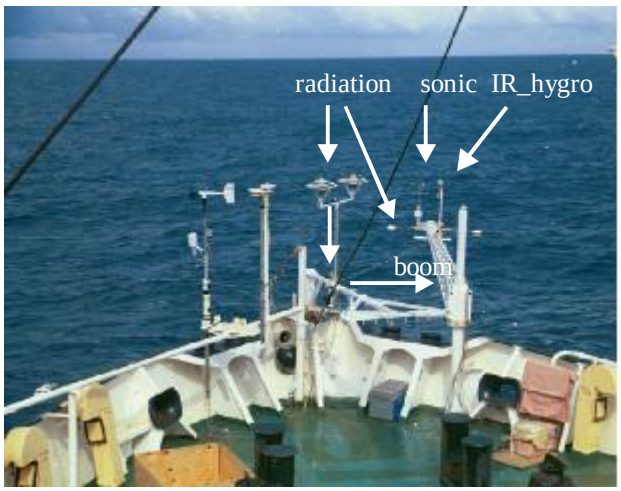

Figure 1. Arrangement of sensors on board *ORV Sagar Kanya*.

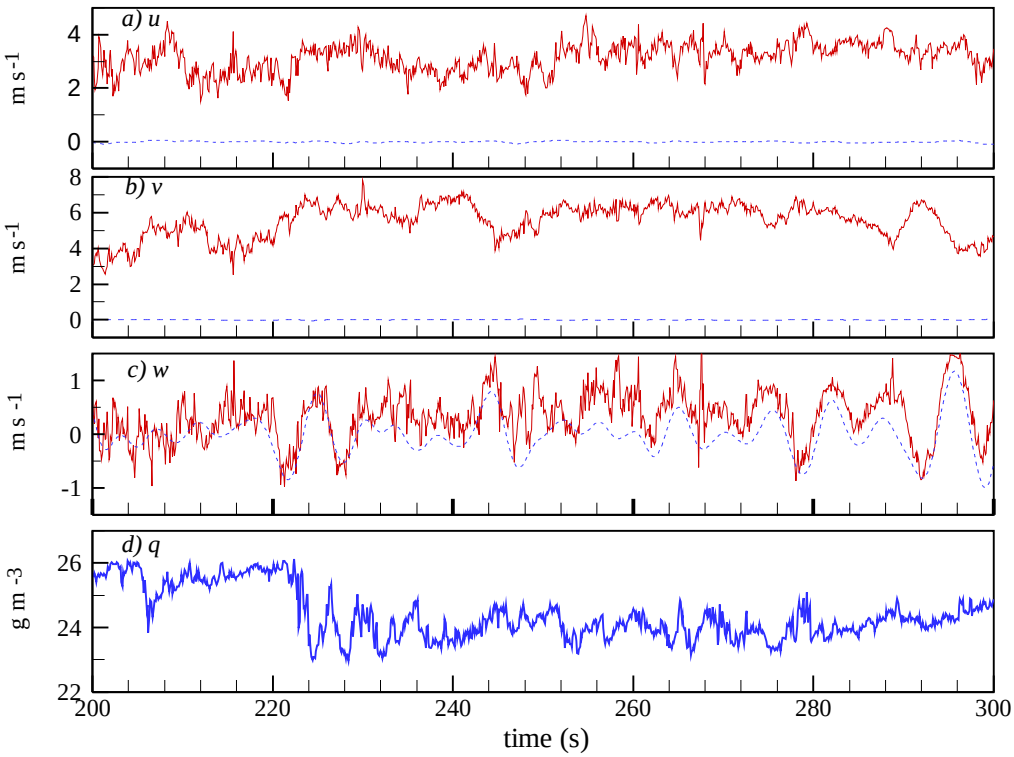

Figure 2. Time series of *u*, *v* and *w* components of velocity measured by the sonic anemometer, and *q* measured by the IR-hygrometer. The dashed line in the top three panels shows the respective velocity component measured by the accelerometer.

instant. Pitching and rolling motions are relatively high frequency components (~0.1 Hz frequency) compared to ship's mean motion. Figure 2 shows typical temporal variation of *u*, *v* and *w* and water

vapour concentration. The velocities measured by the accelerometer along the respective directions are also shown. It is observed that the velocity induced by the ship motion in the horizontal are small compared to the measured wind components, whereas, in the vertical it dominates. Since vertical velocity directly appears in the correlations that estimate *SHF*, *LHF* and *t* [Eqns. (2)-(4)], correction to the vertical component of the measured velocity is most crucial.

Fluxes are normally computed from three different methods, namely, the bulk method [5] [which uses only time averaged values, e.g., terms following the last equality sign in equations in (2)-(4)], inertial dissipation method (IDM)[6] (employs Monin-Obukhov similarity relations for the convective boundary layer along with dissipation rates obtained using Kolmogorov theory for isotropic turbulence) and eddy correlation method that directly computes the co-variances [Eqn. (2)-(4)]. In the present study, fluxes have been computed using all three methods, however, owing to space constraints only results on *LHF* are shown in the following. Time series were examined and only those stretches where all variables appeared to remain stationary over a period of 15-20 minutes were selected. Calculated values of *LHF*

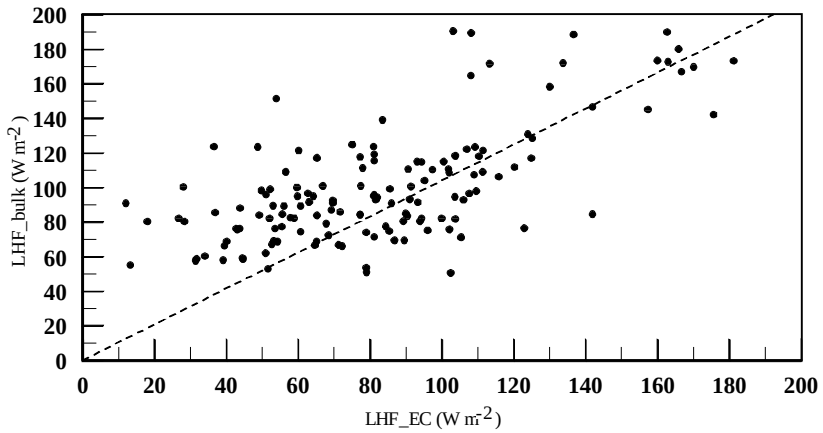

Figure 3. Comparison of the *LHF* calculated from eddy correlation and bulk methods.

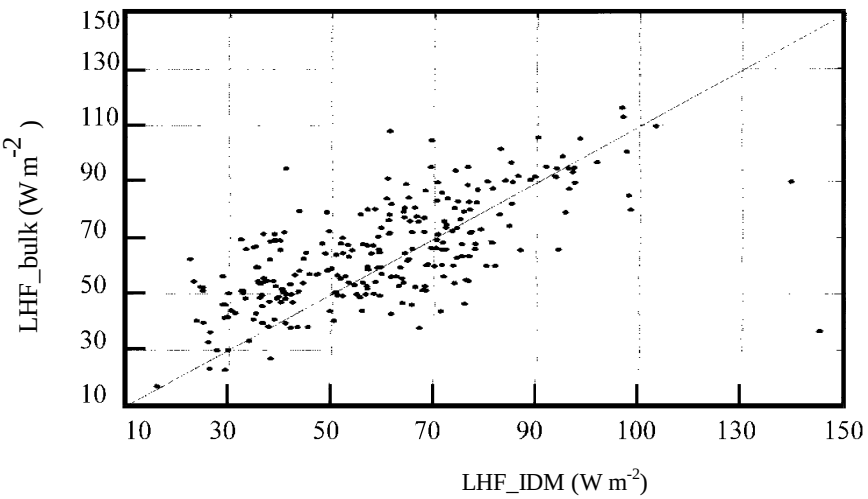

Figure 4. Comparison of the LHF calculated from inertial dissipation and bulk methods.

scatter. For example, when only those cases where wind blew head on (within ±45^o to ship axis) were considered, then the scatter is considerably reduced and the *LHF* calculated from all the three methods are compared in figures 3 and 4. While there is reasonable agreement in the mean, considerable scatter

cannot be ignored. Detailed analysis of the cases where the scatter is large revealed that in addition to flow stationarity, the angle between the wind and the ship axis is another major factor responsible for the agreed within 5 Wm^{-2}. The main problem is that the number of cases where both these conditions are met are relatively few, thus limiting the number of data points. When clouds develop, conditions change rapidly on time scales of few minutes. Which is the better approach to estimate fluxes in these cases where either one or both conditions are not satisfied, remains open.

Ship rolling and pitching motions are undesirable. However, as shown next, this also provides an opportunity for calculating the mean and its slope at the measurement height. Boom moves up and down, swaying the instruments by more than 2 meters in the vertical. Thus, the instantaneous value of a variable measured by the instrument, say u, can be split into three parts,

$$u(t) = \bar{u} + u_t' + u_s' \tag{5}$$

where the over bar denotes the time average value, u_t' is due to the turbulent fluctuations in the flow and u_s' is due to the instrument displacement in the vertical. Since the mean gradient of u is nonzero in the boundary layer and the instrument samples at different heights at different times, u_s' is nonzero. Thus, the fluctuations observed in the time series includes a contribution from sensor displacement. Since ship movement and turbulent fluctuations in the flow are independent, we do not expect u_t' to have any correlation with that due to sensor displacement. Thus, if the fluctuating component is stratified according to height and averages are taken, then the turbulent part vanishes leaving behind the contribution from sensor motion. From the accelerometer data, the vertical position of the sensor as a function of time is obtained and used for stratifying data with height. The outcome of this exercise for

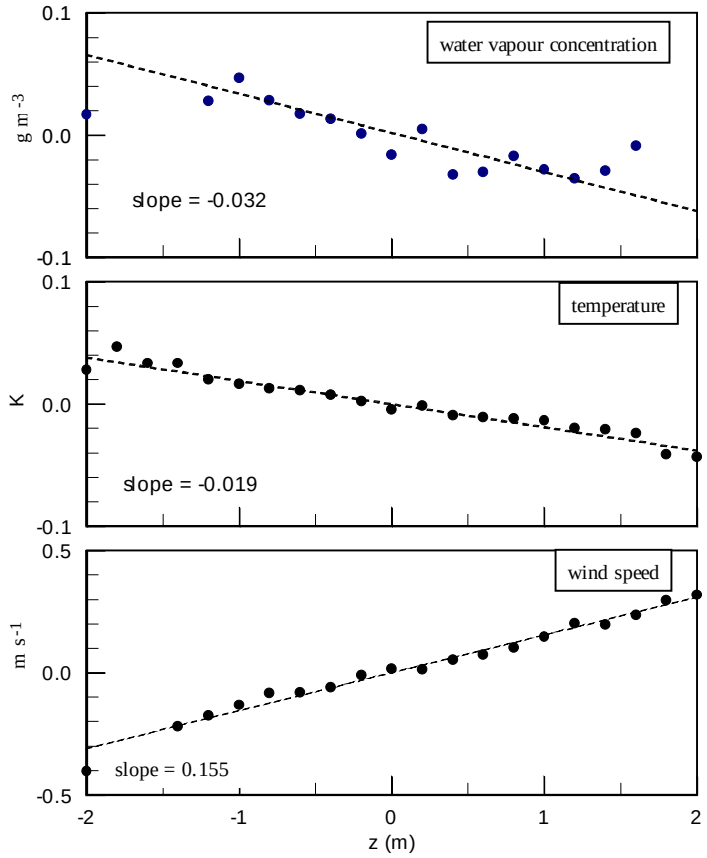

Figure 5. Mean profiles of (a) water vapour concentration, (b) temperature, and (c) horizontal wind speed with height about the mean height of boom oscillation. The mean position of the sensor is taken as z=0.

one case is shown in Fig. 5. In this figure, fluctuating parts were binned in every 0.2 m height interval and then averaged. The mean profiles shown in Fig. 5 are along the expected lines, namely, water vapour concentration and temperature decrease with height and the mean wind speed increases with height. Horizontal wind speed and temperature show a smooth variation with height about the mean position. There is a little larger scatter in humidity. The slopes of the lines give the average gradients of respective variables. It may be noted that the mean height of the sensors was 11.5 m. At this height, the gradients are small, and the change over a height interval of say 1 m are comparable or smaller than the sensor accuracy. In the present case, since the same instrument sampled at different heights, the gradient is captured more accurately compared to that of measuring this by placing different sensors at close height intervals. Once the mean and its gradients are available, it is possible to use these for estimating the mean profiles and surface layer scales [Eqns. (2)-(4)] using the Monin-Obukhov similarity relations[5]. These can be used to calculate the gradient Richardson number and in the calculation of fluxes. This work is currently in progress. It may be noted here that there is no mention in the literature of taking this type of approach to the calculation of fluxes over the oceans and our preliminary results are encouraging.

4. CONCLUSIONS

An experimental arrangement used for measuring the fluxes over the Indian Ocean is described. Once high frequency sampled wind, temperature and humidity data are available, then the fluxes can be computed using three different methods. There is good agreement between the values obtained from different approaches when the flow is stationary and wind blows at certain angles to the ship. The possibility of accurately measuring the mean as well as its gradient at the measurement height is attractive and likely to provide another method to calculate fluxes. A detailed study is required in this direction.

ACKNOWLEDGEMENTS

The first author thanks the Organizers of the 10th ACFM for inviting him to deliver a special talk. The work reported here was partially supported by a grant from the Department of Science and Technology, New Delhi, India and we thank the agency for the support. BOBMEX and ARMEX are part of Indian Climate Research Programme, involved the participation of a large number of organizations and people, and we thank all those who contributed to these programmes.

REFERENCES

[1] Gadgil, Sulochana, P. V. Joseph, and N. V. Joshi: Ocean-atmosphere coupling over monsoon regions. *Nature*, 1984, **312**, 141-143.

[2] Bhat, G S, J Srinivasan and Sulochana Gadgil: Tropical deep convection, convective available potential energy and sea surface temperature. *J. Meteor. Soc. Japan*, 1996, **74**,155-166.

[3] Bhat G. S, S. Gadgil, P. V. Harish Kumar, S. R. Kalsi, Madhusoodanan, V. S. N. Murty, C. V. K. Prasada Rao, V. Ramesh Babu, L. V. G. Rao, R. R. Rao, M. Ravichandran, K. G. Reddy, P. Sanjeeva Rao, D. Sengupta, D. R. Sikka, J. Swain, P. N. Vinayachandran: BOBMEX - the Bay of Bengal Monsoon Experiment. *Bull. Amer. Meteor. Soc.*, 2001, **82**, 2217-2243.

[4] Bhat, G. S. and S. Ameenulla: Surface meteorological instrumentation for BOBMEX. *Proc. Indian Acad. Sci.,* (*Earth Planet. Sci.*), 2000, **109**, 221-227.

[5] Zeng, X., M. Zhao, and R. E. Dickinson: Intercomparison of bulk aerodynamic algorithms for computation of sea surface fluxes using TOGA COARE and TAO data. *J. Climate*, 1998, **11**, 2628-2644.

[6] Wyngaard, J. C. and S. F. Clifford: Estimating momentum, heat and moisture fluxes from structure function parameters. *J. Atmos. Sci*., 1978, **35**, 1204-1211.

Proceedings of the Tenth Asian Congress of Fluid Mechanics
17-21 May 2004, Peradeniya, Sri Lanka

MOTION OF ROD-LIKE PARTICLES IN PARTICULATE FLOW

J.Z. Lin
Department of Mechanics, the State Key Laboratory of Fluid Power Transmission and Control, Zhejiang University, Hangzhou, China, 310027, E-mail:mecjzlin@yahoo.com

ABSTRACT: The properties of rod-like particulate flows are of fundamental interest in many scientific and industrial applications. In this paper, several topics on the dynamics of rod-like particulate flows including the motion of particles in shear flows, sedimentation of particles, turbulent rod-like particle suspension flows, interaction of particles, hydrodynamic instability were reviewed.

1. INTRODUCTION

Rod-like particulate flows occur in a variety of natural and man-made materials such as paints, slurries, mineral concentrates, mine tailings, cements, etc. The mechanical, thermal, and electrical properties of rod-like particulate flows are greatly influenced by the way in which the particles are distributed within the polymer matrix, for example, the particle orientation patterns strongly affect the rheological properties of the flow. Besides, the flow can induce a preferred orientation of the particles which, upon solidification, influences the mechanical properties of the resulting particle-reinforced composite. The composite is stiffer and stronger in the direction of greatest orientation, and weaker and more compliant in the direction of least orientation.

Rod-like particulate flows are broadly divided into three regimes: dilute, semi-dilute and concentrated regimes: The flow is called dilute if there is only one rod-like particle in a volume of $V=L^3$ (L is the length of the particles), each particle can freely rotate without any hindrance from surrounding particles with three rotational degrees of freedom. The volume fraction satisfies $\phi = n\pi d^2 L/4$ (n is the number density, d is the diameter of the particle). Since there is only one particle in a volume V, this leads to $\phi < d^2 L/V$. In the semi-dilute regime, each particle is confined in the volume $d^2 L < dL^2$. The spacing between two neighboring particles is greater than the particle's length. Finally, the flow is called concentrated if the average distance between two neighboring particles is less than its diameter, and therefore a particle can not rotate independently, except about its symmetry axis.

Over the past decades, the dynamics of rod-like particulate flows has received much attention. A brief review on the several topics is given as follows.

2. THE MOTION OF PARTICLES IN SHEAR FLOWS

Jeffery studied the motion of a single spheroidal particle in an unbounded linear shear flow at zero Reynolds number, and found the formulation of time rate of change of the particle's orientation.

Bretherton extended Jeffery's solution to all axisymmetric particles by simply replacing the aspect ratio of particles with an effective aspect ratio. When the effect of inertia is present, both the theory and the experiments revealed that the axis of a prolate spheroid gradually turns into flow-gradient plane, whereas a oblate spheroid eventually aligns its axis with the vorticity axis.

Anczurowski et al. investigated experimentally the motion of rod-like particles in a Couette flow. They found that the steady-state orbit-constant distributions for dilute particle suspensions are different from the Jeffery's predictions and independent of concentration. As the suspension concentration increases towards the semi-dilute regime, the behavior of particles changes because of interactions between particles. Folgar and Tucker suggested an isotropic, orientational diffusivity tensor to model interactions between particles.

In the concentrated regime, direct mechanical contacts between rod-like particles increase, causing particles to flip more frequently and to drift towards flow-gradient plane. Sundararajakumar et al. simulated the dynamic behavior of particles interacting solely by frictionless contacts, the results showed that both the increased orientational dispersion and the direct stress transmitted through the contacts enhance the shear viscosity of the suspensions significantly.

Both the translational and the rotational motions of a spheroid moving in shear flow near a wall were examined numerically by Gavze and Shapiro [1] under the conditions that the fluids inertia was negligible, and the rotation was confined to the flow-gradient plane. Broday et al.[2] investigated the motion of both neutrally and non-neutrally buoyant prolate spheroidal particles in vertical shear flows at low Reynolds numbers by using the generalized Faxen law.

Lin et al.[3] investigated the behavior of rod-like particles in an evolving mixing layer numerically. The effects of the Stokes number, the density ratio and the particle aspect ratio on the spatial and orientation distributions of particles were examined. The results show that the Stokes number is the key parameter in determining the spatial distribution of particles in the large-scale vortex structures, but its effect on the orientation distribution of particles is insignificant. The orientation distributions of particles are controlled mainly by the flow dynamics. Both the particle-to-fluid density ratio and the particle aspect ratio have marginal effects on the spatial and orientation distributions of particles. In addition, the validity of the numerical method is verified by comparing the visualization results to the experiments at a low Stokes number. Lin et al.[4] used 3-D vortex filament method and two-way coupling model to simulate the turbulent jets of rod-like particulate flows. The results show that the rod-like particle additives modify the K-H instability mechanism, enhance the large-scale vortices. The difference between the vortex structure of the jets in the single phase flow and in the rod-like particulate flows is not likely to be explained in terms of different shear viscosities.

3. SEDIMENTATION OF PARTICLES

The sedimenting behavior of rod-like particles plays a critical role in many branches of science such as aerosol physics and atmospheric science. Unlike spheres, an isolated non-spherical particle falling in a fluid at zero Reynolds number can have motion perpendicular to gravity. Many investigations have

shown that non-spherical particles like rod will tend to exhibit preferential orientation while under going free fall through a quiescent fluid at intermediate Reynolds numbers. The torque induced on particle causes the body to rotate into a stable position with its symmetry axis aligned horizontally.

The velocity of a falling rod-like particle depends strongly on its orientation and can be evaluated with the slender body theory. When the effect of inertia is present, a particle with the broadside across the stream is stable. Liu & Joseph [5] investigated extensively the effects of both inertia and viscoelasticity on the orientation of a long body. Huang et al. [6] reported the numerical results on the sedimentation of an elliptic particle in Oldroyd-B fluids. Herzhaft et al.[7] demonstrated experimentally that particles tend to align in the gravitational direction. For small number densities, the sedimentation velocity was found to exceed the rate expected for a well-mixed, homogeneous suspension. For some particle aspect ratios and concentrations, the suspension was found to sediment with a velocity in excess of the settling velocity of an isolated particle which is aligned with gravity and sedimenting in a fluid of infinite extent. Butler and Shaqfeh[8] simulated the dynamic of suspensions of particles sedimenting in the limit of zero Re number. The results show that an initially homogeneous, settling suspension develops clusters, or streamers, which are particle rich surround by clarified fluid. The instability which causes the heterogeneous structure arises solely from hydrodynamic interactions which couple the particle orientation and the sedimentation rate in particle clusters. Depending upon the concentration and aspect ratio, the formation of clusters of particles can enhance the sedimentation rate of the suspension to a value in excess of the maximum settling speed of an isolated particle. Lin et al. [9] simulated the sedimentation of particles by considering the particle oscillation and effect of particle on the fluid. The results show that the sedimentation velocities of particle increase slowly with the increase of particle aspect ratio *r*. For sedimentation of a crowd of high-frequency oscillating particles with arbitrary initial orientation, both vertical velocity and horizontal velocity oscillate dramatically, the degree of oscillation of the former is stronger than the later. A crowd of particle falls more quickly than an isolated particle. Particles tend to align strongly in the direction of gravity. Lin et al. [10] used lattice Boltzmann method to investigate the effects of the aspect ratio on the sedimentation of particles. The results show that the stable orientation of a single particle is the horizontal direction. The terminal Re number increases as the aspect ratio increases, and basically remains invariable when the aspect ratio is high enough, which is consistent with the experimental results. The lateral drift of the particle is more apparent at higher aspect ratios and the orientation of the particle at which the lateral drifting velocity reaches the maximal is not sensitive to the value of the aspect ratio. When the aspect ratio is around 2.8, the particle rotates fastest from the vertical location to the horizontal.

4. TURBULENT ROD-LIKE PARTICULATE FLOWS

The behavior of particles in a turbulent flow influences the rheology, transport and light scattering properties of suspensions. Bernstein and Shapiro [11] studied experimentally the motion of particles in the vicinity of the pipe centerline and concluded that the increase in Re number leads gradually to a uniform orientation distribution of particles in turbulence, which is opposite to the effect of Re numbers in laminar flow. In addition, the study of the 2-D orientation properties of relatively large fibrous aerosols dispersed

in the turbulent atmospheric boundary layer were performed, and a distinctive correlation was found between the horizontal orientation averaged over an ensemble of dispersed particles and the turbulence level under real atmospheric conditions. Olson and Kerekes [12-13] simulated numerically the motion of short rod-like particles in a homogeneous and isotropic turbulence and obtained their rotational diffusion coefficient, under the assumptions that there is no velocity difference between the particles and the local fluids and the total moment on each particle is zero.

Some works on the motion of non-spheroidic particles in wall-bounded shear flows have been reported, which revealed that the effect of the coherent structures on the particle dispersion is basically the same for all particles with different shapes. In turbulent shear flows, the effect of fluid inertia on the motion of particles generally exists, therefore, in the dilute case where the interaction between the particles can be neglected, the principal axis of an ellipsoid-like particle turns into the flow-gradient plane and the particle mainly rotates about the vorticity-axis.

Gao and Lin [14] derived the equations of mean and fluctuating velocities in rotation and translation for rod-like particles moving in a turbulent flow with consideration of Stokes drag and virtual mass force. The rotational and translational dispersion coefficients of particles were obtained. The relations of the dispersion coefficients and flow length scale as well as particle characteristic parameters were analyzed. The resulting dispersion coefficients were shown to decrease as the increase of particle length. Zhang and Lin [15] simulated the motion of rod-like particles in turbulent pipe flow by 3-D integral method. The orientation distribution of particles in the computational area for different Re numbers was computed. The results show that the fluctuation velocity of turbulence causes particles to orient randomly. The orientation distributions become broader as the Re number increases. Both fluctuation velocity and angular velocity of particles are affected by the fluctuation velocity of turbulence.

5. INTERACTION OF ROD-LIKE PARTICLES

For dilute suspensions, it is reasonable to neglect the interactions between fibers. For non-dilute suspensions, however, one has to consider particle-particle interactions, which can affect the flow behavior. In the semi-dilute regime, long-range hydrodynamic disturbances are the most likely of particle-particle interaction. A given particle creates a disturbance flow field that can alter the orientation of any neighbors that are within roughly one particle length of its center. When the particle concentration is higher, interactions between fibers have a profound effect on the microstructure of a suspension, and hence on its macroscopic properties. At higher particle loadings, direct mechanical contact between the particles is possible, creating another mechanism for changes in the orientation distribution.

The presence of mechanical contacts between the particles increases significantly the effective stress of the suspension. Numerical simulations indicated that the effective viscosity is enhanced due to mechanical contacts between the particles. Mechanical contacts between particles could also give rise to many nonlinear rheological characteristics such as finite normal stress differences, yield stress, rod climbing and shear thinning. The interactions between fibers play an important role for the properties of rod-like particulate flows, in which the process and duration of interactions are crucial. Therefore, it is

necessary to investigate the factors affecting the process and duration of interactions. These factors include the initial contact point, the aspect ratio and specific weight of fiber, the solvent viscosity. It is especially meaningful to generalize a synthetic parameter to describe the total interaction duration of the fibers. Lin et al. [16] constructed a mathematical model for the mechanical interactions between two contact particles, based on which numerical simulation was performed. The settling particle begins to slide at earlier time and the entire interaction duration diminishes as the initial position of the contact point, the initial orientation of particle and the particle specific weight increase or the solvent viscosity decreases. Both the slipping start-up time and the departing time delay as the particle aspect ratio increases, however, the effect caused by reducing the diameter is more significant than that caused by increasing the length. A synthetic parameter that describes the start-up time and finishing time of the sliding motion of the particles was derived.

6. HYDRODYNAMIC STABILITY

Very limited attention has been devoted to the instability of rod-like particulate flows. Azaiez [17] presented a linear stability analysis of the mixing layer in the presence of rod-like particle additives. It is found that, for large Re numbers, the flow instability is governed by a dimensionless group H, analogous to a reciprocal Re number representing the importance of inertial forces versus viscous forces associated with the anisotropic elongational viscosity of the suspension; and a coefficient C that accounts for inter-particle hydrodynamic interactions. The results reveal that both parameters can induce an important attenuation of the flow instability. The stabilizing effects arise from the orientation diffusion due to hydrodynamic interactions, and not from the anisotropy induced by the presence of particles in the flow. Azaiez [20] discussed the differences and similarities in the mechanisms of reduction of instability in free shear flows induced by rod-like particle additives. For a rod-like particulate flows with hydrodynamic interactions, the shear stress disturbance induced by the misalignment of the particles is the main driving term behind the decrease of the flow instability. On the other hand, the normal stress disturbance acts as a destabilizing factor. In the case of highly viscoelastic polymers, the already known stabilizing role of the normal stress disturbance is counterbalanced by the destabilizing role of the shear stress disturbance.

The instabilities of rod-like particulate flows in channel and circular pipe flows are still to be explored. Lin and You [21] established the constitutive equation of particle suspensions in channel flows on the basis of particle orientation tensors. The modified Orr-Sommerfeld stability equation was obtained further and numerically solved. The results indicate that the presence of particles attenuates the instability of flow, increases the critical Reynolds number, reduces the growth rate of perturbations and narrows the range of unstable waves. The extent of the effect of particles on the flow stability is in direct proportion to the volume fraction and aspect ratio of the particles. You and Lin [22] presented a linear stability analysis on the circular pipe flow of rod-like particulate flows. The particle orientation tensors were used to describe the characteristics of the orientation distribution of particles. The constitutive equation for the rod-like particulate flows was set up and the modified Orr-Sommerfeld stability equation was derived. The Newtonian pipe Poiseuille flow was also analyzed for comparison. The results reveal that the particle

additives will enhance the flow stability, the degree of enhancement becomes high with the increases of the parameter H which accounts for the particle resistance to the stretching along its axis. Rod-like particulate flows with large H can suppress the influence of high Reynolds number on the flow stability. Particularly, fibers give a higher attenuation on the short waves of disturbance.

ACKNOWLEDGEMENT

This research was supported by the National Natural Science Foundation of China (No. 10372090).

REFERENCES

[1] Gavze E and M.Shapiro: Motion of inertial spheroidal particles in a shear flow near a solid wall with special application to aerosol transport in microgravity. *J. Fluid Mech*. 1998, 37, 59-79.

[2]Broday D, Fichman M, Shapiro M and Gutfinger C: Motion of spheroidal particles in vertical shear flows. *Phys. Fluids*, 1998, 10(1), 86-100.

[3]Lin JZ, Shi X and Yu ZS: The motion of fibers in an evolving mixing layer. *Int. J. Multiphase flow,* 2003, .29(8), 1355-1372.

[4]Lin JZ, Wang CB and Shen LP: Effect of fiber additives on the turbulent jets. *Int.. J. Nonlinear Sciences and Numerical Simulation*, 2003, 4(3), 227-232.

[5]LiuYJ and Joseph DD: Sedimentation of particles in polymer solutions. *J. Fluid Mech*. 255, 565-595.

[6]Huang PY, Hu HH and Joseph DD: Direct simulation of the sedimentation of elliptic particles in Oldroyd-B fluids. *J. Fluid Mech.* 1998, 362, 297-325.

[7]Herzhaft B and Guazzell E: Experimental study of the sedimentation of dilute and semi-dilute suspensions of fibres. *J. Fluid Mech*. 1999, 384, 133-158.

[8]Butler JE and Shaqfeh ESG: Dynamic simulations of the inhomogeneous sedimentation of rigid fibers. *J. Fluid Mech.* 2002, 468, 205-237.

[9]Lin JZ, Wang YL, Wang WX and Yu ZS: Numerical simulation of the sedimentation of cylindrical pollutant particles in fluid. *J. of Environmental Sciences*, 2002, 14(4), 433-438.

[10]Lin JZ, Shi X and You ZJ: Effects of the aspect ratio on the sedimentation of a fiber in Newtonian fluids. *J. Aerosol Sci*. 2003, 34(7), 909-921.

[11]Bernstein O and Shapiro M: Direct determination of the orientation distribution function of cylindrical particles immersed in laminar and turbulent shear flows. *J. Aerosol. Sci.* 1994, 25(1), 113-136.

[12]Olson JA and Kerekes RJ: The motion of fibres in turbulent flow. *J. Fluid Mech*. 1998, 377**,** 47-64.

[13]Olson JZ: The motion of fibres in turbulent flow, stochastic simulation of isotropic homogeneous turbulence. *Int. J Multiphase Flow.* 2001, 27**,** 2083-2103.

[14]Gao ZY and Lin JZ:, Research on the dispersion of cylindrical particles in turbulent flows. *J. of Hydrodynamics*, 2003, (to appear)

[15]Zhang WF and Lin JZ: Research on the motion of particles in the turbulent pipe flow of fiber suspensions. *Applied Mathematics and Mechanic*s, 2003 (to appear)

[16]Lin JZ, Zhang ZC and Yu ZS: Investigation of the interactions between two contacting fibers in the fiber suspensions. *Journal of Mater. Sci.*, 2003, 38(7),1499-1505.

[17]J.Azaiez (2000), Linear stability of free shear flows of fiber suspensions, *J Fluid Mech.* 404, 179-209.

[18]Azaiez J: Reduction of free shear flows instability: Effects of polymer versus fiber additives. *J Non-Newtonian Fluid Mech.* 2000, 91, 233-254.

[19]Lin JZ and You ZJ: Stability in channel flow with fiber suspensions, *Progress in Progress in Natural Science*, 2003, 11(2), 95-99.

[20]You ZJ and Lin JZ: Stability in the circular pipe flow of fiber suspensions, *Journal of Hydrodynamics*, 2003, Ser.B, 15(2), 12-18.

Proceedings of the Tenth Asian Congress of Fluid Mechanics
17-21 May 2004, Peradeniya, Sri Lanka

INSTABILITIES IN BLUFF BODY FLOWS

S.P. Singh, S. Mittal
Deptt of Aerospace Engineering , Indian Institute of Technology Kanpur, UP 208 016 , India, smittal@iitk.ac.in

ABSTRACT : Flow past a circular cylinder is associated with almost all the instabilities observed in bluff body flows. Results are presented for numerical solution of the Navier-Stokes equations, via a stabilized finite element formulation, for Re=100 to 10^7. A possible relationship between the drag crisis (sudden loss of drag at Re ~ 2 x10^5) and the instability of the separated shear layer is investigated. It is generally believed that the transition of the boundary layer from a laminar to turbulent state is the cause of this drag reduction. A possible mechanism for this transition process is proposed.

1. INTRODUCTION

The flow past a circular cylinder is associated with various instabilities. These instabilities involve the wake, separated shear layer and boundary layer. Williamson[2] has given a comprehensive description of the flow phenomena at different Reynolds numbers (Re). Upto Re ~ 47, the flow is steady with two symmetric vortices on each side of the wake center line. The first wake instability, manifestation of a Hopf bifurcation, occurs at Re~47. For Re > 47, although it remains laminar, the flow becomes unsteady and asymmetric. Von Karman vortex shedding is observed for slightly larger Re. At Re ~ 190, three-dimensional instabilities, such as formation of vortex loops, deformation of primary vortices and stream wise and span wise vortices, appear in wake. The wake flow undergoes a series of complex three-dimensional instabilities, eventually making it turbulent. Beyond a certain critical Re, the shear layer separating from the upper and lower surface of the cylinder, starts becoming unstable via the Kelvin-Helmholtz mode of instability. The transition point, beyond which the separated layer becomes unstable, moves upstream with increase in Re. At Re ~ 2x10^5, the boundary layer on the cylinder surface undergoes a transition from laminar to turbulent. This transition leads to a delay of the separation of flow from the cylinder surface causing a substantial reduction in the drag force that the cylinder experiences. This is often referred to as *Drag crisis*.

In the present study, two-dimensional flow past a circular cylinder is simulated for Re=100-10^7 using a stabilized finite element formulation. It is well known that beyond Re ~ 190 the flow ceases to be two-dimensional. In that sense, the present two dimensional computations are expected to fall well short of accurately predicting the various quantities associated with flows at high Re. The objective of the present work is to investigate a possible connection between the shear layer instability and drag-crisis. It has been reported in the literature [1,2] that the shear layer instability is primarily two dimensional. A very fine finite element mesh, that is capable of resolving the boundary layer at the cylinder surface and the flow structures associated with the shear layer vortices, is utilized. Computations are carried out at various Re to study the shear layer instability. The variation of the frequency of the shear layer vortices with Re is compared to the trends from experimental studies. Good match between the present and published results is observed. It is found that the present computations are able to reproduce the significant drop in the drag coefficient at the critical Re. The results indicate that the shear layer instability plays an important role in this phenomenon. A possible mechanism for the phenomenon is discussed. For high subcritical flow the transition point, beyond which the separated shear layer is unstable, is located shortly downstream of the point of laminar separation of the boundary layer from the cylinder surface. At Re_c the transition point moves very close to the separation point and causes local remixing in the boundary layer leading to reattachment of flow.

2. RESULTS AND DISCUSSIONS

A cylinder, of diameter D, is placed in a domain whose outer boundary is a rectangle. The center of the cylinder is located at the origin of the coordinate system. The free-stream flow is along the x axis. The Reynolds number, Re, is based on the diameter of the cylinder, free-stream velocity and viscosity of the fluid. Free-stream values are assigned for the velocity at the upstream boundary. No slip condition for the velocity is applied on the cylinder boundary. At the downstream boundary a Neumann type boundary condition for the velocity is specified that corresponds to zero viscous stress vector. On the upper and lower boundaries the component of stress vector along these boundaries and the velocity normal to them are assigned zero values.

2.1 Finite element mesh

The finite element mesh consists of two parts: a structured grid close to the cylinder and an unstructured mesh in the remaining domain. The structured mesh allows for having adequate control on the resolution of the flow in the boundary layer. The unstructured mesh is generated via the Delaunay's triangulation technique. This kind of a hybrid mesh is useful in handling complex geometries by providing adequate resolution close to the body without requiring the same distribution of grid points in the remaining domain. Most of the computations in this paper have been done with a mesh with 47,011 nodes and 93,574 elements. The time-averaged drag-coefficient (C_d) for $Re=10^6$ obtained with this mesh is 0.591. The value of C_d with a more refined mesh with 116,166 nodes and 231,484 elements is 0.607. Other mean and fluctuating quantities also show a good match between the results from the two meshes. This establishes the adequacy of the meshes utilized here to resolve most of the large scale structures of the flow in this range of Re.

2.2 General overview of the flow

Figure 1 shows the variation, with Re, of the time-averaged drag and base suction coefficients. Data from computations on various finite element grids has been shown along with experimental results from other researchers. It is observed that the values from present computations match well with the results from experiments for $Re < 200$. Beyond $Re \sim 180$ the wake flow undergoes three-dimensional transitional instabilities. Therefore, for $Re > 200$, the drag and base suction coefficient and Strouhal number are over predicted by two dimensional computations. Also shown in the figure is a straight line that passes through the data points for $Re<200$. It can be observed that the results from two-dimensional computations for $2x10^3 < Re < 3.2x10^4$ lie close to the line extrapolated from the two-dimensional behavior.

2.3 Shear layer instability

The lowest frame in Figure 1 shows the ratio of shear layer and primary vortex shedding frequencies (f_{SL}/f_K) from the present computations for various Re and their comparison with the measurements from other researchers. The "histogram" technique proposed by Prasad and Williamson [3] has been utilized in the present work. Good match is observed with the $Re^{0.67}$ variation for Re upto 2×10^5. This confirms the observation of Braza, Chassaing & Ha Minh [1] that the origin of the shear layer instability and the subsequent development of small scale vortices is essentially a two dimensional phenomenon. The agreement at $Re=10^6$ is poor. This is because at this Re, the transition point at which the separated shear layer becomes unstable reaches the cylinder surface. Consequently, the generation and time evolution of the shear layer vortices is influenced by the cylinder surface and the boundary layer on it. As a result the separated boundary layer ceases to behave as a free shear layer.

2.4 Drag crisis and shear layer instability

Figure 2 shows close-up views of the instantaneous vorticity field at various Re near the upper and lower surfaces of the cylinder. The instability of the separated shear layer and its interaction with the boundary layer on the cylinder surface can be observed from this figure. For the $Re= 3.2 \times 10^4$ flow the transition point, for the onset of shear layer instability, is located fairly downstream of the cylinder. It moves upstream, towards the cylinder, with increase in Re. At $Re=10^5$ the shear layer becomes unstable

shortly downstream of the point of flow separation from the cylinder surface. At $Re=10^6$ the point of instability reaches very close to the un-separated boundary layer on the surface of the cylinder. As a result of these eddies the boundary layer experiences mixing with the outer flow causing reattachment of flow and delay of separation. This is associated with narrowing of wake and significant reduction in drag and base suction coefficients. At $Re=10^7$, the instability of the shear layer propagates further upstream and causes mixing of a significant portion of the boundary layer prior to its eventual separation. The mixing of flow results in a significant increase in the Reynolds stresses in this region.

These results suggest that the transition of the boundary layer, on the surface of cylinder, is initiated by the instability of the separated shear layer. For the sub-critical flow, the instability of the separated shear layer commences sufficiently downstream of the point of separation. At the critical Reynolds number, the separated laminar boundary layer experiences significant mixing shortly downstream of its separation, due to the eddies generated by the shear layer vortices. This marks the transition of the separated boundary layer from laminar to turbulent and causes the flow to reattach. The eventual separation of the re-attached flow occurs at a much downstream location and results in drag-crisis. For higher Re the shear layer instability moves upstream and so does the transition point of the boundary layer. Eventually, the entire boundary layer on the cylinder surface becomes turbulent. This results in an increase in the drag experienced by the cylinder due to the increased skin-friction on its surface. This can also be observed from Figure 1 which shows the variation in the time-averaged drag coefficient for various Re. As is observed from experimental data, the drag coefficient for $Re=10^7$ is larger than that at $Re=10^6$.

Figure 3 shows time averaged pressure coefficient (C_P) distribution on the surface of the cylinder. Compared to the flow at $Re=10^5$, the delay in flow separation for $Re=10^6$ results in a higher peak suction, near the shoulder of the cylinder, and a higher base pressure. The higher base pressure results in a lower drag coefficient. It is also seen that for the $Re=10^6$ flow, the 2D LES with a Smagorinsky turbulence model results in virtually identical pressure distribution as the model free computations.

3. CONCLUDING REMARKS

Flow past a circular cylinder is simulated for Re=100 to 10^7 via a stabilized finite element formulation in two dimensions. For Re~2000 and larger, the ratio of the shear layer and vortex shedding frequencies varies as $Re^{0.67}$, in agreement with results from other researchers. The transition point beyond which the separated shear layer becomes unstable moves upstream with Re. The unstable shear layer is responsible for the small scale vortices. At a certain critical Reynolds number (Re_c), the transition point moves very close to the separation point leading to an interaction between the boundary layer and the shear layer vortices. These vortices cause mixing of flow in the boundary layer, thereby energizing it and leading to its reattachment. An increase in the Reynolds shear stress near the separation point is observed as a result of this vortical activity. The entire boundary layer, till the point of separation, is laminar for $Re < Re_c$.At $Re=Re_c$ even though a significant part of the boundary layer is laminar, the latter part, beyond the point of reattachment, undergoes a transition to a turbulent state. The flow is associated with narrowing of wake and a significant reduction in the time averaged drag- and base suction coefficients. Beyond Re_c, the boundary layer achieves a turbulent state well ahead of the flow separation. This leads to increased skin friction and drag coefficient.

ACKNOWLEDGEMENTS

The authors wish to acknowledge the support of Department of Science & Technology (DST), India towards this research.

REFERENCES

[1] Braza M., Chassaing P., and Minh H. Ha: Prediction of large-scale transition features in the wake of a circular cylinder. *Physics of Fluids A*, **2**:1461-1471, 1990.

[2] Williamson C.H.K.: Vortex dynamics in the cylinder wake. *Annual Review of Fluid Mechanics*,

28:477-539, 1996.
[3] Prasad A. and Williamson C.H.K.: The instability of the shear layer separating from a bluff body. *Journal of Fluid Mechanics*, **333**:375-402, 1997.

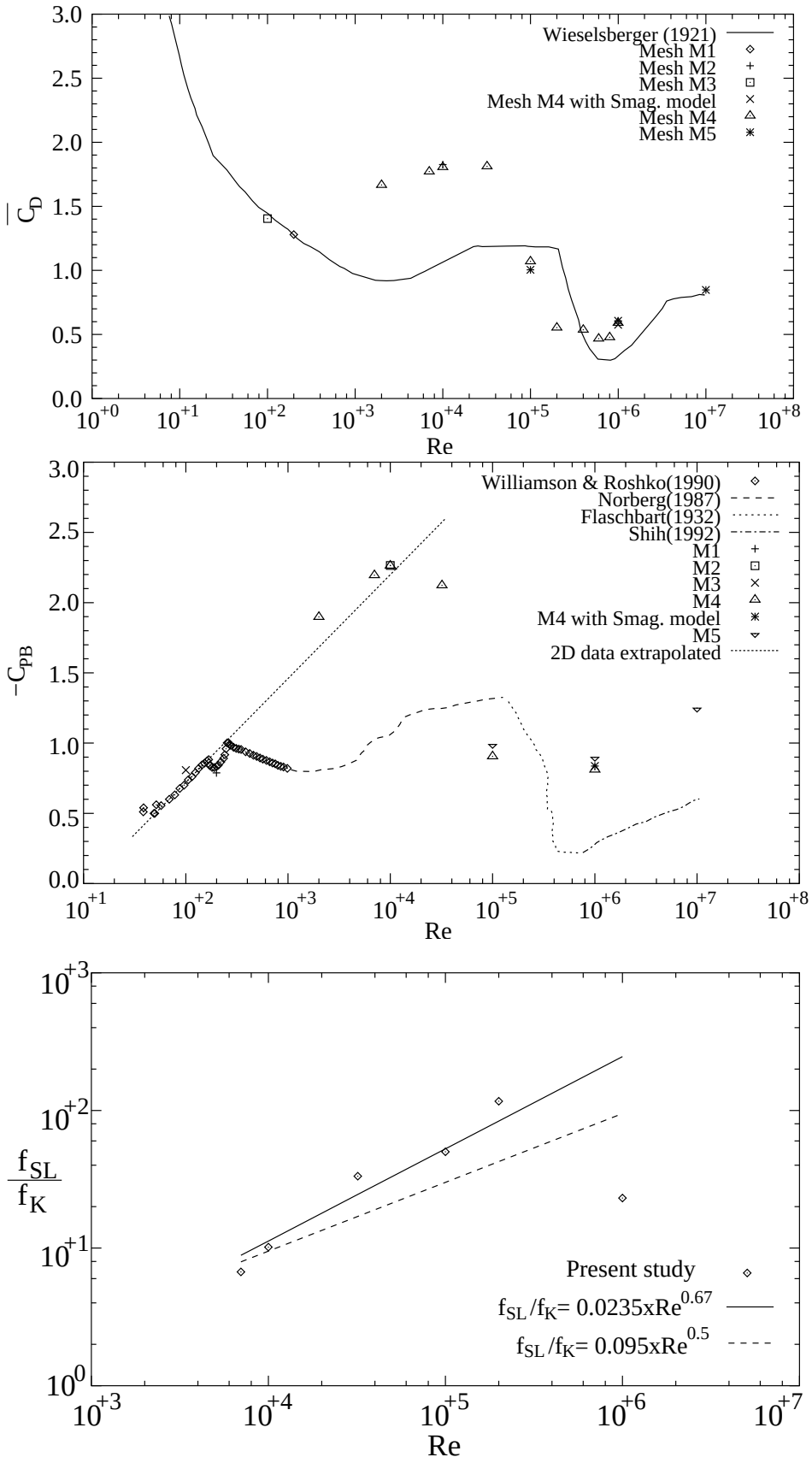

Figure 1: Flow past a cylinder: variation of the time averaged drag and base suction ($-C_{PB}$) coefficients and shear layer frequency (f_{SL}) normalized with vortex shedding frequency (f_K) with Re.

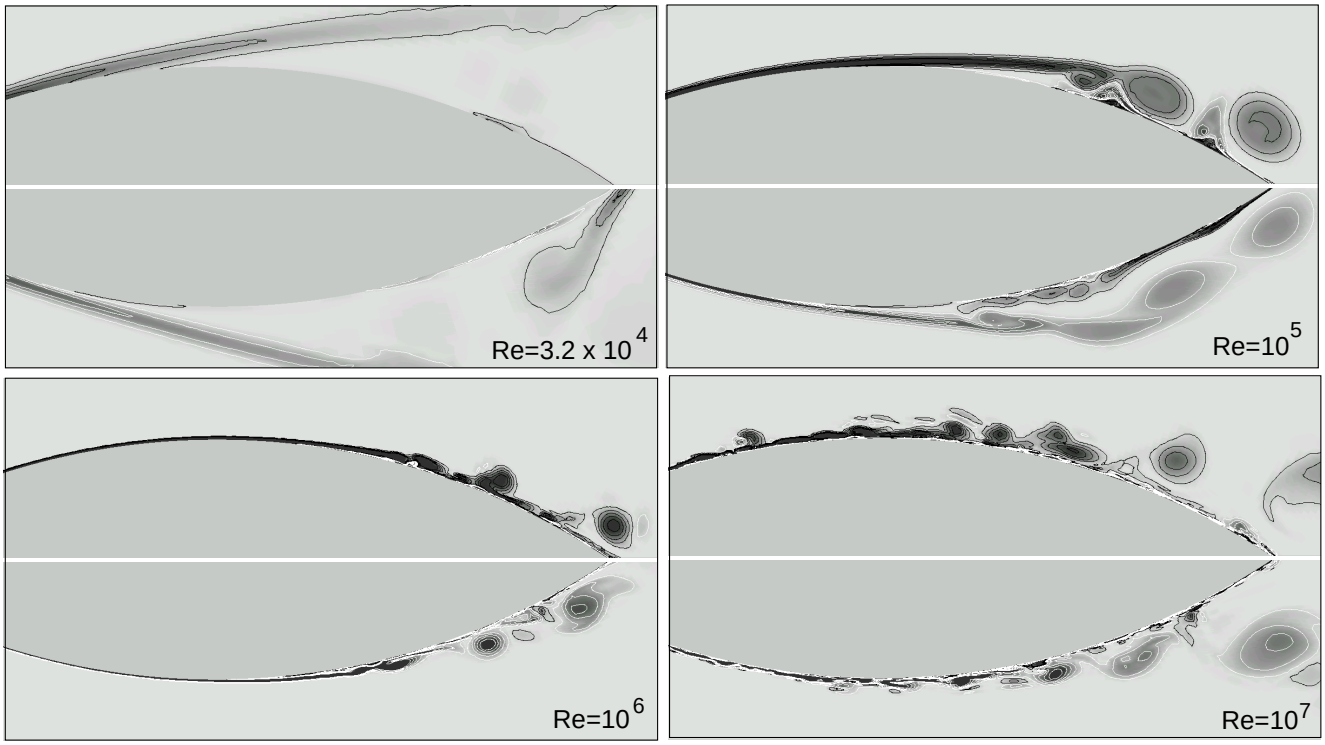

Figure 2: Flow past a cylinder: close-up view, near the upper and lower shoulder of the cylinder, of the instantaneous vorticity field for various Re.

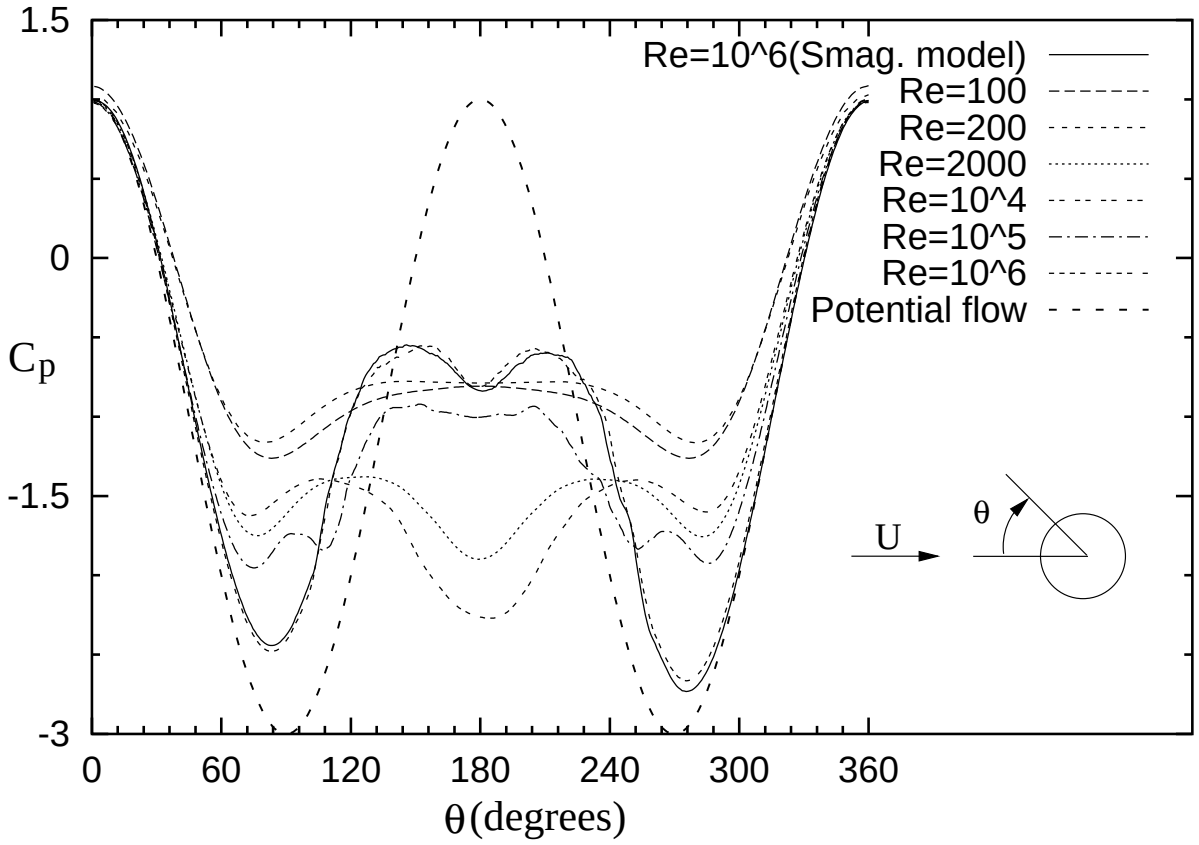

Figure 3: Flow past a cylinder: pressure distribution on the surface of the cylinder for the time averaged flow field.

Proceedings of the Tenth Asian Congress of Fluid Mechanics
17-21 May 2004, Peradeniya, Sri Lanka

DYNAMIC PIV

H. Hayami
Inst. for Materials Chemi. & Eng., Kyushu University, Kasuga 816-8580, Japan

ABSTRACT: Particle image velocimetry (PIV) can capture velocity vector fields with high spatial resolution. A dynamic PIV system with 2 kHz at mega-pixel frame up to 10 kHz at 512x256 pixels was developed by combining a high-speed camera, a high-speed pulse laser with double pulse option, and a pulse controller. The system has been applied to various types of jet flow as well as a channel flow.

1. INTRODUCTION

Particle image velocimetry (PIV) can capture velocity vector fields with high spatial resolution. Two-dimensional PIV (2D2C) and stereoscopic PIV (2D3C) systems have been commercialized. PIV systems are now widely used for fluid flow measurement applicable to low speed up to even high speed flow using a double-pulse and double-frame PIV system, large-scale to micro-scale flows, using so called a micro PIV, and so on. In these standard PIV, high-resolution CCD camera and double pulse Nd:YAG laser are used. The image resolution is at least 1,000x1,000 pixels. Sometimes, 2,000x2,000 pixel CCD can be used. Because of limit of the camera's readout time and laser repetition frequency, these PIV systems can measure the flow field at 15 Hz or less. Recently, a dynamic PIV system has been successfully developed based on the combination of a high-speed CMOS camera, a high-speed pulse laser, and a timing controller [1][2].

2. WHAT'S A DYNAMIC PIV ?

"Dynamic PIV" means a higher temporal resolution PIV system for analyzing the dynamic information on the flow field [3]. This type of PIV is sometimes called as a time-resolved PIV [4] or a high-speed PIV [3], and so on.

3. DYNAMIC PIV SYSTEM

The present system consists of a high-speed camera, a laser light source with an optical fiber and a lens unit to supply a light sheet, and a pulse timing controller. A high-speed CMOS camera (Photoron FASTCAM APX), monochrome 10 bit in gray scale, is used. The frame rate is basically 2 kfps at a full size of 1,024x1,024 pixels. The memory size is normal 2.6 GB, and then the sequential images in about 1 second can be captured. The maximum frame rate is up to 120 kfps at 128x16 pixels, but for practical use as PIV, it might be up to 6 kfps at 512x512 pixels or 10 kfps at 512x256 pixels for instance. A single-rod and diode-pumped Nd:YLF laser (Positive Light Evolution-30 (Coherent Inc, since January 2004)), 527 nm in wave length, with a double pulse option (DPO), is used as a light source. The power is more than 20 mJ/pulse and the Q-switched output pulse is about 150 ns FWHW at a 1 kHz repetition rate. The maximum repetition rate is 10 kHz with 4 mJ/

pulse. It should be noted that it is very important to developed a control system of the high-speed camera and the high-speed pulse laser with high accuracy. A flip-flop pulse generator was in-house made to control the timing of laser pulse as well as camera frame rate. All setting of a laser unit and a camera unit are controlled by two note-type personal computers (OS: Windows XP), respectively.

The frame interval every 100 μs is not enough for a high speed flow measurement. Furthermore, the evaluated velocities are area-mean values for the interrogation area as well as time-mean values for the interval time. That is, PIV system inherently gives a low-pass filtered information for the interrogation area, 8x8 pixels for instance, as well as for the interval time between a pair of laser pulses. Then, so called a frame straddling technique is applied against higher time resolved data and/or against higher cutoff frequency of low-pass filtering. In the present system with a single laser rod, a single pulse is divided or chopped into two pulses, with controlling the Q-switch. The interval between the double pulses can be varied from 1 to 150 μs. The pulse energy is 10 mJ/pulse at 1 kHz with frame straddling mode. Since the beam is generated by one rod, no beam alignment is needed. However, the beam characteristics (e.g., pulse duration) of the 1st pulse is a little bit different from that of the 2nd pulse. Then, the user should understand the differences to use the laser for the frame straddling illumination. Synchronizing the double pulse system (1 kHz / double pulse mode) with the high-speed camera (2 kHz), the velocity vectors can be measured under 1 kHz. The time interval between the double pulse is also limited by the camera dead time (about 4 μs). The timing chart of the camera and the laser control for a frame straddling mode is shown in Fig. 1.

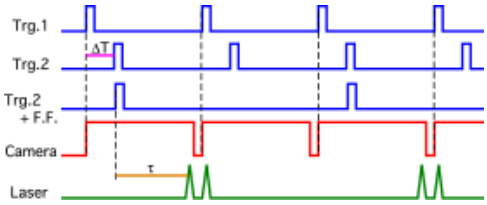

Fig. 1 Timing chart of camera and laser

4. APPLICATION OF DYNAMIC PIV

The unsteady flow information can be obtained with 2 kHz or up to 10 kHz of velocity information. Then high spatial-resolution and high temporal-resolution velocity vectors can be measured using these camera and laser. The water-droplet jet flow has been measured using the present dynamic PIV system [1][2]. A tested commercial based humidifier, AKIMist "D" Dry Fog Humidifier, consisted of two coaxial nozzles at an angle of 120 deg in a horizontal plane. The upstream tank pressure was set to be 0.2 MPa in gauge pressure. The droplet size was about 10 μm. The horizontal plane of jet flow field between 0 to 100 mm downstream of nozzle including nozzle axis was visualized using a laser light sheet of 4 mm thick and 140 mm wide.

In case 1, the camera frame rate was 2 kfps, with 1,024x1,024 pixels. The time interval between the double pulses was 0.1 ms with frame straddling technique. Example of the cap-

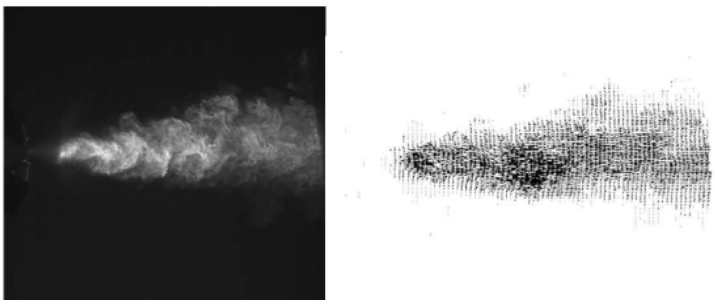

(a) Example of captured image (b) Measured velocity field

Fig. 2 Mist velocity measurement with frame straddling technique at 1 kHz sampling rate (1024x1024 pixels) [1][2]

tured image and measured velocity vector map are shown in Fig. 2. The vectors were calculated based on two successive images with 0.1 ms time difference, using the gradient cross-correlation technique [5]. These image pairs were recorded in 1 kHz. Therefore, high-resolution vectors were captured with 1 kHz.

In case 2, the camera frame rate was 10 kfps, with 512x256 pixel resolution. In this case, the single pulse mode was applied for the laser illumination, so that the time interval between the images was also 0.1 ms. Example of the captured image is shown in Fig. 3. The 16,000 images were captured sequentially, i.e., 1.6 second. Velocity vectors were calculated between two sequential images, or every 0.1 ms. So, the velocity vectors can be measured at 10 kHz in sampling rate. The time-mean velocity vectors for the total 16,000 images are shown in Fig. 4. Figure 5(a) shows the temporal variation of the velocity vectors measured by the PIV. The vortex movements are shown in these figures. To clarify the flow characteristics, the unsteady fluctuation term, $\boldsymbol{u'} = \boldsymbol{u} - \overline{\boldsymbol{u}}$, is shown in Fig. 5(b), where $\overline{\boldsymbol{u}}$ is the time-mean velocity vector. In the fluctuation vector map, the vortex is clearly shown and the vortex transportation is also easily recognized. The velocity fluctuation at one point is quite similar to that by LDV with 10 kHz in sampling rate, for instance. That is, the present dynamic PIV is equivalent to an array of 128x64 or 8,000 LDV sensors.

Fig. 3 Mist image at 10 kHz (512x256) [1][2]

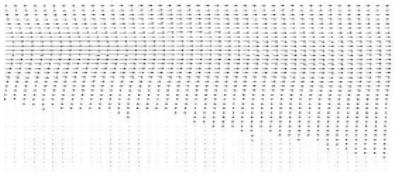

Fig. 4 Time-mean velocity vectors [1][2]

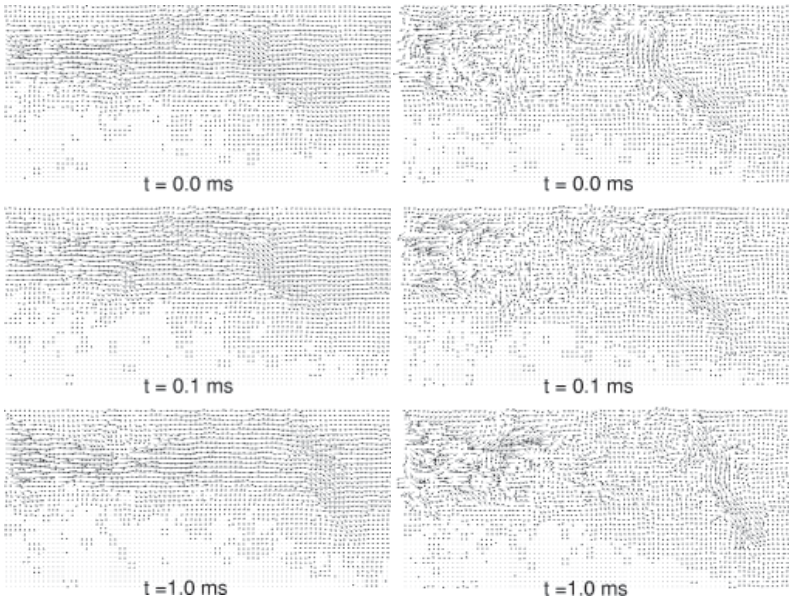

(a) Instantaneous velocity vectors, $\boldsymbol{u}$ (b) Fluctuation term, $\boldsymbol{u'}$

Fig. 5 Temporal fluctuation of mist flow (10 kHz, 512x256 pixels) [1][2]

In the 2D PIV analysis, POD (proper orthogonal decomposition) technique is widely used to extract the spatial characteristics of the flow field. However, in these techniques, the temporal domain information is not taken into account. Since there is enough information in the temporal direction for the dynamic PIV, the three-dimensional (2D in space, 1D in time) POD analysis can be carried out, showing the 3D dominant mode of the phenomenon. The 3D-POD analysis for the dynamic PIV had been developed [6]. The modes for spatial and temporal domain are extracted from the measured dynamic PIV data. Then, the 3D flow field is reconstructed as the summation of the dominant modes. The 3D-POD analysis is considered as the low-

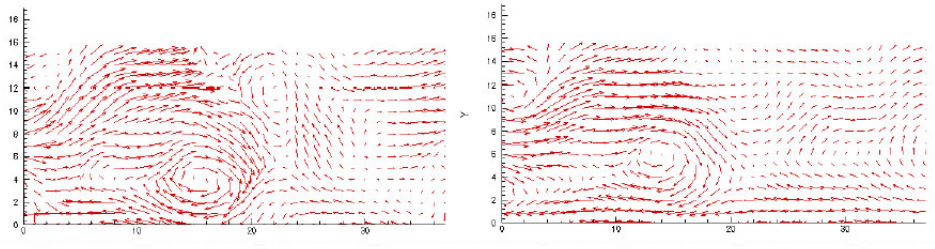

(a) Orginal fluctuation velocity vector for POD (b) Filtered vectors (sum of first 6 modes)

Fig. 6 3D POD analysis for 10 kHz [2]

pass filtering in 3D (2D space, 1D time).

Using 16,000 images for 10 kHz, the POD analysis has been applied [2]. The two-dimensional velocity information with temporal variation was analyzed to get the modes. For the frequency domain, maximum 5 kHz eigenmodes were calculated. Based on the distributions of the eigenmode for the spatial and temporal modes, it was understood the lower modes contain the larger energy. Figure 6 shows the instantaneous velocity distribution and the reconstructed one. The sum of first 6 modes is shown as the filtered (reconstructed) velocity. The basic component of the flow structure is correctly reconstructed. The noise and error are considered to belong to the higher order mode, and then they can be removed by the POD analysis. It is the low-pass filtering in the 3D frequency domain (2D spatial, 1D temporal).

The present 2D dynamic PIV system has been also applied to the complex turbulent flow of a circular impinging jet flow at 2 kHz in sampling rate [7].[8]. The random occurrence of ejection of high-speed lumps from the jet axis was clearly measured, which would contribute high heat-transfer rate near the impingement region [8].

This dynamic PIV was also applied to the flow instability measurement in a multi-curved pipe, which emulates the internal carotid artery (ICA) [9][10], where the sampling rate was 2 kHz. The result shows that the secondary flow pattern at the exit of last curvature became unstable beyond a certain value of Reynolds number, and furthermore, the peak frequency of the unstable motion could be got based on the FFT analysis using the dynamic PIV data, which was quite similar to the LDV data [10].

5. EXTENDED APPLICATION

Adding another CMOS camera, a stereoscopic PIV system has been constructed with a pair of Scheinmpflug positioning devices (made in-house). The system was applied to the 3D structure measurement of a multi-gas-jet flow issued from a multi-hole nozzle being used in gas turbines [11][12], where the sampling rate was 1 kHz with frame straddling mode at 11 μs in double-pulse interval time. The results clarified that the ambient air flows generated by the entrainment with jets and by the expansion of the whole jet flow in radial direction cause instability, unsteadiness and complicated velocity field of the jet flow.

Furthermore, a scanning stereoscopic PIV system has been developed in success to measure the three-dimensional distribution of three-component velocity in a turbulent water round jet [13]. The jet Reynolds number was set as 900, and streamwise location of the measurement was fixed at 45 times of nozzle diameter downstream of the nozzle exit. A measurement volume (~ 100x80x50 mm^3) containing 25 velocity planes

was scanned within 0.1 s, which is short enough to capture the instantaneous vortical structure. An example of vortical structure is shown in Fig. 7. The system has been improved to a larger volume (100x100x100 mm^3) containing 50 velocity planes scanned in 0.208 s [14].

A holographic PIV is very attractive for the volume flow measurement. The present camera has been applied for a dynamic digital holographic PIV system [15]. Due to a low resolution of 1024x1024 pixels, the view area and the resolution was limited. But, the temporal variation of volume flow was captured in success.

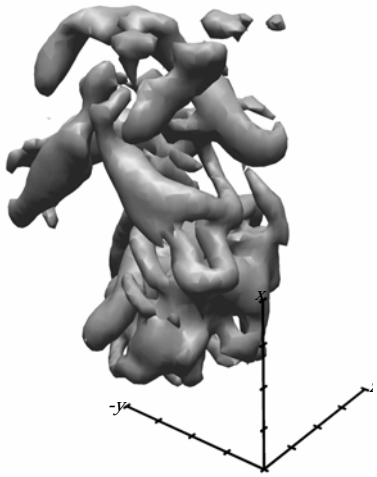

Fig. 7 Surface of constant vorticity magnitude by a scanning stereoscopic PIV [13]

6. SUMMARY

A dynamic PIV system with 2 kHz at mega-pixel frame and up to 10 kHz at 512x256 pixels has been developed in success. The combination of a high-speed CMOS camera and a high-speed single-rod Nd:YLF laser materialized the present dynamic PIV system with an in-house timing controller.

There are some alternative combinations of a high-speed camera and a high-speed pulse laser including a high power CW laser. The dynamic PIV can give the huge amount of data. It can resolve the dynamics of the flow field. The dynamic PIV will be a standard tool for the flow analysis.

There will be various kinds of applications, such as the fields of turbulent flow, transient flow, micro flow, 3D volume flow, and so on, while following procedures should be investigated. To obtain the high-reliability vector data, the low-pass filtering technique for spatial and temporal domain should be standardized, including the PIV evaluation algorithm. The advanced technique of comparison between the measured results and computer simulation will be needed. The spatial and temporal frequency analysis would be necessary. The wavelet analysis or advanced POD analysis may be applicable.

ACKNOWLEDGMENTS

The present project is being partly supported by JSPS Grant-in-Aid for Scientific Research, No. 14205031, for three years since April in 2002. The author is grateful to group members. And they have developed wide fields of application using the present dynamic PIV system.

REFERENCES

[1] Hayami H, Okamoto K, Aramaki S, Kobayashi T, Development of a New Dynamic PIV System, Proc. 7th Int Symp of Fluid Control, Measurement and Visualization, 2003, 1-6.

[2] Hayami H, Okamoto K, Aramaki S, Kobayashi T, Development of Dynamic PIV System for Transient Analysis, Proc. 5th Int. Symp. on Particle Image Velocimetry, 2003, Paper 3212, 1-5.

[3] Okamoto K, Ota J, Sugii Y, High Speed PIV Transient Velocity Measurement, SEIKEN Symposium 33, 2002 167-194.

[4] Kaehler C, Significance of Dynamic Evaluation of Time Resolved PIV Images for Complex Flow Investigations, Proc. International Workshop on Dynamic PIV, 2004.
[5] Sugii Y, Nishio S, Okuno T, Okamoto K, A Highly Accurate Iterative PIV Technique Using a Gradient Method, Measurement Science Technology, 11, 2000, 1666.
[6] Bi, WT, Okamoto, K, Madarame H, POD analysis on Dynamic PIV, Proc. ASME FED Summer Meeting, 2003.
[7] Nishino K and Takahashi T, High-speed PIV applied to a submerged circular impinging jet, Proc. 5th International Symposium on Particle Image Velocimetry, paper No.3217, 2003.
[8] Nishino K and Takahashi T, Dynamic Behaviors of Circular Impinging Jet, Proc. International Workshop on Dynamic PIV, 2004.
[9] Oishi M, Oshima M, Kobayashi T, PIV Measurement of Flow in the Modeled Artery Using High Speed Camera, Proc. ASV7, 2003.
[10] Oishi M, Oshima M, Kobayashi T, Saga T, Dynamic PIV Measurement of Flow Instability in the Multi-Curved Pipe, International Workshop on Dynamic PIV, 2004.
[11] Zama Y, Kawahashi M, Hirahara H, Ooasa T, Tominaga S, Nagakubo T, Hayami H, Aramaki S, Three-Dimensional Measurements of Multi-Gas-Jets Flow Issuing From a Gas Turbine Nozzle with Multiple Holes, Proc. 5th Int. Symp. on Particle Image Velocimetry, 2003, Paper 3130, 1-6.
[12] Zama Y, Kawahashi M, Dynamic Stereo PIV for Multi-Hole Gas Jet Flow, International Workshop on Dynamic PIV, 2004.
[13] Hori T, Sakakibara J, Aramaki S, Hayami H, Scanning Stereo-PIV for 3D Velocity Measurement, Proc. 5th Int. Symp. on Particle Image Velocimetry, 2003, Paper 3109, 1-10.
[14] Sakakibara J, Hori T, High Speed Scanning Stereoscopic PIV for 3D Vorticity Measurement, Proc. International Workshop on Dynamic PIV, 2004.
[15] Okamoto K, Ikeda K, Murata S, Dynamic Holographic PIV, Proc. International Workshop on Dynamic PIV, 2004.

INTERACTION AND DISINTEGRATION OF LIQUID SHEETS FROM COAXIAL ATOMIZERS

B.N. Raghunandan
Department of Aerospace Engineering
Indian Institute of Science, Bangalore – 560012, India

ABSTRACT: Fluidic interaction of coaxial liquid sheets are encountered in liquid bipropellant rockets and gas turbine combustors employing dual orifice injectors. The liquid atomization process in such devices is preceded and governed by the interaction of the two sheets emanating by a central and a concentric annular orifice. This process, especially with varying flow rates, is associated with many interesting physical phenomena such as entrainment, coalescence, hysteresis and periodic oscillations which also cause significant changes in the final spray characteristics. The dynamics of the contact point acted upon by forces of inertia, cavity pressure and surface tension is of critical importance to describe all the experimental observations.

1. INTRODUCTION:

Coaxial exit configuration of injectors of liquid bipropellant rockets is known to cause efficient mixing and atomization of fuel and oxidizer and hence is identified with good combustion efficiency. Similar jet interactions are encountered in gas-turbine combustors where duplex or dual-orifice injectors are employed mainly to meet the demand of high turn-down ratio as well as good starting characteristics. The two liquid streams from the core and the annular orifices emerge as swirling, conical liquid sheets which meet within a short distance from the injector face and produce a combined spray. The interaction and coalescence of the two liquid sheets are not only associated with very fascinating physical phenomena but also of practical importance in terms of eventual spray characteristics and hence the combustor performance. As a two-phase system the pressure differences across the sheets and surface-tension also come into play along with the inertia and viscous forces to produce a rather complex interaction and disintegration machanics.

A large number of studies have been reported on jet interaction with many variations like the interaction of a jet with an adjacent surface, interaction of dual and multiple jets, turbulent interaction of concentric jets in the absence or presence of swirl effect, interaction of an annular air jet on a central liquid jet and so on [1,4]. Entrainment effect is the dominant theme in most of these studies. For instance in the jet-jet interaction dealing with gaseous jets, the jets merge at a short distance from the exit plane by bending under a mutual influence and behave like a single jet down stream. Considerable interest has been shown in recent years on the influence jet interaction on the spray characteristics of coaxial atomizers [5 – 7] . In their work on liquid jet disintegration, Mayer and Krulle [5] state that liquid jet turbulence is responsible for the initiation of wave patterns, whereas the flowing ambient gas is responsible for the eventual atomization of the liquid jet. While even an unswirled air flow is said to cause strong disturbances over the liquid sheet, swirling effect seems to generate stronger recirculatory motion and hence cause rapid disintegration of a liquid jet [6,7].

The fluid dynamic interactions of jets from a liquid – liquid coaxial atomizer could be quite different from those observed in liquid – gas coaxial atomizers. Although a few studies [8-10] on the liquid – liquid jet interactions have been reported, none has described features such as hysteresis, drastic variations of jet dimensions and the consequent drop-size distributions. The present author and his group [11 – 12] have investigated the fluid dynamic interactions of liquid sheets in the context of injectors of gas – turbine and liquid propellant rocket and have confirmed that the two liquid conical jets influence each other's spray characteristics like the spray cone angle and disintegration distance even before they merge to become a single hollow cone. It is also demonstrated that the merging and separation of liquid sheets as the flow rates are varied exhibit hysteresis and the transition from one state to other which has been described quantitatively in terms of the dynamics of the contact point. The present work provides an overview of these investigations highlighting the principal features of coaxial liquid jet interaction.

2. EXPERIMENTAL ARRANGEMENTS

Experiments are carried out in a standard spray test rig using a coaxial atomizer assembly shown schematically in Fig. 1 with water as the experimental liquid with known properties such as density = 998 kg / m^3, surface tension, = 0.0728 N / m, and viscosity, = 0.001003 Ns/m^2. The orifice exit diameter, d for the inner (primary) and outer (secondary) atomizers are 1.5 mm and 5 mm respectively. Swirl motion is imparted to the sheets by forcing the liquid to flow through double start helical paths of rectangular cross section of width, w and depth, h made on the periphery of the swirler body of diameter, D_s placed upstream of the orifice section as seen in Fig. 1. The atomizer constant, $K = 2wh / D_s d$ for the inner atomizer is kept constant as 0.0625 and is varied for the outer atomizer in the range 0.007 to 0.013.

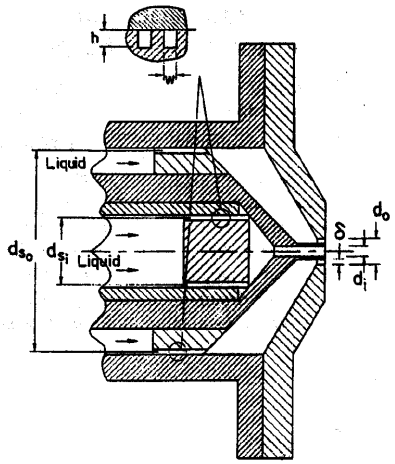

Fig. 1 : Geometric features of the coaxial injector

Evidently higher K values imply relatively lower swirling intensity and hence poorer atomization. The images of liquid sheets are captures using a 16mm cine photographic camera with varying frame speed and analyzed using a cine film motion analyzer. Drop-size measurement is made with a laser diffraction instrument.

3. RESULTS AND DISCUSSION:

Generation of a conical liquid sheet from the central circular orifice necessarily requires a swirl component in the stream, but it is not essential for the annular jet. Nevertheless, swirling is introduced to the outer sheet too keeping with the practices in atomizer design. A number of preliminary experiments have been conducted to characterize the individual jets before embarking on a study of their interaction. Measurables that characterize the sheets are the cone angle, sheet break-up length and the mean drop-size following complete disintegration.

3.1 Influence of the Inner Jet On the Outer Jet:

Depending on the flow rate or the jet Reynolds number (Re_o) the outer liquid sheet may either converge to acquire a tulip bulb shaped contour or a divergent conical contour. At a given outer flow condition, the inner flow rate (or Re_i) is slowly increased and the observations are made on the outer jet contour and other characteristics. Figures 2 and 3 show the shrinking of the sheet width and reduction of break-up length for the two distinct cases of outer jet contour. It is to be noted that with increasing Re_i, the inner sheet expands because of the swirl effect and the outer sheet contracts. This effect prevails even when the sheets do not come in contact with each other as seen in the figures. The presence of an inner jet in the core augments the entrainment of air between the two liquid sheets and thereby reduces the static pressure. This ejector effect results in a

pressure difference across the sheets making them move towards each other and eventually leading to merging of two jets. It has been observed that the break-up length of the jet also tends to decrease under mutual influence [12].

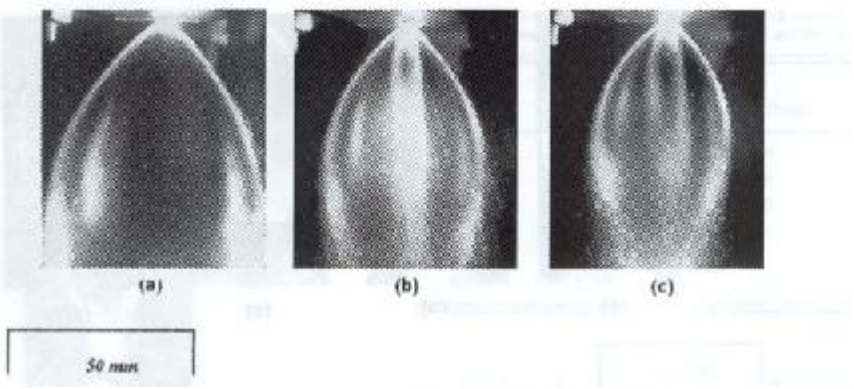

Fig. 2: Influence of the inner jet on the outer sheet at high Re_o.
(a) $Re_i = 0$, (b) $Re_i = 10{,}790$ and (c) $Re_i = 12{,}200$

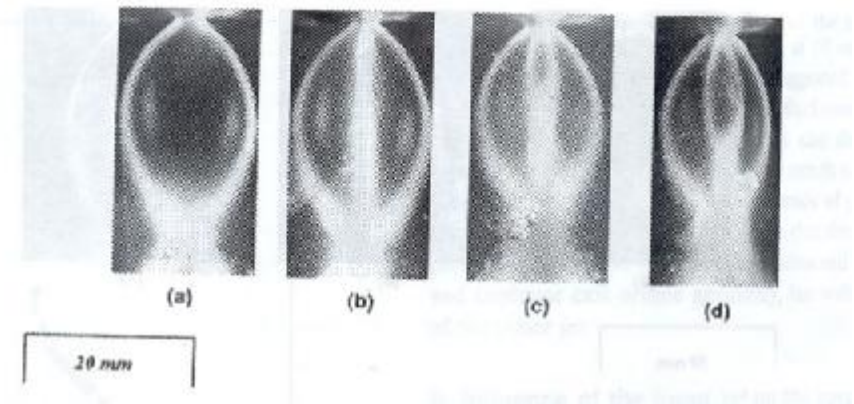

Fig.3: A tulip shaped outer sheet under the influence of inner jet.
(a) $Re_i = 0$, (b) $Re_i = 3575$ and (c) $Re_i = 6325$ and (d) $Re_i = 8172$

3.2 Hysteresis in Merging and Separation Process of the Coaxial Liquid Sheets:

As mentioned in the previous section, a gradual increase in the inner jet flow rate at a constant outer flow conditions will lead to coalescence or merging of the two sheets. Indeed, the merging of the liquid sheets is accomplished through a well-behaved, rapid transition process which is accompanied by a dramatic change in the outer jet configuration. Any further increase in Re_i retains the sheets in the merged state and the final jet behaves like a conical sheet from a simple pressure swirl atomizer. A reduction in flow rate from the merged state as would be demanded by a throttling requirement does make the sheets separate or peel-off from each other, but at a condition quite distinct from the merging condition described above. This is pictorially shown in Fig. 4.

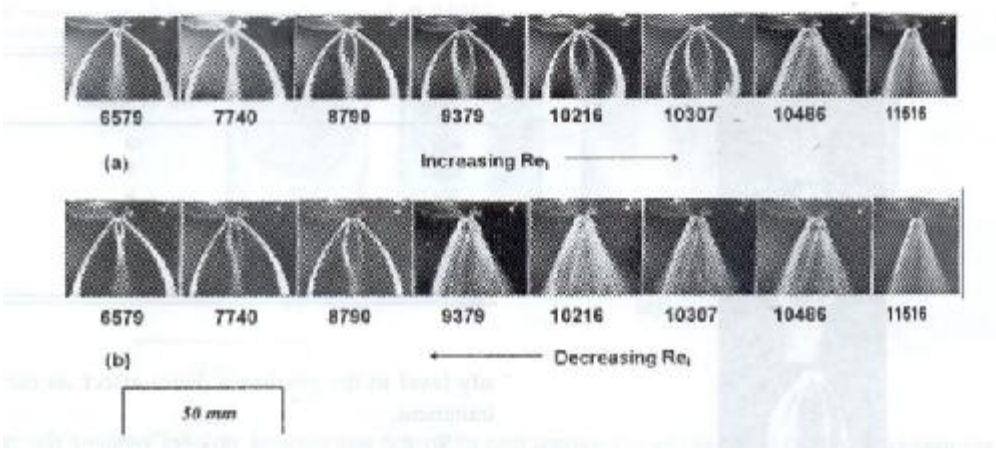

Fig.4 : A photographic sequence showing hysteresis in merging and separation of Coaxial sheets.

The series of images in Fig. 4 corresponds to a particular Re_o with varying Re_i. With increasing Re_i, as presented in Fig. 4 (a), the merging occurs in the seventh frame. One may also notice the drastic change that occurs from the sixth to the seventh frame for a marginal change in Re_i. In Fig. 4(b), the corresponding jet configurations are shown for the same flow conditions as in Fig. 4(a) but for decreasing Re_i. The separation, of the liquid sheets from the merged state is seen in the third frame which corresponds to Re_i distinctly lower from that for merging. The range of Re_i between these two merging and separation conditions represents the zone of hysteresis in which the final state of the jet depends on the direction in which the flow rates are changed.

Experimental runs of this type for different Re_o, lead to a plot of hysteresis shown in Fig. 5. Thus in a liquid – liquid coaxial swirl atomizer, the jets could be in any of the three regimes indicated in the figure. In regime I, which occurs at high Re_i, the jets are always in a merged state with liquid sheet contact point close to the orifice and form a single conical jet. In contrast, the jets are always in separated state in regime II at low Re_i. In regime III, the jets assume any one of the two stable states depending on how the corresponding flow conditions are attained.

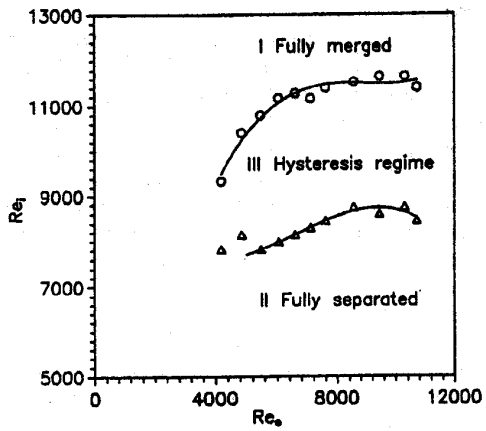

Fig.5 : Boundaries of hysteresis regime in terms of Reynolds numbers of the core and annular jets.

The hysteresis can be simplistically explained in terms of distinctly different suction pressure in the annular cavity formed by the two sheets between the orifice exit and the contact point for the two cases of increasing and decreasing Re_i. However, one cannot rule out the importance of surface tension effects that dominate the movement of the contact point once the merging occurs. In fact, some of the recent results with several different injector configurations show that the data collapse to a single curve when plotted in terms of Weber number thus indicating the importance of surface tension.

3.3 Influence of Hysteresis on Final Spray Characteristics:

Variation of spray width at a reference distance of 10 mm from the injector face(SW_{10}) as recommended in literature may be used to describe the changes in jet contour in the hysteresis loop. Figure 6 shows the spray width normalized by the mean diameter of the annular orifice ( ) as a function of Re_i. Remarkably different widths and the sharp transitions at boundaries of merging and separation are clearly evident.

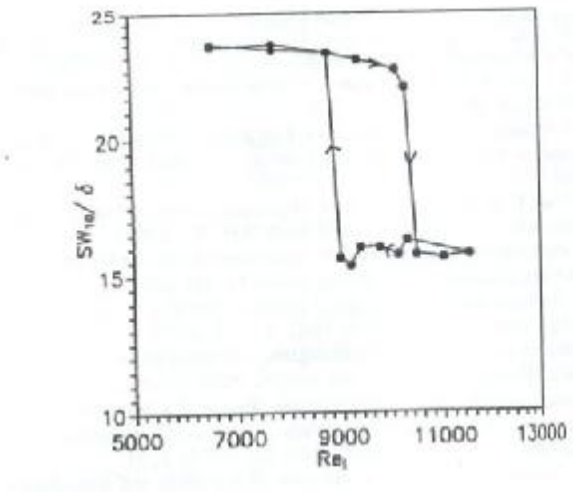

Fig.6 : Jet width changes in the hysteresis loop.

Measurements have been carried out to get the sauter mean diameter (SMD) variations of the spray in regime III around the hysteresis loop using a Malvern particle sizer. The variation of SMD in regime III with changes in the inner jet flow condition is shown in Fig. 7 for two different atomizer configurations with constant Re_o. The plot reveals that there is a significant increase in SMD value due to merging of the liquid sheets. In the merged state, the mixing of two sprays would lead to an increase in droplet sizes of the combined spray along the branch "R" in Fig. 7. This is perhaps due to an effectively thicker sheet before disintegration and also droplet coalescence and collisions in the resultant dense spray zone. It is observed that the presence of the inner jet in the core of the outer jet in the separated mode (branch "F") causes little change in the distribution or SMD from that corresponding to the total absence of the inner jet.

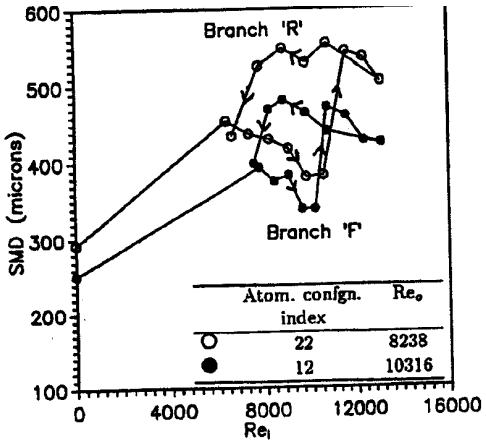

Fig. 7 : Influence of hysteresis on mean drop size of the global spray

3.4 Periodic Merging and Separation at Low Flow Rate Conditions:

High speed cine photography has been made use of to capture the events leading to transition at the two boundaries shown in Fig. 5. At high flow rates (or high Re_o), the merging process involves the contact point moving rapidly towards the atomizer exit. A reverse process of rapid downstream movement of contact point occurs during separation of merged sheets. It has been possible to record these movements and quantify the time required for transition.

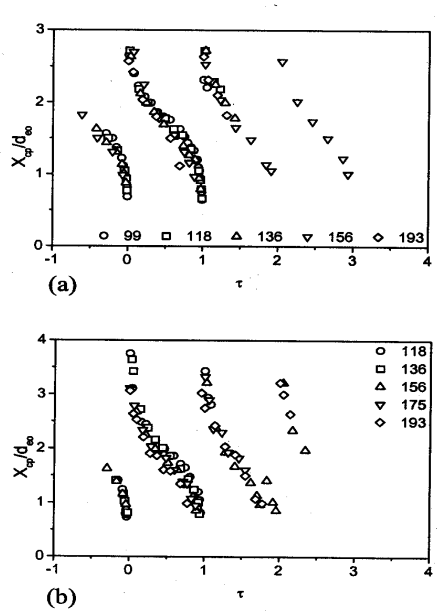

Fig 8 : Movement of the contact point during the oscillatory merging and separation at Low flow rates (a) We_o= 15.3 (b) We_o= 17.9

A more interesting phenomenon occurs at low Re_o. The merged liquid sheets exhibit a periodic separation and remerging process. This occurs indefinitely without any change in the flow conditions of inner and outer liquid sheets. The movement of contact point is represented in Fig. 8 in terms of normalized distance from the orifice as a function of , a time parameter nondimensionalized by the period of this oscillatory phenomenon. A remarkable regularity of the movement for several low Weber number is evident in the figure. A direct outcome of this process is a periodic variation of mixed spray characteristics like spray dispersion, mean dropsize and so on at a low frequency of the order of 3 – 10 Hz.

4. CONCLUDING REMARKS:

The interaction of coaxial liquid sheets followed by disintegration into a spray involves several interesting mechanistic elements which have been captured by flow visualization techniques. Entrainment effects leading to variation in sheet contours, hysteresis in merging and separation processes and the consequent changes in mean drop size of the final spray and the movements of the sheet contact point during transition are some of the interesting features which are also of serious consequence to practical sprays.

ACKNOWLEDGEMENTS

The author wishes to acknowledge his student, Dr. D. Sivakumar from whose doctoral thesis this material is drawn and Mr. S. Nagaraj whose skills in still and cine photography enabled capturing of intricate details.

REFERENCES

[1] Chigier NA and Beer JM, "The flow region near the nozzle in double concentric jets," Trans ASME J. Basic Eng. **89**, 443 (1964).
[2] Miller DR and Comings EW, "Force-momentum fields in a dual-jet flow," J. Fluid Mech. **7**, 237 (1960).
[3] Villermaux E and Hopfinger EJ, "Periodically arranged co-flowing jets," J. Fluid Mech. **263**, 63 (1994).
[4] Ribeiro MM and Whitelaw JH, "Coaxial jets with and without swirl," J. Fluid Mech. **96**, 769 (1980)
[5] Mayer W and Krulle G, "Rocket engine coaxial injector liquid/gas interface flow phenomena," J. Propul. Power **11**, 513 (1995)
[6] Hopfinger EJ and Lasheras JC, "Explosive breakup of a liquid jet by a swirling coaxial gas jet," Phys. Fluids **8**, 1686 (1996)
[7] Mansour A and Chigier N, "Disintegration of liquid sheets,"Phys. Fluids **A 2**, 706 (1990)
[8] Amagni K and Arai M, "Disintegration process of a liquid jet injected from a coaxial dual nozzle,"Proceedings of the ICLASS – 94, edited by A. J. Jule and C. Dumouchel (Begell House Inc., 1994).p 71
[9] Hautman DJ, "Spray characterization of liquid/gas and liquid/liquid coaxial injectors with the center liquid swirled," Report No. UTRC89-31, UTRC, 1990.
[10] Ramamurthi K and John Tharakan T, "Experimental study of liquid sheets formed in coaxial swirl injectors," J. Propul. Power **11**, 1103 (1995).
[11] Sivakumar D and Raghunandan BN, "Jet interaction in liquid-liquid coaxial injectors," Trans ASME J. Fluid Eng. **118**, 329 (1990).
[12] Sivakumar D and Raghunandan BN, " Hysteretic interaction of conical liquid sheets from coaxial atomizers," Phy Fluids, 1998, **10(6)**, 1384-1897

Proceedings of The Tenth Asian Congress of Fluid Mechanics
17–21 May 2004, Peradeniya, Sri Lanka

TEMPORAL STATISTICS: A NEW CHALLENGE TO LARGE EDDY SIMULATION

Guowe He
Chinese Academy of Sciences, Beijing , China

Editor's Note: Paper not received in time for publication.

Proceedings of the Tenth Asian Congress of Fluid Mechanics
17-21 May 2004, Peradeniya, Sri Lanka

APPLICATION OF STOCHASTIC METHODS IN THE STUDY OF FLUID FLOW, SOLUTE TRANSPORT, AND MULTIPHASE FLUID BEHAVIOR IN HETEROGENEOUS POROUS MEDIA

T.H. Illangasekare and S. Saenton
Center for Experimental Study of Subsurface Environmental Processes (CESEP), Division of Environmental Science and Engineering, Colorado School of Mines, Golden Colorado 80401 U.S.A.

ABSTRACT: Deterministic prediction of fluid flow and contaminant migration using numerical models in naturally heterogeneous subsurface media is generally infeasible due to many factors. Primary among these is it is cost prohibitive to fully characterize the relevant properties governing flow and transport at appropriate scales to use as model inputs. Model input parameters such as hydraulic conductivity, porosity and dispersivity cannot be fully defined using limited spatially distributed measurements or observations. Use of interpolated values as inputs results in significant uncertainty in model predictions. This uncertainty inherent in these predictions has to be taken into consideration in evaluating potential future risks to ecological and human health due to groundwater contamination. Introduction of stochastic methods to subsurface hydrology has helped regulators, subsurface hydrologists and engineers to identify such uncertainty in predictions that has implications in the use of models as management and decision tools. Stochastic approaches assign probability distributions to model input parameters and provide a means to deal with these parameter and prediction uncertainties. Successful application of stochastic methods to groundwater-related field problems has been reported. This paper discusses how stochastic theory is used in hydrogeologic studies primarily in the context of contaminant transport and migration of immiscible liquids (e.g. chlorinated solvents and petroleum waste) in the subsurface. Stochastic theory and geostatistical methods as applied to heterogeneous porous media are briefly discussed, and recent intermediate-scale laboratory studies and numerical modeling investigations are presented. The methods and tools developed in this research are currently being evaluated and validated for field applications at government owned and industrial waste sites.

1. INTRODUCTION

Groundwater constitutes an important component of domestic, industrial and agricultural water supply both in US and rest of the world. Increasing demand placed on limited supplies has made it imperative to protect scarce groundwater resources from pollution from industrial waste and agricultural chemicals. Numerical models with the capability to predict the fate and transport of these chemicals are useful as tools for management and remediation design. The accuracy of model predictions depends on the accuracy of the input parameters that characterize the flow and transport processes. Basic input parameters such as hydraulic conductivity and porosity vary in space. It is generally infeasible and cost-prohibitive to conduct detailed site characterization to obtain exact information to define this spatial variability. Hence, the distributed values of these parameters have to be inferred from observations or measurements made at discrete set of sampling points or observations that in general are sparsely distributed over the aquifer. The uncertainty associated with these undefined input parameters results in model prediction errors. Hence, it is necessary to incorporate parameter uncertainty into models to increase confidence in predictions. Stochastic approaches that assign probability distributions to these parameters provide a means to deal with these parameter and prediction uncertainties. These approaches proposed in the early eighties[1,2] have increasingly been accepted in subsurface studies. Stochastic-based modeling provides a *possible range* of solutions (e.g. contaminant concentrations and hydraulic heads) to groundwater-related problems accounting for uncertainty associated with flow and transport parameters.

Successful application of stochastic methods in field-scale modeling of flows and transport, and risk analysis has been reported in literature. This paper focuses on the application of stochastic methods, specifically based on geostatistical techniques in intermediate-scale laboratory studies involving fluid flow, multiphase flow in heterogeneous porous media. Controlled experiments in a laboratory allows for the study of the method more rigorously as the heterogeneity field can be defined accurately. First, the

theoretical background used in developing numerical models for flow and transport in porous media is presented. This will be followed by example problems through which the application of stochastic methods is presented.

2. THEORY AND BACKGROUND

2.1 Fluid Flow in Porous Media

A porous medium can be characterized by several physical parameters, such as porosity and hydraulic conductivity. Porosity (ϕ) is the ratio of the void space to the total volume of the medium. The hydraulic conductivity (K) is a function of both the porous medium and fluid properties. The hydraulic conductivity is related to the intrinsic permeability of the medium (k) and fluid properties through $K = k\rho g/\mu$, where ρ and μ are the fluid density and dynamic viscosity, respectively. Darcy's law incorporates this hydraulic conductivity to an expression that predicts fluid flux q when the gradient of the hydraulic head dh/dx is known: $q = -K(dh/dx)$. A generalized form of Darcy's equation for a system containing multiple fluids is given by:

$$\mathbf{q}_\alpha = -\frac{k_{r,\alpha}\mathbf{k_{ij}}}{\mu_\alpha}(\nabla p_\alpha - \rho_\alpha g \nabla z), \tag{1}$$

where $\mathbf{q}_\alpha$ is the flux for α phase, $\mathbf{k_{ij}}$ is permeability tensor, p_α is pressure of phase α, z is elevation, and k_r is relative permeability. The mass conservation (i.e. continuity) equation for multiphase fluid flow system is expressed as

$$-\vec{\nabla}\cdot(\rho_\alpha \mathbf{q}_\alpha) + Q_\alpha = \frac{\partial}{\partial t}(\phi \rho_\alpha S_\alpha), \tag{2}$$

where Q_α is source-sink term, and S_α is the saturation of the α phase which is the ratio between the volume of void occupied by α phase to the total void volume. Combining Darcy's equation with mass conservation, the generalized multiphase flow equation for incompressible fluids can be obtained as:

$$\vec{\nabla}\cdot\left[\frac{k_{r,\alpha}\mathbf{k_{ij}}}{\mu_\alpha}(\nabla p_\alpha - \rho_\alpha g \nabla z)\right] + Q_\alpha = \phi\frac{\partial S_\alpha}{\partial t} \tag{3}$$

The solution of the system of equation given by Eq. (3) requires additional constitutive models that relate permeability and capillary pressure to partial fluid saturations. A number of numerical models exist to solve this coupled, non-linear system of equations.

2.2 Contaminant Transport in Porous Media

The fate and transport of dissolved contaminants in groundwater can be described by the advection-dispersion-reaction equation:

$$\frac{\partial(\phi c)}{\partial t} = \vec{\nabla}\cdot(\mathbf{D_{ij}}\nabla c - \phi\bar{\mathbf{v}}_\mathbf{i} c) + \sum R_n \tag{4}$$

where $\mathbf{D_{ij}}$ is dispersion coefficient tensor, R_n is a reaction term, and $\bar{\mathbf{v}}_\mathbf{i}$ is the pore velocity which can be calculated from Darcy's law given as $\bar{\mathbf{v}}_\mathbf{i} = -\mathbf{K_{ij}}\nabla h/\phi$. Advection represents the movement of a contaminant with the flowing groundwater. Hydrodynamic dispersion on the other hand, involves both molecular diffusion and mechanical mixing. The latter is a result of local variations in velocity around some mean velocity of the flow as a result of soil heterogeneity. Laboratory investigations indicate that at the macroscopic scale, dispersion is a function of pore velocity and a factor called dispersivity. The dispersion of solutes in groundwater can occur not only in the direction of groundwater flow, but also lateral to the direction of flow. The last term in Eq. (4) represents the total mass loss or generation due to other physical, chemical and biological processes such as adsorption, biodegradation, and self decay (e.g. radionuclides).

2.3 Non-Aqueous Phase Liquids

Nonaqueous phase liquid (NAPLs) are chemicals that are slightly soluble in water (e.g. petroleum products, organic solvents and wood preservatives) that remains as a separate phase for long periods of time after a spill thus contributing soils and groundwater contamination. Migration of NAPLs in the subsurface is controlled by gravity, buoyancy, and capillary forces. Lighter-than-water NAPL (or LNAPL) such as gasoline and diesel fuels, after percolating downward through unsaturated zone, can float and move on top of water table. On the other hand, denser-than water NAPLs (or DNAPL) such as organic solvents and wood treatment compounds are able to migrate downward past water table and penetrate deep into the saturated zone. During migration, a fraction of the NAPL enters pore spaces by capillary forces and they are left behind in the soil as discontinuous blobs or ganglia. When free-phase DNAPL reaches impermeable layers during migration, it may 'pool' on top of interfaces resulting in high saturation entrapment zones. These entrapped NAPLs slowly dissolve into a flowing groundwater generating a downstream plumes generating risk at receptor locations such as wells, rivers and lakes.

The presence of NAPLs in aquifers impacts groundwater quality and remediation is challenging as it is difficult to locate and remove all of the entrapped NAPL mass. Although a number of NAPL removal technologies are currently being tested, there is mixed success in achieving cleanup goals. Uncertainty associated with achieving cleanup goals can be attributed largely to the inability to locate free-phase NAPL in heterogeneous subsurface.

2.4 Stochastic Methods

The flow and transport parameters that appeared in the equations governing equations (1)-(4), are generally measured or determined at only a few locations despite the fact that they are highly variable in space at all length scales (macroscopic to regional). A combination of sparsity of observations and measurement errors lead to uncertainty in the values of the formation properties and thus uncertainty of predictions using simulation models that solve the governing equations. The stochastic theory provides a method for evaluating these uncertainties using probability or related quantities such as statistical moments[3]. Material properties that define field heterogeneity are not completely random, but assumed to exhibit some correlation structure resulting from natural depositional processes that created the formation. This spatial correlation structure is defined using random space functions that are quantified using joint probability distributions or joint statistical moments.

A commonly used geostatistical approach used in stochastic formulations is to characterize the heterogeneity (in terms of permeability) of the aquifer by the first and second moments of a probability distribution function (pdf) which are referred to as mean, and variance/covariance, respectively. In modeling flow and transport, the hydraulic conductivity (K) introduces the greatest uncertainty as its value varies over a very wide range in aquifer materials. The uncertainty is not only associated with the measurement at a point but also with the uncertainty of the value at locations where it is not measured. The general approach used in developing the technique assumes that the log of K is normally distributed: $y = \ln K$. If n points in the aquifer are sampled, the estimate of the population mean is obtained from

$$\bar{y} = \frac{1}{n}\sum_{i=1}^{n} y_i \tag{5}$$

and the estimate of the variance is given by,

$$S_y^2 = \frac{1}{n}\sum_{i=1}^{n} (y_i - \bar{y})^2 \cdot \tag{6}$$

The pdf of the *ln K* distribution is defined by the mean and the variance. The variance measures the degree of heterogeneity of the aquifer. If the y_i is measured at a fixed set of points, and if it is necessary to estimate the value of y at other locations where measurements are not made, the mean and the standard deviation (square root of variance) can be used to provide the most likely estimate of the un-measured value. That is, the estimated value is the mean with an uncertainty that is normally distributed with a standard deviation equal to the standard deviation of the measurements. The lognormal variable K can be described by the following pdf,

$$f_K(K) = \frac{1}{K\sigma\sqrt{2\pi}} \exp\left[-\frac{(\ln K - \mu)^2}{2\sigma^2}\right] \tag{7}$$

where μ and σ^2 are the mean and variance of $\ln K$.

A stochastic random process is a collection of random variables that vary continuously in space (or time). The stochastic process K(x) can be thought of as a collection (or ensemble) of realizations with the same statistical properties. A realization is single observation of the spatial variation of the process. If the pdf of a spatially random process is invariant under shifts of the spatial origin, then it is considered to be second-order stationary and commonly referred to as "stationary." The importance of stationarity is the suggestion of underlying repetitive structure of the parameter. A physical description of the stationarity is captured in the covariance function that is given as,

$$\text{cov}[y_1 - y_2] = E[\{y_1 - \mu_1\}\{y_2 - \mu_2\}] \tag{8}$$

whose estimator is,

$$R_y(r) = \frac{1}{N-r}\sum_{i=1}^{n}(y_{i+r} - \bar{y})(y_i - \bar{y}) \tag{9}$$

where *N-r* term is the number of pairs separated by a distance *r*. The covariance is independent of the origin but depends on the distance between observations. The heterogeneous aquifers can be represented as a spatially correlated random field. The descriptive statistics of the random field include the mean and variance of $\ln K$ and correlation length. Spatial correlation increases the probability that a given point will have permeability similar to that of a neighboring point. *K* values at points that are separated by a short distance are more likely to be similar and as the separation becomes larger they are less likely to be similar. The correlation scale is a characteristic length of the average spatial persistence of $\ln K$. A geoststistical tool for the quantification of spatial structure is the experimental semivariogram (referred to as variogram). Variograms are useful in identifying the underlying spatial structure and identifying trends. The classical experimental semivaraigram estimator $\gamma(h)$, for Gaussian data is calculated as,

$$\gamma(h) = \frac{1}{2n(h)}\sum_{i=1}^{n(h)}[y(x_i + h) - y(x_i)]^2 \tag{10}$$

where *h* is the separation distance between observations and *n(h)* is the number of data pairs separated by distance *h*. If the $\ln K$ data are statistically homogeneous (stationary), then the variogram is dependent only on *h*. A theoretical exponential model can be fitted to the variogram as,

$$\gamma(h) = \sigma^2(1 - e^{-h/\lambda}) \tag{11}$$

The model parameter λ is the correlation length that is a measure of the distance over which the *y* values are correlated. Fig. 1 shows a plot of the theoretical and a measured semivariagram from a laboratory sand packing experiment conducted by Compos[4]. For a small separation distance *h*, the correlation between sample pairs is high and $\gamma(h)$ is small. When distance between points increases, the correlation decreases (i.e. $\gamma(h)$ increases) and variogram will eventually reach a plateau.

In general, two approaches of stochastic formulations are used. In the first approach, uncertainty analysis is incorporated directly into the model to define the predictions in terms of their mean and covariance. The second approach uses a Monte Carlo-type analysis involving a series of realizations of the uncertain parameters[1]. In our laboratory experiments and numerical studies, the second approach was used. Several realizations of hydraulic conductivity field (more correctly, log *K*) were generated and used for further analyses.

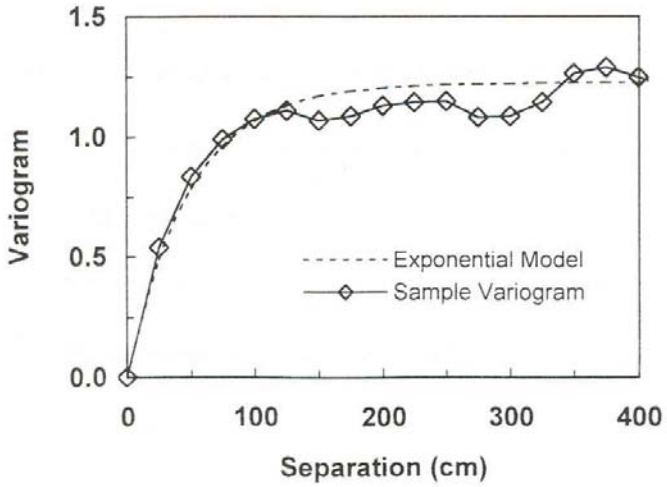

Fig. 1: Typical semivariogram for stationary process[4].

3. EXPERIMENTAL STUDIES

3.1 Chemical Transport in Heterogeneous Test Aquifer

Experimental investigations of the transport of dissolved species in heterogeneous porous media were conducted in both 2- and 3-dimensional test systems. Tracer experiments in either laboratory or a field site are used to characterize transport parameters of the porous medium. Barth et al.[5,6] conducted conservative tracer experiments in a 2-D heterogeneous porous medium (Fig. 2). Analyses based on stochastic theory and tracers test data led to the development of a guideline for selecting conservative tracer's density as a function of local hydraulic gradient which is related to $\ln K$ and $\sigma^2_{\ln K}$.

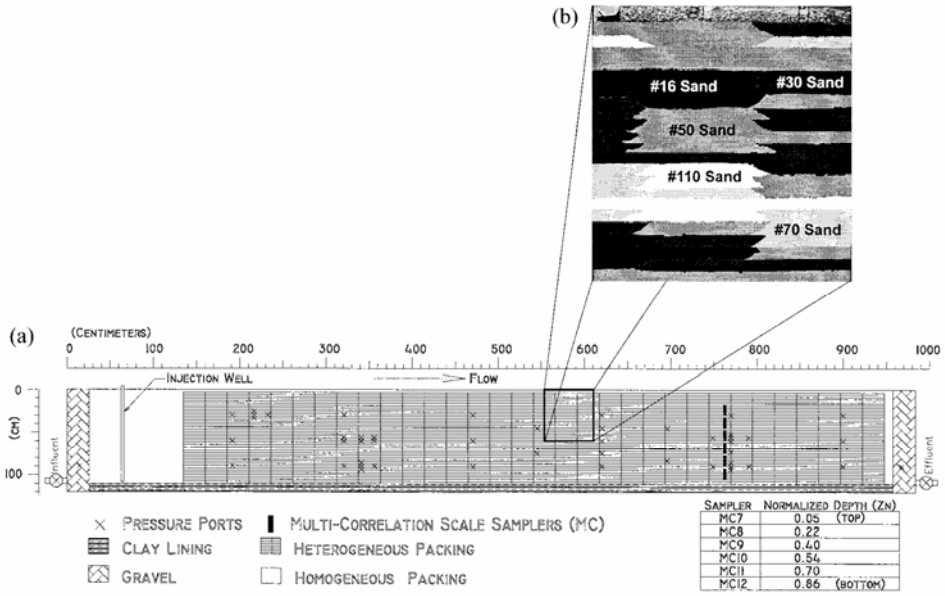

Fig. 2: Two-dimension, intermediate-scale test tank[5,6].

Garcia et al.[7] conducted conservative and reactive tracers test in a physically and chemically heterogeneous 3-D test aquifer (see Fig. 3). The inherent heterogeneity of the aquifer usually obscures the interpretation of field tracer tests. The goal of these experiments was to correctly evaluate transport parameters (specifically, scale-dependent dispersivity and retardation factor) of a heterogeneous aquifer that are required in the solution of advection-dispersion equation, Eq. (4). Guidelines for accurate data interpretation and determination of transport parameters from field tracers test were developed. Monte Carlo-type of simulations of tracer tests were conducted to validate and support the findings.

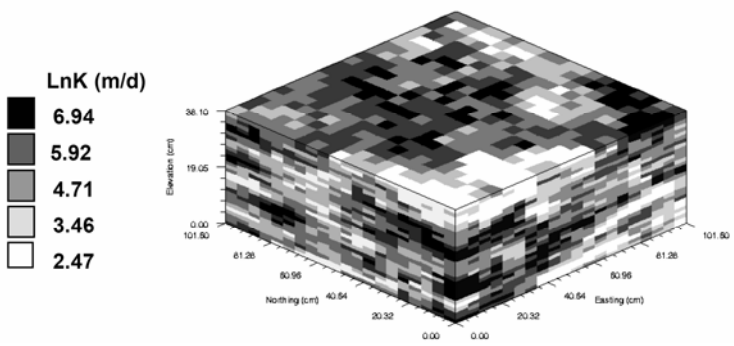

Fig. 3: Three-dimensional view of the distribution of the sand in the test aquifer[7].

3.2 Multiphase Flow

Locating free-phase NAPL in heterogeneous subsurface is a challenging task. Estimation of highly variable saturation distribution of NAPL in the heterogeneous is required in remediation design and risk assessment. Prediction of how NAPL migrates and becomes entrapped in heterogeneous formations is of practical interest. The migration as well as the entrapment architecture (i.e. NAPL distribution) depends strongly on porous media characteristics. Compos[4] conducted DNAPL (trichloroethane) spreading experiments in five different permeability fields (i.e. realizations based on the same formation statistics such as mean, variance and anisotropic correlation lengths). Fig. 4 show the 2-D test cell containing a random field (packed using five different types of silica sands). It was found that NAPL entrapment architectures has spatial structure that can be defined using statistical parameters.

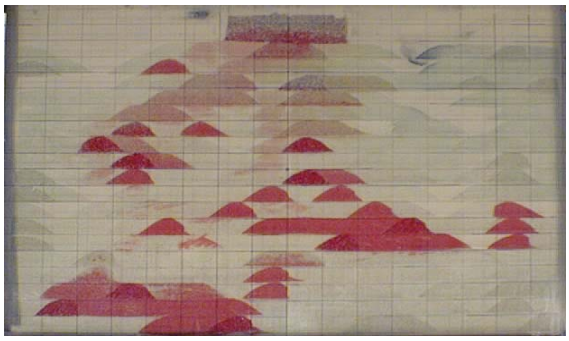

Fig. 4: Entrapment architecture created from a spill in a spatially correlated random filed[4].

4. NUMERICAL MODELING INVESTIGATIONS

4.1 Effect of Heterogeneity on Entrapment Architecture of NAPL

As mentioned earlier, soil heterogeneity can cause complex entrapment architecture of spilled NAPLs. Saenton[8] conducted numerical experiments (80 realizations) using multiphase flow code[9] to generate DNAPL source zone entrapment architecture. Fig. 5 shows two examples of final entrapment architecture created through model simulations. Even though all realizations have the same statistics (average ln *K* and variance), entrapment architecture can be significantly different. Fig. 6 shows the centers of mass for all realizations are in general clustered at the mid-depth of the spill zone, and at the center in *x*-direction. Their spreading however varies significantly in *z*-direction. In some realizations the source zones contain only high saturation pools whereas, in some cases, PCE dispersed throughout the source zone in a residual form. This observation is used in the development of up-scaling methods for mass transfer from the entrapped DNAPLs[10].

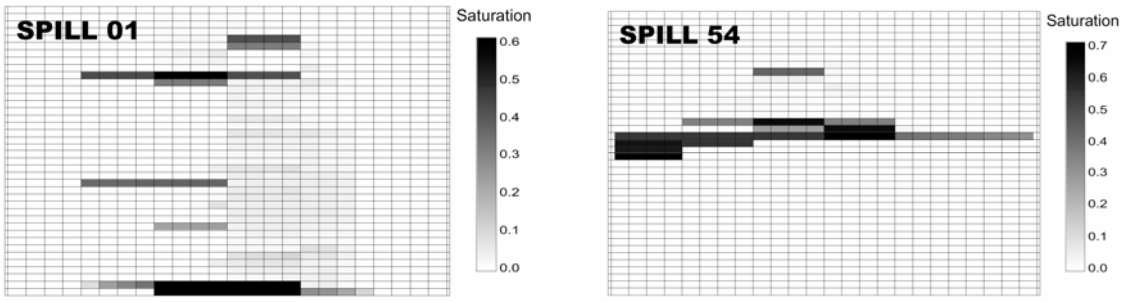

Fig. 5: Example of PCE (tetrachloroethene) spills in realizations #1 and #54.

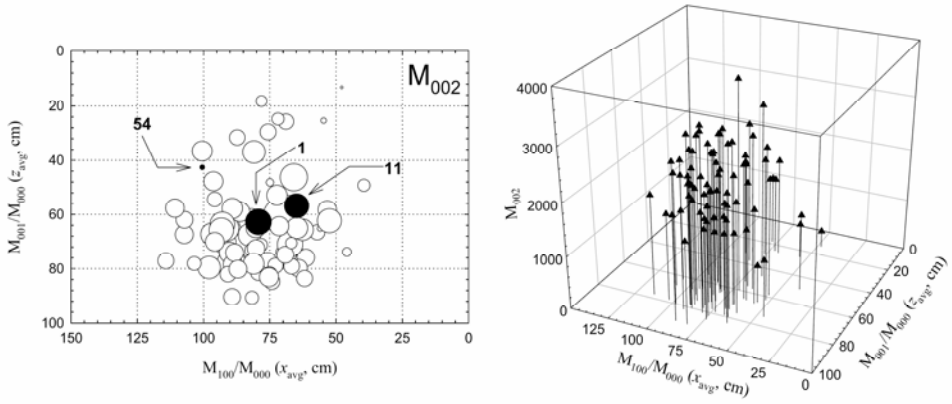

Fig. 6: Second moment (or mass spreading) in *z* direction for all 80 spills.

4.2 Effect of Entrapment Architecture on Clean-Up Efficiency

The remediation of entrapped NAPL in source zone containing different entrapment architecture can result in varying clean-up efficiency. Saenton et al.[11] conducted a set of Monte Carlo-type numerical simulations of surfactant-enhanced NAPL remediation from the heterogeneous source zone based on 10 NAPL spills in intermediate-scale test tank. The heterogeneity was created using stochastically generated random field (Fig. 1). Fig. 7 shows the problem domain (test tank) and the simulation results. Gray lines, in Fig. 7 (right), indicate the complete delivery where the injected surfactant solution is assumed to fully

sweep the entrapped NAPL. However, when by-passing due to heterogeneity is taken in to account the surfactant does not reach all the entrapped NAPL, thus affecting cleanup time significantly. A large variability in the removal efficiency was observed die to the uncertainty in delivery associated with heterogeneity.

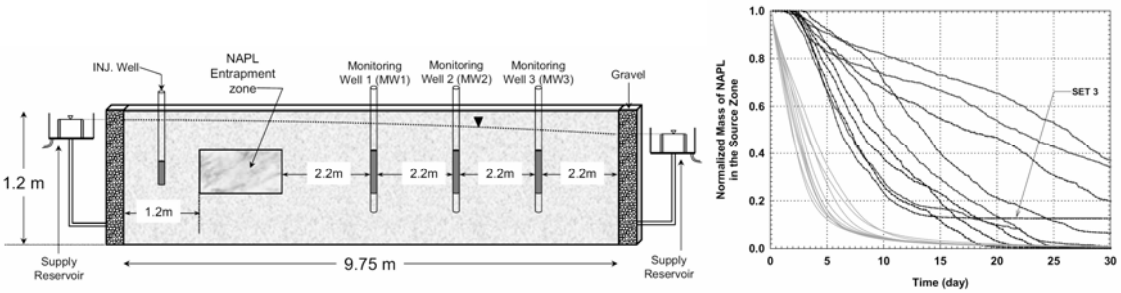

Fig. 7: (Left) Intermediate-scale test tank, and (Right) Normalized mass depletion as a function of time for surfactant-enhanced dissolution (incomplete delivery). The gray lines represent complete delivery cases.

5. DISCUSSION AND CONCLUSIONS

From the above numerical and laboratory study examples, it can be seen that stochastic method as applied to hydrogeology problems can be used as a tool to evaluate uncertainty in prediction and remediation efficiency. In any type of risk assessment, uncertainty associated with parameters describing the system must always be considered. When the heterogeneity cannot be fully characterized, there exists significant uncertainty regarding the achievement of cleanup goals and the reduction of risk.

ACKNOWLEDGMENTS

The work presented here is based on research by Dr. Gilbert Barth, Dr. Daniel Fernandez Garcia, Mr. Ron Compos. The authors gratefully acknowledge their contributions. Financial support for this research was provided by the Army Research Office and Strategic Environmental Research and Development Program (SERDP) administered by the US Department of Defense.

REFERENCES

[1] Gelhar, L.W., Axness, C.L. 1983. Three-dimensional stochastic analysis of macrodispersion in aquifers. Water Resource Research. 19(1): 161-180.

[2] Neuman, S.P., Winter, C.L., Newman, C.M. 1987. Stochastic theory of field-scale fickian dispersion in anisotropic porous media. Water Resource Research. 23(3): 453-466.

[3] Zhang, D., 2002. Stochastic Methods for Flow in Porous Media, Academic Press, pp 350.

[4] Compos, R. 1998. Hydraulic conductivity distribution in a DNAPL entrapped zone in a spatially correlated random field. M.S. Thesis, University of Colorado.

[5] Barth, G.R., Illangasekare, T.H., Hill, M.C., Rajaram, H. 2001. A new tracer-density criterion for heterogeneous porous media. Water Resources Research, 37(1): 21-31.

[6] Barth, G.R., Illangasekare, T.H., Hill, M.C., Rajaram, H. 2001. Predictive modeling of flow and transport in a two-dimensional intermediate-scale, heterogeneous porous medium. Water Resources Research, 37(10): 2503-2512.

[7] Fernàndez-Garcia, D. Illangasekare, T.H., Rajaram, H. 2004. Conservative and sorptive forced-gradient and uniform flow tracer tests in a three-dimensional laboratory test aquifer. Water Resources Research. In revision.

[8] Saenton, S. Prediction of mass flux from DNAPL source zone with complex entrapment architecture: Model development, experimental investigation, and up-scaling. PhD Thesis, Colorado School of Mines.

[9] Delshad, M. Pope, G.A., Sepehrnoori, K. 1996. A compositional simulator for modeling surfactant enhanced aquifer remediation. Journal of Contaminant Hydrology, 23(1-2): 303-327.

[10] Saenton, S., Illangasekare, T.H. 2004. Up-scaling of mass transfer of entrapped DNAPLs in heterogeneous aquifers: Theoretical development, numerical implementation, and experimental validation. In preparation.

[11] Saenton, S., Illangasekare, T.H., Soga, K., Saba, T.A. 2002. Effect of source zone heterogeneity on surfactant enhanced NAPL dissolution and resulting remediation endpoints. Journal of Contaminant Hydrology, 53(1-2): 27-44.

AN EXPERIMENTAL AND NUMERICAL STUDY OF INTERACTION OF FIVE SUPERSONIC JETS

Ramjee, V[†]., Sasi Kumar, S[†].and Sundararajan, T.[$]
[†] Department of Applied Mechanics, IIT Madras, Chennai 36, India.
[$] Department of Mechanical Engineering, IIT Madras, Chennai 36, India.

Abstract
The spreading features of five supersonic jets, in the configuration of one central bigger jet surrounded by four smaller equi-distant peripheral jets have been studied numerically and experimentally for different Mach numbers and spacing ratios. The computed values are in good agreement with the experimental results. The jets maintain their individual behavior up to twelve diameters and thereafter they merge to form a single jet. For smaller spacing ratio and lower Mach number, the merger occurs earlier compared to higher spacing ratio and larger Mach number. The mass flux rate increases with the spacing ratio**.**

Introduction
Supersonic jets are encountered in a variety of engineering applications such as high speed civil transport aircrafts, rockets, V/STOL aircrafts, strap-on boosters etc. Raghunathan and Reid [1] studied the problem of multiple supersonic jets for five and nine nozzles with one central jet. The main objective was to achieve noise reduction. Vijayakumar et al. [2] studied numerically the spreading features of five supersonic jets at M = 1.0 to 1.5 and spacing ratios of 1.25, 1.67 and 2.08. The five jets coalesce to form a single jet at about ten diameters. Manohar [3] had studied numerically five supersonic jets with and without canting (cant angle = 4°) in external flow at M = 1.5, 2.0 and 2.5 and spacing ratios of 1.5, 2.0, 2.5, where the spacing is the distance between the centres of the central bigger jet and that of any smaller peripheral jets.
In this paper, the experimental studies are done on five jets of unequal diameters. The five supersonic jets corresponding to exit Mach number of M = 1.25 and various nozzle spacings of S/D = 2.1, 2.5 and 3.0 have been studied. Here, S is the spacing between the centres of the central jet and the peripheral jets and D is the throat diameter of the bigger jet. Numerical studies are also done using the FLUENT code. A numerical study of five equal jets is done for comparison.

Experimental Details
A reciprocating compressor, with a discharge of 14.6 m^3/min, driven by a 3-phase 150 hp electric motor is used to charge two storage tanks of 10 m^3 capacity each (Fig. 1). The compressed air from the storage tank flows into the settling chamber through a pressure-regulating valve. A three-dimensional traverse, with 6 degrees of freedom and motorised in axial and radial directions is used to locate the pitot tube (OD = 2.5 mm and ID = 1.5 mm) to measure the stagnation pressure in the jet. A pressure transducer connected with the data acquisition system is used to record the pressure values in the computer. The static pressure is measured using a cone type probe with two holes in the periphery at a distance of 15 mm from the tip. Axisymmetric convergent-divergent Laval nozzles were fabricated for M = 1.25, 1.5, 1.75 and 2.0. The throat diameter of the bigger jet (D) is 12mm and that of the smaller jet (d) is 6 mm. Depending on the area ratio, the exit diameter of the nozzles has been varied for the particular Mach number. Different spacer plates are used for the three spacing ratios namely S/D = 2.1, 2.5 and 3.0. The measurements are made at X/D = 2, 4, 6, 8, 10, 15, 20, 25, 30 and 35. Precautions were taken during the experimental runs to achieve proper results. The experiments were conducted twice to ensure repeatability and average was taken in each case. The error involved in maintaining pressure is around ±1.7 %. The machining accuracy of the nozzle is ±1 %.

Numerical Procedure
In cartesian tensor notation, the equations of continuity, momentum, energy and equation of state for a compressible viscous flow are given by:

$$\frac{\partial}{\partial x_i}\left(\rho U_i\right) = 0 \tag{1}$$

$$\frac{\partial}{\partial x_j}\left(\rho U_i U_j\right) = -\frac{\partial p}{\partial x_i} + \frac{\partial \tau_{ij}}{\partial x_j} \tag{2}$$

where,

$$\tau_{ij} = \left[\mu\left(\frac{\partial U_i}{\partial x_j} + \frac{\partial U_j}{\partial x_i}\right)\right] - \frac{2}{3}\mu\frac{\partial U_l}{\partial x_l}\delta_{ij} \tag{3}$$

$$\frac{\partial}{\partial x_i}\left(\rho U_i h\right) = \frac{\partial}{\partial x_i}\left(k\frac{\partial T}{\partial x_i}\right) + U_i\frac{\partial p}{\partial x_i} + \tau_{ij}\frac{\partial U_i}{\partial x_j} \tag{4}$$

$$p = \rho RT \tag{5}$$

The local viscosity μ is taken as a sum of the laminar and turbulent viscosities. The turbulent viscosity, in turn, is calculated from the k-ε model. The above set of equations has been solved using FLUENT code.

A five-jet flow configuration consisting of a central larger jet surrounded by four smaller jets arranged on the periphery of a circle at equal interval is shown in Fig. 2a. In this problem, there is four-fold symmetry and hence only one-quarter geometry is chosen for simulation as shown in Fig 2b. In order to test the grid independence of the predicted solutions, grids with 62x31x31. 72x41x41, 92x31x31 nodes have been employed. The prediction of Mach number along the axis of the central jet is shown in Fig. 3. The centreline predictions does not show marked variations for the range of grids employed, even though the total number of nodes employed in each grid is significantly different. Hence, a grid of 72x41x41 has been used for all further computations. Grid points are clustered in such a way that the steep gradients existing near the nozzle exit and jet boundaries are captured accurately.

RESULTS AND DISCUSSIONS

(a) Total Pressure Profiles

The total pressure profiles at various axial locations are shown, for nozzle exit Mach number equal to 1.25 and S/D = 2.1 in Fig 4. Here both the experimental and numerical results are shown and they are in good agreement except in the near field (i.e. up to X/D = 4) where complex shock structures are encountered. The deviations can be due to the interference of the probe with the shock cells in the near field and the almost laminar behaviour of the supersonic jets in the initial zone is not captured well by the turbulence model used in the numerical simulations. However, in the far-field region the comparison between experimental data and theoretical predictions is reasonably good.

It is seen from the profiles that the smaller jets in the periphery decay at faster rate compared to that of the central jet. This is due to the fact that the decay distance scales approximately linearly with the jet diameter. Also, the smaller jets bend more towards the larger jet due to entrainment and merge to form a single jet, which adds to their rates of decay. The merger distance for the present five-jet configurations is of the order of X/D = 12. In all the cases studied, it was observed that a low sub-atmospheric pressure value occurs in the region between jets due to the combined entrainment of the entrapped fluid by all the five jets. However, since the entrainment associated with this configuration is symmetric, the axis of the final combined jet is not altered and is the same as the axis of the central jet.

(b) Mass Flow Rate Profiles

The variation of dimensionless mass flow rate with axial distance is shown in Fig. 5 for various nozzle spacings. The mass flow rate at the inlet plane is used as the scale for normalisation. It is evident from the figure that the mass flow rate increases with increase in inter-nozzle spacing. In the near field, there is no

marked variation in the mass entrained for the different spacings considered. However, a significant increase occurs in the entrainment for larger spacings and intermediate axial locations. The above trend is in conformity with the argument that bending of the jets towards each other induces greater lateral velocities and hence larger level of entrainment. Figure 6 shows the effect of Mach number on the mass flow rate for S/D = 2.1. The mass flow rate decreases with the increase in exit Mach number.

Fig.7 shows the Mach Number profiles at M = 1.5, S/D = 2.1 and p_o/p_a = 3.67 for the five equal jets and the unequal jets. The smaller peripheral jets decay faster than the equal jets because of lower momentum and the merger distance is lower. The Reynolds shear stress is shown in Fig.8 for different locations at M = 1.5, S/D =2.5 and p_o/p_a = 3.67. the shear stress decays faster for the unequal jets.

CONCLUSIONS

- The five jets maintain their individual characteristics up to a distance of X/D = 12. Thereafter, they coalesce to form a single jet. The merger distance increases for larger spacing ratio and higher Mach Number.
- All the jets entrain ambient air from the inter-jet region and hence a sub-atmospheric region is formed which causes the jet bending. The jets spread with distance due to entrainment of fluid from the ambient atmosphere, resulting in a net increase in mass flow rate.
- The peripheral jets bend towards the central jet and mix to form a single jet at around X/D = 12. The five equal jets merge at a larger distance.
- The axis of the central larger jet is not affected by the presence of surrounding smaller jets because of symmetric entrainment of ambient fluid.
- The spacing between the jets is seen to affect the mixing of five-jets significantly. With increase in spacing, the jet bending increases. The merger distance also increases, which can be attributed to the jets retaining their individual characteristics for a larger axial distance due to the wider separation between the jets.
- As the spacing increases for a given Mach number, the mass flow rate increases. For a given spacing, the mass flow rate decreases with the increase in exit Mach number.

REFERENCES

[1] Raghunathan, S. and Reid ,I.M., "A Study of Multiple Jets", AIAA Journal, Vol.19, No.1, pp.124-127, 1981.

[2] Vijayakumar, S., Sundararajan, T., Ramjee, V., "A Computational Study of Equal and Unequal Supersonic Jets", Journal of Aero. Society of India, Vol.54, pp.1-15, 2002.

[3] Manohar, I., "Experimental and Numerical Study of Incompressible Jet Flows", MS thesis, IIT Madras, June 2001 and FMFP Conference, 2003, NIT Suratkal.

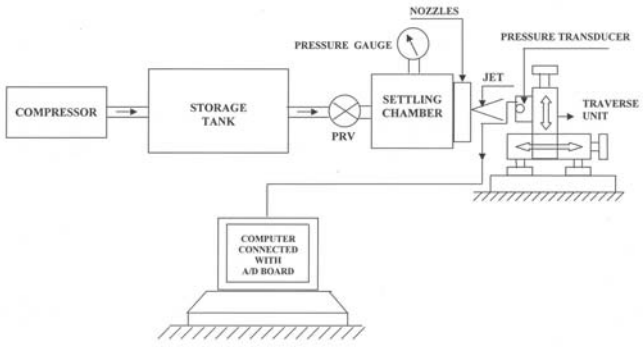

Fig 1 Schematic of the experimental set up

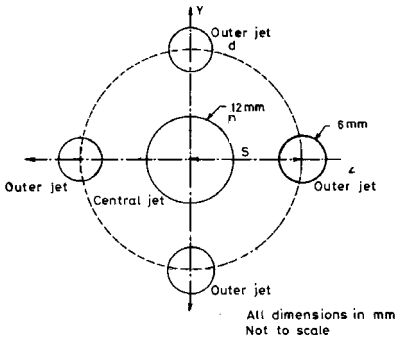

Fig 2a Total Geometry

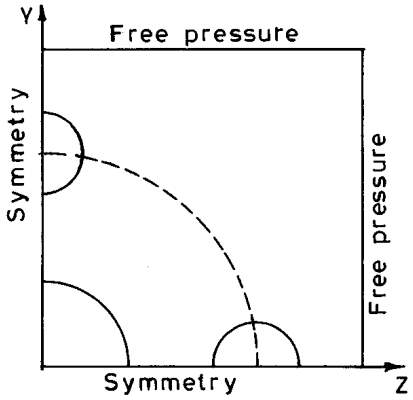

Fig 2b Quarter Geometry

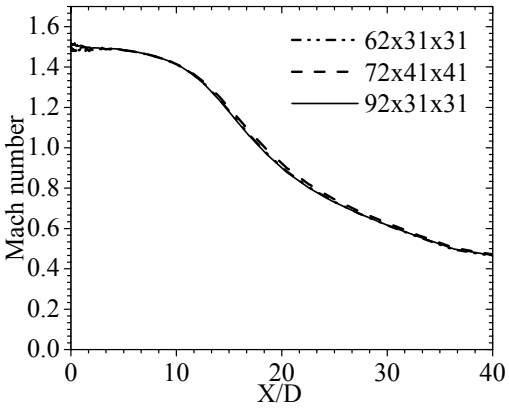

Fig 3 Grid independence study

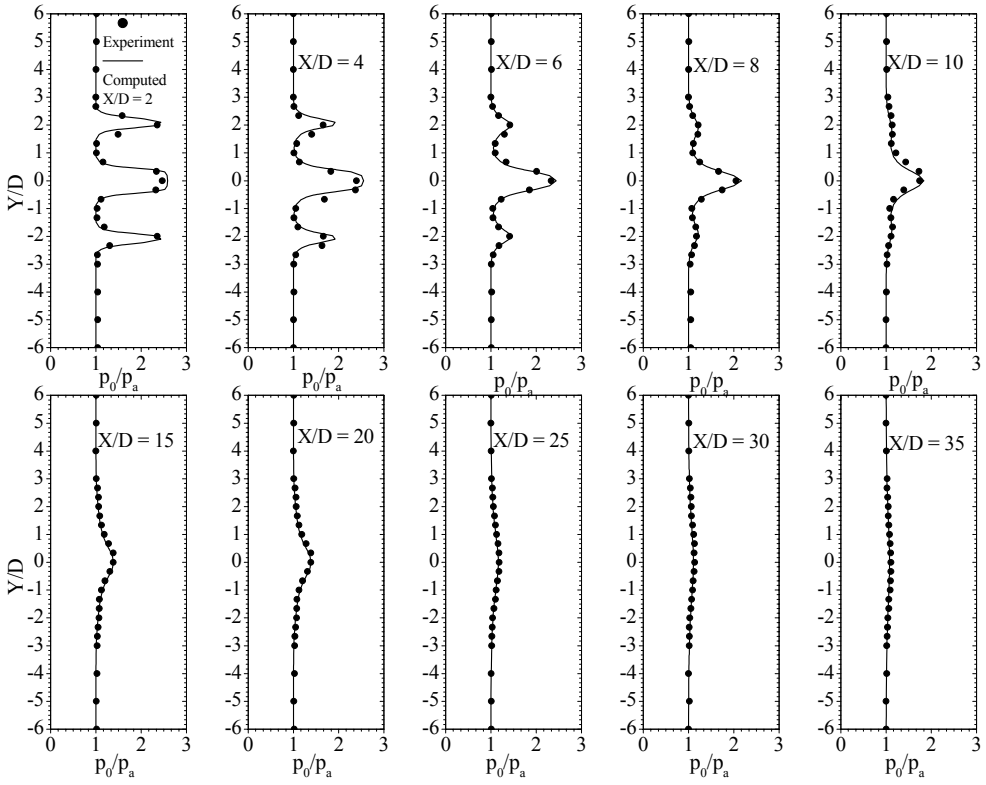

Fig 4 Total pressure profiles for M=1.25,S/D=2.1 and p_o/p_a=2.591

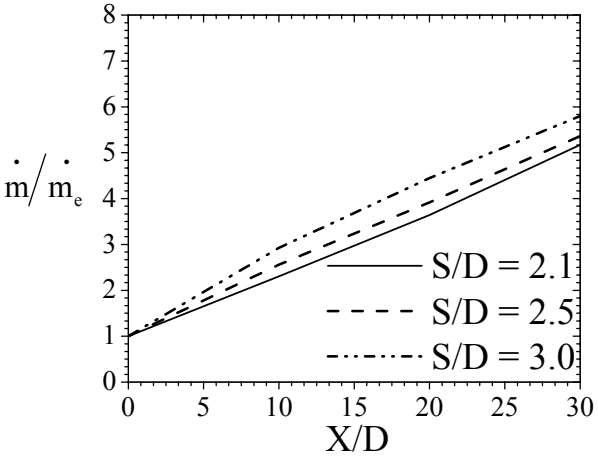

Fig. 5 Comparison of mass flow rate for various nozzle spacings (at M = 1.25 and p_0/p_a = 2.591)

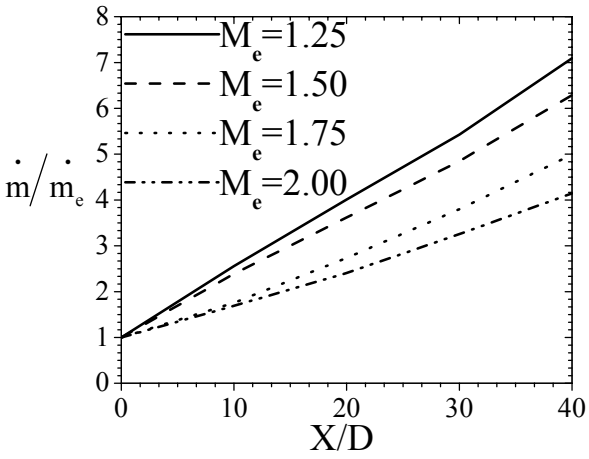

Fig. 6 Comparison of mass flow rate for various Mach numbers (at S/D = 2.1)

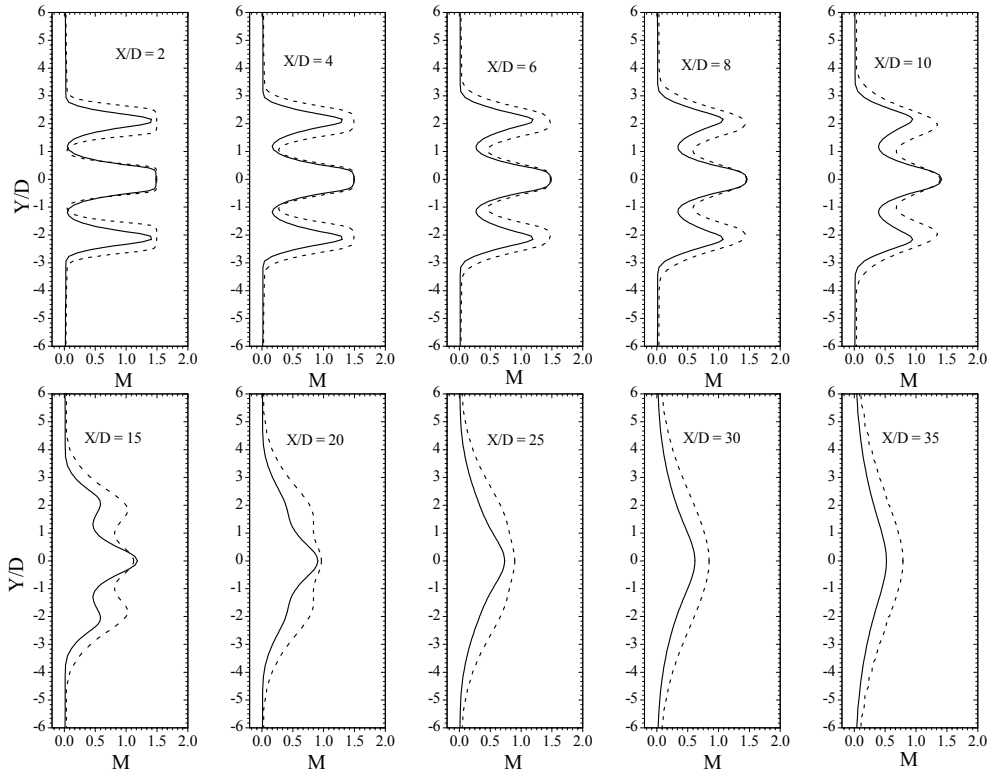

Fig 7 Comparison of Mach number profiles for five equal and five unequal jets at M=1.5, S/D=2.1 and p_o/p_a=3.67 (_____ unequal jet; ---------- equal jet)

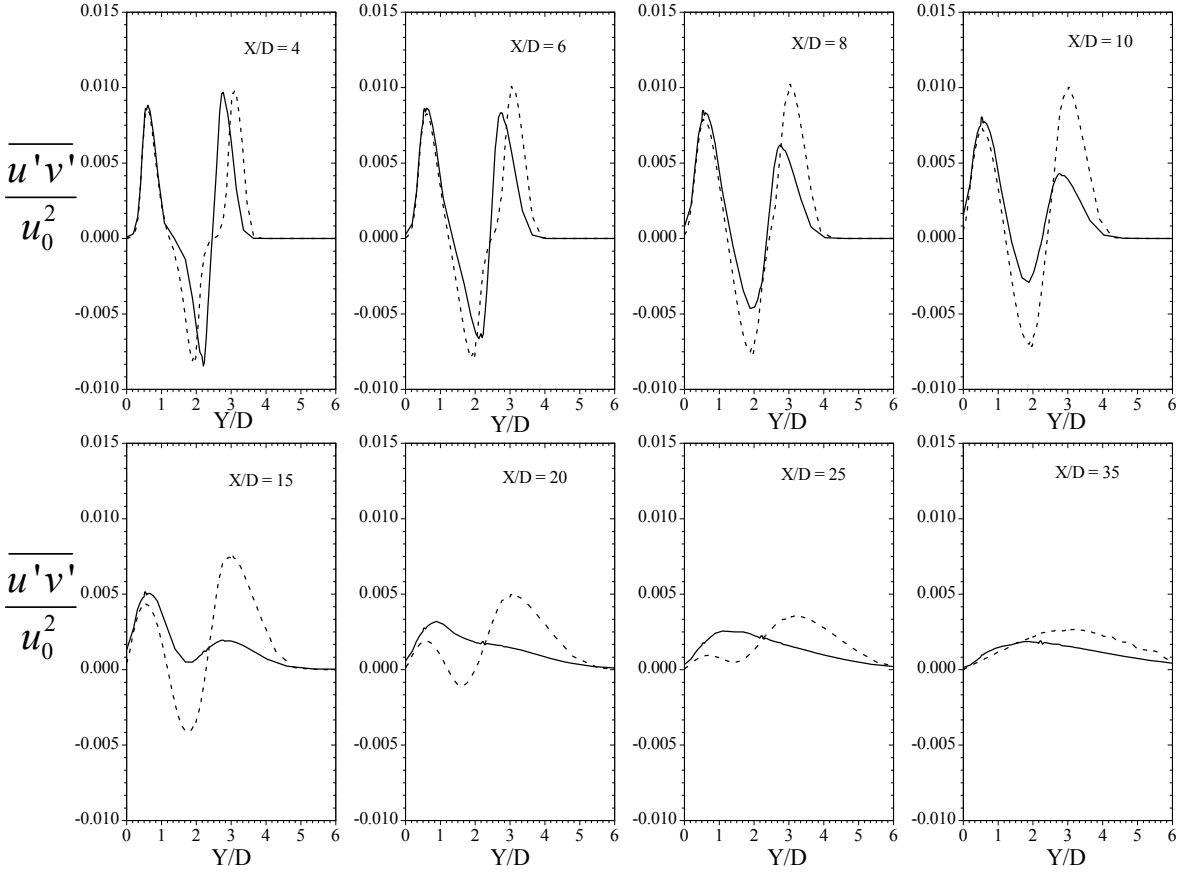

Fig 8 comparison of Reynolds shear stress for five unequal and equal jets at M=1.5, S/D=2.5 and p_o/p_a=3.67 (_____ unequal jet ; ---------- equal jet)

Proceedings of the Tenth Asian Congress of Fluid Mechanics
17-21 May 2004, Peradeniya, Sri Lanka

ALLEVIATION OF SUPERSONIC FLOW INSTABILITY OF A PITOT INTAKE

L. Merchant and S. Ahmed
National Aerospace Laboratories, Bangalore 560 017, INDIA

ABSTRACT: This paper presents the results of the tests carried out on a pitot intake with emphasis on alleviating the flow instability seen at moderate mass flow conditions. Ingestion of large low energy flow at the entry of intake was observed to be the triggering factor for the initiation of flow instability. An attempt is made to delay the occurrence of instability, by reducing the amount of low energy viscous flow at the entry through modifications in the splitter plate by extending its length and also providing perforations. Results obtained with this modifications are discussed and compared with those obtained with varying diverter heights.

1. INTRODUCTION:

Flow instability in the form of shock wave oscillations colloquially known as *buzz* has been observed on intakes operating at supersonic speeds. Studies have been made to investigate the cause for the occurrence of such type of flow instability (refs. 1 to 4). These studies have indicated the criteria for onset of flow instability and the mechanism leading to flow instability is far from understood. Recent studies on a wing shielded twin intake configuration having a bifurcated Y duct have shown the presence of such a flow instability at moderate mass flow conditions at supersonic speeds (ref. 5). As the flow field around the intake is complex due to the diverter system, the splitter plate and shielding of the intake by the wing, the mechanism leading to the onset of flow instability is not known. To understand this mechanism an experimental study is initiated through building block experiments. This study enables to simulate the various geometrical parameters of intake such as diverter, splitter plate etc., in a modular way and study the effect of these parameters on the flow through the intake including the onset of flow instability. To start with, studies were undertaken on an isolated pitot intake of constant area duct and later extended to a variable area duct with different diverter heights. These studies have suggested that the ingestion of low energy flow of size comparable to the intake entry height leads to formation of aerodynamic throat and later resulting in the flow instability in the form of shock wave oscillations (refs.6 and 7). It is therefore possible to alleviate the flow instability by delaying the formation of aerodynamic throat i.e., by reducing the amount of low energy flow ingestion into the duct. To investigate this concept, a study is undertaken on a pitot intake having a splitter plate and diverter of fixed height and the reduction of low energy flow ingestion at the entry is attempted through modifications in the splitter plate geometry by extending its length and providing perforation. Results of this study are presented and discussed in this paper.

2. EXPERIMENTAL DETAILS:

The pitot intake model tested consists of a 'D'type convergent-divergent duct, splitter plate and diverter system (fig.1). The model is of modular construction and made out fiber- reinforced plastic. The duct has entry radius of 35.8mm(h) and throat of 0.97h located at 0.79h and has a total length of about 14h. The splitter plate has a length of 25mm (0.7h) with a ramp angle of about 6.9degree. The model is mounted at height of 0.6 (= boundary layer thickness) from the floor of the tunnel. The diverter system includes top and bottom diverters at 20 degree inclination and a rectangular passage to bleed the boundary layer flow. Flow through the duct was varied by varying the exit area of the duct through a semi conical plug located near the exit of the duct. The tests were carried out in the 0.3 m trisonic wind tunnel at a freestream Mach number of 1.6. A specially fabricated nozzle block was located downstream of the

nozzle to mount the pitot intake model. During the tests, the operating pressure of the tunnel was kept at about 2 bar which corresponds to unit Reynolds number of 30 million per meter. Static pressure ports of diameter 1.06mm were located along the centerline of the inner duct surface, splitter plate and mounting block.

Tests were conducted for different exit area (Ae) of the duct ranging from 0 to 1.0 Amax (Amax is the maximum area of the duct at the exit). Surface pressures were measured using ESP scanners of range ±10psid. Static and total pressure of the freestream was measured using Druck transducers of range ±10psid and 0 to 50psid respectively. Surface flow ahead of the intake was photographed using tri color schlieren technique and surface flow patterns were obtained using a mixture of oleic acid, titanium dioxide and vacuum pump oil. The unsteadiness of the flow was detected by mounting KULITE transducers of 3.2mm diameter and of range ±10psid in flush with the surface - upstream and downstream of the duct entry. The boundary layer of the flow was measured at the location of the intake entry (in the absence of the model) using a pitot rake and the thickness of the boundary layer (δ) was observed to be about 16mm. Tests were also conducted for two configurations of the splitter plate viz., extended length and perforated splitter plate.

3. RESULTS AND DISCUSSION

Results of the tests are shown in figures 2 to 5. The surface pressures (p) measured are non dimensionalized with respect the free stream total pressure (P_0). The unsteady pressures measured are represented in the form of power spectrum to identify the frequency of shock wave oscillations.

Flow field ahead of intake is characterized by a nearly normal shock wave on the splitter plate (fig.2a). Flow behind the shock wave is subsonic and reaches sonic condition at the throat and expands to supersonic conditions in the divergent portion of the duct (fig.2b). As the exit area is reduced supersonic flow terminates through the shockwave and this shock wave moves upstream inside the duct with further decrease in the exit area. At the exit area of 0.75, flow becomes subsonic through out the duct; and flow ahead of intake is able to communicate the pressure downstream and any decrease in exit area beyond 0.75 results in mass flow decreasing through the duct causing the intake shock to move upstream due to the spillage of flow. Further decrease in the exit area, in this case beyond exit area of 0.51, makes the shock to travel beyond the leading edge of the splitter plate and interact with the approaching boundary layer. This leads to local thickening of boundary layer resulting in ingestion of more low energy viscous flow at the entry. The continuous feeding of increasing low energy flow into the duct with decrease in exit area leads to formation of aerodynamic throat upstream of geometric throat, causing the flow confined between the ingested viscous flow and the inner surface of the duct to accelerate to sonic condition at aerodynamic throat. As the flow downstream is subsonic, the flow has to decelerate through a shock wave and as the shock could not be established in the convergent portion, it gets expelled out of the duct along with some mass of fluid leading to triggering of flow instability in the form of shock wave oscillations at the frequency of about 110Hz (figs.2c and 2d). Details of the mechanism causing flow instability are explained in ref 7.

To alleviate the flow instability, the low energy flow ingested at the entry has to be decreased or the local area near the location of aerodynamic throat has to be increased to provide relief to the confined flow. In this paper different techniques adopted to minimize the ingestion of low energy flow at the duct entry are presented. There are several approaches to reduce the low energy flow entering the duct. The ingestion of low energy viscous flow can be reduced by delaying the interaction of shock wave with the approaching boundary layer by keeping the shock travel on the splitter plate or by bleeding a part of low energy flow from the upper surface of splitter plate. The entry of low energy flow can also be minimized by controlling the scale of interaction by varying the boundary layer profile on the splitter plate by using different diverter heights. All these approaches are attempted and the results obtained from these methods are briefed below:

For a given exit area, location of the shock wave ahead of the duct / on the splitter plate is a function of the internal geometry of the duct and also the amount of mass flow through the duct. It has been observed that the shock starts moving upstream in sub critical operation and for an increase in spillage of mass flow due to increase in the backpressure, the travel of the shock wave on the splitter plate can be maintained by increasing its length. To ascertain the effect of splitter plate length on the flow entering the duct, the plate length ahead of intake was increased by about 25 percent of its original length. This is achieved by moving the entry of duct downstream to keep the same condition of the boundary layer at the leading edge of the plate (fig.3a). Results show travel of the shock wave on extended splitter plate length up to exit area of 0.47 compared to 0.53 on the earlier splitter plate length (fig.3b). Once the shock wave travels over the leading edge of splitter plate, its interaction leads to ingestion of higher amount of viscous flow into the entry and no unsteadiness in the flow can be seen (fig. 3c). Further decrease of exit area to 0.36 leads to flow instability in the form of shock wave oscillations around 110Hz (figs. 3d and 3e); similar to flow filed seen at exit area of 0.47 for the case of an un-extended splitter plate. A decrease of 11 percent exit area in the onset of unsteadiness can be seen due to this modification.

Surface pressures distribution show lower pressures beneath the splitter plate as compared to the pressures on its top surface (fig.4a). As the pressure difference is significant, it is proposed to bleed a part of the flow on the top surface to the region underneath the splitter plate there by minimizing the ingestion of low energy flow at the entry of duct. To start with a perforation of 2 percent open area in the form of distributed circular holes of 1mm diameter over the area of splitter plate was chosen (fig.4b). Perforations make strength of the shock weaker due to communication of pressures and also permit a part of the mass flow spilled at the entry to bleed. Results show occurrence of flow instability at higher exit area of 0.51 Amax contrary to what is expected (Fig.4c). From the schlieren picture, it can be seen that the boundary layer has slightly thickened compared to the unmodified splitter plate (fig.2a). Probably, the spilled flow bled through the perforations could have propagated upstream making the boundary layer thicker and also when the shock travels into the boundary layer, the increase in pressure behind the shock causes the flow underneath the plate to move up resulting in more ingestion of flow into the entry causing the flow instability to occur at higher exit area. More experiments are needed in particular to the quantification of velocity field to get an understanding of perforation effects.

Tests have been carried out earlier with a diverter height h/ of 0.4 and 0.8 (ref.7). Data obtained from the present tests of 0.6 is compared to get the effect of varying diverter heights on the occurrence of flow instability. As the diverter height is increased higher amount of low energy flow due to approaching boundary layer is bled through the diverter. The amount of low energy flow ingested into the duct due to interaction is also a function of the boundary layer velocity profile at the location of interaction and the diverter height. From the analysis of flow field pictures it was observed that the amount of separated flow ingested reduces with increasing diverter height resulting in the delay in the occurrence of flow instability. A summarized plot of the delay in occurrence of flow instability obtained through different approaches is shown in fig. 5. For a given diverter height, a considerable delay in flow instability can be obtained for the case of extended splitter plate while for the perforated configuration, the occurrence is at higher exit area. Significant delay is observed with the increase in diverter height. This study has demonstrated that the delay in occurrence of flow instability can be obtained by reducing the ingestion of low energy flow at the entry of duct either by delaying the interaction by keeping the shock travel on the splitter plate at lower mass flow conditions or by controlling the scale of ingestion by varying the diverter height.

3.1 Uncertainty in the Measured Data:

The pressure transducers, and the pressure scanners were calibrated using a DRUCK pressure calibrator. The calibration showed errors, which were typically of the order of ± 0.1 per cent of the full scale. Taking into account, the calibration error and repeatability of data, the estimated uncertainty in

pressure ratio p/ P_0 is less than ± 0.0015. The maximum uncertainty in the measurement of exit area Ae/Amax is with in ± 0.01.

4. CONCLUSIONS

Experimental studies have been carried out at a free stream Mach number of 1.6 on a pitot intake having a convergent-divergent shape with diverter and splitter plate. The diverter height is kept at 60 percent of the approaching boundary layer thickness. Studies have revealed the occurrence of flow instability in the form of shock wave oscillations at moderate mass flow conditions. The mechanism for the occurrence of flow instability was observed to be due to the ingestion of separated flow at the entry arising from the intake shock interaction with the approaching boundary layer. Two methods are attempted to alleviate the occurrence of flow instability to lower exit area by controlling the ingestion of low energy flow at the entry. The first method relates to the delaying the interaction of intake shock wave with the approaching boundary layer by extending the splitter plate length so as to keep the shock travel on the splitter plate for larger range of exit area; the second method is through perforations of splitter plate to bleed the flow from the upper part of the splitter plate to the region below the plate. Results with extended splitter plate show the delay in occurrence of flow instability to lower exit area, while with perforations the triggering of flow instability shifted to higher exit area. This study has demonstrated that by reducing the ingestion of low energy flow at the entry, the flow instability seen can be delayed to lower exit area.

REFERENCES

[1] Ferri,A and Nucci, L.M; The origin of aerodynamic instability of supersonic inlets at subcritical conditions, NACA RML50K30, 1951.

[2] Dailey, C L; Supersonic diffuser instability, Journal of Aeronautical Sciences, Vol. 22, No.11, p733-749, November 1955.

[3] Jung Claus, G; New experimental studies on the onset and the structure of Ferri and Dailey instabilities (English version of Zeitschrift fuer Fugwissenchaften und Weltraumforchung, ZE No.14, 1990, pages 25-262, Springer Verlag, 1990).

[4] Hall, G R; A criterion for prediction of airframe integration effects on inlet stability with application to advanced fighter aircraft, AGARD CP-150, 1974.

[5] Jolly R, Pai T G and Jayasimha P; Design and development of a Bifurcated Y-Duct Intake for a Modern combat Aircraft; ISABE 2001-1247, 15th International Symposium on Air Breathing Engines, Bangalore, September 2001.

[6] Ahmed.S and Vipan kumar; Investigation of flow instability in a pitot intake at Mach number of 1.6; Proceedings of 9th Asian Congress of Fluid Mechanics, Isfahan, Iran, May 2002.

[7] Ahmed.S and Vipan kumar; Mechanism of flow instability associated with a pitot intake duct; ISABE 2003-1115, 16th International Symposium on Air Breathing Engines, Cleveland, Ohio, USA, August 2003.

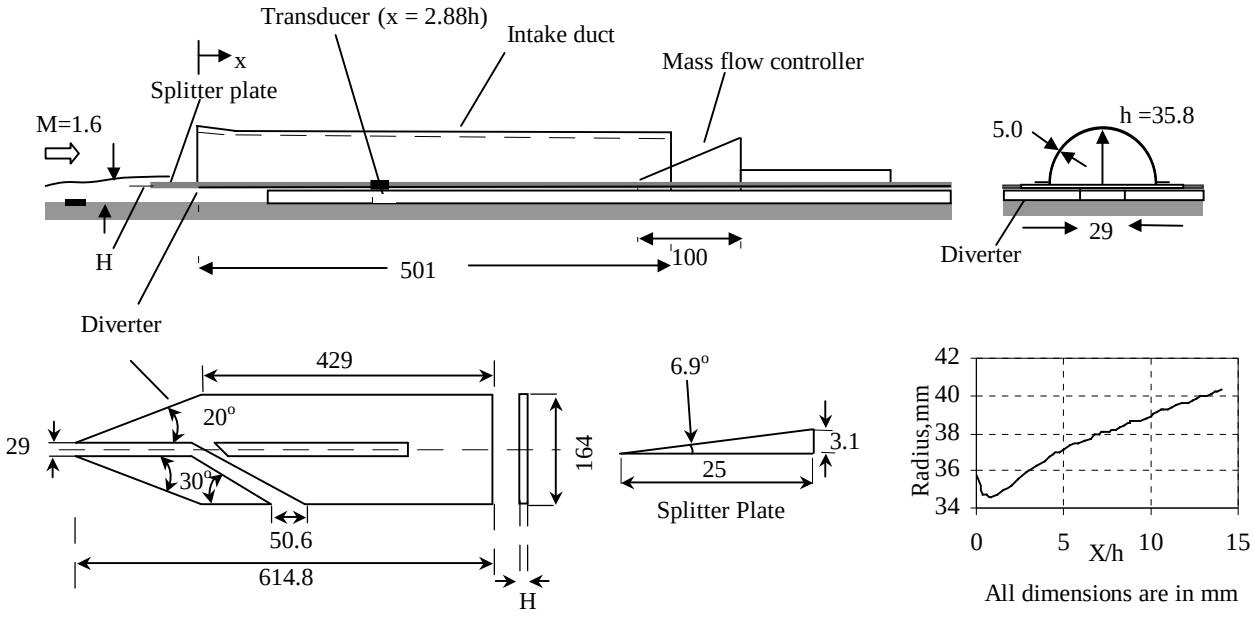

Fig.1 Details of model assembly, diverter, splitter plate and duct

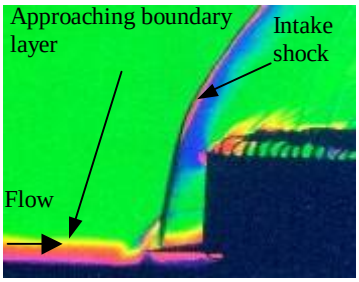

Ae/Amax = 1.0

(a)

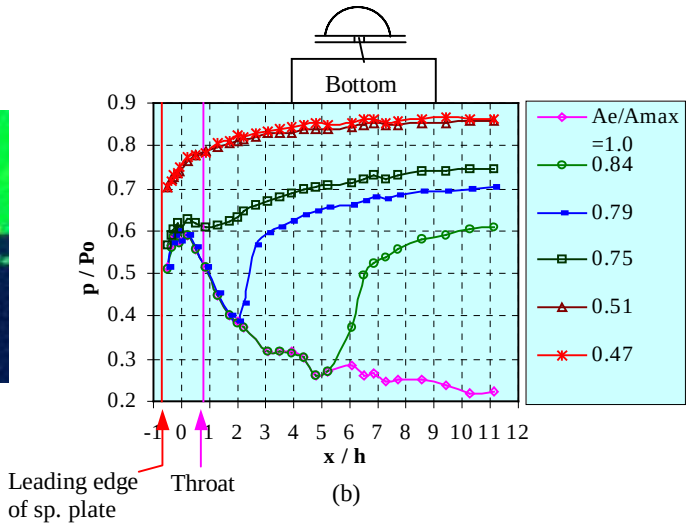

(b)

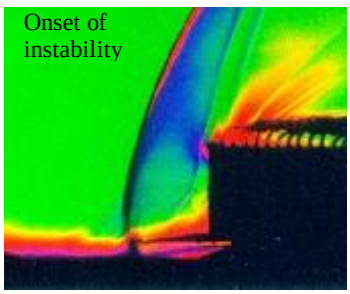

Ae/Amax = 0.47

(c)

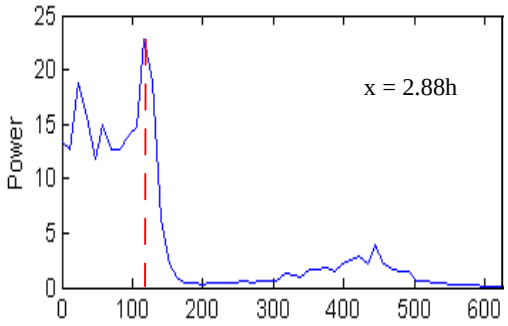

(d)

Fig. 2 Flow characteristics; splitter plate (L = 0.7h)

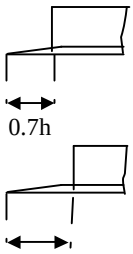

(a)

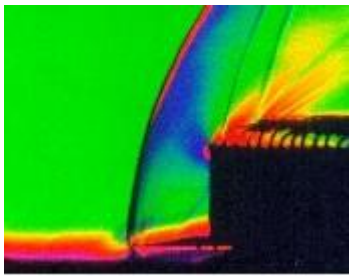

Ae/Amax = 0.47

(b)

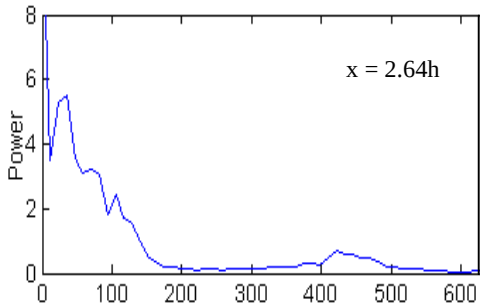

(c)

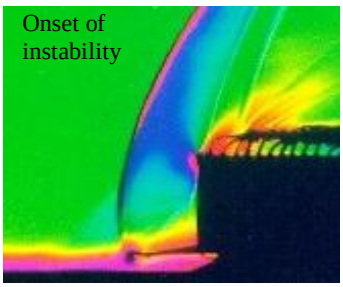

Ae/Amax = 0.36

(d)

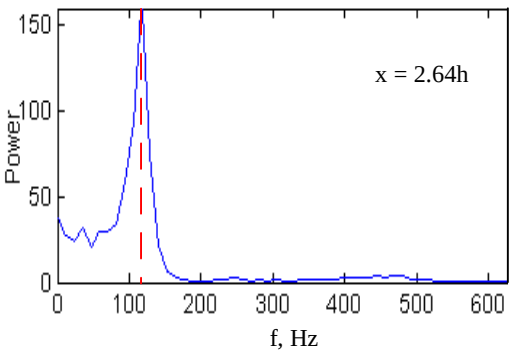

(e)

Fig. 3 Flow characteristics with extended splitter plate length (L = 0.94h)

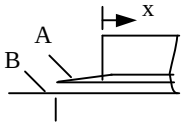

Ae/Amax	Surface A	Surface B
1.0	◆	◇
0.84	■	□
0.75	▲	△
0.51	●	○
0.47	●	○

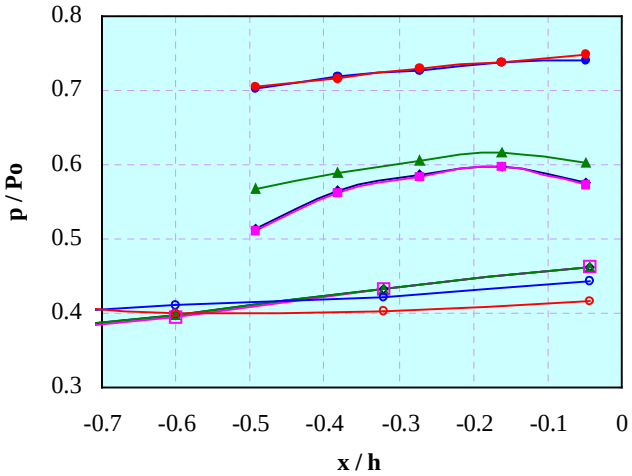

Fig. 4a Surface pressure variation, splitter plate (L = 0.7h)

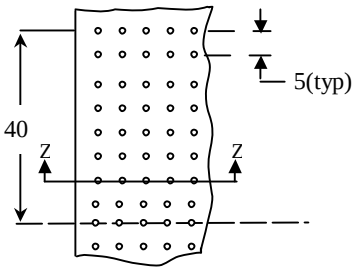

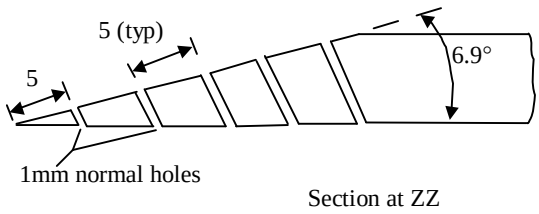

Fig. 4b Geometry of perforations on the splitter plate (L = 0.7h)

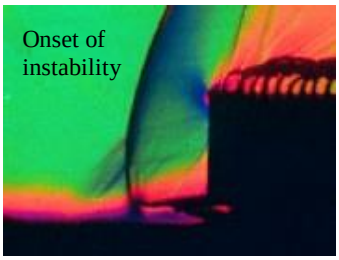

Ae/Amax = 0.51

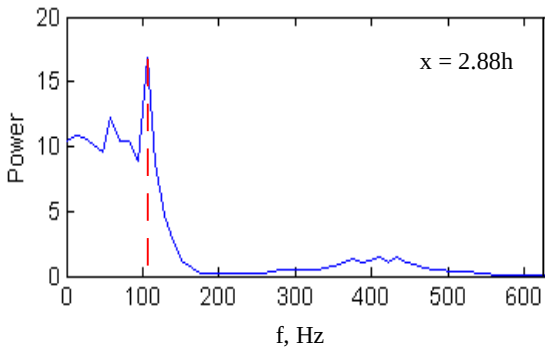

Fig. 4c Flow characteristics; perforated splitter plate (L = 0.7h)

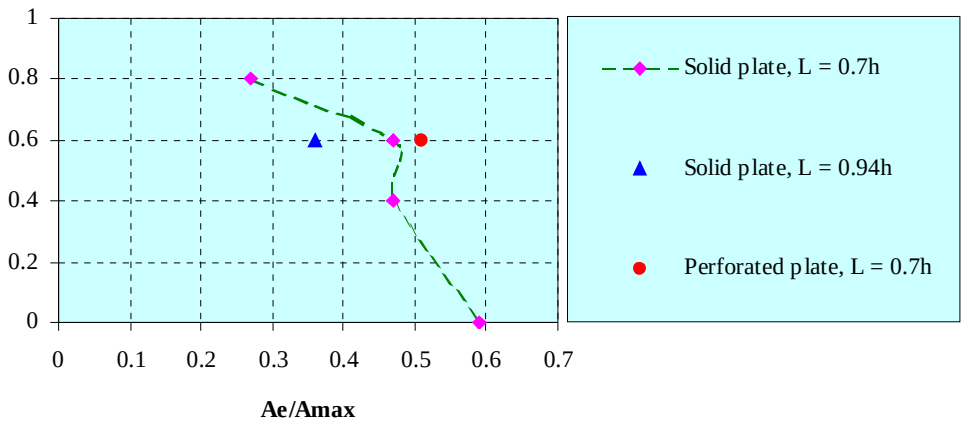

Fig.5 Comparison of onset of flow-instability for different approaches

Proceedings of the Tenth Asian Congress of Fluid Mechanics
17-21 May 2004, Peradeniya, Sri Lanka

FLOW CHARACTERISTICS OF HIGH PRESSURE LIQUID JET NOZZLE DEPENDING UPON THE ASPECT RATIO

B. J. Rho, J. Y. Jung
Faculty of Mechanical & Aerospace System Eng., College of Eng., RIIT, Chonbuk National Univ., Republic of Korea
S. J. Lee, S. M. Kim
Department of Precision Mechanical Eng., Graduate School of Chonbuk National Univ., Republic of Korea
W. T. Jeung
Korea Electric Power Research Institute, Republic of Korea

ABSTRACT: The aspect ratio of a nozzle is the main parameter that governs the jet flow pattern and nozzle performance. And in this study, some flow characteristics with the variation of nozzle aspect ratios such as mean pressure distributions along the centerline, flow coefficients and the diffusion angles have been experimentally investigated. Through the experimental analyses, the higher aspect ratio was found to decrease the jet kinetic energy because of the friction losses passing through the nozzle tip. As the results, the available semi-empirical equations for momentum and kinetic energy deficit could be correlated.

1. INTRODUCTION

A high-pressure jet is normally defined as a jet injected into a stagnant atmosphere of 100 bar or more. It is further divided into two types by the inlet pressure. Generally, the cutting jet and the washing jet are mainly used in industrial devices; the former is used with high pressure approximately from 1000 bar to 4000 bar. There are several parameters that describe high-pressure nozzle performance. Among them, the contraction ratio (nozzle outer area/inner area) and contraction angle have been mainly investigated by experiments or numerical methods, and the effects of the contraction ratio and contraction angle for nozzle performance are generally known. But the nozzle performance is also affected by nozzle aspect ratio (nozzle tip length/nozzle exit diameter), and some paper have been published in this field. McCarthy et al. [1] have studied on the correlation between the nozzle shape and issuing jet shape. The major requirement of a nozzle is the efficient conversion of potential energy to kinetic energy, which can be best achieved by a sudden, smooth contraction of the flow area from the supply line to the desired nozzle diameter. The nozzle aspect ratio L/d has a significant effect on the initial jet velocity profile and

subsequent jet surface shape up to *L/d* values where the shear stress and static pressure gradient are fully developed. And there is some evidence favoring the rounding and polishing of the nozzle internal surface in order to get maximum performance. Through the investigation of the geometrical effects on discharge coefficient for plain orifice, Ohrn et al. [2] showed that the rounding of inlet orifices increases the discharge coefficient. Detailed measurements of discharge coefficients have been carried out by Kiljanski and Pearce et al. [3-6]. The flow in the orifice is categorized as separated flow, reattached flow and cavitated flow. The separated and cavitated flows give small values of discharge coefficient in view of the contracted area of flow. The discharge coefficients at the higher values of Reynolds number (exceeding 2×10^5) have been shown to be insensitive to variations of Reynolds number [4] for the reattached flow regime. From experiments with various aspect ratios and orifice diameters, Ramamurthi et al. [7] showed the internal flow of orifices and the discharge coefficient with aspect ratios. Smaller diameter orifices give higher discharge coefficients in the separated flow region. The values of C_d for separated and cavitated flows do not depend on *Re*. This paper presents results of experimental measurements carried out for the development of high-pressurized liquid jet nozzle used in a lancing unit.

2. EXPERIMENTS

The nozzles used in this experiment were designed with 1.2 mm diameter and three types of aspect ratio. Table 1 shows the experimental conditions for this experiment.

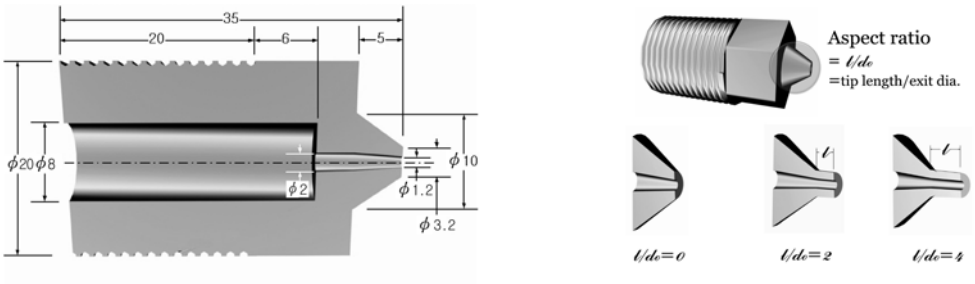

Fig 1. Schematic configuration and aspect ratio of using nozzle

Table 1 Experimental Condition

	Details	Remarks
Working Fluid	Water	Room temperature
Working Condition	9.5, 10.2, 10.8, 11.6	Q_i(*L/min*)
Measurements Section	$50d_o$ ~ 1000 d_o	Measured at a displacement of 12 *mm* to 36 *mm*

Fig. 2 shows the experimental device of high-pressurized jet nozzle, which is consisted of 3 parts; water supply part, transparent channel for getting flow visualizations and data and the atomized mist suction part. The flow channel as a test section was set up with transparent glass. For the acquisition of data, two pressure sensors [Hydro-Technik 250 bar (HT-250), Pressure-Systems 17 bar (PS-17)] were used. One (HT-250) was used for the measurement of nozzle chamber pressure, and another one was linked to a Pitot-tube set for measuring the jet static pressure.

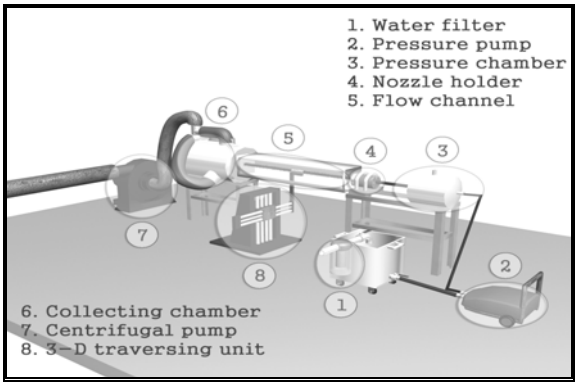

Fig 2 Experimental apparatus of high-pressurized system

3. RESULTS AND DISCUSSION

3. 1 Influence of aspect ratio on initial jet

Table 2 and 3 show the variations of the internal pressure measured in the nozzle chamber and the discharge coefficients with aspect ratio for used nozzle. The internal pressure of nozzle chamber was affected by the aspect ratio (Table. 2). It may be explained that the longer tip length makes the higher friction losses in ejecting process. As shown in Table 2, they were increased depending on the nozzle tip length independent of liquid flow-rates, in other words, the longer tip length brings the higher back pressure. But the coefficient of discharge was decreased with the increase of aspect ratio, which means that the back pressure was increased caused by tip length. Fig. 3 shows the results of the pressure distributions with aspect ratios and inlet flow rates. Higher inlet flow rates with same aspect ratio produce higher pressure at the exit of the nozzle (Fig. 3 a), and at different aspect ratio, higher aspect ratio made the initial pressure decreased (Fig. 3 b). In spite of the initial pressures, the pressures were decreased to almost same level regardless of aspect ratio.

Fig. 4 shows the image of the diffusion angle of the jet measured from the nozzle tip to 60 d_o. The diffusion angle was increased with aspect ratio. This shows that the nozzle tip length is a very important

parameter affecting on friction losses. Consequently, the nozzle with a longer tip length shows a large pressure drop between nozzle chamber and exit, and the jet injected to stagnant air shows a larger diffusion angle than the shorter tip length. It gives another descriptions that the higher-pressure drop caused by the longer tip length brings more kinetic energy loss in jet flow. This phenomenon is clearly shown in Fig. 4.

Table 2 Internal Pressure of Nozzle

(unit = kg_f/cm^2)

	$L/d_o = 0$	$L/d_o = 2$	$L/d_o = 4$
Q_i = 9.5 *L/min*	115.72	116.33	125.30
Q_i = 10.2 *L/min*	130.35	141.18	147.66
Q_i = 10.8 *L/min*	149.23	152.12	163.24
Q_i = 11.6 *L/min*	175.09	179.82	186.93

Table 3 C_d experimentally defined

	$L/d_o = 0$	$L/d_o = 2$	$L/d_o = 4$
C_d	0.93	0.91	0.89

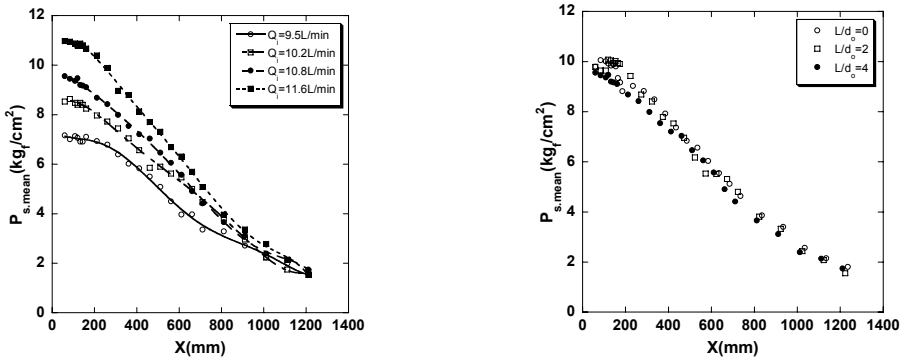

(a) (b)

Fig 3 Pressure distributions; (a) L/d_o = 4, (b) Q_i = 10.8 *L/min*

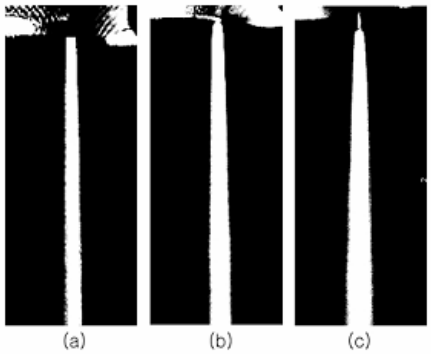

Fig. 4 Visualization of diffusion angle with aspect ratio (Q_i = 10.8 *L/min*); (a) L/d_o = 0, (b) L/d_o = 2, (c) L/d_o = 4

3. 2 Momentum and Energy Variations

In order to analyze the variations of momentum and kinetic energy in the flow direction, the data obtained are plotted in Fig. 5 (a), (b). It is generally known that the maximum velocity of the jet does not decrease up to X/d_o = 100. And this region is theoretically defined as a potential core. This description as may be seen from Fig. 5, and in the farther flow regions ($100 \leq X/d_o$), the non-dimensional profiles of momentum and kinetic energy can be formulated as semi-empirical equations as following.

Momentum deficit profiles;

$$M_o/(M_o)_{T.\ Theo} = (73.4e\text{-}12)(X/d_o)^3 - (98.6e\text{-}9)(X/d_o)^2 - (41.4e\text{-}6)(X/d_o) + (81.1e\text{-}3) \qquad (1)$$

Kinetic energy deficit profiles;

$$E_k/(E_k)_{T.\ Theo} = (20.1e\text{-}12)(X/d_o)^3 - (17.6e\text{-}9)(X/d_o)^2 - (24.2e\text{-}6)(X/d_o) + (23.6e\text{-}3) \qquad (2)$$

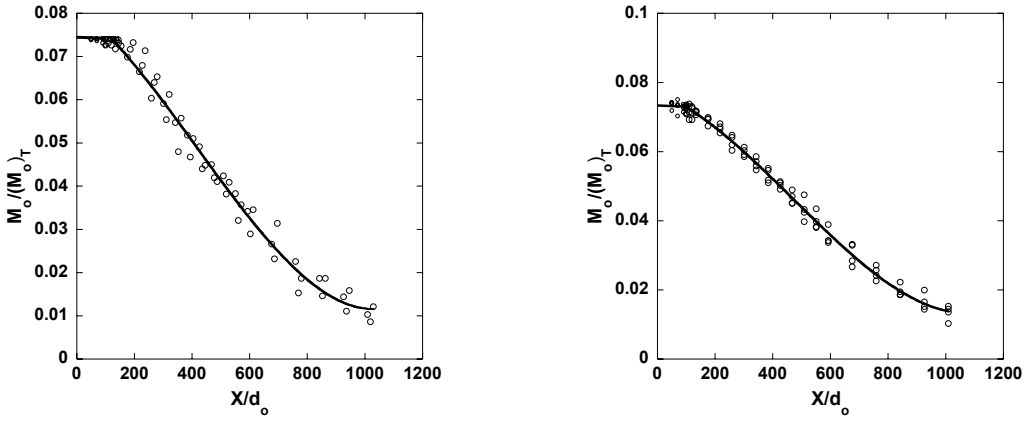

(a) (b)

Fig. 5 Momentum deficit profile; (a) Q_i = 11.6 *L/min* (b) L/d_o = 4

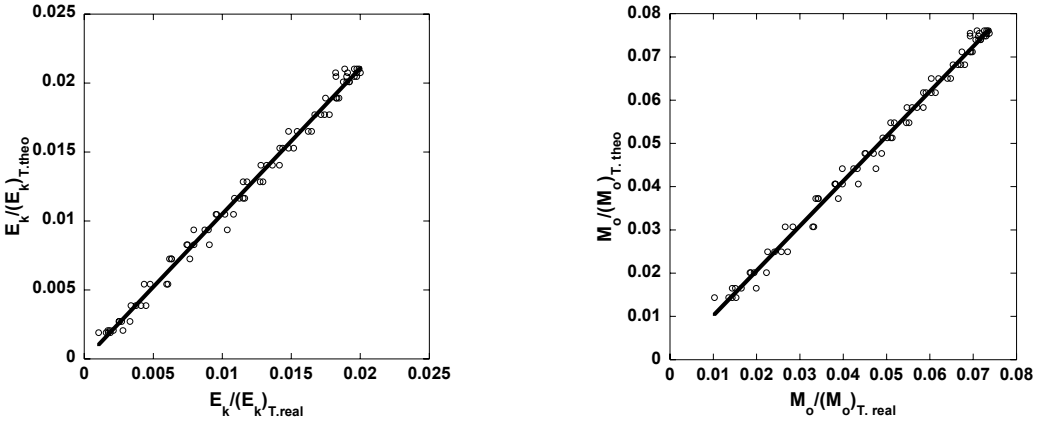

(a) (b)

Fig. 6 Correlation between empirical equations and experimental data; (a) Kinetic energy (b) Momentum

4. Concluding Remarks

As seen from the results of the experimental analysis, the pressure increases in nozzle chamber with aspect ratio, which means the longer tip length of nozzle gives the higher back pressure due to the ejecting friction losses. And the spreading rates also increased with aspect ratio, because the higher friction losses decrease the kinetic energy in the jet flow, and this results in an increase of spreading rate. For the optimum design of the high-pressure liquid jet nozzle, further analyses and measurements are going on, and only a small portion of the preliminary results are presented in this paper.

ACKNOWLEDGEMENTS

This work was supported by the Korea Electric Power Research Institute, and we sincerely thank them.

REFERENCES

[□] M. J. McCarthy, N. A. Molloy. "Review of Stability of Liquid Jets and the Influence of Nozzle Design". The Chemical Engineering J. Vol. 7 (1974) pp 1~20

[□] T. R. Ohrn, D. W. Senser, A. H. Lefebvre. " Geometrical Effects on Discharge Coefficients for Plain Orifice Atomizers". Atomization and Sprays . (1991) pp 137~153

[□] T. Kiljanski, Discharge coefficients for free jets from orifices at low Reynolds number. ASME J. Fluids Engineering (1993), pp. 778–781.

[□] I. D. Pearce, A. Lichtarowicz, Discharge performance of long orifices with cavitating flow, in: Proc. Second Fluid Power Symposium, January 1971, Guildford Paper D2, University of Surrey, 1971, pp. D2-13–D2-35.

[□] R. H. Spikes and G.A. Pennigton, Discharge coefficient of small submerged orifice. *Inst. of Mechanical Engineers* (1959), pp. 661–665.

[□] T. Hasegawa, M. Suganuma and H. Watanbe, Anomaly of excess pressure drops of the flow through very small orifices. *Phys. Fluids* (1997), pp. 1–3.

[□] K. Ramamurthi, K. Nanakumar. " Characteristics of Flow through Small Shape-edged clinderical Orifices". Flow Measurement and Instrumentation, Vol. 10, Issue 3, (1999) pp 133~143

Proceeding of the Tenth Asian Congress of Fluid Mechanics
17-21 May 2004, Peradeniya, Sri Lanka

THE INFLUENCE OF UPRIGHT AIR FLOW ON THE MOTION OF SPRAYS: PART A –THE VISUALIZATION TECHNIQUE

Tsai, R.F., Lee, C.K. and Chang, J.S. and Lee, C.F.
Dept. of Automation Eng., National Hu-wei Institute of Technology, Hu-wei, Yun-lin, 632, Taiwan

ABSTRACT: An image processing program was successfully developed to allow quantification of droplet area, equivalent diameter, and perimeter. The program was composed of several image processing operators, including contrast enhancement, low-pass filter, thresholding, labeling, edge detection, object filling, and digital analysis techniques to quantify area and perimeter of interested objects. The program processed 10 images per second, and its accuracy of area and equivalent diameter is the same as those by a commercial software, and that of perimeter is up to 2 % better than the commercial software due to the use of a fuzzy weighting method. The program processed spray images with ambiguous background to quantify spray characteristics in the near-field region. Measurements of compactness may be used to estimate the possibility of secondary atomization or appraise the performance of atomizers, and to quantify the influence of possible mechanisms and parameters on breakup. And it will combine microscope, pulse laser, and the program itself to form a micro-droplet visual analysis system, which will be used to quantify geometric characteristics of micro or smaller size droplets. The program will add sub-programs to quantify shape factor and roundness of droplets to quantify their characteristics in the breakup region, and examine the mechanisms and parameters of primary breakup, and secondary atomization of droplets.

1. INTRODUCTION

Atomizers and spraying systems have been widely used in many industrial applications. Spray characteristics are essential to quantify the performance of atomizer, and important to applications such as liquid-fuel spray flame [1], spray drying, evaporative cooling, and production of metal powder. Spray characteristics such as droplet velocities, size and flux, far from the nozzle exit, may be provided by laser diffraction instrumentations, and laser and Phase Doppler velocimetrys [2-4]. However, these techniques are not suitable to quantify droplet size in the near field region, in which the flow is of too high droplet number density, and of non-spherical or breaking-up droplets [5].

Maeda [7] developed a shadow Doppler velocimetry to quantify droplet velocity and size of non-spherical shapes. A commercial image processing system, VisiSizer, was developed to quantify droplet size by analyzing spray images of short-exposure photography. However, these techniques require expensive instrumentation, and do not provide the amount of breaking-up droplets nor the information of atomization progress.

Photography is considered as one of the most powerful techniques to overcome measurement difficulty in the near field region since it offers “seeing-is-believing” evidence. The cost of an efficient image processing system has been largely reduced to an economical level due to the promotion of hard-ware and soft-ware of PC. Existing image processing techniques can quantify the area, perimeter, and ratio of the long and short axes of interested objects of a digital image, which allow quantification of droplet diameter, area, perimeter, and atomization progress. The study, therefore, integrated existing techniques as a program to quantify droplet geometric characteristics with ease, and its accuracy was examined with a series of simplified figures similar to real droplets.

This paper is divided into four sections including this introductory section, which is followed by a description of the procedure of digital image processing. The third section presents results and discussion, which estimate the accuracy of the program. The paper ends with a summary of the more important findings.

2. PROCEDURE OF DIGITAL IMAGE PROCESSING

The processing program was composed of a series of mathematics operations, which will be explained as follows (Figure 1). A clear or readable spray image may be acquired by short-exposure

photography by using a short-pulse flash or laser to illuminate the object, or a camera of fast shutter speeds. Such images should be digitized as an 8-bit format (256 gray levels, Figure 1a) in advance of further digital image processing. The readability of an image may be improved by enhancing its contrast and filtering the background noise (Equations 1 & 2, Figure 1b) with low-pass filters.

$$f_c(x,y)=\begin{cases}240 & f(x,y)\geq T_{up}\\ \dfrac{240(f(x,y)-T_{low})}{T_{up}-T_{low}} & T_{up}>f(x,y)>T_{low}\\ 0 & f(x,y)\leq T_{low}\end{cases} \tag{1}$$

$$\frac{1}{16}\begin{bmatrix}1 & 2 & 1\\ 2 & 4 & 2\\ 1 & 2 & 1\end{bmatrix} \tag{2}$$

Droplets of interest in Figure 1b could be separated from the background by using a thresholding operator (Equation 3). The black spots of Figure 1c correspond to droplets, and each region was grouped as a droplet and tagged by number sequence by a labeling technique.

$$f_b(x,y)=\begin{cases}1 & f(x,y)>=T\\ 0 & f(x,y)<T\end{cases} \tag{3}$$

The information of droplet perimeter (P) and area (A) allows quantification of equivalent diameter (D_e, Equation 4), hydraulic diameter (D_{hy}, Equation 5), and compactness (C, Equation 6). It should be noted that ellipses of the same area are of the same equivalent diameter (D_e), which is used to estimate mean droplet size (SMD, Equation 7) and size distribution. However, a longer and thinner object is of smaller D_{hy} and larger compactness (C) than a circle, unity compactness, due to a longer perimeter. Consequently, C is useful to predict atomization progress of a spray. For example, sprays of larger C imply more longer droplets and higher possibility of secondary atomization, and its droplet size may be reduced further downstream.

$$D_e=\sqrt{\frac{4A}{\pi}} \tag{4}$$

$$D_{hy}=\frac{4A}{P} \tag{5}$$

$$C=\frac{D_e^2}{D_{hy}^2}=\frac{4A/\pi}{16A^2/P^2}=\frac{P^2}{4\pi A} \tag{6}$$

$$SMD=D_{32}=\frac{\sum n_i D_{ei}^{\ 3}}{\sum n_i D_{ei}^{\ 2}} \tag{7}$$

A detecting operator (Figure 1d) was used to identify the horizontal and vertical coordinates of the pixels on the edge of a droplet, and an object-filling operator was used to color the pixels within the edge. Precise determination of perimeter (P) and area (A) of an object requires numerical calculus along the edge, which takes too much calculation time to be used in practical use. The study, therefore, developed a fast method allows quantification of P and A of many droplets with a reasonable accuracy to reduce statistic error. It should be note that an incomplete droplet is not measured to avoid uncertainty.

The sum of pixels within the edge of a droplet is used to estimate its area (A), and to determine its equivalent diameter D_e by Equation 4. The precision increases with size of the droplet, and the error is of 2 % for droplet larger than 30x30 pixels. Very small droplets are of too small volume and weighting

values of *SMD* (Equation 7), and, therefore, they may be neglected as noise without introducing uncertainty. If small droplets are of interest, lens of higher magnification ratio is strongly recommended to increase its spatial resolution.

Rafael et al. [8] suggest that there is a lower (P_{low}) and upper (P_{up}) limit of the perimeter of an object with a smooth profile determined by Equations 8a, and 8b, and Figures 2b and 2c, respectively. A preliminary study shows that the values of P_{low} & P_{up} were of errors of 10 %, and their arithmetic average were of errors of less than 5 %. The error was further decreased to 2 % by weighting P_{low} & $P_{up}$with a parameter (*W*), Equation 9. A preliminary study suggests that the value of *W* is between 0.4 and 0.8, and may be simplified as a function of area (*A*) and compactness (*C*) by a fuzzy method.

$$P_{low} = \text{Number of pixels on the edge of an object} \tag{8a}$$

$$P_{up} = P_{low} + (\sqrt{2} - 1)N_{RT} \tag{8b}$$

$$N_{RT} = \text{Times the next edge pixel found at right - front position in edge - detection}$$

$$P_w = w \cdot P_{up} + (1 - w)P_{low} \tag{9}$$

3. RESULTS AND DISCUSSION

A real droplet may be simplified as an elliptic ball due to its motion and surface tension, and its image is similar to an ellipse. Figure 3a shows a series of ellipses of a constant area and different aspect ratios, the ratio of long to short axes. The precise values of perimeter of the ellipses were estimated by a cubic spline method with an error of less than 0.2 %. Figure 3b shows that the values of P_{low} and P_{up} are of error less than 10 and 5 % by Equations 8a, and 8b, respectively. Figure 3c shows that a proper weighting value of *W* may reduce the error to 1% with hundreds times calculation speed. It should be noted that the values of *W*, *C*, and P_W have little influence on D_e and *SMD*. The determination of *W* and P_W is to quantify compactness *C* to estimate the possibility of secondary atomization or the level of irregular shapes of a spray.

Figures 4a to 4c show the photographs of real sprays and their corresponding results with image processing. The droplets are of irregular shapes, and the images were ambiguous due to the limitations of instrumentation and operation conditions. The programs demonstrated its superiority to overcome the measurement difficulty of ambiguous images and quantified their values of *A*, D_e, P_W, and *C*. Three droplets （NO. 1, 3 & 4）of Figures 4c seemed to be disintegrated further downstream, and were associated with compactness C larger than 3.6. The results suggest that compactness C may be a useful index to predict the progress of atomization or the possibility of further atomization. However, the determination of a criterion or critical value to predict the possibility of re-atomization requires more detailed studies of different flows.

4. CONCLUSION

The study has successfully developed an image processing system that allows quantification of the geometric characteristics of a spray in the near field region. The system can process 10 images with 521x480 pixels by using a PC with a 700MHz CPU. Its accuracy of area and equivalent diameter is the same as that of commercial software, and that of perimeter is of an error of 2 % better than the commercial one. The study will combine microscope, pulse laser and high-speed camera to form a system to quantify geometric characteristics of sprays or powder of diameter less than 10 μm. The mathematical functions to determine of shape factor and roundness will be included in the program to examine the possible mechanisms of breakup and secondary atomization in the near field region.

ACKNOWLEDGMENTS

The research was supported by National Science Council of Taiwan. (NSC) through contracts NSC-91-2212-E-150-028 & 90-2212-E-150-029. The authors are indebted to Mr. J. Chang and S.Y. Lin for their contributions in the initial stage of the image processing work. Mr. I.M. Yan, W.S. Su, J.J. Chen and B. C. Liang help to take the spray images are also acknowledged.

REFERENCES

1. Lefebvre, A.W. (1989) **Atomization and sprays**, Hemisphere Publishing Corporation
2. Bate, C.J., Jolly, A. J. (1997) Phase Doppler Measurement on a pressurised spray nozzle using scattering angles of 72°and 150º, Proceedings of 7th Int. Conference on Atomisation and Spray (ICLASS-'97), ISBN 89-950039-2-8 94550, 102-109, Seoul, South Korea.
3. Chang, J.-C. and Tsai, K.-C. (1997) Effects of Light-absorbing Droplets and Optical Factors on A Phase Doppler Particle Size Analyzer, Proc. of ICLASS-'97, 942-947.
4. Zaidi, S. H. and Altunbas, A (1997)A comparative study of annular two-phase flow using phase Doppler and laser diffraction techniques, In Proc. of ICLASS-'97, 975-982.
5. Ikeda, Y., Sekihara, F., and Nakajima, T. (1997) Set-up parameter optimization of phase Doppler techniques for spray measurement, Proc. of ICLASS-'97, 983-990.
6. Ayob, m. R., and Bate, C. J. (1997) Entrained water atomization experiments and ist size measurements using optical measurement tscnique, Proc. of ICLASS-'97, 991-998.
7. Maeda, M. (1997) LDA based optical particle sizing of sphreical and irregular shape, Proc. of ICLASS-'97, 3-22.
8. Rafael C. Gonzalez, Richard E. Woods, **Digital Image Processing**, ADDISON WESLEY (1992).

NOMENCLATURE

(x, y) : The coordinates of a pixel in an image.

$f(x, y)$: The gray level function of a pixel.

$f_c(x, y)$: The gray level function of a pixel after contrast enhancement.

$f_b(x, y)$: The gray level function of a pixel after binary thresholding.

T : The threshold for binary thresholding.

T_{up} : The upper threshold for contrast enhancement.

T_{low} : The lower threshold for contrast enhancement.

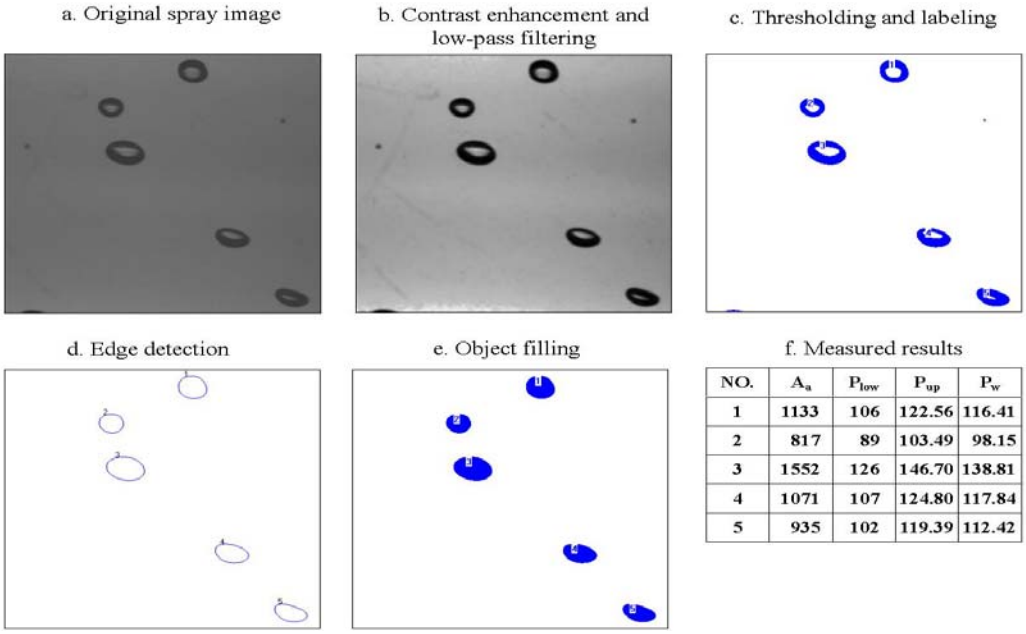

NO.	A_a	P_{low}	P_{up}	P_w
1	1133	106	122.56	116.41
2	817	89	103.49	98.15
3	1552	126	146.70	138.81
4	1071	107	124.80	117.84
5	935	102	119.39	112.42

Fig. 1 The flow chart of image processing

a. Line sections **b. Lower limit of perimeter, P_{low}** **c. Upper limit of perimeter, P_{up}**

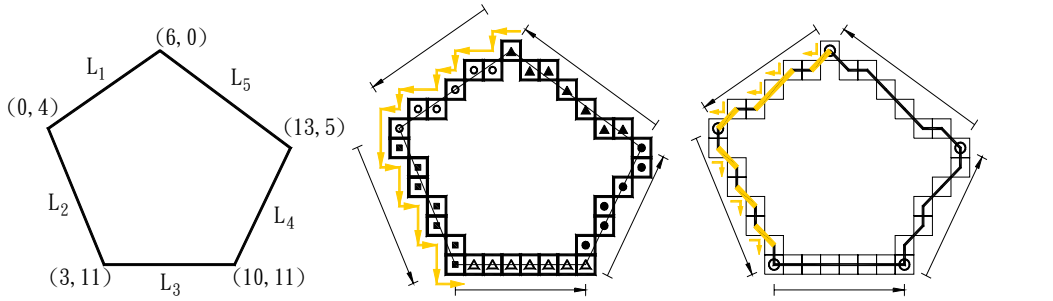

d. Measured results of perimeters and weightings

Line sections	L_1	L_2	L_3	L_4	L_5
P_{real}	7.21	7.62	7	6.71	8.6
P_{low}	6	7	7	6	7
P_{up}	7.66	8.24	7	7.24	9.07
Weighting	0.73	0.50	0~1	0.57	0.77

Fig. 2 The quantification of the lower and upper limits of perimeter

a. Simulated ellipses

$a = r / k$, $b = r \times k$,

Area = $\pi ab = \pi r^2$

r = 1 :

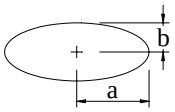

k	a	b	Image
1.0	1.00	1.00	
0.9	1.11	0.90	
0.8	1.25	0.80	
0.7	1.43	0.70	
0.6	1.67	0.60	
0.5	2.00	0.50	
0.4	2.50	0.40	
0.3	3.33	0.30	
0.2	5.00	0.20	

b. Perimeter of figure a.

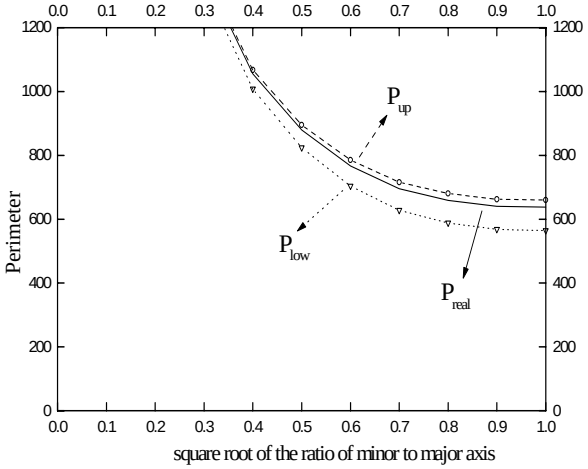

c. Errors of figure a.

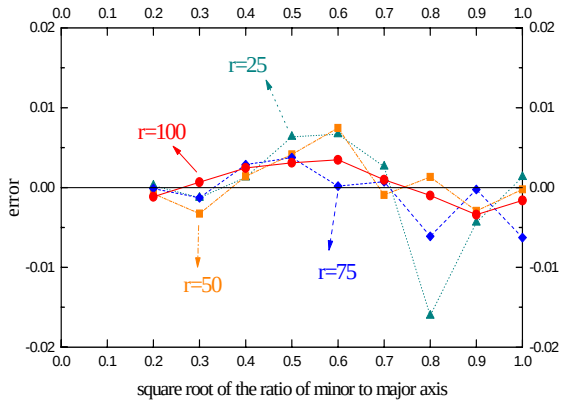

Fig. 3 Measurements of perimeter of simulated ellipses

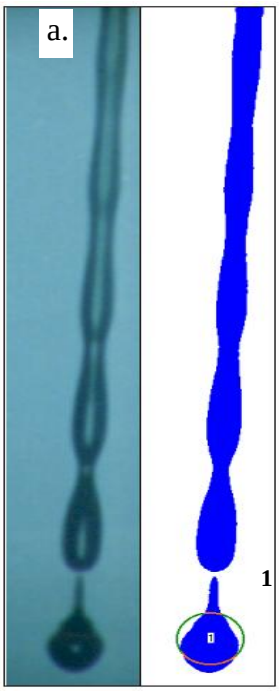

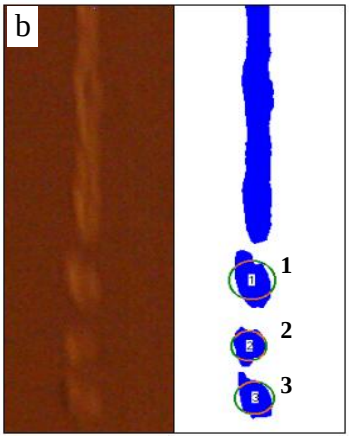

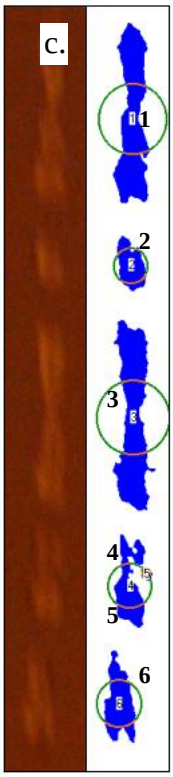

d. Measured result

Fig. No.	Droplet NO.	A_a	P_w	C_w
4a	1	3450	279.06	1.80
4b	1	1513	161.79	1.38
	2	921	119.67	1.24
	3	1094	137.19	1.37
4c	1	3931	422.25	3.61
	2	1056	143.28	1.55
	3	4352	458.14	3.84
	4	1619	279.32	3.83
	5	93	35.92	1.10
	6	1745	239.09	2.61

Fig. 4 The Photographs of processed results of spray in the near-field region
Fig. 4a Breakup of liquid jet; Fig. 4b Ambiguous background; Fig. 4c Droplets of irregular shapes;

Proceedings of the Tenth Asian Congress of Fluid Mechanics
17-21 May 2004, Peradeniya, Sri Lanka

EXCITATION OF A LAMINAR BOUNDARY LAYER BY A PERIODIC JET

M. Gaster & E. Caloupis
Department of Engineering, Queen Mary, University of London, UK

ABSTRACT: Analytical/numerical solutions of the flow field created by a periodic axi-symmetric jet issuing from a small hole in the wall into a boundary layer are compared with velocities measured by a hot-wire anemometer in a wind tunnel experiment for the same geometry. For the specific case of a normal jet in a zero pressure gradient boundary layer the agreement between the two approaches was found to be excellent. This suggested that the simple analytical scheme can be used to predict the flows arising in situations involving different base flows, possibly with a pressure gradient, or when the Reynolds number or frequency of excitation are changed.

1. INTRODUCTION

There is current interest in using jet actuators to modify boundary layers to improve the overall flows over aerofoils and bodies. In particular, if the jet can be used to encourage greater mixing with the high momentum external flow then a delay in the separation position can be expected. The research discussed here examined in detail the perturbed flow field created in a laminar boundary layer when it was excited by a periodic axi-symmetric jet issuing from a small hole in the boundary surface. The study[1] has been carried out in laminar flows so that simple analytical methods can be used to make predictions of the resulting flows. If the scheme is found to be satisfactory, the same analytical process can be extended to describe the disturbance field in more complex situations. In many real applications the boundary layers will, in most instances be turbulent, but this study will, we believe, help to describe much of the basic fluid mechanics involved.

Detailed measurements have been made of the streamwise velocity perturbations created by normal and inclined jets issuing from surface holes of different dimensions and orientations. The focus of the project was initially concerned with validating the simple linear theory. The experimental exploration of the flow field is quite slow and therefore it cannot be used to cover an extensive range of different flow parameters, whereas analysis followed by calculation can be employed in this way once it has been properly validated. The modelling scheme used in this work was based on the parallel mean flow approximation to the boundary layer, and the perturbation equations are linearized. Although the analysis will then only be applicable to small excitation levels the approach can readily be used to show the effects of pressure gradient, Reynolds number and excitation frequency on the resulting disturbance levels and flow patterns. In addition, the analytical approach can provide the other velocity components as well as the three vorticities, quantities that are virtually impossible to measure in an experiment.

Comparisons have been made between the measured velocities and the computed values over regions of the flow for some zero pressure gradient situations. The predicted behaviour under other flow conditions will then been explored using the analytical approach.

2. WINDTUNNEL SETUP

The measurements were made in the boundary layer of a flat plate mounted in the low turbulence wind tunnel at Queen Mary. The tunnel is of conventional closed circuit design with a contraction ration of 7.3, a honeycomb and 4 fine screens. The working section is 0.914 m square and 1.83 m long. At the typical free-stream velocities used in these experiments of 10 m/sec the turbulence intensity was less that 0.01% in the frequency band 4 - 20 kHz.

The test surface was made from an aluminium plate of 10 mm thickness and 1.2 m in length. The leading edge was of elliptic form to provide a smooth start to the boundary layer and the trailing edge was fitted with a flap and trim tab to enable a zero pressure gradient to be set. A circular instrumentation insert disc of 190 mm dia was fitted into the plate centred 500 mm from the leading edge. The various

jets used to excite the flow were formed in these inserts. An electromagnetic vibrator was coupled to a small piston device to provide a periodic flow with a mass flow that could be measured. Pistons of 2 mm and 4 mm dia were used so that a range of amplitudes could be explored. The piston motion was measured by an electronic sensor capable of resolving a few microns displacement. The exciter mechanism, which was mounted on wires to avoid vibration of the plate, was coupled to the jet by a short flexible plastic pipe.

Flow perturbation velocities were measured with a hot-wire probe mounted on the computer controlled three-dimensional traverse. The A/D recording the hot-wire anemometer output, after proper filtering and amplification, was phase locked to the signal driving the oscillatory jet. By capturing a large number of periods of excitation response and using the phase averaging approach much of the random noise in the signal was rejected. This was necessary in regions of the flow where the measurement of relatively weak signals far from the source was made. The whole experiment was controlled and appropriate data recorded by a PC. The PC controlled an IEEE interface that drove the modular instrumentation system that activated the piston motion, set the wind tunnel speed, moved the hot-wire traverse, recorded the temperature and barometric pressure and collected all the hot-wire signals. This enabled a whole region of the flow to be systematically explored without manual intervention. Even though 15 hours were needed for recording data over some of the traverses the tunnel could be left to run unattended overnight if necessary.

3. ANALYTICAL METHOD

The flow field created by a jet is defined by the solution of the equations of motion with boundary values chosen specifically to represent the jet. The work reported here was concerned with isolated small diameter jets. They were modelled by delta functions of the appropriate variable on the boundary wall. For the case of a normal jet this is just the normal velocity component, while for inclined jets an additional surface velocity component had to be included. In order to make the problem tractable two approximations were made. Namely, that the mean flow was treated as parallel and also that the disturbances were small enough to allow linearisation. These two approximations are commonly used in problems concerned with boundary layer stability. They allow the equations to separate in space co-ordinates and hence enabled them to be cast in Fourier space with respect to the wavenumbers in the stream and spanwise directions. The sixth-order system of equations for the three orthogonal velocity components and the three vorticities can be integrated inwards from the free-stream towards the wall, where the boundary values are applied. Care has to be taken to remove the divergent parts of the solution at each integration step. The solution in physical space is then obtained by Fourier inversion. A particular problem arises because the solutions in physical space are unbounded in the stream direction. It is necessary to window the solution so that over the domain of interest the solution is unaffected, while far downstream it is forced to zero. The required window in the Fourier space is found in terms of the eigen solutions of the two-dimensional wave component as well as all the oblique waves. The solutions obtained then provide the three velocities and vorticity components over the entire domain covered by the calculations.

4. THE EXPERIMENT

Measurements were first recorded for a normal jet issuing from a 2 mm diameter circular hole 500 mm from the leading edge. For all the results to be shown the velocity was set at 10 m/s. Various frequencies were used but here we will only show data recorded at a frequency of 96 Hz. The signal from the vibrator was monitored to make sure that the harmonic distortion was less that 0.01%. This was important because the nonlinear work to be carried out later required a pure excitation so that the nonlinear response in the harmonics could be measured. With the hot-wire probe positioned some 50 mm downstream from the source traverses through the boundary layer were recorded at different levels of excitation. From these data sets a suitable excitation level was chosen so that the response was a linear function of the excitation in order to provide data consistent with the analysis. Figure 1 shows the streamwise perturbation velocity in a plane directly along the centre-line of the disturbed in flow for a

2 mm dia. normal jet. Typically a data set like this would take some 15 hours to acquire. After each traverse through the boundary layer the flow speed was re-set so that the Reynolds number was constant and the hot-wire was automatically re-calibrated. The ensemble averaging was carried out on the fly and only the first three Fourier coefficients were stored for each hot-wire probe locations. The slight variations in excitation amplitude, that inevitably occurred, were scaled out of the data at each sample point and the mean excitation amplitude stored.

5. VALIDATION

In order to validate the linear analytical scheme the case of a normal periodic jet of small diameter was chosen. The flow field was measured along a slice through the source covering a region of 25 mm ahead of the source and passing some 175 mm downstream. The signals from the hot-wire were ensemble averaged and the fundamental Fourier component extracted and stored for each of the positions through the boundary layer at each streamwise location. A similar spanwise section was traversed at 100 mm downstream from the source. The reconstructed perturbation fields are shown on figures 1 & 2. Similar measurements were made to find the effect of jet diameter and the inclination of the jet to the surface, both across the span and along the stream.

6. RESULTS

Calculations for the flows resulting from boundary conditions intended to model the jets used in the experiments and having the same flow parameters were also made. The results are displayed on figures 1 & 2 together with the measured values. In both cases the plots show both the in-phase component and the out-of-phase element. Contours have been drawn at amplitude levels of root 10 so that alternate contours, which have been draw with thicker lines, are decades. The spanwise traverse section on figure 2 shows the in-phase component and the modulus for both calculation and measurement.

7. DISCUSSION

The agreement between the predicted and measured flows is remarkable, every detail of the contours of the two sets of data are virtually identical to one another. The main differences occur far downstream where the experimental and computed patterns differ very slightly. This is presumed to arise because in the analytical model the nonparallel geometry of the real boundary layer is neglected. Apart from that the patterns obtained from the experimental measurements are modelled faithfully. The amplitude levels also agree closely with those predicted. The experimental results obtained with different hole sizes are not shown here, but the data collapsed well on the basis of jet mass flow as predicted by the model. Some of the measurements on the spanwise inclined jets are drawn on figure 3 together with the calculated patterns. Again, the agreement between experimental data and computation is sufficient to give confidence in the prediction scheme. The flow field created by a boundary value in the stream or spanwise velocity component is very weak compared with that created by the normal component. Flows created by inclined jets therefore only differ slightly from those from normal jets with the same mass flow.

8. CONCLUSIONS

Linear theory provides accurate models of the flows created by jets issuing through the boundary wall into a Blasius boundary layer.

The flow field is dominated by the normal mass flow and is only weakly influenced by the angle of orientation of the jet.

9. ACKNOWLEDGEMENTS

The results were part of a study for the USAirforce AFOSR Grant Number F49620-99-1-0015

REFERENCES

[1] Fasel H F, Wygnanski I J and Gaster M. Actuator Effectiveness AFOSR F49620-99-1-0015 2002.

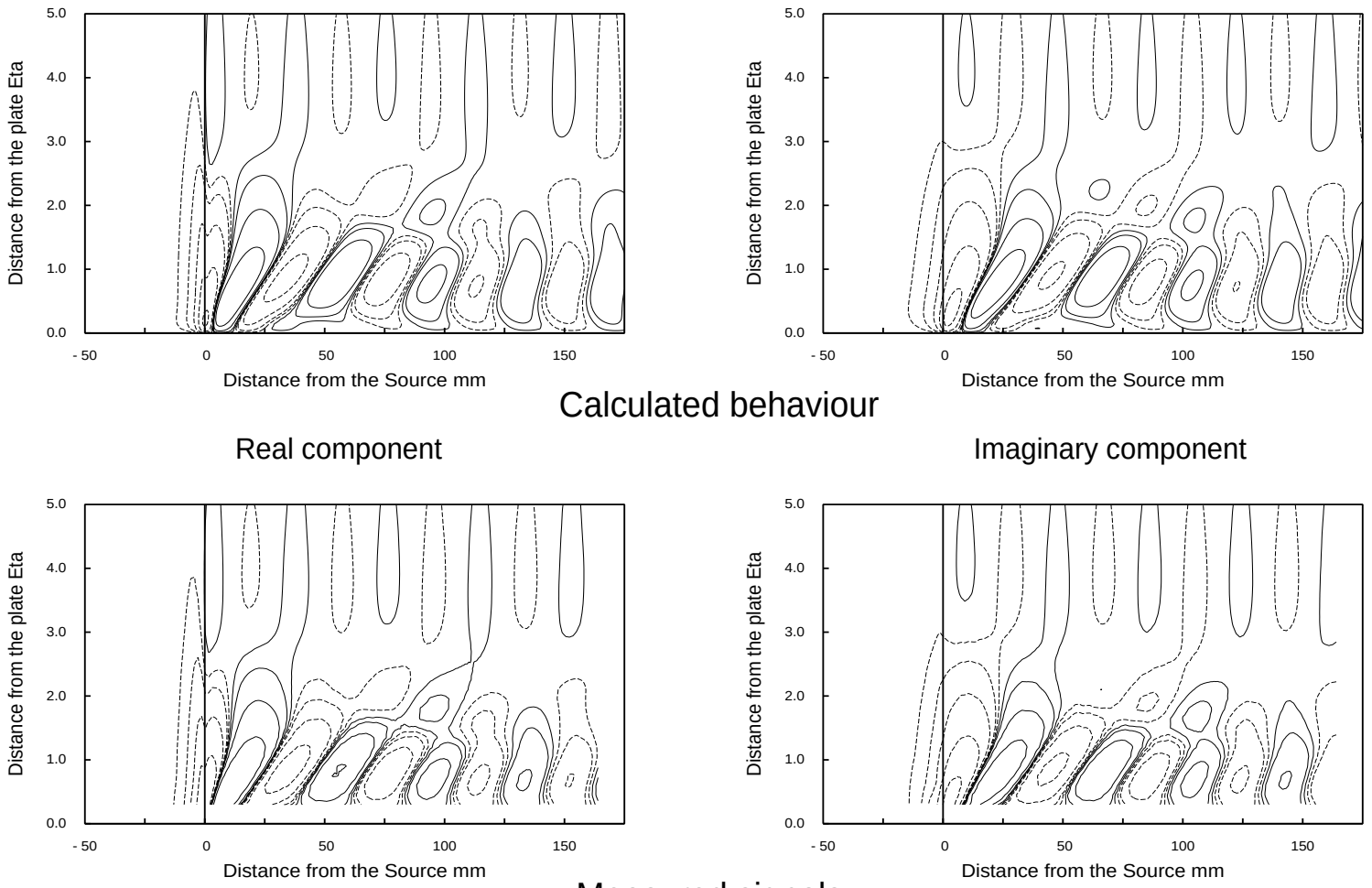

Figure 1 Streamwise Velocity Perturbations on Centre Line for a Normal Jet

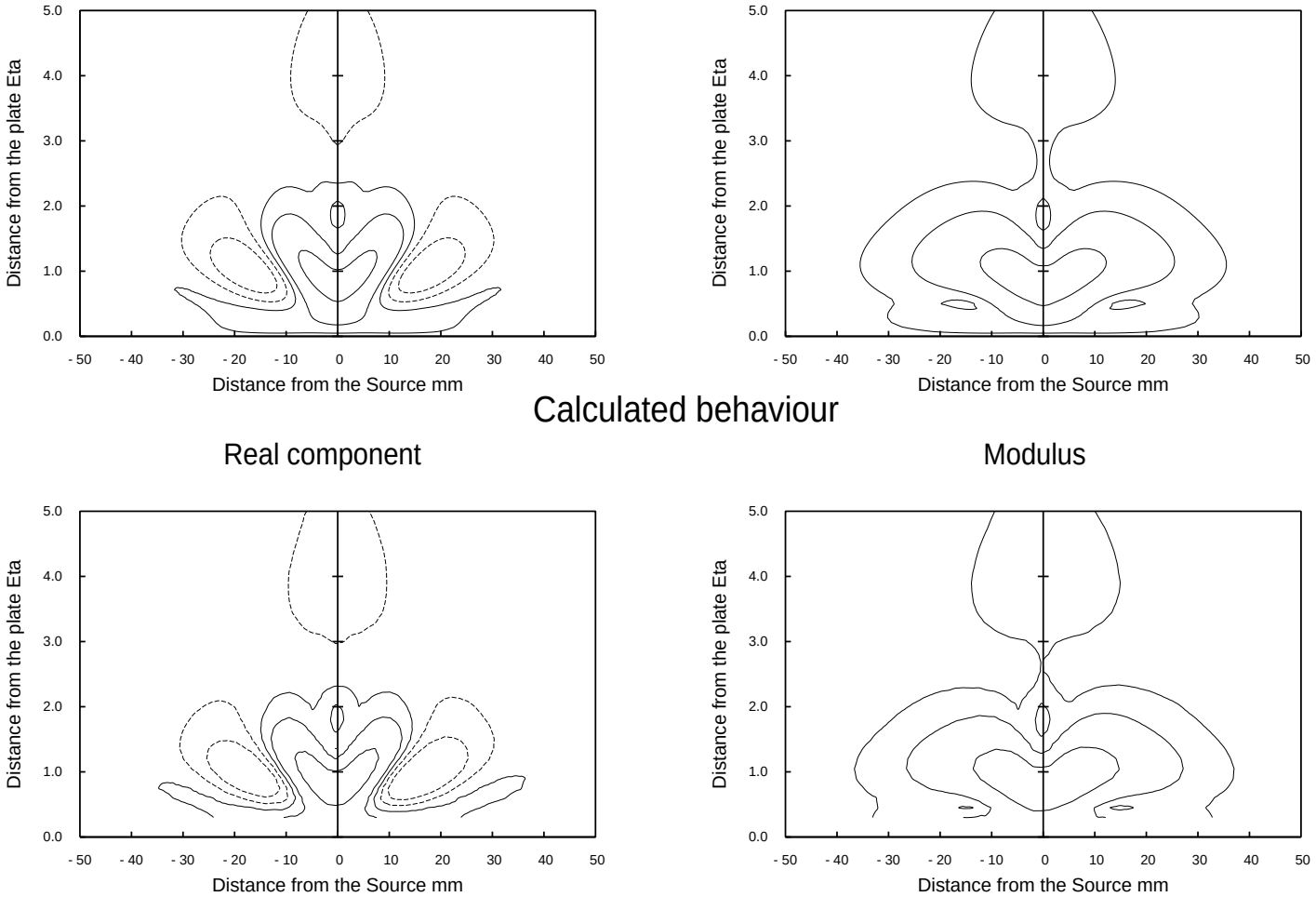

Figure 2 Streamwise Velocity Perturbations across the Span at 100 mm from the Source

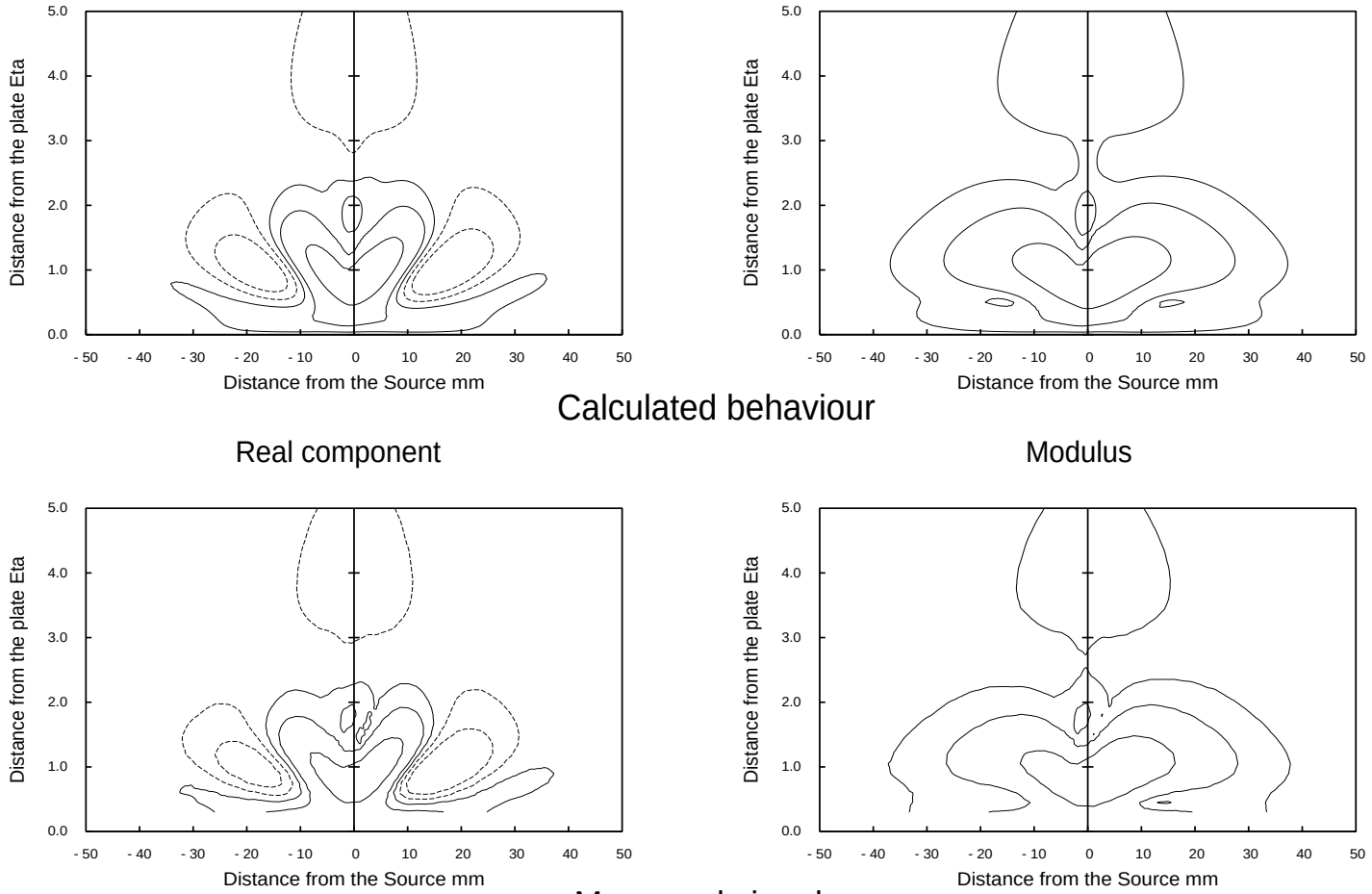

Figure 3 Flowfield across the Span when the Jet is aligned 30 degrees Spanwise